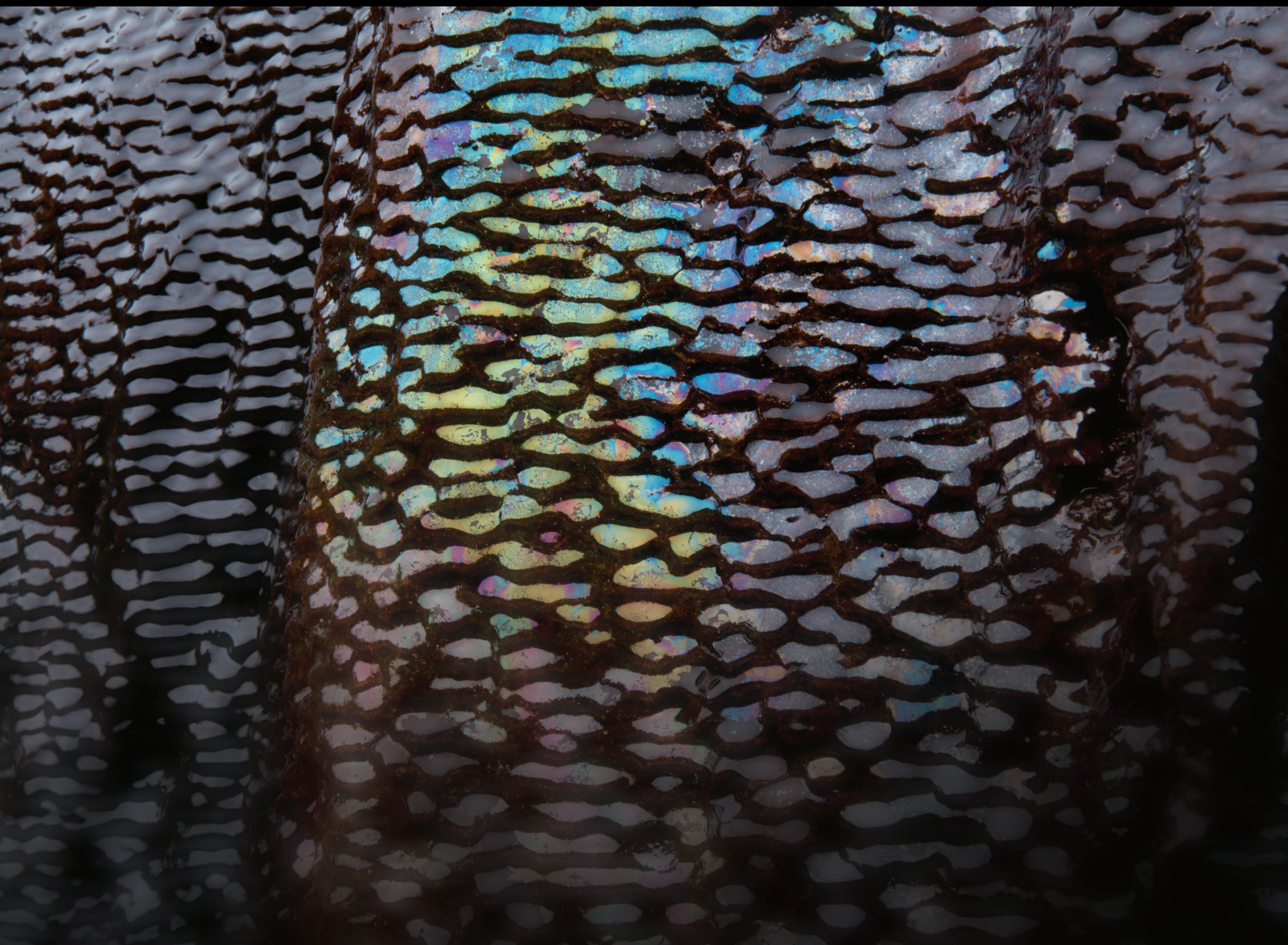


# Innovative Research for Geofluid Flow and Solute Transport in Subsurface from Pore to Terrestrial Scales

Lead Guest Editor: Jet-Chau Wen

Guest Editors: Walter A. Illman, Shujun Ye, and Tianchiyi Yeh



---



# **Innovative Research for Geofluid Flow and Solute Transport in Subsurface from Pore to Terrestrial Scales**

## **Innovative Research for Geofluid Flow and Solute Transport in Subsurface from Pore to Terrestrial Scales**

Lead Guest Editor: Jet-Chau Wen

Guest Editors: Walter A. Illman, Shujun Ye, and Tianchiyi Yeh



Copyright © 2018 Hindawi. All rights reserved.

This is a special issue published in "Geofluids." All articles are open access articles distributed under the Creative Commons Attribution License, which permits unrestricted use, distribution, and reproduction in any medium, provided the original work is properly cited.

## **Editorial Board**

Maurizio Barbieri, Italy  
Mauro Cacace, Germany  
Timothy S. Collett, USA  
Mercè Corbella, Spain  
Cinzia Federico, Italy  
Tobias P. Fischer, USA  
Paulo Fonseca, Portugal  
Paolo Fulignati, Italy

Salvatore Inguaggiato, Italy  
Francesco Italiano, Italy  
Karsten Kroeger, New Zealand  
Cornelius Langenbruch, USA  
Stefano Lo Russo, Italy  
John A. Mavrogenes, Australia  
Ferenc Molnar, Finland  
Julie K. Pearce, Australia

Daniele Pedretti, Finland  
Marco Petitta, Italy  
Christophe Renac, France  
Andri Stefansson, Iceland  
Richard E. Swarbrick, UK  
Mark Tingay, Australia  
Umberta Tinivella, Italy  
Micol Todesco, Italy

# Contents

## **Innovative Research for Geofluid Flow and Solute Transport in Subsurface from Pore to Terrestrial Scales**

Jet-Chau Wen , Walter A. Illman, Shujun Ye, and Tianchiyi Yeh  
Editorial (3 pages), Article ID 8675398, Volume 2018 (2018)

## **Evaluation of the Potential for Dissolved Oxygen Ingress into Deep Sedimentary Basins during a Glaciation Event**

Sergio A. Bea , Danyang Su, K. Ulrich Mayer, and Kerry T. B. MacQuarrie  
Research Article (20 pages), Article ID 9475741, Volume 2018 (2018)

## **High-Resolution Wellbore Temperature Logging Combined with a Borehole-Scale Heat Budget: Conceptual and Analytical Approaches to Characterize Hydraulically Active Fractures and Groundwater Origin**

Guillaume Meyzonnat , Florent Barbecot, José A. Corcho-Alvarado, Antoine Tognelli, Hermann Zeyen, Alexandra Mattei, and Renald McCormack  
Research Article (19 pages), Article ID 9461214, Volume 2018 (2018)

## **Material Exchange and Migration between Pore Fluids and Sandstones during Diagenetic Processes in Rift Basins: A Case Study Based on Analysis of Diagenetic Products in Dongying Sag, Bohai Bay Basin, East China**

W. Meng, J. H. Zeng , Z. Cao, G. Q. Song, Y. S. Wang, J. L. Teng, and Z. Guo  
Research Article (20 pages), Article ID 1653632, Volume 2018 (2018)

## **Predicting Erosion-Induced Water Inrush of Karst Collapse Pillars Using Inverse Velocity Theory**

Banghua Yao, Zhongwei Chen , Jianping Wei, Tianhang Bai, and Shumin Liu  
Research Article (18 pages), Article ID 2090584, Volume 2018 (2018)

## **A Novel Boundary-Type Meshless Method for Modeling Geofluid Flow in Heterogeneous Geological Media**

Jing-En Xiao, Cheng-Yu Ku , Chih-Yu Liu, and Wei-Chung Yeih   
Research Article (13 pages), Article ID 9804291, Volume 2018 (2018)

## **Characterization of Aquifer Multiscale Properties by Generating Random Fractal Field with Truncated Power Variogram Model Using Karhunen–Loève Expansion**

Liang Xue, Diao Li, Cheng Dai, and Tongchao Nan  
Research Article (11 pages), Article ID 1361289, Volume 2017 (2018)

## **Characterization of Origin and Evolution of Formation Water in Buried Hill of Jizhong Depression, China, Using Multivariate Statistical Analysis of Geochemical Data**

Fei Li and Jianhui Zeng  
Research Article (15 pages), Article ID 5290686, Volume 2017 (2018)

## **Three-Dimensional Hydromechanical Modeling during Shearing by Nonuniform Crust Movement**

Yuqing Zhao, You-Kuan Zhang, and Xiuyu Liang  
Research Article (14 pages), Article ID 9605313, Volume 2017 (2018)

## Editorial

# Innovative Research for Geofluid Flow and Solute Transport in Subsurface from Pore to Terrestrial Scales

Jet-Chau Wen<sup>1</sup>, Walter A. Illman,<sup>2</sup> Shujun Ye,<sup>3</sup> and Tianchiyi Yeh<sup>4</sup>

<sup>1</sup>Department and Graduate School of Safety and Environment Engineering, Research Center for Soil & Water Resources and Natural Disaster Prevention, National Yunlin University of Science and Technology, Douliu, Taiwan

<sup>2</sup>Department of Earth and Environmental Sciences, University of Waterloo, Waterloo, ON, Canada

<sup>3</sup>School of Earth Sciences and Engineering, Nanjing University, Nanjing, China

<sup>4</sup>Department of Hydrology and Atmospheric Sciences, University of Arizona, Tucson, AZ, USA

Correspondence should be addressed to Jet-Chau Wen; wenjc@yuntech.edu.tw

Received 22 March 2018; Accepted 25 March 2018; Published 29 April 2018

Copyright © 2018 Jet-Chau Wen et al. This is an open access article distributed under the Creative Commons Attribution License, which permits unrestricted use, distribution, and reproduction in any medium, provided the original work is properly cited.

## 1. Motivation and Background

The subsurface is the world's largest reservoir of fresh water, oil, gas, and ores. Due to climate change resulting in an increased variability in precipitation, soil moisture, and surface water (i.e., more frequent and intense floods and droughts), the global water and food security, maintenance of ecosystems, and large-scale geohazard (e.g., landslides and sinkholes) mitigation have become strategically very important in recent years. Therefore, the sustainable management of subsurface natural resources has become a key element for climate change adaptation. In response to this need, high-resolution characterization, long-term monitoring, and prediction of subsurface processes from pore to terrestrial scales have become necessary. This special issue presents ongoing work on comprehensive analyses of geofluid transport at different scales.

## 2. Contents of the Special Issue

Papers in the special issue are organized into the following themes: exchange and migration of basin materials due to geofluids, three-dimensional hydromechanical modeling, potential for dissolved oxygen ingress into two deep sedimentary basins during a glaciation event, modeling of geofluid flow in heterogeneous geological media, characterization of origin and evolution of formation water in buried hill, prediction of erosion-induced water inrush of karst collapse

pillars, and characterization of hydraulically active fractures and pumped groundwater origin.

In the paper "Material Exchange and Migration between Pore Fluids and Sandstones during Diagenetic Processes in Rift Basins: A Case Study Based on Analysis of Diagenetic Products in Dongying Sag, Bohai Bay Basin, East China" by W. Meng et al., this study referred to the exchange and migration of basin materials that were carried by pore fluids. Specifically, it used 300 core samples from 46 wells for preparation of casting thin sections, SEM, BSE, EDS, inclusion analysis, and isotope analysis in Dongying Sag, Bohai Bay Basin, that is located in East China. According to the results, the material exchange of pore fluids was divided into 5 stages: the evaporation concentration stage, the shale compaction stage, the carboxylic acid dissolution stage featured by predominant dissolution of plagioclases, the organic CO<sub>2</sub> stage, and the alkaline fluid stage.

In the paper "Three-Dimensional Hydromechanical Modeling during Shearing by Nonuniform Crust Movement" by Y. Zhao et al., this research focused on the hydromechanical modeling of a geological formation under shearing by the nonuniform crust movement during the last 10,000 years. It investigated the solid stress and pore pressure coupling processes of the formation from the intact state to that being fractured or faulted. Specifically, two, three-dimensional numerical models were created in which velocities in opposite directions were applied on the boundaries in order to produce the shearing due to the nonuniform crust movement.

According to the results, the stress and pore pressure became more concentrated in and around the middle of the formation as time progressed. In Model I that did not include a fault, the stress and pore pressure concentrated in the middle of the model during shearing, whereas, in Model II that included a fault zone of weakened mechanical properties, they concentrated along the sides of the fault. The distribution of stress determined the pore pressure and that controlled fluid flow. The results of this study could further support practical investigations in geological formations.

In the paper “Evaluation of the Potential for Dissolved Oxygen Ingress into Deep Sedimentary Basins during a Glaciation Event” by S. A. Bea et al., this research used the reactive transport code Par-MIN3P-THCm in order to perform an informed, illustrative set of simulations assessing the depth of penetration of low salinity, O<sub>2</sub>-rich, subglacial recharge. According to the results, the large-scale basic hydrostratigraphy combined with the presence of dense brines at depth resulted in low groundwater velocities during glacial meltwater infiltration. This restricted the vertical ingress of dilute recharge waters. By applying relative simulation models, it was observed that the effective oxidative mineral dissolution rates were low; therefore, they were more conservative compared to other rates found in the literature.

In the paper “A Novel Boundary-Type Meshless Method for Modeling Geofluid Flow in Heterogeneous Geological Media” by J.-E. Xiao et al., this research developed a novel boundary-type meshless method for modeling geofluid flow in heterogeneous geological media based on the integration of the T-Trefftz and F-Trefftz methods [1–3]. It estimated the numerical solutions of geofluid flow by applying a set of particular solutions of the subsurface flow equation. These solutions were expressed in terms of sources located outside the domain of the problem. In order to minimize the impacts of the subsurface flow problems of heterogeneous geological media, the domain decomposition method was adopted. According to the numerical results, the innovative method of this study was highly accurate and computationally efficient, and it presented great numerical stability for solving subsurface flow with a nonlinear free surface in layered heterogeneous geological media even with large contrasts in hydraulic conductivity.

In the paper “Characterization of Origin and Evolution of Formation Water in Buried Hill of Jizhong Depression, China, Using Multivariate Statistical Analysis of Geochemical Data” by F. Li and J. Zeng, this research used the statistical analyses of hierarchical cluster analysis (HCA) and principal component analysis (PCA) in order to evaluate the groundwater samples from the buried hill of Jizhong Depression. The combination of the HCA and PCA within the hydrogeological contexts resulted in the division of the study area into five dynamic areas. According to the findings of this study, the buried hill reservoir in Jizhong Depression was primarily distributed in hydrodynamic blocking and discharge area which can be also favorable for petroleum migration.

In the paper “Predicting Erosion-Induced Water Inrush of Karst Collapse Pillars Using Inverse Velocity Theory” by B. Yao et al., this study presented a suite of fully coupled governing equations considering the processes of water flow,

fracture erosion, and change of rock permeability due to erosion. According to the results, the inverse velocity theory could predict the occurrences of water inrush under different conditions. Also, the time of water inrush had a power relationship with rock heterogeneity, water pressure, and initial particle concentration and an exponential relationship with initial fracture apertures. Tunneling, tailing dam erosion, and other related engineering applications could also be benefited by the findings and the general approach developed through this research.

In the paper “High-Resolution Wellbore Temperature Logging Combined with a Borehole-Scale Heat Budget: Conceptual and Analytical Approaches to Characterize Hydraulically Active Fractures and Groundwater Origin” by G. Meyzonnat et al., this study presented an overview of the thermal processes that shape wellbore temperature profiles under static and dynamic conditions. By using the heat budget developed at the borehole scale, it explained that the temperature logging can be quantitatively enhanced and allow for the calculations of the inflow temperatures through the simultaneous use of a flowmeter. Furthermore, this research showed applied examples that used high-resolution temperature logging, spinner flow metering, and televiowing for three wells installed in fractured bedrock aquifers in the St-Lawrence Lowlands, Quebec, Canada. An improved understanding of inflow temperatures could result in more information on the depth from which groundwater originates during pumping.

In the paper “Characterization of Aquifer Multiscale Properties by Generating Random Fractal Field with Truncated Power Variogram Model Using Karhunen–Loëve Expansion” by L. Xue et al., it is known that the generation of a multiscale random fractal field by directly using a nonstationary power variogram model due to the lack of explicit covariance function is not always easy. Therefore, this study adopted the stationary truncated power variogram model in order to avoid this problem and to generate multiscale random fractal fields using the Karhunen–Loëve (KL) expansion. According to the results, either the unconditional or the conditional (on measurements) multiscale random fractal fields could be generated by using truncated power variogram model and KL expansion when the upper limit of the integral scale was sufficiently large. The main structure of the spatial variation could be described by using only the first few dominant KL expansion terms associated with large eigenvalues. This could result in substantial savings of computational effort when analyzing stochastic flow and transport problems.

### 3. Concluding Remarks

The papers in this special issue provided high research excellence, original ideas, and revolutionary strategies for the characterization, modeling, and analyses of geofluid flow and solute transport in subsurface from pore to terrestrial scales. In addition, the aforementioned research works could lead to a new level of managing the Earth’s natural resources. The thorough understanding of geofluid transport properties is critical in order to adapt more effectively to the extreme

climatic changes, especially in the sustainable usage of natural water resources.

*Jet-Chau Wen  
Walter A. Illman  
Shujun Ye  
Tianchiyi Yeh*

## References

- [1] C.-M. Fan, H.-F. Chan, C.-L. Kuo, and W. Yeih, "Numerical solutions of boundary detection problems using modified collocation Trefftz method and exponentially convergent scalar homotopy algorithm," *Engineering Analysis with Boundary Elements*, vol. 36, no. 1, pp. 2–8, 2012.
- [2] E. Kita and N. Kamiya, "Trefftz method: an overview," *Advances in Engineering Software*, vol. 24, no. 1-3, pp. 3–12, 1995.
- [3] E. Kita, N. Kamiya, and T. Iio, "Application of a direct Trefftz method with domain decomposition to 2D potential problems," *Engineering Analysis with Boundary Elements*, vol. 23, no. 7, pp. 539–548, 1999.

## Research Article

# Evaluation of the Potential for Dissolved Oxygen Ingress into Deep Sedimentary Basins during a Glaciation Event

Sergio A. Bea<sup>1</sup>, Danyang Su,<sup>2</sup> K. Ulrich Mayer,<sup>2</sup> and Kerry T. B. MacQuarrie<sup>3</sup>

<sup>1</sup>CONICET-IHLLA, República de Italia 780, C.C. 47, Azul, Buenos Aires B7300, Argentina

<sup>2</sup>Department of Earth, Ocean and Atmospheric Sciences, University of British Columbia, 2207 Main Mall, Vancouver, BC, Canada V5T 1Z4

<sup>3</sup>Department of Civil Engineering, University of New Brunswick, P.O. Box 4400, Fredericton, NB, Canada E3B 5A3

Correspondence should be addressed to Sergio A. Bea; [sabea@faa.unicen.edu.ar](mailto:sabea@faa.unicen.edu.ar)

Received 24 August 2017; Revised 9 February 2018; Accepted 18 February 2018; Published 24 April 2018

Academic Editor: Tianchiyi Yeh

Copyright © 2018 Sergio A. Bea et al. This is an open access article distributed under the Creative Commons Attribution License, which permits unrestricted use, distribution, and reproduction in any medium, provided the original work is properly cited.

Geochemical conditions in intracratonic sedimentary basins are currently reducing, even at relatively shallow depths. However, during glaciation-deglaciation events, glacial meltwater production may result in enhanced recharge (Bea et al., 2011; and Bea et al., 2016) potentially having high concentrations of dissolved oxygen ( $O_2$ ). In this study, the reactive transport code Par-MIN3P-THCm was used to perform an informed, illustrative set of simulations assessing the depth of penetration of low salinity,  $O_2$ -rich, subglacial recharge. Simulation results indicate that the large-scale basin hydrostratigraphy, in combination with the presence of dense brines at depth, results in low groundwater velocities during glacial meltwater infiltration, restricting the vertical ingress of dilute recharge waters. Furthermore, several geochemical attenuation mechanisms exist for  $O_2$ , which is consumed by reactions with reduced mineral phases and solid organic matter (SOM). The modeling showed that effective oxidative mineral dissolution rates and SOM oxidation rates between  $5 \times 10^{-15}$  and  $6 \times 10^{-13} \text{ mol dm}^{-3} \text{ bulk s}^{-1}$  were sufficient to restrict the depth of  $O_2$  ingress to less than 200 m. These effective rates are low and thus conservative, in comparison to rates reported in the literature. Additional simulations with more realistic, yet still conservative, parameters reaffirm the limited ability for  $O_2$  to penetrate into sedimentary basin rocks during a glaciation-deglaciation event.

## 1. Introduction

In intracratonic sedimentary basins, reducing geochemical conditions are widespread and commonly dominate even at shallow depths close to the ground surface. The maintenance of reducing conditions is often cited as one of the desirable features for deep geological repositories (e.g., [1, 2]). In general, oxygen ( $O_2$ ) ingress to repository depth is considered an exclusion criterion for the construction of deep geologic repositories in view of the potential for oxidative dissolution reactions and the corrosion of copper canisters containing the spent fuel (e.g., [3]). One of the explanations for the rapid development of reducing conditions with increasing depth is that  $O_2$  in the recharge water is consumed due to interactions with redox-buffering minerals (e.g., pyrite and chlorite) present as coatings on the aquifer matrix and solid organic

matter (SOM) [2, 3]. However, over long time periods, glaciation and deglaciation events may affect groundwater flow patterns and the distribution and rate of recharge. For instance, during deglaciation events, melting of ice sheets may result in enhanced recharge of glacial meltwater (e.g., [4–9]). McIntosh et al. [7] summarized geochemical and isotopic evidence for freshwater ingress in North American Paleozoic basins as a consequence of glaciation cycles. For example, McIntosh et al. [7] and references therein showed that freshwater significantly diluted saline brines in the Upper Devonian Antrim Shale across the northern margin of the Michigan Basin as evidenced by a decrease (up to 80%) in bromide concentrations to a depth of 300 m [6]. The source of the freshwater recharge was inferred to be subglacial meltwater, because the  $^{14}\text{C}$  ages correspond to periods of ice cover, and the low  $\delta^{18}\text{O}$  values provide evidence for mixing of

ice sheet derived waters with saline brines and modern precipitation [10, 11]. Several other associated studies reported evidence for recharge and storage of glacial meltwaters in the Michigan Basin, documented by low salinity,  $^{14}\text{C}$  ages ranging from modern to >50 ka, and oxygen isotope values ranging from  $-18$  to  $-13\text{\textperthousand}$  [4, 12–14]. In addition, noble gas signatures have also been used to infer the ingress of cold glacial meltwaters [15, 16].

These recharge waters may also be enriched with dissolved  $\text{O}_2$  relative to present-day interglacial conditions by a factor of 3–5 (e.g., [2, 20]), providing an enhanced oxidation capacity. Oxygen enrichment can be attributed to air entrapment in ice during periods of the glacial advance. During melting of an ice sheet entrapped air may be released into meltwater under elevated hydraulic head conditions, explaining the enriched dissolved  $\text{O}_2$ -concentrations [2, 20]. It is therefore of interest to evaluate the probability for enhanced dissolved  $\text{O}_2$  ingress and migration under these changed recharge conditions. This information can be used to improve the formulation of conceptual and quantitative models for geological repository safety assessment.

The key parameters controlling  $\text{O}_2$  ingress and attenuation in crystalline rocks have been previously identified and evaluated using reactive transport modeling (e.g., [2, 3, 20]). In crystalline rocks, the penetration depth of  $\text{O}_2$  depends largely on the spatial distribution and interconnectivity of subsurface pathways within the fractured porous medium, controlling advective flow. Sidborn and Neretnieks [3] determined that  $\text{O}_2$  may travel long distances in the absence of readily degradable organic matter but also acknowledged that large uncertainties regarding key model parameters remain, leading to the conclusion that the results must be treated with caution pending more accurate and validated data. Although these studies provide information on the redox stability of crystalline environments, we are unaware of observational or modeling studies focused on  $\text{O}_2$  ingress, migration, and attenuation in deep sedimentary basins, in particular over long time frames involving glaciation-deglaciation cycles. Deep sedimentary basins are complex systems requiring the use of a thermo-hydro-chemical and mechanical approach to simulate regional groundwater flow and transport processes in a more realistic way (e.g., see [8, 9]).

The objective of this paper is to evaluate dissolved  $\text{O}_2$  ingress and attenuation in a hypothetical sedimentary basin during a glaciation/deglaciation event by exploring key physical and geochemical parameters that affect the persistence of  $\text{O}_2$ , thereby contributing to an improved understanding of the phenomena governing redox stability of deep geological repositories in sedimentary environments. To achieve this objective, Par-MIN3P-THCm [8, 9, 21–23] is used to perform reactive transport modeling on the basin scale combined with a parameter sensitivity analysis. Transient surface boundary conditions are imposed on the upper part of the model domain to mimic ice sheet advance and retreat (e.g., [9, 24]). Processes included in the current model are non-isothermal density-driven flow and transport, a simplified model accounting for vertical mechanical deformation, as well as geochemical reactions (e.g., aqueous complexation

and mineral dissolution and precipitation including the interaction of dissolved  $\text{O}_2$  with redox-buffering solid phases such as pyrite, chlorite, biotite, and SOM). We acknowledge that the selected mineral phases and SOM represent only a small subset of reduced phases present in sedimentary rocks. However, they represent some of the most abundant and redox active phases, providing an adequate framework to assess  $\text{O}_2$  ingress and attenuation. Regrettably, it is not possible to directly determine oxidative dissolution and SOM oxidation reaction rates to allow for deterministic simulations. Rates are affected by mineral abundance, surface normalized rate constants, effective reactive surface areas, are often microbially mediated, and differ as a function of lithology. In the absence of quantitative knowledge of  $\text{O}_2$  consumption rates in sedimentary basins, the model is used to identify the effective reaction rates required to restrict  $\text{O}_2$  ingress to depths of less than 200 m over the duration of an entire glaciation-deglaciation cycle and to compare these rates to published data on oxidative mineral dissolution rates and oxidation of SOM. This approach allows to evaluate the effectiveness of the redox-buffering capacity of sedimentary basins during periods of glacial meltwater ingress. A relatively shallow depth of 200 m was chosen as tolerable for  $\text{O}_2$  ingress because deep geologic repositories in sedimentary basins are being planned at significantly greater depths (e.g., 500 to 700 m), and 200 m thus provides a conservative redox buffer depth relevant to such repositories. In addition, the sensitivity of  $\text{O}_2$  ingress towards effective rates and  $\text{O}_2$  content in recharge water is investigated.

## 2. General Features of Deep Sedimentary Basins and Impact of Glaciation Cycles on the Groundwater System

Intracratonic sedimentary basins in North America and Eurasia are commonly characterized by Paleozoic sequences of limestones/dolostones interbedded with shales and sandstones and in some cases evaporites (e.g., [1, 4–7]). In the Illinois, Michigan, and Appalachian basins in North America, for instance, the basal Cambrian-Ordovician aquifers are principally comprised of sandstones and carbonates (dolomite and limestone) and confined by shales (e.g., [4]), whereas the Silurian-Devonian aquifers are primarily composed of dolostones and limestones confined by the overlying Upper Devonian black shales, Mississippian grey shales, and siltstones. Furthermore, Silurian-Devonian aquifers in the Michigan and Appalachian basins contain thick sequences of interbedded halite [ $\text{NaCl}$ ] and anhydrite [ $\text{CaSO}_4$ ], which are nearly impermeable (e.g., [4]). Formational waters in these deep Paleozoic sedimentary basins are brines (e.g., [4, 6, 7]) representing in some cases (e.g., in the Michigan Basin) the most saline fluids in the Earth's crust [5, 6]. Notably, brines within these basins are of different types ( $\text{CaCl}_2$  and  $\text{NaCl}$ -type), showing a spatially variable density distribution [6, 8, 9].

The formation and melting of large ice sheets have been proposed as a mechanism for influencing regional-scale groundwater flow systems during the Late Pleistocene

in sedimentary basins located in the interior of the North American and Eurasian cratons. Hydrochemical and isotopic evidence suggests that glacial meltwaters may have displaced high salinity fluids and thus stored freshwater resources on the continents [4, 6, 7, 24–26]. During ice sheet loading, small changes in pore volume as the rock expands or compresses may result in substantial localized changes in the pore fluid pressure [24]. Glacial loading and unloading are considerably faster processes than sedimentation and erosion [24], while these changes in fluid pressure quickly dissipate in highly permeable units, the effects of loading and unloading cycles could induce anomalous fluid pressures that require thousands of years to return to equilibrium conditions in low-permeability units like shales (e.g., [8, 24, 27]). These effects on the flow regime may also affect the ingress and fate of dissolved O<sub>2</sub> into the sedimentary units.

Under present-day conditions, advective solute migration in shallow permeable aquifer units, including transport of dissolved O<sub>2</sub> contained in the surficial recharge water, is limited to shallow depths [8, 9]. In addition, dissolved O<sub>2</sub> could potentially be consumed by reactions with reduced mineral phases (e.g., pyrite, chlorite, or biotite) and SOM, further contributing to O<sub>2</sub>-depleted conditions near the ground surface. The depth to which O<sub>2</sub> can migrate will depend on the interplay between altered fluid circulation patterns, the O<sub>2</sub> concentration in recharge water, and the abundance and reactivity of SOM, as well as sulfide and Fe(II)-bearing mineral phases in the sedimentary units.

### 3. Simulation Approach and Material Property Assignment

Reactive transport simulations were carried out with the code Par-MIN3P-THCm [8, 9, 22, 23]. This code includes the modeling capabilities of previous versions (i.e., MIN3P [21]; MIN3P-D, [28]) but has been enhanced to account for the coupling of thermo-hydro-chemical and mechanical processes [24]. Specific enhancements include (1) calculation of ion activity corrections in high ionic strength solutions using the Harvie-Möller-Weare (HMW) model [29] based on the Pitzer [30] equations; (2) fluid density calculations based on fluid volumetric predictions derived from the Pitzer equations according to Monnin [31]; (3) one-dimensional hydromechanical coupling [27] due to ice sheet advance and retreat; and (4) a numerical formulation to couple energy (heat) transport (following Voss and Provost; [32]) with fluid and solute transport (i.e., density-driven flow controlled by thermohaline convection). In addition, the code has been parallelized to increase its computational efficiency and reduce execution times [23].

**3.1. Conceptual Model and Physical Parameters.** The conceptual model and parameterization for the hypothetical sedimentary basin considered here include the key features of several of the main Paleozoic sedimentary basins in North America. Physical and geochemical model parameters were mainly derived from previous studies in the Michigan and Illinois basins as described in detail in Bea et al. [8, 9]

(i.e., porosity, horizontal and vertical hydraulic conductivity, elastic modulus, Poisson's ratio, volumetric heat capacity, and bulk density).

The simulated basin domain (Figure 1) extends over a horizontal distance of 400 km, has a maximum depth of 4 km, and is composed of a sequence of carbonates (dolostones and limestones, Dol1, Dol2, Dol3, and Lim1), interbedded by sandstones (Sand1, Sand2, Sand3, and Sand4, constituting the main aquifers), and shales (Sh1, Sh2, and Sh3, constituting the main confining units). These units overlay a crystalline basement (Cr). A weathered zone in the crystalline basement (Crw) is assumed to be in direct contact with the sedimentary units. Interbedded evaporites (Ev) are also included within the dolostone units. Note that thin layers (e.g., <50 m) of unconsolidated glacial drift are not included in the current conceptual model. These units are removed and reform during periods of glacial advance and retreat and are not relevant for considering meltwater and solute ingress into the deeper sedimentary rock formations.

The main physical parameters (e.g., porosity and hydraulic conductivity) are considered to decrease with depth following an exponential relationship based on the approach of Bahr et al. [33]. The depth dependence of the hydraulic conductivities was captured by applying the Carman-Kozeny relationship using the depth-dependent porosities and a hydraulic conductivity determined at a reference depth. The depth dependence of other parameters, such as the specific storage coefficient and mechanical loading parameters, was determined in a similar fashion. This approach captures the general trends in parameter variation as a function of depth and is well suited for conceptual simulations (for more details, see [9]).

**3.2. Geochemical Parameters and Initial Conditions.** Formation waters present in Paleozoic sedimentary basins in North America possess chemical compositions that vary between meteoric water and evaporated seawater [4, 6, 19, 34, 35]. Chemical components included in the present reactive transport simulations are H, Ca, Mg, Cl, SO<sub>4</sub>, K, Total Inorganic Carbon (TIC), Na, Br, O<sub>2</sub>, and H<sub>2</sub>O. For the sake of simplicity, the components Al, Fe(II), Fe(III), and H<sub>4</sub>SiO<sub>4</sub> are only considered as part of mineral phases but are neglected for solute transport, since they do not significantly affect solution density and aqueous speciation. The complete set of homogeneous and heterogeneous geochemical reactions included in the simulations is shown in Table 1. Thermodynamic constants for the reactions were taken from Wolery and Daveler [17], whereas the selectivity coefficients for cation exchange reactions were obtained from Appelo and Postma [18]. The virial coefficient database used for the HMW model [29] (at 25°C and 1 atm) was originally developed as a part of the Yucca Mountain project [36]. The fluid density calculations were also based on Pitzer's equations [31, 37] for consistency with the thermodynamic model.

Mineral phases considered include halite [NaCl], anhydrite [CaSO<sub>4</sub>], calcite [CaCO<sub>3</sub>], and dolomite [CaMg(CO<sub>3</sub>)<sub>2</sub>], together with the redox-buffering solids pyrite [FeS<sub>2</sub>], biotite [K(Mg<sub>2</sub>Fe)(Si<sub>3</sub>Al)O<sub>10</sub>(OH)<sub>2</sub>], chlorite [Mg<sub>2</sub>Fe<sub>3</sub>Al<sub>2</sub>Si<sub>3</sub>O<sub>10</sub>(OH)<sub>8</sub>], and SOM (represented

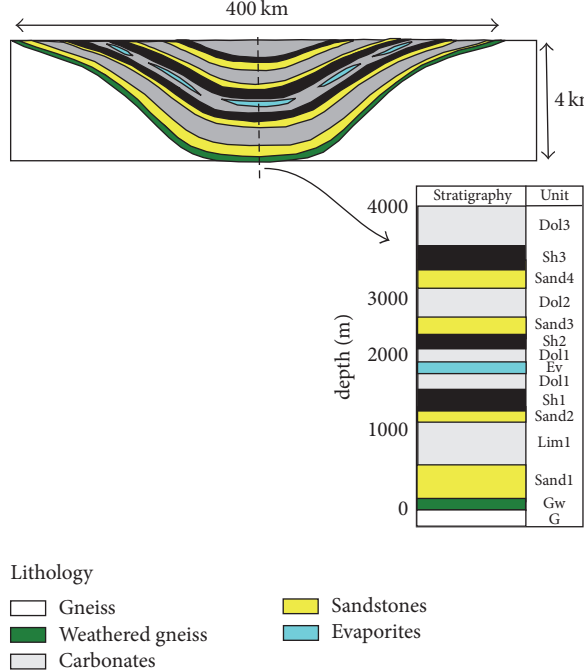


FIGURE 1: Domain, geology, and stratigraphy used to simulate the impact of continental glaciation on O<sub>2</sub> ingress and attenuation in a hypothetical sedimentary basin.

stoichiometrically as CH<sub>2</sub>O). These redox-buffering solids were chosen based on their typical abundance and level of reactivity. Pyrite reacts readily with O<sub>2</sub> (e.g., [38]), while chlorite and biotite also belong to the group of the most reactive Fe-bearing silicate minerals [2]. Organic matter is commonly present in sedimentary rocks, considering the depositional environment. Although this approach provides a highly simplified representation of rock composition in sedimentary basins, it allows making conservative assumptions regarding the abundance of reduced phases in these rocks, which is adequate for this study. Initial mineral contents for the different units are tabulated in Table 2. The initial spatial distribution of volumetric fractions for calcite, dolomite, halite, and anhydrite is identical to those shown in Bea et al. [9], whereas the distribution of the redox-buffering solid phase is shown in Figure 2. Note that calcite, dolomite, and SOM are considered as primary phases in the entire domain, except for the evaporite units (Ev, Figure 1). In the evaporite units, only halite and anhydrite are considered as primary phases. In addition, pyrite is considered to be initially present in shale and sandstone units (Figure 2(a)), while biotite and chlorite are present in the crystalline basement and in the weathered layer (Figure 2(c)). Chlorite is also assumed to be present in the shale units (Figure 2(d)).

The aforementioned redox-buffering mineral phases (i.e., pyrite, biotite, and chlorite) and SOM were modeled as irreversible kinetic reactions in the presence of O<sub>2</sub>. The rate expression for the oxidative dissolution of pyrite is derived from the work of Weaver et al. [12], assuming that only the O<sub>2</sub> pathway is active, with a square root dependence on O<sub>2</sub>. Considering the limited dependence on pH and relatively stable pH conditions in sedimentary basins, the rate

expression was simplified by evaluating the rate constant for a pH = 7 to yield

$$R_{\text{pyr}} = S_{\text{pyr}} \varphi_{\text{pyr}} \rho_{\text{pyr}} k_{\text{pyr}} [\text{O}_2]^{0.5}, \quad (1)$$

where  $R_{\text{pyr}}$  [mol dm<sup>-3</sup> bulk s<sup>-1</sup>] is the oxidative dissolution rate of pyrite,  $[\text{O}_2]$  is the dissolved oxygen concentration [mol l<sup>-1</sup>],  $k_{\text{pyr}}$  is the kinetic rate constant evaluated at pH = 7 [mol<sup>0.5</sup> l<sup>0.5</sup> m<sup>-2</sup> mineral s<sup>-1</sup>],  $\varphi_{\text{pyr}}$  is the mineral volumetric fraction of pyrite [dm<sup>3</sup> mineral dm<sup>-3</sup> bulk],  $\rho_{\text{pyr}}$  is the density of pyrite [g dm<sup>-3</sup> mineral], and  $S_{\text{pyr}}$  is reactive surface area of pyrite [m<sup>2</sup> g<sup>-1</sup>].

The kinetic rate expressions for chlorite and biotite have been adopted from reactive transport simulations in crystalline rock environments ([2] and references therein) and are described by the rate expression:

$$R_i = S_i \varphi_i \rho_i k_i \left( \frac{[\text{O}_2]}{[\text{O}_2] + K_{i,\text{O}_2}} \right), \quad (2)$$

where  $R_i$  [mol dm<sup>-3</sup> bulk s<sup>-1</sup>] is the oxidative dissolution rate of chlorite or biotite,  $k_i$  is the corresponding kinetic rate constant [mol m<sup>-2</sup> mineral s<sup>-1</sup>],  $\varphi_i$  is the mineral volumetric fraction of the phase considered [dm<sup>3</sup> mineral dm<sup>-3</sup> bulk],  $\rho_i$  is the relevant mineral density [g dm<sup>-3</sup> mineral], and  $S_i$  is the reactive mineral surface area [m<sup>2</sup> g<sup>-1</sup>].

The oxidation of SOM is represented by an expression similar to (2), using an effective rate coefficient, but also depending on the abundance of SOM to account for the

TABLE 1: Geochemical reactions considered in the illustrative sedimentary basin example.

	Ref.
Homogeneous reactions	
$\text{HSO}_4^- \rightleftharpoons \text{H}^+ + \text{SO}_4^{2-}$	(1)
$\text{MgOH}^+ + \text{H}^+ \rightleftharpoons \text{H}_2\text{O} + \text{Mg}^{2+}$	(1)
$\text{CaOH}^+ + \text{H}^+ \rightleftharpoons \text{H}_2\text{O}$	(1)
$\text{OH}^- + \text{H}^+ \rightleftharpoons \text{H}_2\text{O}$	(1)
$\text{HCO}_3^- \rightleftharpoons \text{CO}_3^{2-} + \text{H}^+$	(1)
$\text{CO}_2(\text{aq}) + \text{H}_2\text{O} \rightleftharpoons \text{CO}_3^{2-} + 2\text{H}^+$	(1)
$\text{CaCO}_3(\text{aq}) \rightleftharpoons \text{CO}_3^{2-} + \text{Ca}^{2+}$	(1)
$\text{MgCO}_3(\text{aq}) \rightleftharpoons \text{CO}_3^{2-} + \text{Mg}^{2+}$	(1)
$\text{CaSO}_4(\text{aq}) \rightleftharpoons \text{SO}_4^{2-} + \text{Ca}^{2+}$	(1)
$\text{CaCl}^+ \rightleftharpoons \text{Ca}^{2+} + \text{Cl}^-$	(1)
$\text{MgHCO}_3^+ \rightleftharpoons \text{Mg}^{2+} + \text{H}^+ + \text{CO}_3^{2-}$	(1)
Cation-exchange reactions	
$\text{MgX}_2 + 2\text{Na}^+ \rightleftharpoons 2\text{NaX} + \text{Mg}^{2+}$	(2)
$\text{CaX}_2 + 2\text{Na}^+ \rightleftharpoons 2\text{NaX} + \text{Ca}^{2+}$	(2)
$\text{KX} + \text{Na}^+ \rightleftharpoons \text{NaX} + \text{K}^+$	(2)
Dissolution/precipitation reactions	Enthalpy [kcal mol <sup>-1</sup> ]
Halite $\rightleftharpoons \text{Na}^+ + \text{Cl}^-$	-0.918
Calcite $\rightleftharpoons \text{CO}_3^{2-} + \text{Ca}^{2+}$	2.585
Dolomite $\rightleftharpoons 2\text{CO}_3^{2-} + \text{Ca}^{2+} + \text{Mg}^{2+}$	8.29
Anhydrite $\rightleftharpoons \text{SO}_4^{2-} + \text{Ca}^{2+}$	3.769
Pyrite + $3.75\text{O}_2(\text{aq}) - 0.5\text{H}_2\text{O} \rightleftharpoons \text{Fe}^{3+} + 2\text{SO}_4^{2-} + \text{H}^+$	(3)
Biotite + $0.25\text{O}_2(\text{aq}) + 11\text{H}^+ \rightleftharpoons \text{K}^+ + 2\text{Mg}^{2+} + \text{Al}^{3+} + \text{Fe}^{3+} + 3\text{H}_4\text{SiO}_4 + 0.5\text{H}_2\text{O}$	(3)
Chlorite + $0.75\text{O}_2(\text{aq}) + 19\text{H}^+ \rightleftharpoons 2\text{Mg}^{2+} + 2\text{Al}^{3+} + 3\text{Fe}^{3+} + 3\text{H}_4\text{SiO}_4 + 7.5\text{H}_2\text{O}$	(3)
OrganicMatter + $\text{O}_2(\text{aq}) \rightleftharpoons \text{CO}_3^{2-} + 2\text{H}^+$	(3)

<sup>(1)</sup>Equilibrium constant taken from Wolery and Daveler [17]. <sup>(2)</sup>Selectivity coefficients taken Appelo and Postma [18]. <sup>(3)</sup>Not controlled by equilibrium [2].

distribution of organic matter in the different sedimentary units:

$$R_{\text{SOM}} = \varphi_{\text{SOM}} k_{\text{eff,SOM}} \left( \frac{[\text{O}_2]}{[\text{O}_2] + K_{\text{SOM,O}_2}} \right), \quad (3)$$

where  $R_{\text{SOM}}$  [mol dm<sup>-3</sup> bulk s<sup>-1</sup>] is the oxidation rate of SOM,  $k_{\text{eff,SOM}}$  is the effective rate coefficient [mol dm<sup>-3</sup> SOM s<sup>-1</sup>], and  $\varphi_{\text{SOM}}$  is the volumetric fraction of organic matter present in the solid phase [dm<sup>3</sup> SOM dm<sup>-3</sup> bulk].

The kinetic parameters used in the simulations are summarized in Table 3. Using the volume fractions listed in Table 2, this approach accounts for the presence and abundance of reduced mineral phases and SOM in the various sedimentary units, when quantifying O<sub>2</sub> consumption rates. For the base case simulation, the reactive surface areas for pyrite, chlorite, and biotite and the effective rate coefficient for SOM were set to achieve oxidative dissolution rates that limit dissolved O<sub>2</sub> ingress with concentrations above  $1 \times 10^{-9}$  mol l<sup>-1</sup> (corresponding to  $3.2 \times 10^{-5}$  mg l<sup>-1</sup>) to a depth of 200 m. As indicated above, this depth was selected to

conservatively define a tolerable depth of O<sub>2</sub> ingress with regard to deep geologic repositories.

The model was run for 30,000 years using present-day boundary conditions to obtain a quasi-steady-state representation of conditions during an interglacial period. Pressure head, Darcy velocity, and fluid density distributions obtained during this simulation were used as the initial conditions for the subsequent glaciation/deglaciation simulation (following the approach of Bea et al. [9]). The initial temperature distribution at the top of the basin linearly varies from 0 to 10°C from the right to left side of the basin. This temperature distribution is representative of the north-south geographic temperature variation during the interglacial period, if the basin is located in northern latitudes. Because Par-MIN3P-THCm uses the Van't Hoff and Arrhenius equations to account for the thermal dependence of the equilibrium constants and kinetic rates [8, 9, 21], respectively, the equilibrium constants were locally adjusted in each cell of the mesh to reflect the initial temperature distribution. Initial chemical water compositions were computed in agreement with these conditions assuming thermodynamic equilibrium with the

TABLE 2: Initial mineral contents (%) considered in the reactive transport simulations (for reference see Bea et al., [9]).

Mineral	Cr	Crw	Sand1	Lim1	Sand2	<sup>(1)</sup> Sh1	Dol1	E <sub>V</sub>	<sup>(1)</sup> Sh2	Sand3	Dol2	Sand4	<sup>(1)</sup> Sh3	Dol3
Calcite	0	0	9	89	9	10	4	9	9	10	9	9	9	10
Dolomite	0	0	1	10	1	89.99	36	1	1	89.99	1	1	1	89.99
Halite	0	0	0	0	0	0	50	0	0	0	0	0	0	0
Anhydrite	0	0	0	0	0	0	0	10	0	0	0	0	0	0
Pyrite	0	0	0.1	0	0.1	2	0	0	2	0.1	0	0.1	0	0
Biotite	4	4	0	0	0	0	0	0	0	0	0	0	0	0
Chlorite	0.7	0.7	0	0	0	10	0	0	10	0	0	0	0	0
Organic matter	0	0	0.1	1	0.1	0.4	0.1	0	0.4	0.1	0.1	0.1	10	0.1
Nonreactive minerals	95.3	90	90.0	0	90	90	0	0	90	90	0	90	90	0

<sup>(1)</sup>Based on rock composition for Queenston, Georgian Bay, and Blue Mountain Formations reported by Mazurek [1].

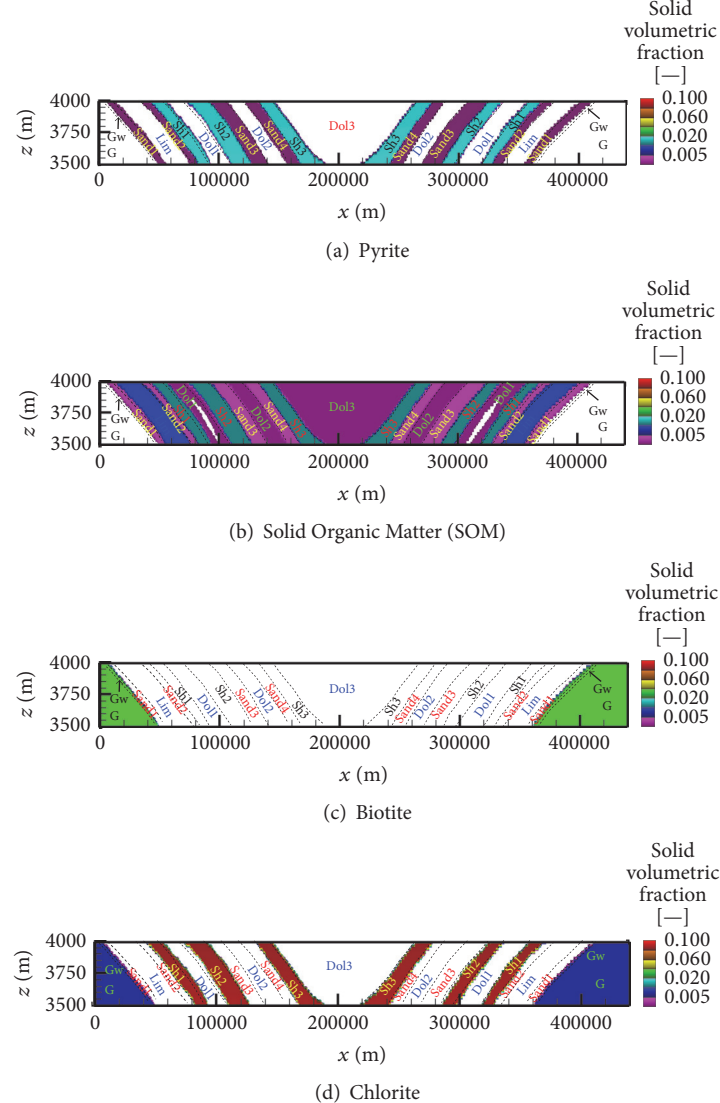


FIGURE 2: Initial distribution of the volumetric contents of redox-buffering minerals. (a), (b), (c), and (d) are pyrite, organic matter, biotite, and chlorite contents, respectively. Vertical exaggeration 100 : 1.

TABLE 3: Kinetic parameters and solid properties for the redox-buffering minerals used in base case simulation.

<sup>(1)</sup> Redox-buffering mineral	$k_i$	$K_{i,O_2}$ [mol l <sup>-1</sup> ]	Density [g dm <sup>-3</sup> mineral]	Reactive surface area [m <sup>2</sup> g <sup>-1</sup> ]
<sup>(2)</sup> Pyrite (diss.)	<sup>(3)</sup> $10^{-9}$	-	5,020	<sup>(6)</sup> $5 \times 10^{-5}$
<sup>(2)</sup> Biotite (diss.)	<sup>(4)</sup> $10^{-12.25}$	$10^{-7}$	2,930	<sup>(6)</sup> $5 \times 10^{-5}$
<sup>(2)</sup> Chlorite (diss.)	<sup>(4)</sup> $10^{-12.25}$	$10^{-7}$	2,600	<sup>(6)</sup> $5 \times 10^{-5}$
<sup>(2)</sup> Organic matter (diss.)	<sup>(5,6)</sup> $5 \times 10^{-12}$	$5 \times 10^{-5}$	-	-

(1) derived from Weaver et al. [12]; (2) following Spiessl et al. [2] and references therein; (3) in [mol<sup>0.5</sup> l<sup>0.5</sup> m<sup>-2</sup> minerals s<sup>-1</sup>]; (4) in [mol m<sup>-2</sup> mineral s<sup>-1</sup>]; (5) in [mol dm<sup>-3</sup> SOM s<sup>-1</sup>]; (6) set for base case.

primary mineral phases calcite and dolomite, in addition to gypsum and halite in the units with evaporites.

### 3.3. Discretization and Boundary Conditions for the Glaciation Scenario.

The computational domain was discretized using 45,000 cells; 450 cells evenly distributed in the  $x$  (horizontal)

direction, and 100 cells distributed in the  $z$  (vertical) direction. The upper part of the mesh was refined in order to better resolve the processes occurring in the shallow part of the aquifers.

The glaciation scenario boundary conditions for flow, energy, and solute transport are the same as used by Bea et

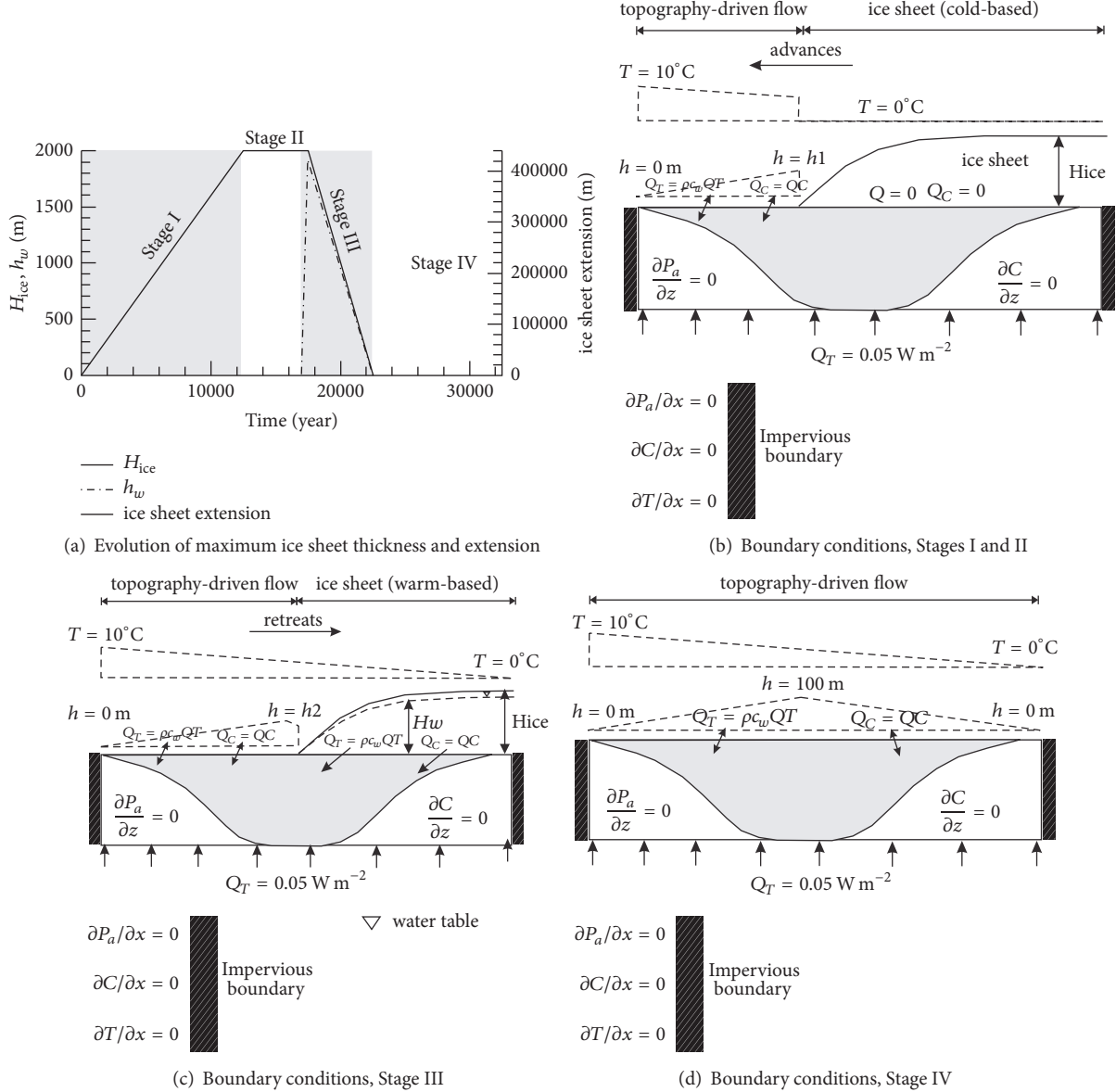


FIGURE 3: Reproduced from [9] with permission. (a) Glaciation scenario used to specify boundary conditions along the top boundary of the model domain. (b), (c), and (d) Model boundary conditions for flow, solute, and energy transport equations.  $h$ : hydraulic head [m];  $T$ : temperature [ $^\circ C$ ];  $C$ : concentration [ $mol L^{-3}$ ];  $Q$ : volumetric recharge [ $L^{-3} T^{-1}$ ];  $Q_c$ : solute mass flux [ $mol T^{-1}$ ]; and  $Q_T$ : heat flux per unit of surface [ $E T^{-1} L^{-2}$ ].

al. [9], and they are shown in Figure 3. Note that, for flow, impervious boundaries were assumed for the two sides and the bottom of the domain. In order to illustrate the potential hydrogeological and geochemical perturbations generated by ice sheet movement over the sedimentary basin described above, a simplified glaciation scenario was applied along the top boundary (Figure 3(a)). The glaciation scenario consists of four stages that generically represent the last glacial maximum episode of ice advance and retreat in North America [39], following an approach similar to that used for previous illustrative basin scale simulations (e.g., [24]): (1) Stage I corresponds to a phase of ice sheet accumulation (i.e., loading, for a period of 12,500 years), (2) Stage II represents

a constant ice sheet thickness for a period of 5,000 years, (3) Stage III corresponds to the phase of ice sheet melting and retreat (i.e., unloading, for a period of 5,000 years), and (4) Stage IV is representative of conditions with no ice present (i.e., return to present-day surface boundary conditions). Note that the loading/unloading cycle shown in Figure 3(a) is asymmetric. It is based on paleoclimatic reconstructions using isotopic data as well as ice sheet models that usually suggest a more rapid ice sheet retreat (driven by rising temperatures) than its previous accumulation (mostly driven by precipitation rates) (e.g., [24, 39]). Taking this asymmetric evolution into account, anomalous fluid pressures in recently glaciated areas should be expected, including regions of

TABLE 4: Chemical composition of brines and brackish waters considered in the reactive transport simulations (chemical compositions taken from Hobbs et al. [19]).

	Formation and boundary water compositions				
	(1)	(2)	(3)	(4)	(5)
pH	6	6	6	6	6
<sup>(6)</sup> Ca	1.5	0.77	0.2	0.19	$6.2 \times 10^{-4}$
<sup>(6)</sup> Mg	$6.5 \times 10^{-3}$	$4 \times 10^{-2}$	$8.6 \times 10^{-3}$	$10^{-2}$	$8.2 \times 10^{-4}$
<sup>(6)</sup> Cl	6	4.15	6.24	3.61	$2.9 \times 10^{-3}$
<sup>(6)</sup> SO <sub>4</sub>	$5.4 \times 10^{-4}$	$4 \times 10^{-3}$	$1.1 \times 10^{-2}$	$5.2 \times 10^{-5}$	$2.6 \times 10^{-4}$
<sup>(6)</sup> K	$3.4 \times 10^{-2}$	$5.7 \times 10^{-2}$	0.07	0.12	$6.4 \times 10^{-5}$
<sup>(6,7)</sup> TIC	$1.2 \times 10^{-4}$	$3.2 \times 10^{-4}$	$5.2 \times 10^{-4}$	$1.8 \times 10^{-3}$	$1.7 \times 10^{-5}$
<sup>(6)</sup> Na	2.85	2.49	5.77	3	$5.2 \times 10^{-4}$
<sup>(6)</sup> Br	$1.8 \times 10^{-2}$	$9.7 \times 10^{-3}$	$7.4 \times 10^{-3}$	$5.6 \times 10^{-3}$	$4 \times 10^{-5}$
<sup>(10)</sup> O <sub>2</sub> (aq)	-	-	-	-	1.0 (or 0.21)
<sup>(6)</sup> Fe(III)	-	-	-	-	-
<sup>(6)</sup> Al(III)	-	-	-	-	-
Chemical signature	Ca-Na-Cl	Na-Cl	Na-Cl	Na-Cl	-
<sup>(6)</sup> Ionic strength	7.6	4.97	6.48	3.82	$5.2 \times 10^{-3}$
<sup>(8)</sup> TDS	0.34	0.24	0.37	0.21	$2 \times 10^{-4}$
<sup>(9)</sup> Density	1217	1150	1204	1128	997
SI <sub>Hal</sub>	-0.22	-0.71	0	-0.78	-7.47
SI <sub>Cal</sub>	0	0	0	0	-4.44
SI <sub>Dol</sub>	0	0	0	0	-7.64
SI <sub>Anhy</sub>	-0.82	-0.25	0	-2.62	-2.76

<sup>(1)</sup>Units G, Gw, Sand1, and Sand2; <sup>(2)</sup>units Lim1, Sh1, and Doll; <sup>(3)</sup>unit Ev; <sup>(4)</sup>units Sh2, Sand3, Sand4, Sh3, Dol2, and Dol3; <sup>(5)</sup>meteoric water; <sup>(6)</sup>units in  $\text{mol l}^{-1}$ ; <sup>(7)</sup>total Inorganic Carbon; <sup>(8)</sup>units in  $\text{kg l}^{-1}$ ; <sup>(9)</sup>units in  $\text{kg m}^{-3}$ ; <sup>(10)</sup>units in partial pressure of O<sub>2</sub>(g) in atm.

overpressure and underpressure (e.g., see [24]). In the current glaciation scenario, the maximum ice sheet thickness and extent were 2,000 m and 440 km, respectively, which implies complete ice sheet coverage of the basin during the Stage II glacial maximum.

At the beginning of the simulation (and also for Stage IV, Figure 3(d)), a prescribed head representing topographically driven flow was imposed on the upper boundary. In this case, solute mass fluxes were based on meteoric water composition and heat fluxes were calculated based on a prescribed temperature distribution that was assumed for the upper boundary of the domain (Figure 3(d)). A constant heat flux of 0.05 W m<sup>-2</sup> was imposed at the bottom of the domain (e.g., [24]) (see Q<sub>T</sub> in Figure 3) during all stages of the simulations.

During ice accumulation (i.e., Stage I), prescribed heads representing topographically driven flow were imposed on the periglacial area, the extension of which depended on the glaciation stage (Figure 3(a)), whereas a cold-based (nonmelting) condition, represented by a zero-flux boundary condition, was assumed under the ice sheet. The latter assumption was based on paleoclimate reconstructions in ice-covered regions during the last glaciation, which implied that groundwater recharge was prevented by overlying glaciers [24] (Figure 3(b)). A prescribed temperature of 0°C was imposed under the ice sheet. Note that, during this initial stage, the ice sheet progressively advanced over the basin from right to left, thus inducing a mechanical load on the

underlying sedimentary units (Figure 3(a)); by 12,500 years the basin was assumed to be entirely glaciated.

During Stage III (Figure 3(a)), warm-based (i.e., melting) conditions were assumed beneath the retreating ice sheet. Under such conditions, a direct hydraulic connection between the glacial meltwater and the land surface is established (Figure 3(c)). A fixed hydraulic head corresponding to 95% of the ice sheet thickness was therefore specified [9, 24] (Figure 3(a)). Boundary solute fluxes beneath the ice sheet during Stage III were computed based on the water flux and an oxygen-enriched meltwater chemical composition (i.e., Solution 5 in Table 4).

The conceptual model for glaciation-deglaciation implies that recharge of oxygenated water occurs: (a) during interglacial periods, (b) during the period of glacial advance in unglaciated regions in front of the advancing ice sheet, and (c) during glacial retreat in unglaciated regions and beneath the retreating ice sheet. During Stages I and II, corresponding to the period of glacial advance and glacial maximum, respectively, no O<sub>2</sub> ingress occurs beneath the ice sheet because cold-based conditions were assumed. During glacial retreat, elevated O<sub>2</sub> concentrations were assumed in the meltwater beneath the ice sheet.

#### 4. Evaluation of O<sub>2</sub> Ingress and Attenuation

To investigate the impact of a glaciation cycle and uncertain geochemical parameters on O<sub>2</sub> ingress and consumption, a

TABLE 5: Description of the simulation scenarios included in the sensitivity analysis.

Scenario Name	Rate parameters	$(^1)\text{O}_2$ contents in meltwater
Base case	$S_i, k_{\text{eff,SOM}}$ from Table 3	1
Scenario 1	$S_i, k_{\text{eff,SOM}}$ increased 10-fold	1
Scenario 2	$S_i, k_{\text{eff,SOM}}$ from Table 3	0.21
Scenario 3	$S_i, k_{\text{eff,SOM}}$ increased 10-fold	0.21

<sup>(1)</sup>Partial pressure of  $\text{O}_2(\text{g})$  in atm corresponds to  $60 \text{ mg l}^{-1}$  for 1 atm and  $12.6 \text{ mg l}^{-1}$  for 0.21 atm.

base case and three sensitivity scenarios were simulated. The main features of these scenarios are summarized in Table 5. The relevant rate parameters for the base case simulation were set such that  $\text{O}_2$  ingress was limited to 200 m at all locations during the entire glaciation-deglaciation cycle for reasons discussed above. Sensitivity analyses were then used to evaluate  $\text{O}_2$  ingress for slightly less conservative and more realistic assumptions. The results of the base case scenario are described in detail, while the sensitivity scenarios are used to provide additional information on the effect of  $\text{O}_2$  consumption rates and  $\text{O}_2$  concentrations in source glacial meltwater on depth of  $\text{O}_2$  penetration.

## 5. Results and Discussion of the Base Case Simulation

For the base case scenario, the evolution of flow, thermal and hydrogeochemical conditions (excluding redox chemistry) are described in detail by Bea et al. [9]. However, to provide the necessary context, we summarize here the key aspects of these modeling results and simultaneously enhance the focus by including results related to the  $\text{O}_2$  attenuation and redox stability of the basin.

**5.1. Fluid Pressure, Flow, Solution Density, and Thermal Evolution.** As a consequence of dense brines at depth and the near horizontal layering of the hydrogeological units that form the basin (note the significant vertical exaggeration, for instance, in Figure 4) the active flow regime is generally restricted to shallow regions (less than 300–400 mbgs) for the full duration of the simulation. In this context, the region affected by active flow is related to the depth of penetration of low salinity waters.

Point pressure heads in the most deformable units increase due to ice sheet loading (e.g., Stage I, ice accumulation) throughout the basin. The magnitudes of the pressure head changes depend primarily on the hydraulic conductivity and the hydromechanical loading efficiency coefficient assigned to the various hydrogeological units (Figures 4(a) and 4(b)). Pressure heads increase beneath the retreating ice sheet in shallow permeable units (see results at 20,000 years, Figure 4(a)) as a consequence of the hydraulic connection between the now warm-based melting ice sheet and these sedimentary units (see Stage III in Figure 4(b)). Some of the highest Darcy velocities are generated in the shallow aquifers during the early stages of glacial retreat (e.g., on the order of  $10^{-1}$  to  $1 \text{ m yr}^{-1}$ ; see Bea et al. [9] for details).

Locally, a decrease of solution density and specific ion concentrations can be observed in response to meltwater ingress during the period of glacial retreat (Figures 4(c) and 4(d)). Isolated lenses of fresh water reach depths of up to 350 m within confined aquifers that subcrop in the model domain (Figure 4(c)). Focusing on the upper 1,000 m of the basin and using chloride concentrations as an indicator for solution density, the ingress of glacial meltwater during the temperate glacial retreat period is observed (exemplified by comparing concentration distributions at  $T = 17,000$  and 20,000 years, Figure 5). Meltwater ingress to depths of approximately 350 m occurs principally within the more permeable dolostone and sandstone units present in the basin (Figure 5).

In addition, the simulation results indicate that the basin remains generally thermally stable with limited perturbations of groundwater temperature in the shallow region as the ice advances (Figures 4(e) and 4(f)).

**5.2.  $\text{O}_2$  Ingress and Attenuation.** In addition to the processes of dedolomitization, evaporite dissolution, and ion exchange (see Bea et al. [8, 9] for more discussion), redox-buffering mineral phases are also expected to contribute to water-rock interactions. In particular, the oxidative dissolution of reduced mineral phases and the oxidation of SOM are expected to significantly attenuate the depth of  $\text{O}_2$  penetration in glacial recharge as is evident in the base case simulation during Stage III, the temperate glacier retreat (see Figure 3(a)).

The base case simulation demonstrates that the distribution and attenuation of  $\text{O}_2$  is controlled by the presence and abundance of the  $\text{O}_2$ -consuming phases, hydrogeological processes, and the bed-boundary conditions assumed during the advance and retreat of the ice sheet. During quasi-steady-state interglacial conditions (e.g.,  $t = 0$  years), only very limited ingress of  $\text{O}_2$  into the sedimentary basin is seen, mostly focused on the dolostone units Dol2 and Dol3 (Figure 6). During the period of glacial advance and glacial maximum (i.e., Stages I and II), dissolved  $\text{O}_2$  concentrations in the sedimentary basin are observed to decline relative to interglacial conditions. This behavior is due to the lack of recharge below the cold-based ice sheet (see results at 17,000 years in Figure 6). Oxygen present in the sedimentary units is consumed under these conditions by reactions with redox-buffering mineral phases and SOM (Figures 6 and 7). This trend is most clearly observed in the dolostone unit Dol2, where dissolved  $\text{O}_2$  concentrations at 25 m depth abruptly

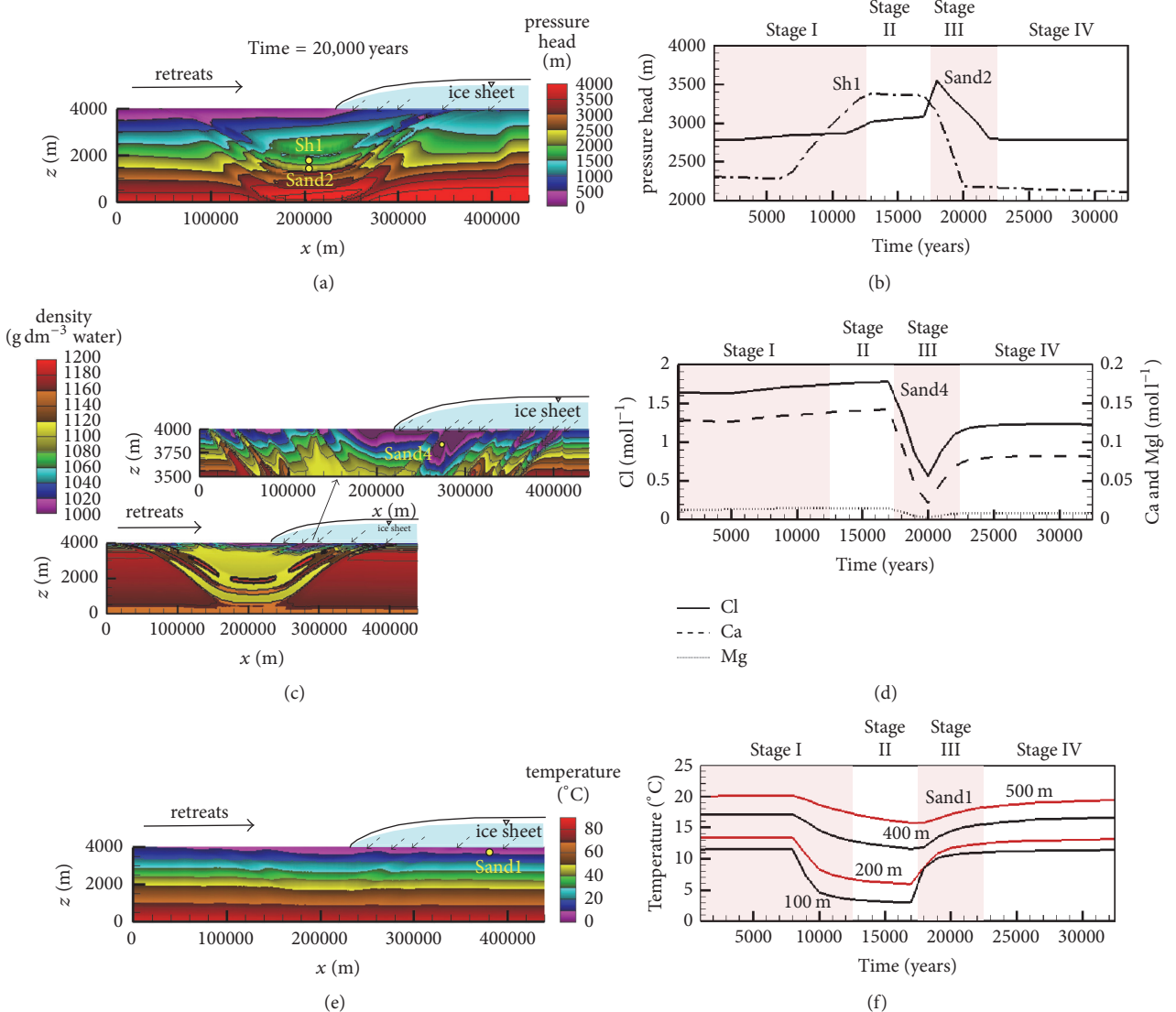


FIGURE 4: Simulation results for the illustrative sedimentary basin simulation. (a) and (b) Spatial distribution of point pressure heads at 20,000 years, and its temporal evolution at observation points located in a sandstone aquifer (Sand2, observation point located at 2,800 m depth) and in a shale aquitard (Sh1, observation point located at 2,300 m depth). (c) and (d) Spatial distribution of density at 20,000 years, and its temporal evolution at observation point located in sandstone aquifer (Sand4 observation point located at 300 m depth). (e) and (f) Spatial distribution of temperature at 20,000 years, and its temporal evolution at observation points located in sandstone aquifer (Sand1, depths indicated on figure).

decrease below the numerical detection limit as the ice sheet overruns this unit at  $T = 4,000$  years (Figure 7(c)). Oxygen does not reappear in this unit until the onset of glacial retreat and the establishment of warm-based glacial conditions. Similar behavior can be observed in other sedimentary units during the stage of glacial advance (Figure 7).

The maximum  $\text{O}_2$  ingress takes place during glacial meltwater production and infiltration (i.e., Stage III) with simulation results showing the highest  $\text{O}_2$ -concentrations in the more permeable units (i.e., Sand1, Sand2, Sand3, Sand4, Dol2, and Dol3, see Figure 6,  $T = 20,000$  years). Oxygen ingress is also clearly depicted in the temporal concentration evolution at different observation locations (Figure 7). For

instance, in Sand3 at 25 m depth,  $\text{O}_2$  concentrations increase by almost five orders of magnitude during the retreat and melting stage; however,  $\text{O}_2$  increase is negligible at greater depths (Figure 7(d)). Maximum  $\text{O}_2$  concentrations at 25 m depth are already close to one order of magnitude lower than the  $\text{O}_2$  content in the ingressing meltwater (i.e.,  $1.3 \times 10^{-3} \text{ mol l}^{-1}$ ), demonstrating the important role of oxidative dissolution reactions.

The rapid  $\text{O}_2$  increases seen at the onset of Stage III, mainly at 25 m depth in several of the more permeable units (see results at 17,500 years in Dol3, Sand3, Dol1, Sand2, and Sand1 in Figures 7(a), 7(d), 7(e), 7(f), and 7(g), resp.), can be attributed to rapid  $\text{O}_2$  ingress as a consequence

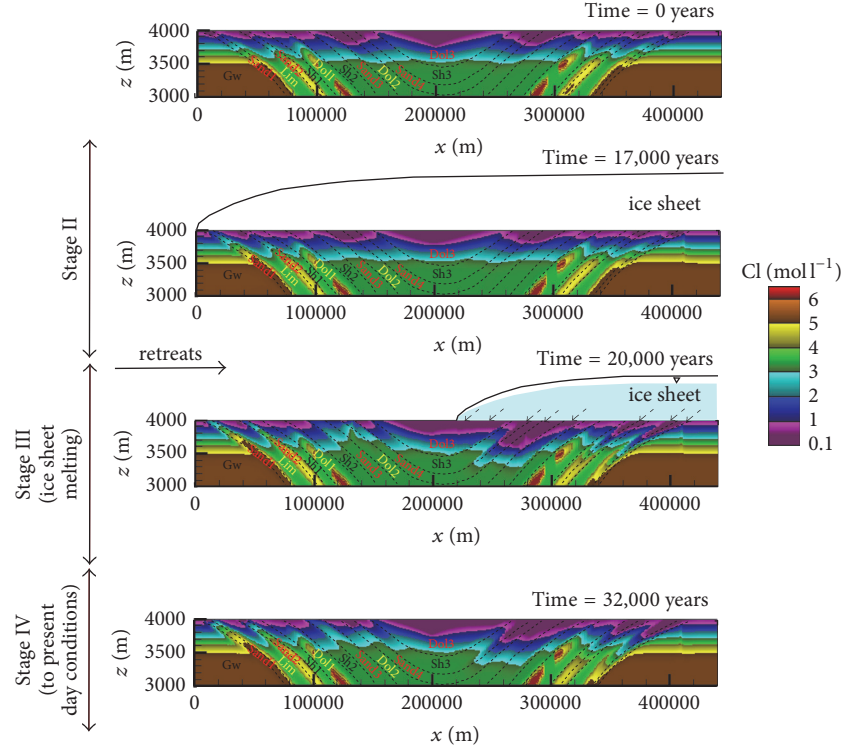


FIGURE 5: Spatial Cl concentration distributions at different times for the base case simulation (i.e., at 0, 17,000, 20,000, and 32,000 years), corresponding to the initial condition, the end of Stage II, Stage III, and the final condition.

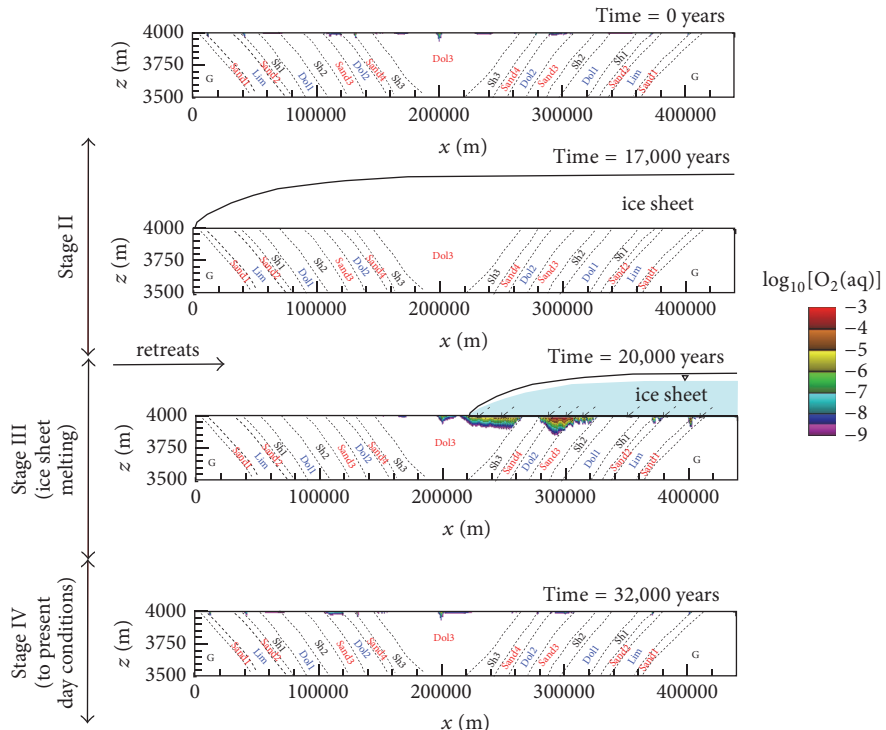


FIGURE 6: Spatial  $\text{O}_2(\text{aq})$  concentration distributions at different times for the base case simulation (i.e., at 0, 17,000, 20,000, and 32,000 years), corresponding to the initial condition, the end of Stage II, Stage III, and the final condition.  $\text{O}_2$  concentrations in  $\text{mol l}^{-1}$ .

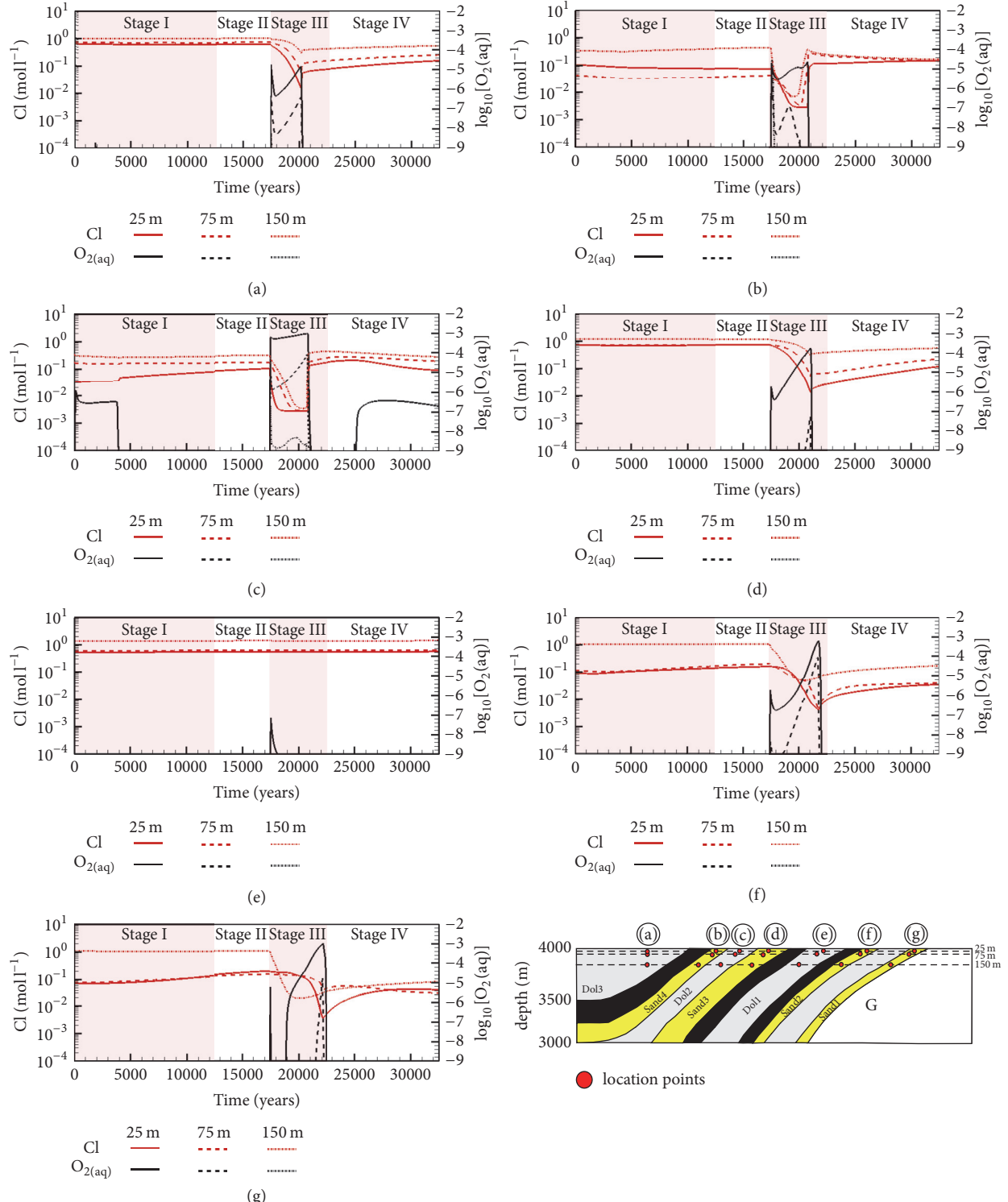


FIGURE 7: Temporal evolution of dissolved  $O_2$  and Cl concentrations at the different observation point locations for the base case simulation. (a), (b), (c), (d), (e), (f), and (g) for Dol3, Sand4, Dol2, Sand3, Doll, Sand2, and Sand1, respectively.  $O_2$  concentrations in  $\text{mol l}^{-1}$ . If  $O_2$  profiles are not visible for a specific depth and unit, concentrations remain below  $1 \times 10^{-9} \text{ mol l}^{-1}$  for duration of simulation.

of the instantaneous change in boundary conditions to a warm-based ice sheet with an imposed piezometric head of 95% of the ice sheet thickness. The subsequent decline and increase in O<sub>2</sub> concentrations (Figure 7) results from the dynamic interactions between declining hydraulic heads as the ice sheet retreats and hydromechanical unloading, affecting hydraulic head distributions and groundwater velocities within the groundwater system.

Later during Stage III, O<sub>2</sub>-concentrations diminish substantially in Dol3, Sand4, Dol2, and Sand3 and towards the end of this stage also in Sand2 and Sand1 as the ice sheet retreats. This decline is due to slowing recharge related to the decrease of the ice sheet thickness and lower hydraulic heads, limiting the driving force for meltwater ingress, while O<sub>2</sub>-consuming reactions remain active at similar rates.

The most significant O<sub>2</sub> ingress is seen in the Dol2 and Dol3 units, even though these units do not possess the highest hydraulic conductivities. In these units, the relative lack of O<sub>2</sub> attenuation is due to the absence of the redox-buffering mineral phases and the low abundance of SOM (see Table 2). On the other hand, the more permeable sandstones show stronger attenuation potential, which can be attributed to the presence of pyrite (Table 2).

A comparison of the results for the depth of freshwater ingress, evidenced by the decline of chloride concentrations and the depth of O<sub>2</sub>-ingress (compare Figures 5 and 6; see Figure 7), illustrates the enhanced attenuation of O<sub>2</sub>. This outcome reaffirms the important role of oxidative dissolution reactions and SOM oxidation, inhibiting O<sub>2</sub> ingress in addition to hydraulic controls imposed by the architecture of the site-specific hydrostratigraphy and the presence of dense brines within the sedimentary basin groundwater system.

At the end of the simulation (representing interglacial recharge conditions), O<sub>2</sub> concentrations in the sedimentary units return to initial O<sub>2</sub> contents (Stage IV, see results at 32,000 years in Figure 6). This behavior is again most clearly observed at 25 m depth in the Dol2 unit (Figure 7(c)).

To obtain these results, reactive surface areas and the effective SOM oxidation rate were set to achieve a maximum O<sub>2</sub> ingress, at concentrations of  $1 \times 10^{-9}$  mol l<sup>-1</sup>, to depths of 200 m during the period of deglaciation and all other times of the simulation. This maximum depth of ingress was achieved using surface areas of  $5 \times 10^{-3}$  m<sup>2</sup> g<sup>-1</sup> and an effective rate coefficient for SOM of  $5 \times 10^{-12}$  mol dm<sup>-3</sup> SOM s<sup>-1</sup> (Table 3). These reactive surface areas correspond to 25, 15, and 13 m<sup>2</sup> dm<sup>-3</sup> mineral for pyrite, biotite, and chlorite, respectively.

The resulting reactive surface areas can be set in context with specific mineral surface areas reported in the literature. For instance, the specific surface area of frambooidal pyrite is approximately 2 m<sup>2</sup> g<sup>-1</sup> for mean diameters ranging from 60 to 150 μm, with values as high as 4 m<sup>2</sup> g<sup>-1</sup> for diameters between 2 and 5 μm [40]. Similarly, the specific surface area for chlorite ranges between 3.4 and 4.4 m<sup>2</sup> g<sup>-1</sup> for grain sizes from 125 to 300 μm and 75 to 125 μm, respectively [41]. Beckingham et al. [42] report specific surface areas for biotite (0.5–4.7 m<sup>2</sup> g<sup>-1</sup>, grain size range from 10 to 420 μm), chlorite (2.8–7.6 m<sup>2</sup> g<sup>-1</sup>, 10–250 μm), and pyrite (0.03–1.1 m<sup>2</sup> g<sup>-1</sup>,

10–250 μm). Although surface area is strongly dependent on mineral morphology and grain size, it can be concluded that the reactive surface areas considered for the base case are typically around three orders of magnitude lower than literature values for specific surface areas, implying that the base case mineral reactivities to limit O<sub>2</sub>-ingress to 200 m are highly conservative, even taking into account the often large discrepancies between laboratory-measured specific surface areas and reactive surface areas in the field. It should be noted that these results were obtained using an equivalent porous medium approach; however, a large degree of conservatism remains, even if the majority of flow occurs within interconnected fracture networks or partially dolomitized horizons.

Using these parameters and the mineral volume fractions listed in Table 2, the maximum reaction rates in the various units can be calculated for the individual minerals and SOM (Table 6). Table 6 shows that the effective reaction rates for the base case range between  $5 \times 10^{-15}$  and  $6 \times 10^{-13}$  mol dm<sup>-3</sup> bulk s<sup>-1</sup> in all units with the exception of the shales, which show higher reaction rates due to more abundant pyrite and chlorite. However, the permeability of the shale units is so low that the reactivity of redox-buffering mineral phases is irrelevant with respect to limiting O<sub>2</sub> ingress.

In comparison to literature data for oxidative mineral dissolution rates and SOM oxidation, effective rates on the order of  $10^{-15}$  to  $10^{-13}$  mol dm<sup>-3</sup> bulk s<sup>-1</sup>, as used for the base case, are very low. For example, utilizing rate data, mineral abundances, and effective surface areas reported by Beckingham et al. [42], effective dissolution rates for pyrite, biotite, and chlorite in a volcanic sandstone are determined as  $2.3 \times 10^{-9}$ ,  $2.1 \times 10^{-10}$ , and  $2.7 \times 10^{-10}$  mol dm<sup>-3</sup> bulk s<sup>-1</sup> for pyrite, biotite, and chlorite, respectively. Mineral volume fractions associated with these calculations are 0.4, 2.6, and 1.2 dm<sup>3</sup> mineral dm<sup>-3</sup> bulk for pyrite, biotite, and chlorite, respectively, within a factor of 5 of the volumetric fractions of the present study. Similarly, reaction rates for SOM reported in the literature for Pleistocene-Holocene sediments at 40 m depth [43] range from  $7 \times 10^{-7}$  to  $4 \times 10^{-9}$  mol dm<sup>-3</sup> SOM s<sup>-1</sup> for fine and coarse fractions, respectively. These rates correspond to  $7 \times 10^{-10}$  to  $4 \times 10^{-12}$  mol dm<sup>-3</sup> bulk s<sup>-1</sup> for a low SOM volumetric fraction of 0.1% assumed here for the sandstone and dolostone units (Table 2). It can be concluded that typical reaction rates reported in the literature are at least two orders of magnitude faster than values used in the base case (Table 6).

Overall, these results indicate that the reaction parameters used for the base case are highly conservative (i.e., low). Even with this high level of conservatism, O<sub>2</sub> ingress is substantially inhibited by the presence of reduced mineral phases and SOM, even under conditions of glacial retreat and substantial O<sub>2</sub>-rich meltwater production.

**5.3. Sensitivity Analysis Results.** To further investigate the role of O<sub>2</sub>-consuming reactions and ingress during a glaciation cycle, a sensitivity analysis was conducted, including the following: (a) Scenario I, increasing the conservative base

TABLE 6: Maximum oxidative dissolution rates and SOM oxidation rates for base case calculated based on parameters provided in Tables 2 and 3 and  $pO_2 = 1$  atm, rates in units of  $[mol\ dm^{-3}\ bulk\ s^{-1}]$ .

Mineral	Cr	$C_{rw}$	Sand1	Lim1	Sand2	$^{(1)}Sh1$	Doll	Ev	Sh2	Sand3	Dol2	Sand4	Sh3	Dol3
Pyrite	0	0	$6.1 \times 10^{-13}$	0	$6.1 \times 10^{-13}$	$2 \times 10^{-11}$	0	0	$2 \times 10^{-11}$	$6.1 \times 10^{-13}$	0	$6.1 \times 10^{-13}$	$2 \times 10^{-11}$	0
Biotite	$3.1 \times 10^{-13}$	$3.1 \times 10^{-13}$	0	0	0	0	0	0	0	0	0	0	0	0
Chlorite	$5.4 \times 10^{-14}$	$5.4 \times 10^{-14}$	0	0	0	$6.7 \times 10^{-13}$	0	0	$6.6 \times 10^{-13}$	0	0	0	$6.5 \times 10^{-13}$	0
Organic matter	0	0	$1.7 \times 10^{-14}$	$4.9 \times 10^{-14}$	$1.7 \times 10^{-14}$	$6.4 \times 10^{-14}$	$4.9 \times 10^{-15}$	0	$6.2 \times 10^{-14}$	$1.7 \times 10^{-14}$	$4.9 \times 10^{-15}$	$1.7 \times 10^{-14}$	$6.2 \times 10^{-14}$	$4.9 \times 10^{-15}$

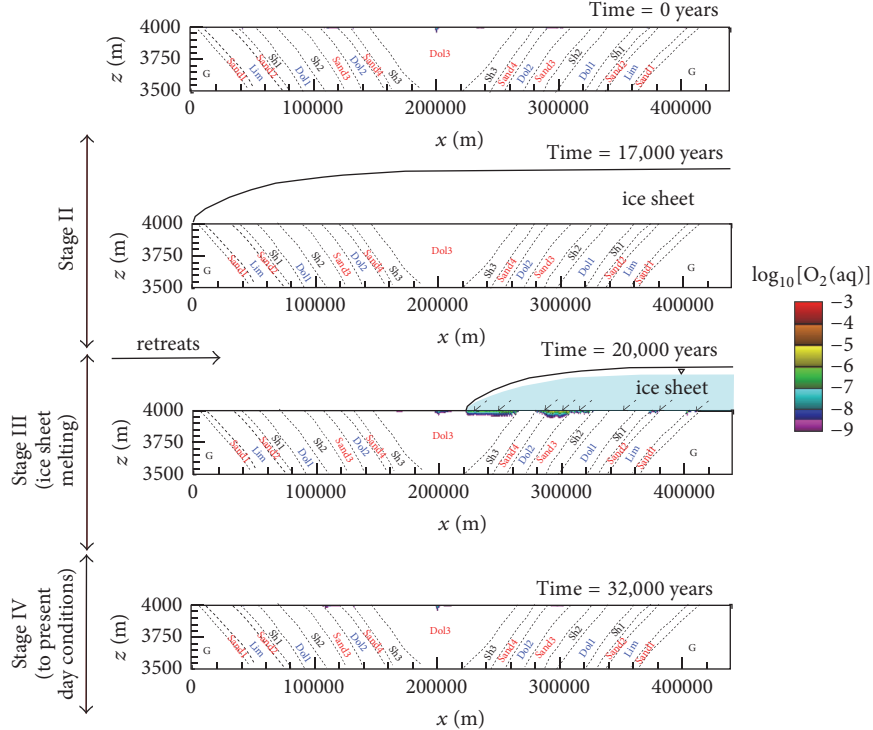


FIGURE 8: Spatial  $O_2(aq)$  concentration distributions at different times for Scenario 1 with a 10-fold increase of  $O_2$ -consumption rates (i.e., at 0, 17,000, 20,000, and 32,000 years), corresponding to the initial condition, the end of Stage II, Stage III, and the final condition.  $O_2$  concentrations in  $\text{mol l}^{-1}$ .

case reaction rates by one order of magnitude; (b) Scenario II, decreasing the  $O_2$ -concentration in the glacial meltwaters to less conservative atmospheric values; and (c) Scenario III, combining both Scenarios I and II.

The results demonstrate that an increase in effective reaction rates by one order of magnitude further limits  $O_2$  ingress, even during periods of glacial meltwater ingress (Figures 8 and 9). With the increased rates, the maximum  $O_2$  concentrations at 25 m depth are almost two orders of magnitude lower than those in the meltwater. The maximum  $O_2$ -ingress depth is now restricted to less than 100 m, with  $O_2$  concentrations at 75 m slightly above the numerical detection limit only in the Dol2 and Sand3 units (see Figures 9(c) and 9(d)).

Comparison of the base case with the three sensitivity scenarios shows how a decline in  $O_2$  in recharge waters and/or higher oxidative dissolution rates limit  $O_2$  ingress at a depth of 75 m (Figure 10). For all three sensitivity scenarios,  $O_2$  concentrations are restricted to the shallowest part of the aquifers, with lower penetration depths than the base case and with none of these scenarios showing  $O_2$  concentrations above the numerical detection limit ( $1 \times 10^{-9} \text{ mol l}^{-1}$ , or  $3.2 \times 10^{-5} \text{ mg l}^{-1}$ ) at 150 m (results not shown).

## 6. Summary and Concluding Remarks

Oxygen migration and consumption in a large-scale hypothetical intracratonic sedimentary basin during a 32,500-year glaciation-deglaciation cycle were investigated using reactive

transport modeling. The sensitivity of  $O_2$ -ingress to  $O_2$  concentration in recharge water and rates of  $O_2$ -consuming reactions was evaluated.

Although illustrative in nature, the numerical model results were intended to capture the main hydrogeological features of the Paleozoic sedimentary basins in North America. To the degree possible, model parameters were based on published data or relationships.

Analysis of a base case reactive transport simulation in this hypothetical sedimentary basin suggests that the evolution of hydraulic head distributions due to mechanical loading during the period of glacial advance and meltwater production during the period of glacial retreat may result in substantial hydraulic gradients. However, the hydrostratigraphy of the interbedded low and high hydraulic conductivity sedimentary rock formations significantly limit groundwater flow velocities and mixing between aquifers and aquitards. The presence of dense brines at depth exerts an important control on fresh water ingress through the maintenance of density gradients, despite the transient hydraulic and mechanical surface boundary conditions created by an advancing and retreating ice sheet.

The key objective of the study was to assess the role of mineral oxidative dissolution reactions and SOM oxidation in inhibiting  $O_2$ -ingress into sedimentary basins. While the simulations suggest that freshwater ingress can occur to a maximum depth of up to 350 m during the deglaciation period, it was shown that even for highly conservative assumptions regarding  $O_2$  consumption rates,  $O_2$  ingress was

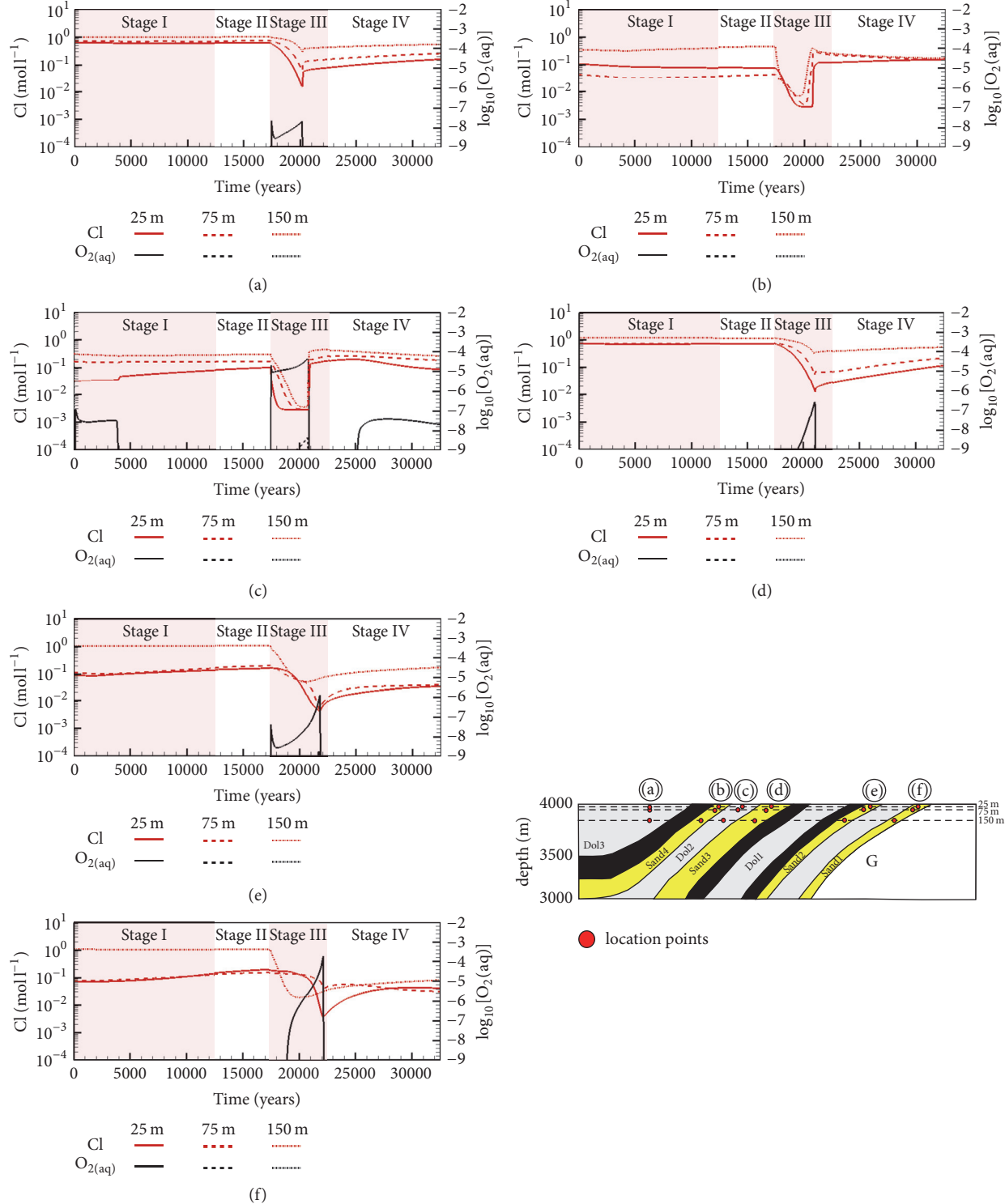


FIGURE 9: Temporal evolution of dissolved  $O_2$  and Cl concentrations at the different observation point locations for Scenario 1 with a 10-fold increase of  $O_2$ -consumption rates. (a), (b), (c), (d), (e), and (f) for Dol3, Sand4, Dol2, Sand3, Sand2, and Sand1, respectively.  $O_2$  concentrations in  $\text{mol l}^{-1}$ . If  $O_2$  profiles are not visible for a specific depth and unit, concentrations remain below  $1 \times 10^{-9} \text{ mol l}^{-1}$  for duration of simulation.

limited to depths of less than 200 m at concentrations not exceeding  $1 \times 10^{-9} \text{ mol l}^{-1}$ . Rates used to allow  $O_2$  to reach depths of 200 m for the mineral phases and SOM were typically 3–5 orders of magnitude lower than rates reported in the

literature, implying a high level of conservatism. For slightly higher, yet still conservative rates and/or lower  $O_2$  concentrations in glacial meltwater,  $O_2$  ingress was even lower, essentially restricted to the top 100 m of the sedimentary

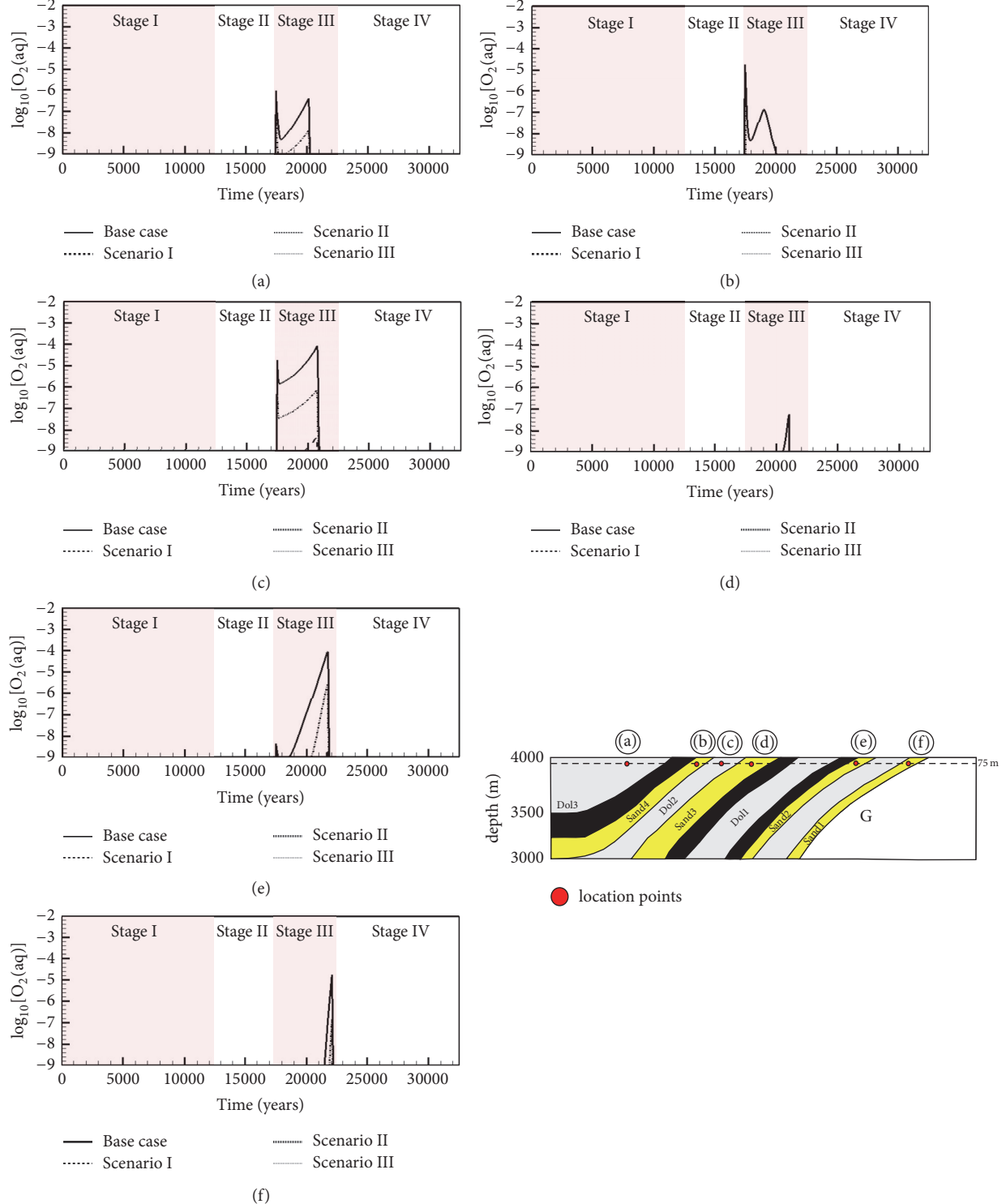


FIGURE 10: Temporal evolution of dissolved  $\text{O}_2$  concentrations at a depth of 75 m comparing results from Scenarios I-III to the results of the base case. (a), (b), (c), (d), (e), and (f) for Dol3, Sand4, Dol2, Sand3, Sand2, and Sand1, respectively.  $\text{O}_2$  concentrations in  $\text{mol l}^{-1}$ . If  $\text{O}_2$  profiles are not visible for a specific unit, concentrations remain below  $1 \times 10^{-9} \text{ mol l}^{-1}$  for duration of simulation.

basin. The simulation results suggest that detailed characterization of the present-day abundance and spatial distributions of reduced mineral phases and SOM would be beneficial to assess  $\text{O}_2$  attenuation capacity of sedimentary basins. On the

other hand, it appears that the difficult task of characterizing field-scale effective  $\text{O}_2$  consumption rates might not be necessary, considering that limited  $\text{O}_2$ -ingress was achieved based on conservative assumptions.

However, the highly complex nature of the simulated system must be taken into consideration and the results must be viewed with care. Although the simulations were constrained by field observations to the degree possible, assumptions had to be made regarding several parameters and processes, including the abundance and distribution of reactive mineral phases and SOM, recharge patterns during periods of glaciation and deglaciation, and the hydraulic and mechanical properties of the various sedimentary units. In addition, simplifications were made regarding dimensionality (restricted to two spatial dimensions), the description of flow and transport processes (an Equivalent Porous Medium approach was used, neglecting the presence of fracture networks), mineralogical composition of the rocks, and the form of the rate expressions describing oxidative dissolution reactions and SOM oxidation. These assumptions and simplifications lead to substantial uncertainties associated with these simulations and limit their predictive capability.

Nevertheless, overall, our results suggest a high degree of geochemical stability of sedimentary basins and a significant capacity to attenuate O<sub>2</sub> in recharge water and to maintain reducing conditions at depth over long time periods including during glaciation-deglaciation events.

## Conflicts of Interest

The authors declare that there are no conflicts of interest regarding the publication of this paper.

## Acknowledgments

Funding for this research was provided by a N.W.M.O. (Nuclear Waste Management Organization, Canada) grant held by K. Ulrich Mayer and Kerry T. B. MacQuarrie. The authors would like to acknowledge WestGrid and Compute Canada for providing computing hardware, software, and technical support. Also they are grateful for financial support from CONICET (National Council of Scientific and Technical Research), Argentina.

## References

- [1] M. Mazurek, Long-term used fuel waste management-Geoscientific review of the sedimentary sequence in southern Ontario. Background Paper 612 prepared by Rock-Water Interactions, Institute of Geological Sciences, University of Bern for the Nuclear Waste Management Organization, 2004.
- [2] S. M. Spiessl, K. T. B. MacQuarrie, and K. U. Mayer, "Identification of key parameters controlling dissolved oxygen migration and attenuation in fractured crystalline rocks," *Journal of Contaminant Hydrology*, vol. 95, no. 3-4, pp. 141–153, 2008.
- [3] M. Sidborn and I. Neretnieks, "Long-term oxygen depletion from infiltrating groundwaters: Model development and application to intra-glaciation and glaciation conditions," *Journal of Contaminant Hydrology*, vol. 100, no. 1-2, pp. 72–89, 2008.
- [4] J. C. McIntosh and L. M. Walter, "Paleowaters in Silurian-Devonian carbonate aquifers: Geochemical evolution of groundwater in the Great Lakes region since the Late Pleistocene," *Geochimica et Cosmochimica Acta*, vol. 70, no. 10, pp. 2454–2479, 2006.
- [5] J. C. McIntosh, L. M. Walter, and A. M. Martini, "Pleistocene recharge to midcontinent basins: Effects on salinity structure and microbial gas generation," *Geochimica et Cosmochimica Acta*, vol. 66, no. 10, pp. 1681–1700, 2002.
- [6] J. C. McIntosh and L. M. Walter, "Volumetrically significant recharge of Pleistocene glacial meltwaters into epicratonic basins: constraints imposed by solute mass balances," *Chemical Geology*, vol. 222, no. 3-4, pp. 292–309, 2005.
- [7] J. C. McIntosh, G. Garven, and J. S. Hanor, "Impacts of Pleistocene glaciation on large-scale groundwater flow and salinity in the Michigan Basin," *Geofluids*, vol. 11, no. 1, pp. 18–33, 2011.
- [8] S. Bea, K. U. Mayer, and K. T. B. MacQuarrie, *Modelling Reactive Transport in Sedimentary Rock Environments-Phase II, Reactive Transport Modeling in a Sedimentary Basin Affected by a Glaciation/Deglaciation Event*, Nuclear Waste Management Organization, 2011.
- [9] S. A. Bea, U. K. Mayer, and K. T. B. MacQuarrie, "Reactive transport and thermo-hydro-mechanical coupling in deep sedimentary basins affected by glaciation cycles: model development, verification, and illustrative example," *Geofluids*, vol. 16, no. 2, pp. 279–300, 2016.
- [10] A. M. Martini, L. M. Walter, J. M. Budat, T. C. W. Ku, C. J. Kaiser, and M. Schoell, "Genetic and temporal relations between formation waters and biogenic methane: Upper Devonian Antrim shale, Michigan Basin, USA," *Geochimica et Cosmochimica Acta*, vol. 62, no. 10, pp. 1699–1720, 1998.
- [11] J. C. McIntosh, L. M. Walter, and A. M. Martini, "Extensive microbial modification of formation water geochemistry: Case study from a Midcontinent sedimentary basin, United States," *Bulletin of the Geological Society of America*, vol. 116, no. 5-6, pp. 743–759, 2004.
- [12] T. R. Weaver, S. K. Frape, and J. A. Cherry, "Recent cross-formational fluid flow and mixing in the shallow Michigan Basin," *Bulletin of the Geological Society of America*, vol. 107, no. 6, pp. 697–707, 1995.
- [13] J. J. Kolak, D. T. Long, J. M. Matty, G. J. Larson, D. F. Sibley, and T. B. Councill, "Ground-water, large-lake interactions in Saginaw Bay, Lake Huron: A geochemical and isotopic approach," *Bulletin of the Geological Society of America*, vol. 111, no. 2, pp. 177–188, 1999.
- [14] M. M. Husain, J. A. Cherry, and S. K. Frape, "The persistence of a large stagnation zone in a developed regional aquifer, southwestern Ontario," *Canadian Geotechnical Journal*, vol. 41, no. 5, pp. 943–958, 2004.
- [15] L. Ma, M. C. Castro, and C. M. Hall, "A late Pleistocene-Holocene noble gas paleotemperature record in southern Michigan," *Geophysical Research Letters*, vol. 31, no. 23, pp. 1–4, 2004.
- [16] S. Klump, T. Grundl, R. Purtschert, and R. Kipfer, "Groundwater and climate dynamics derived from noble gas, 14C, and stable isotope data," *Geology*, vol. 36, no. 5, pp. 395–398, 2008.
- [17] T. Wolery and S. Daveler, EQ6, A computer program for reaction path modeling of aqueous geochemical system: Theoretical manual, user's guide, and related documentation (version 7.0). UCLR-MA-110662 PT IV, Lawrence Livermore Natl. Lab. Livermore, California, 1992.
- [18] C. Appelo and D. Postma, *Geochemistry, Groundwater and Pollution*, A. A. Balkema, Ed., 1993.
- [19] M. Hobbs, S. Frape, O. Shouakar-Stash, and L. Kennell, Phase I Regional Hydrogeochemistry, Southern Ontario. Ontario

- Power Generation, Department of Earth and Environmental Science, University of Waterloo, OPG 00216-REP-01300-00006-R00, 2008.
- [20] J. Guimerà, L. Duro, and A. Delos, Changes in groundwater composition as a consequence of deglaciation: implications for performance assessment. Report no. R-06-105. Svensk Kärnbränslehantering AB, 2006.
  - [21] K. U. Mayer, E. O. Frind, and D. W. Blowes, "Multicomponent reactive transport modeling in variably saturated porous media using a generalized formulation for kinetically controlled reactions," *Water Resources Research*, vol. 38, no. 9, pp. 13-1-13-21, 2002.
  - [22] S. A. Bea, S. A. Wilson, K. U. Mayer, G. M. Dipple, I. M. Power, and P. Gamazo, "Reactive transport modeling of natural carbon sequestration in ultramafic mine tailings," *Vadose Zone Journal*, vol. 11, no. 2, 2012.
  - [23] D. Su, K. U. Mayer, and K. T. B. MacQuarrie, "Parallelization of MIN3P-THCm: A high performance computational framework for subsurface flow and reactive transport simulation," *Environmental Modeling and Software*, vol. 95, pp. 271-289, 2017.
  - [24] V. F. Bense and M. A. Person, "Transient hydrodynamics within intercratonic sedimentary basins during glacial cycles," *Journal of Geophysical Research: Earth Surface*, vol. 113, no. 4, 2008.
  - [25] S. E. Grasby and Z. Chen, "Subglacial recharge into the Western Canada Sedimentary Basin—impact of Pleistocene glaciation on basin hydrodynamics," *Bulletin of the Geological Society of America*, vol. 117, no. 3-4, pp. 500-514, 2005.
  - [26] A. M. Provost, C. I. Voss, and C. E. Neuzil, "Glaciation and regional groundwater flow in the Fennoscandian shield," *Geofluids*, vol. 12, no. 1, pp. 79-96, 2012.
  - [27] C. E. Neuzil, "Hydromechanical coupling in geologic processes," *Hydrogeology Journal*, vol. 11, no. 1, pp. 41-83, 2003.
  - [28] T. H. Henderson, K. U. Mayer, B. L. Parker, and T. A. Al, "Three-dimensional density-dependent flow and multicomponent reactive transport modeling of chlorinated solvent oxidation by potassium permanganate," *Journal of Contaminant Hydrology*, vol. 106, no. 3-4, pp. 195-211, 2009.
  - [29] C. E. Harvie, N. Møller, and J. H. Weare, "The prediction of mineral solubilities in natural waters: The Na-K-Mg-Ca-H-Cl-SO<sub>4</sub>-OH-HCO<sub>3</sub>-CO<sub>3</sub>-H<sub>2</sub>O system to high ionic strengths at 25°C," *Geochimica et Cosmochimica Acta*, vol. 48, no. 4, pp. 723-751, 1984.
  - [30] K. S. Pitzer, "Thermodynamics of electrolytes. I. theoretical basis and general equations," *The Journal of Physical Chemistry C*, vol. 77, no. 2, pp. 268-277, 1973.
  - [31] C. Monnin, "Density calculation and concentration scale conversions for natural waters," *Computers & Geosciences*, vol. 20, no. 10, pp. 1435-1445, 1994.
  - [32] C. Voss and A. Provost, "SUTRA-A Model for saturated-unsaturated variable-density ground-water flow with solute or energy transport (Version 2.1)," 2008.
  - [33] D. B. Bahr, E. W. H. Hutton, J. P. M. Syvitski, and L. F. Pratson, "Exponential approximations to compacted sediment porosity profiles," *Computers & Geosciences*, vol. 27, no. 6, pp. 691-700, 2001.
  - [34] S. T. Brennan and T. K. Lowenstein, "The major-ion composition of Silurian seawater," *Geochimica et Cosmochimica Acta*, vol. 66, no. 15, pp. 2683-2700, 2002.
  - [35] J. S. Hanor and J. C. McIntosh, "Are secular variations in seawater chemistry reflected in the compositions of basinal brines?" *Journal of Geochemical Exploration*, vol. 89, no. 1-3, pp. 153-156, 2006.
  - [36] USDOE (United States Department of Energy): In-drift precipitates/salts model. Argonne National Laboratory Report EBS-MD-000045 REV 03. Chicago, USA, 2007.
  - [37] S. A. Bea, J. Carrera, C. Ayora, and F. Batlle, "Modeling of concentrated aqueous solutions: Efficient implementation of Pitzer equations in geochemical and reactive transport models," *Computers & Geosciences*, vol. 36, no. 4, pp. 526-538, 2010.
  - [38] M. A. Williamson and J. D. Rimstidt, "The kinetics and electrochemical rate-determining step of aqueous pyrite oxidation," *Geochimica et Cosmochimica Acta*, vol. 58, no. 24, pp. 5443-5454, 1994.
  - [39] J. Johnson and J. L. Fastook, "Northern Hemisphere glaciation and its sensitivity to basal melt water," *Quaternary International*, vol. 95, no. 96, pp. 65-74, 2002.
  - [40] C. E. Pugh, L. R. Hossner, and J. B. Dixon, "Pyrite and marcasite surface area as influenced by morphology and particle diameter," *Soil Science Society of America Journal*, vol. 45, no. 5, pp. 979-982, 1981.
  - [41] M. Malmström, S. Banwart, J. Lewenhagen, L. Duro, and J. Bruno, "The dissolution of biotite and chlorite at 25°C in the near-neutral pH region," *Journal of Contaminant Hydrology*, vol. 21, no. 1-4, pp. 201-213, 1996.
  - [42] L. E. Beckingham, E. H. Mitnick, C. I. Steefel et al., "Evaluation of mineral reactive surface area estimates for prediction of reactivity of a multi-mineral sediment," *Geochimica et Cosmochimica Acta*, vol. 188, pp. 310-329, 2016.
  - [43] N. Hartog, J. Griffioen, and C. H. Van der Weijden, "Distribution and reactivity of O<sub>2</sub>-reducing components in sediments from a layered aquifer," *Environmental Science & Technology*, vol. 36, no. 11, pp. 2338-2344, 2002.

## Research Article

# High-Resolution Wellbore Temperature Logging Combined with a Borehole-Scale Heat Budget: Conceptual and Analytical Approaches to Characterize Hydraulically Active Fractures and Groundwater Origin

Guillaume Meyzonnat<sup>1</sup>, Florent Barbicot,<sup>1</sup> José A. Corcho-Alvarado,<sup>2</sup> Antoine Tognelli,<sup>3</sup> Hermann Zeyen,<sup>4</sup> Alexandra Mattei,<sup>1,5</sup> and Renald McCormack<sup>6</sup>

<sup>1</sup>Department of Earth and Atmospheric Sciences, Geotop-UQAM, Montréal, QC, Canada

<sup>2</sup>Spiez Laboratory, Federal Office for Civil Protection, Spiez, Switzerland

<sup>3</sup>CEA, DAM, DIF, F-91297 Arpajon, France

<sup>4</sup>Department of Earth Sciences, GEOPS Laboratory, Paris-Saclay University, Paris-Sud University, CNRS, Orsay, France

<sup>5</sup>MINES Paris Tech, Paris, France

<sup>6</sup>Envir'Eau-Puits Inc., Saint-Nicolas, QC, Canada

Correspondence should be addressed to Guillaume Meyzonnat; meyzonnat.guillaume@uqam.ca

Received 29 June 2017; Revised 18 October 2017; Accepted 20 February 2018; Published 3 April 2018

Academic Editor: Walter A. Illman

Copyright © 2018 Guillaume Meyzonnat et al. This is an open access article distributed under the Creative Commons Attribution License, which permits unrestricted use, distribution, and reproduction in any medium, provided the original work is properly cited.

This work aims to provide an overview of the thermal processes that shape wellbore temperature profiles under static and dynamic conditions. Understanding of the respective influences of advection and conduction heat fluxes is improved through the use of a new heat budget at the borehole scale. Keeping in mind the thermal processes involved, a qualitative interpretation of the temperature profiles allows the occurrence, the position, and the origin of groundwater flowing into wellbores from hydraulically active fractures to be constrained. With the use of a heat budget developed at the borehole scale, temperature logging efficiency has been quantitatively enhanced and allows inflow temperatures to be calculated through the simultaneous use of a flowmeter. Under certain hydraulic or pumping conditions, both inflow intensities and associated temperatures can also be directly modelled from temperature data and the use of the heat budget. Theoretical and applied examples of the heat budget application are provided. Applied examples are shown using high-resolution temperature logging, spinner flow metering, and televiwing for three wells installed in fractured bedrock aquifers in the St-Lawrence Lowlands, Quebec, Canada. Through relatively rapid manipulations, thermal measurements in such cases can be used to detect the intervals or discrete positions of hydraulically active fractures in wellbores, as well as the existence of ambient flows with a high degree of sensitivity, even at very low flows. Heat budget calculations at the borehole scale during pumping indicate that heat advection fluxes rapidly dominate over heat conduction fluxes with the borehole wall. The full characterization of inflow intensities provides information about the distribution of hydraulic properties with depth. The full knowledge of inflow temperatures indicates horizons that are drained from within the aquifer, providing advantageous information on the depth from which groundwater originates during pumping.

## 1. Introduction

Aquifer hydraulic properties are most commonly determined through pumping and slug tests. These techniques provide fast and reliable measurements of mean transmissivity and effective porosity, which often yield sufficient information

to manage groundwater resources in terms of productivity. However, for applications where solute transport processes cannot be neglected (i.e., wellhead protection area delineation, contaminated site remediation), the knowledge of mean hydraulic parameters alone is insufficient, and groundwater flow paths need to be assessed. Hydrogeologists always

have to deal with a certain degree of spatial heterogeneity, because aquifer architectures originate from complex geological processes (i.e., sedimentology, tectonics), which generate heterogeneous [1] and scale-dependent patterns [2]. Despite the heterogeneous nature of aquifers, the use of borehole logging techniques to address this heterogeneity remains uncommon. For instance, pumping tests usually carried out for drinking water supply wells do not typically address the vertical variability of the production zones within the boreholes [3]. Since the most common borehole logging technique, known as the packer test, is more difficult to implement, more time-consuming, and thus more expensive than usual pumping tests, the vertical investigation of aquifer heterogeneities is still rare in hydrogeological surveys.

The heterogeneous nature of aquifers has been investigated and highlighted worldwide. In the Canadian context of this study, examples dealing with aquifer heterogeneity have been provided for both granular [4] and fractured [5] matrices. Nastev et al. [6] described the lognormal decrease of hydraulic conductivities with depth in postglacial fractured bedrock in Quebec, Canada. Recent regional groundwater characterizations, also carried out in Quebec, between 2008 and 2015, included the investigation of vertical bedrock fracturing patterns. These generally showed no correlation between well productivity and type of bedrock formation [7–9]. Packer tests and acoustic televiewing performed by Carrier et al. [7] showed that decreasing fracture densities are generally associated with decreasing hydraulic conductivities with depth. However, these results have high standard deviations, revealing strong vertical heterogeneities from one well to another. Indeed, packer tests performed for some wells in the same period [8, 9] did not reveal systematic decreases in bedrock fracturing with depth.

Other borehole logging techniques have garnered the attention of hydrogeologists over the last two decades. For instance, tracer experiments allow fluid velocities [10] or concentration dilution [11] to be measured following the injection of a tracer into boreholes during pumping, or tracer breakthrough in boreholes neighboring the injection well to be measured [12]. Spinner [13] or electromagnetic [14, 15] flowmeters allow water velocities to be measured very efficiently and directly inside the borehole with high spatial resolution. Such fluid velocity measurements inside boreholes during pumping allow the vertical distribution of the hydraulic properties of the surrounding rocks to be determined [13]. For the same application, but under low flow conditions, heat pulse flowmeters [15, 16] are especially useful to measure ambient borehole flow. Temperature logging in boreholes is another type of investigation technique. Applications specifically dedicated to hydrogeology make use of temperature logging in boreholes to estimate recharge rates [17–19], to trace local [20, 21] or regional [22] groundwater flows, or to infer the lateral heterogeneity of hydraulic properties for a section of an aquifer [23]. These applications typically address large-scale heat transport processes within the subsurface and/or involve heat transport processes over relatively long time scales.

At the borehole scale, high-resolution temperature profiling is of particular interest in hydrogeology, and its use

has become more frequent over the last decade, coinciding with temperature sensor resolution improvement to  $0.001^{\circ}\text{C}$ . Hydrogeological information obtained from recent passive and/or active temperature measurement techniques [24, 25] are now capable of competing with other, more conventional investigation techniques (e.g., involving hydraulic packer tests or solute tracing) to provide valuable information about aquifer hydraulic and fracturing structure, used to infer groundwater flow paths.

Passive temperature measurements consist of logging temperature in a wellbore without introducing a heat source, so that obtained profiles only depend on natural hydrogeological conditions, thermal properties of the rock, and/or aquifer solicitation through pumping. For instance, the vertical distribution and interconnectivity of fractures in wellbores can be well-described by coupling flow and passive temperature measurements. Such examples are given by Chatelier et al. [26] and Le Borgne et al. [27], who have explicitly pointed out the advantage of combining passive temperature and flowmeter logs, where the passive temperature log gives the precise depth at which inflow occurs, and the flow log gives a precise measurement of the flow rate in the interval between inflow and outflow zones. Discussions of groundwater origin from identified fractures are also found in the literature. One such example is also provided by Chatelier et al. [26], by coupling passive temperature measurement and flow logs with elaborate in situ data. Other recent technical advances make it possible to measure instantaneous temperature profiles using optical fiber. This technology is often implemented with an active measurement of temperature by heating a section or the entire length of the water column. Pehme et al. [28] used active temperature measurements to detect lateral ambient flow through hydraulically active fractures by measuring the thermal recovery of the water column in the borehole after it was heated. In another example, Bense et al. [29] used a coaxial system of heating cable and optical fiber and then used the variation in temperature profiles during pumping to calculate the depth-flow distribution in wellbores.

Although these latter active technologies allow direct quantitative results, their setup remains rather delicate and time-consuming for in situ applications. Moreover, the effectiveness of the method is not guaranteed in all in situ cases, because the resolution of optical fiber temperature measurements ( $\pm 0.5^{\circ}\text{C}$ , or at best  $\pm 0.02^{\circ}\text{C}$  with the use of the calibration baths) is still low compared with those of the current thermistors ( $\pm 0.001^{\circ}\text{C}$ ), which are preferentially used for passive measurements. Thermal numerical modelling has been used by Klepikova et al. [30] and Klepikova et al. [31] to present the concepts and numerical methods behind the inversion of temperature profiles to flow profiles in wellbores, thus using the temperature probe as a high-resolution flowmeter. Previous work has made use of thermal analytical models, especially in the case of (low) ambient flows in wellbores for fractured media. An explicit thermal analytical solution considering a semi-infinite plane geometry was provided by Drury and Jessop [32] to model transient temperature shifts within the aquifer with increasing distance from the active fracture intercepting the wellbore. With an

application for ambient inflow, which flows through the wellbore, Ge [33] proposed a theoretical model to estimate both fluid flow velocity and temperature for a given inflow. Previous work has focused on experiments under thermal steady-state conditions during pumping and was generally applied at depth or at locations where the geothermal gradient is linear.

This study investigates the vertical distribution of hydraulic properties in fractured bedrock wells using flow metering and televideo, but with a main focus on temperature borehole logging. As cited above, numerous works have already highlighted the pertinence of temperature logging to identify the occurrence and the positions of productive zones in wellbores. Through the introduction of a new heat budget model, this work aims to enhance the qualitative interpretation of depth-temperature profiles against advection and conduction fluxes at the borehole scale, across a range of static and dynamic conditions in fractured aquifers. The second objective is to enhance the potential of passive temperature logging to quantify flow and the temperature of inflows into boreholes with the use of a heat budget. Previous analytical models found in the literature typically allowed calculations for only a limited number of fractures (i.e., one or two fractures at best, in the case of ambient flows) and did not attempt to model the complete depth-temperature profile when several inflows occurred and mixed in the wellbore. The heat budget proposed in this work aims to model depth-temperature profiles for the entire wellbore length, for several inflows that mix in the borehole, and depending on pumping conditions (duration and discharge intensity). Simultaneous temperature measurement and flow metering are applied within the heat budget to quantify information about the origin of several groundwater inflows based on their temperature. The use of this analytical procedure is also theoretically investigated to test its potential to quantify both flow and temperature of inflows in wellbores through the single logging of depth-temperature profiles.

The following abbreviations are used throughout the text for brevity: the temperature of the water column measured in the borehole under ambient ( $T_s$ ) and under dynamic (i.e., pumping) ( $T_D$ ) conditions; the temperature of groundwater discharging into the borehole at depth ( $T_i$ ), originating from a discrete or distributed interval of hydraulically active fracture(s); and the temperature of the aquifer ( $T_A$ ), depending on depth as function of geothermal heat flux, seasonal and climatic variation of the soil surface temperature, regional groundwater circulation, and recharge fluxes, but excluding the influence of fluid advection due to the presence of a wellbore or the pumping thereof.

## 2. Materials and Methods

**2.1. Site Description.** The study area is located in southern Quebec, within two geological regions that correspond to the St. Lawrence Platform and the Appalachian Mountains (Figure 1). The Ordovician geological units of the St. Lawrence Platform are of sedimentary origin and consist of thick sequences of sandstone of the Potsdam Group, dolomite of the Beekmantown Group, limestone of the Chazy, Black

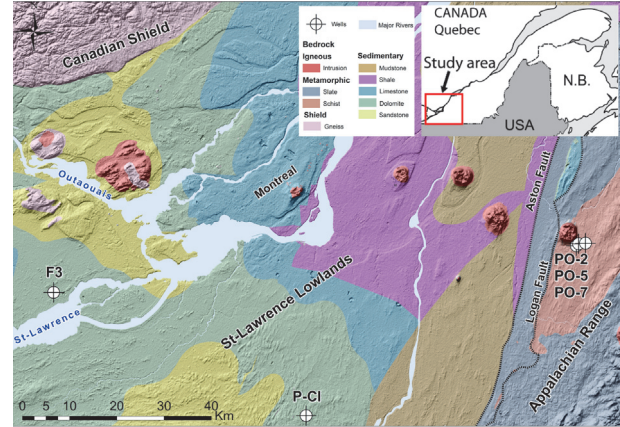


FIGURE 1: Location of wells in the current study and geological map.

River, and Trenton Groups, Utica shales, and mudstones of the Queenston Group. In the eastern part of the study area, the Appalachian range corresponds to complex, imbricated metamorphic thrust sheets produced during the Taconian Orogeny: slates with a bedded shaly matrix containing chaotic blocks of cherts, sandstone, and dolomitic schists. These geological units are represented in Figure 1 as a simplified version of the detailed mapping by Globensky [34]. The geomorphology of Quebec is marked by glaciation-deglaciation phases, with unconsolidated sediments of glacial and postglacial origin overlying the fractured bedrock. The complex stratigraphy of the unconsolidated sediment largely controls the hydrogeological context of the underlying fractured bedrock aquifers. In such a glacial geomorphological context, the unconformity between Quaternary unconsolidated sediment and the bedrock is very sharp, and bedrock fracturing generally decreases strongly with depth over the first hundred meters [7].

Three (F3, P-Cl, and PO-7) of the five wells presented in Figure 1 have been studied in detail. PO-2 and PO-5 are only used as references for ambient temperature profiles with depth (see Section 4.2.1). All investigated wells have a 150 mm diameter, are steel-cased for the total thickness of unconsolidated sediment, and are anchored one meter into the bedrock. Below the steel tubing, boreholes are uncased. Well F3 has a total depth of 20.4 m and was drilled for a regional hydrogeological mapping study [35]. Sediment at this location consists of 4.3 m of Champlain silty-clays and 5.7 m of glacial till covering the bedrock. Sedimentary bedrock is Ordovician calcareous dolomite of the Beekmantown Group, Beauharnois Formation. The bedrock aquifer is confined under impermeable clay and till sediments, and a pumping test provided a transmissivity of  $3.7 \times 10^{-3} \text{ m}^2/\text{s}$  and a productivity of approximately 287 L/min. The productivity is defined here as the maximum total discharge rate obtained when the drawdown in the wellbore has stabilized. Wells PO-7, PO-2, PO-5, and P-Cl were drilled for municipal groundwater investigation, and access to these wells was kindly provided by the lead hydrogeologist. Well PO-7 has a total depth of 61 m, a productivity of 340 L/min, and a transmissivity of  $4.2 \times 10^{-3} \text{ m}^2/\text{s}$ . At this location, 8 m of

fine sand, including silty lenses, overlay the bedrock, which consists of red schists of the Cambrian Shefford Group, Mawcock Formation. Wells PO-2 (92 m depth; productivity 45 L/min) and PO-5 (91 m depth; productivity 15 L/min) are located 200 m and 1 km from well PO-7, respectively, within the same bedrock formation, with land cover, as well as the nature and thickness of the unconsolidated sediments varying only slightly. Well P-Cl has a total depth of 37 m and a productivity of 80 L/min. Glacial till less than 0.6 m thick overlies the bedrock, which consists of Ordovician dolomitic sandstone of the Beekmantown Group, Theresa Formation.

**2.2. Borehole Logging with a Spinner Flowmeter and Televiwing.** Water velocities in wells PO-7 and F3 were measured during pumping with a spinner flowmeter [36] operated with a winch controller [37]. Pumping rates were set to be as high as possible to maximize water velocities flowing into the borehole and thus maximizing flowmeter sensitivity. Discharge rates, however, were carefully constrained in order to avoid well dewatering below the base of the steel-casing, allowing measurements within the whole uncased section of the wellbores. The spinner flowmeter was calibrated for each well under static conditions, with winch down speeds varying from 1 to 3 m/min. During pumping tests, the pumps were placed at the top of the well and water velocities were logged with the spinner flowmeter trolled downward, in order to maximize fluid velocities and thus to maximize the flowmeter sensitivity. Measurements were performed at a resolution of 5 cm and a winch down speed of 2 m/min. Raw, noisy signals measured with the flowmeter were smoothed using a moving average of 10 measurements. Flow velocities were converted into flow rates by dividing the measured flow velocities by the section area of the borehole. Flow rates at depth were converted into a percentage of pumping discharge by dividing them by the total pumping rate. Total water discharged during pumping was measured with a volumetric counter placed at the hose outlet, and with bucket and chronometer, and compared with the total discharge measured with the flowmeter within the steel-casing. Discrepancies in the total discharge obtained by these two means were less than 5%. Fluid velocity measurements in the borehole during pumping were taken when steady state was reached (i.e., with residual drawdown of less than 1 cm/20 min). Pumping tests performed at different discharge rates for F3 and PO-7 did not reveal any variation in the vertical distribution of water inflows into the borehole measurable by the flowmeter. Televiwing with an optical borehole imager [38] was coupled with flowmeter measurements to better constrain the location and the discrete or distributed nature of hydraulically active fractures.

**2.3. Passive Temperature Borehole Logging.** Temperature profiles in water columns were measured with a 0.01°C resolution thermistor probe [39]. Measurements were always taken facing downward, with a maximum interval of one meter. For all temperature logging under dynamic conditions, the pump was placed at a shallow depth within the casing or just below the bottom of the casing, avoiding temperature

disturbance and allowing space for the uncased length of the studied borehole. Static profiles were systematically taken before initiating measurements under pumping conditions. Depths to the water table under static conditions are shown in Figure 9(a). Discharge rates, as well as drawdown stabilized during pumping, are shown in Figures 9(b), 9(c), and 9(d) for wells PO-7, P-Cl, and F3, respectively. For a given well, all static and dynamic temperature logs were taken on the same day. Wells PO-2, PO-5, and PO-7 were installed in the same red schist formation and were drilled at a 200 m spacing. Wells PO-2 and PO-5 were not accessible for logging under dynamic conditions, but the presentation of their ambient temperature logs together with both the static and dynamic PO-7 logs is useful, because PO-2 and PO-5 reach greater depths (92 m).

**2.4. Calculation of Hydraulic Properties from Velocity Logs.** The distribution of horizontal hydraulic conductivity along the length of the borehole was obtained directly from flowmeter measurements. As described by Barahona-Palomo et al. [13], the hydraulic conductivity of each fractured zone ( $K_i$ ) can be calculated using (1), where  $T$  is the total hydraulic transmissivity obtained from a pumping test,  $Q$  is the total pumping rate, and  $q_i$  is the inflow associated with the fracture zone interval of vertical thickness  $b_i$ .

$$K_i = \frac{1}{b_i} \frac{q_i}{Q} T. \quad (1)$$

### 3. Background for Wellbore Temperature Profile Analysis in Fractured Aquifers

**3.1. Heat Fluxes under Ambient and Dynamic Conditions.** In hydrogeology, heat fluxes relate to heat advection and heat conduction. Heat advection concerns the flowing and the mixing of groundwater in the aquifer. Heat conduction tends to reequilibrate the temperature of flowing fluids with the temperature of the aquifer and vice versa.  $T_S$  and  $T_D$  profiles measured in a wellbore are dependent on these two types of heat fluxes, occurring at two scales:

1. Strictly at the borehole scale, heat advection occurs within the water column of the borehole. It is determined by the distribution of groundwater inflows with depth and their respective intensities and temperatures. Free convection due to the variable density of fluids could also drive very slow ambient flows in wells, but this phenomenon is not discussed further in this work. When water flows vertically inside the borehole, its temperature distribution differs from that of  $T_A$ . In this case, the vertical temperature profile of the borehole wall is largely controlled by the temperature of the flowing water ( $T_D$ ). If no flowing water is impacting the wellbore, the temperature of the aquifer surrounding the borehole ( $T_A$ ) is in equilibrium with the geothermal gradient. If there is a temperature difference between the borehole wall and the aquifer because of flowing fluids, conduction flux occurs between them.

2. Within the portion of the aquifer influenced by the presence of the well or the pumping thereof, heat advection occurs, with groundwater flowing and mixing in fractures, from the furthest extent of the fracture until its interception with the borehole itself. If the orientation of the active fractures is not parallel to the aquifer isotherms ( $T_A$ ), heat transfer will occur between flowing fluid and the surrounding porous or fractured aquifer. Under such conditions, the temperature of the flowing fluid tends to equilibrate with  $T_A$  along its flow paths into the fractured media. Where active fractures intercept the borehole, groundwater finally discharges at a certain temperature ( $T_i$ ) into the wellbore.

**3.1.1. Ambient Water Flows under Static Conditions.** In crystalline aquifers, flow patterns are defined by various parameters, such as fracture density, orientation, and hydraulic interconnectivity. In such an environment, and even without artesian conditions, water circulation (i.e., ambient flows) may be induced by the presence of the wellbore itself [40]. The presence of a borehole can actually act as a hydraulic by-pass between fractures that were not connected prior to drilling. For a fractured aquifer without significant porosity, ambient flow inside a borehole has the following main characteristics: (1) it only occurs if two or more hydraulically active discrete fractures or distributed fractured intervals intercept the well, (2) its direction is determined by the head difference between each pair of fractures, (3) its intensity is determined by the combination of hydraulic transmissivity and hydraulic gradients between each pair of fracture zones, (4) it only impacts the length of the interval between hydraulically active fracture(s) that intercept the borehole, (5) its intensity may vary (over the flowing interval) if more than two discrete or distributed fractured intervals are involved, and (6) it can only be unidirectional (the fracture with highest hydraulic head is on one side of the flow interval in the borehole) or bidirectional (discrete or distributed fractures with lower heads are both above and below the fracture with highest hydraulic head).

**3.1.2. Water Flow under Pumping Conditions.** Under pumping conditions, the discharge of water from the well induces the drawdown of the water column into the borehole. The total resulting drawdown will generally counterbalance ambient flows driven by a small natural head gradient between fractures (e.g., Hess [16] measured ambient flow only as high as 0.3 L/min). When pumping is initiated, all fractures would be drained into the borehole. In this case, groundwater discharge rates into the borehole are essentially proportional to the hydraulic transmissivity of the fractures. If ambient flow has been active in the system for quite a long time, the  $T_S$  profile may be significantly different from  $T_A$ . When pumping is initiated,  $T_i$  would be briefly influenced by ambient  $T_S$  rather than  $T_A$  profiles. However, as pumping time increases,  $T_i$  would be determined by the heat advection of groundwater circulating and mixing in the aquifer (depending on the extension and orientation of fractures) and by the conductive reequilibration of flowing water with the aquifer at  $T_A$ .

**3.2. Conceptual Example of Temperature Profiles in a Fractured Aquifer.** Figure 2 aims to conceptually describe a scenario whereby the hydrogeological context, the bedrock fracture network, and the presence of a well (pumped or not) will drive advection and conduction heat fluxes induced by flowing water. These heat fluxes will modify the temperature field within the system, which could be revealed and described through the measurement of temperatures within the borehole. To simplify, the background geothermal gradient in Figure 2 is considered to be linear; that is, it does not represent a realistic gradient, which is usually multicurved in the upper part, because of seasonal and climatic atmospheric temperature variations [19]. The bedrock aquifer in Figure 2 has three distinct fractures, not connected with one another except at the location of the borehole. These fractures have different inclinations, hydraulic conductivities ( $K_2 \gg K_1 \approx K_3$ ), original temperatures (according to the linear geothermal gradient  $T_3 > T_2 > T_1$ ), and hydraulic heads ( $h_1 > h_2 > h_3$ ) at their furthest extents from the borehole. In this example, heads arbitrarily decrease with depth.

The situation under ambient conditions is presented in Figure 2(a). The highest hydraulic head at the outermost extent of fracture 1 induces an ambient flow that is redistributed between fractures 2 and 3. The flow distribution between the fractures is controlled by the hydraulic potential, which combines the hydraulic transmissivity and the hydraulic gradient between the fractures. In this example, even if  $K_2 > K_3$ , it is possible that fracture 3 drains a larger proportion of the ambient flow. This can occur if the head gradient between fracture 1 and fracture 3 is high enough that the hydraulic potential is higher than that between fracture 1 and fracture 2. This ambient flow induces a specific temperature profile ( $T_S$ ) in the wellbore (Figure 2(c)).  $T_i$  from fracture 1 is slightly colder than  $T_A$ , because the heat advection due to ambient flow along the fracture 1 network is strong enough to avoid its complete reequilibration with  $T_A$ . The water flowing upwards then exchanges heat with the borehole walls by heat conduction, implying that the  $T_S$  profile differs from the  $T_A$  profile. At fracture 2, part of the flow is drained out, so that the total flow within the borehole is reduced, inducing a relatively greater potential for temperature reequilibration by conduction with the borehole wall (increasing the slope of the  $T_S$  profile between fracture 2 and fracture 3). Up to fracture 3,  $T_S$  is the same as  $T_A$ , since no ambient flow influences its profile.

The situation under pumping conditions is presented in Figure 2(b). Due to the pumping, water drawdown into the well imposes the drainage of all active fractures into the wellbore, proportionally to the transmissivity of each fracture. As the pump is placed at the top of the well, flow in the borehole is unidirectional and gradually increases from the lowest to the highest active fracture. Flow intensities during pumping depend on hydraulic properties. However, compared to ambient conditions, flow intensities would be much higher during pumping because active fractures are more strongly solicited and the advection heat flux will become greater than the conduction heat flux. Consequently, the temperature of each inflow discharging into the borehole would be much closer to the temperature of the groundwater

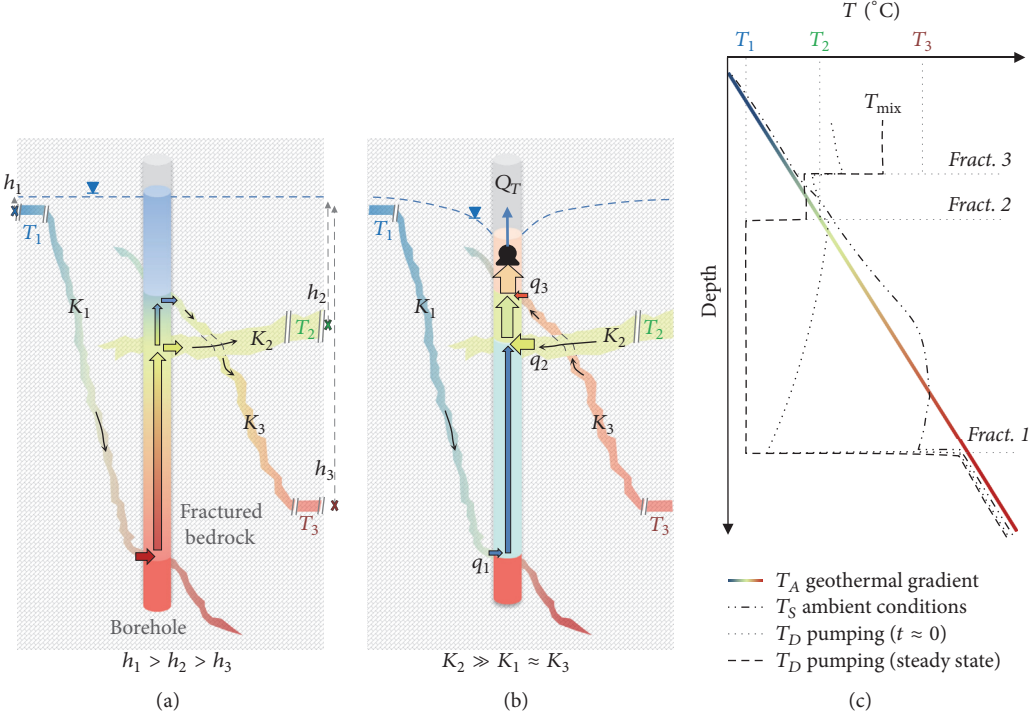


FIGURE 2: Conceptual schematic of temperature profiles in a fractured aquifer: (a) ambient scenario, (b) pumping scenario, and (c)  $T_S$  and  $T_D$  temperature profiles in the borehole.

at the far end origin of its fracture network.  $T_i$  at fracture 1 becomes colder under pumping conditions, because advection dominates over conduction. Once inside the borehole, upward flowing water from fracture 1 would still be subject to conduction-driven reequilibration with the temperature of the borehole wall. However, as its flow rate is much greater during pumping, the relative conductive heat flux is much lower than under ambient conditions. For the short pumping duration ( $t \approx 0$ ) in Figure 2(c), the  $T_D$  profile can still slightly reequilibrate with  $T_S$ , but as advection will quickly dominate during pumping, the  $T_D$  profile is less influenced by conductive reequilibration with the borehole wall.  $T_D$  between fractures 2 and 3 is determined by the advective mixing of inflow from fractures 1 and 2 (flow rates and  $T_i$ ) at the beginning of pumping. With increasing pumping duration, a thermal steady state would eventually be reached (Figure 2(c)). Every  $T_i$  will be influenced by the orientation of the fracture system. If the fracture network is inclined, thermal reequilibration within the aquifer could occur, so  $T_i$  would range between  $T_A$  (at the far end of the fracture network) and  $T_A$  (where the fracture intercepts the borehole).  $T_i$  resulting from very inclined fractures and high flows would be closer to the temperature at the far end of the drainage system. Conversely, if the fracture network is horizontal and flow is weak,  $T_i$  would be nearly equal to the temperature imposed by the background geothermal gradient,  $T_A$ , at the given depth. When advection controls over conduction (i.e., at steady state in Figure 2(c)):  $T_{i,\text{fracture } 2} \approx T_2$ ,  $T_{i,\text{fracture } 1} \gtrapprox T_1$ , and  $T_{i,\text{fracture } 3} \lesssim T_3$ . The temperature of the total flow

discharged at the wellhead ( $T_{\text{mix}}$  in Figure 2(c)) would mainly be determined by the mixing of inflows from fractures 1, 2, and 3, in proportion to their respective inflow intensities and temperatures.

**3.3. Heat Budget at the Borehole Scale.** The heat budget at the scale of a given volume ( $dV$ ) of the borehole is presented in Figure 3.  $dV$  is defined by the interval separating two passive temperature measurements,  $T(z+1)$  and  $T(z-1)$ . During pumping, water mixing occurs between groundwater inflow,  $q(z)$  (being positive if water enters the borehole and negative if water flows outward) at temperature  $T_i(z)$ , and water flowing upward ( $Q(z-1)$ ) in the borehole at temperature  $T_D(z-1)$ . The heat budget of mixing these volumes corresponds to the difference in heat transported by the volume of water entering the base ( $Q(z-1)$ ) and flowing through the wall between  $z-1$  and  $z+1$  (inflow  $q(z)$ ) and that transported by the water leaving  $dV$  at  $z+1$  ( $q(z) + Q(z-1)$ ).

For a quantity of water that is either heated or cooled, the general expression of advection heat flux,  $\phi_{\text{adv}}$  (W), is given by (2) [41], where  $Q$  ( $\text{m}^3/\text{s}$ ) is the water flow rate,  $C$  ( $\text{J m}^{-3}\text{K}^{-1}$ ) is the specific volumetric thermal capacity of water, and  $T_i$  and  $T_f$  are the initial and final temperatures of the water, respectively.

$$\phi_{\text{adv}} = QC(T_f - T_i). \quad (2)$$

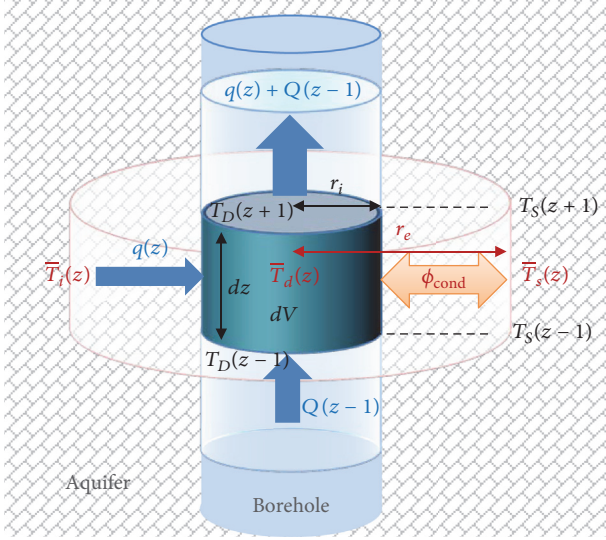


FIGURE 3: Heat budget at the borehole scale.

Considering (2) and the adiabatic mixing of two fluids at different temperatures, the heat balance of water fluxes  $q(z)$  and  $Q(z - 1)$  that mix in the borehole is given by

$$\begin{aligned} q(z)C[T_D(z) - \bar{T}_i(z)] \\ + Q(z - 1)C[T_D(z + 1) - T_D(z - 1)] = 0. \end{aligned} \quad (3)$$

Once pumping is initiated, the borehole wall temperature quickly shifts from  $T_S$  to  $T_D$ . Heat conduction then occurs radially through the surface of the borehole. The general expression of radial conductive heat transfer at steady state through a semi-infinite solid [41] is applied. In this case, the finite boundary is the borehole wall, which is subject to a temperature shift due to pumping. The temperature anomaly will propagate within the semi-infinite solid (e.g., the aquifer). Heat conduction flux between the borehole wall and the aquifer is then given by (4), where  $dz$  is the length of the interval,  $\bar{T}_s(z)$  and  $\bar{T}_D(z)$  are the mean temperatures of the water in the borehole under static conditions and during pumping respectively, averaged for the interval  $dz$ ,  $r_i$  (m) is the radius of the well,  $r_e$  (m) is the time-dependant radius of the heat conduction influence around the borehole, and  $x = r_e - r_i$  is the annular distance of propagation of the temperature anomaly due to pumping ( $T_D - T_S$ ), which dissipates into the aquifer. With increasing pumping duration,  $r_e$  increases in (5), so that the heat conduction flux fades during pumping.  $\lambda$  ( $\text{W m}^{-1}\text{K}^{-1}$ ) is the bulk thermal conductivity of the aquifer.

$$\phi_{\text{cond}} = \frac{2\pi\lambda dz [\bar{T}_S(z) - \bar{T}_D(z)]}{\ln(r_e/r_i)}. \quad (4)$$

Considering advection and conduction heat fluxes, the heat balance at the borehole scale is given by (5), which combines (3) and (4):

$$q(z)C[T_D(z) - \bar{T}_i(z)]$$

$$\begin{aligned} & + Q(z - 1)C[T_D(z + 1) - T_D(z - 1)] \\ & = \frac{2\pi\lambda dz [\bar{T}_S(z) - \bar{T}_D(z)]}{\ln(r_e/r_i)}. \end{aligned} \quad (5)$$

This equation then links the measured temperature-depth profiles (i.e.,  $T_S(z)$  and  $T_D(z)$ ) with three variables:  $q(z)$ ,  $\bar{T}_i(z)$ , and  $r_e$  (which increases with pumping duration).  $q(z)$  distribution could also be measured independently, for example, with a flowmeter.

## 4. Results

**4.1. Depth-Temperature Profiles Modelled with the Heat Budget.** In this section, temperature-depth profiles were modelled for dynamic conditions ( $T_D(z)$ ), considering a conceptual well which intercepts six hydraulically active fractures (Figure 4). In this example, the percentage of total pumping discharge (%  $Q_T(z)$ ) and temperature ( $\bar{T}_i(z)$ ) associated with each inflow have been randomly and arbitrarily set with depth. In order to simplify the thermal static conditions, a linear geothermal gradient was applied (arbitrarily set to  $-1^\circ\text{C}/100\text{ m}$ ), with an absence of ambient flows so that  $T_S(z) = T_A(z)$ . Pumping occurs at the top of the wellbore, inducing upward water flows. Blue arrows in Figures 4(b) and 4(c) represent water flow directions in the water column and inflow from the aquifer. The  $T_D(z)$  response to pumping was modelled using the heat budget (see (5)) implemented in a spreadsheet, with a vertical resolution  $dV = 0.5\text{ m}$ . Fixed parameters used for the model are as follows: radius of the well,  $r_i = 0.075\text{ m}$ , bulk thermal conductivity of the aquifer,  $\lambda_s = \lambda_s^{(1-n)}\lambda_w^n = 1.88\text{ W m}^{-1}\text{K}^{-1}$ , effective porosity,  $n = 0.05$ , and thermal conductivity of sedimentary bedrock,  $\lambda_s = 2.0\text{ W m}^{-1}\text{K}^{-1}$  and of water,  $\lambda_w = 0.6\text{ W m}^{-1}\text{K}^{-1}$  [42]. Various conditions for heat advection and conduction fluxes were simulated to evaluate their effect on the shapes of the  $T_D(z)$  profiles. The effect of heat advection (at the given heat conduction,  $r_e = 0.091\text{ m}$ ) was investigated by varying the total pumping rate from  $Q_T = 1\text{ L/min}$  to  $Q_T = 100\text{ L/min}$  (Figure 4(b)), and the effect of heat conduction (at the given heat advection,  $Q_T = 40\text{ L/min}$ ) was investigated by varying  $r_e$  from 0.076 to 0.101 m (Figure 4(c)). In both simulations,  $T_D(z)$  profiles are also provided by considering only heat advection. Conduction is neglected by setting  $\phi_{\text{cond}} = 0$  in (5). This is theoretical, because in reality conduction always occurs, but the latter  $T_D(z)\phi_{\text{cond}} = 0$  profiles are helpful to Figure 4 for visually distinguishing when heat advection becomes dominant over heat conduction.

**4.1.1. General Patterns and Processes Controlling Modelled Depth-Temperature Profiles.** The positions of water inflows into the wellbore are easily identifiable in the dynamic temperature profiles in Figure 4. However, even if  $q(5\text{ m}) = 20\% Q_T$  and  $q(20\text{ m}) = 10\% Q_T$  (Figures 4(b) and 4(c)), the occurrence of these large inflows is not very well-revealed from the  $T_D$  profile, because  $T_i(5\text{ m}) \approx T_D(5\text{ m})$  and  $T_i(20\text{ m}) \approx T_D(20\text{ m})$ . These slight  $T_D$  shifts are thus enhanced when

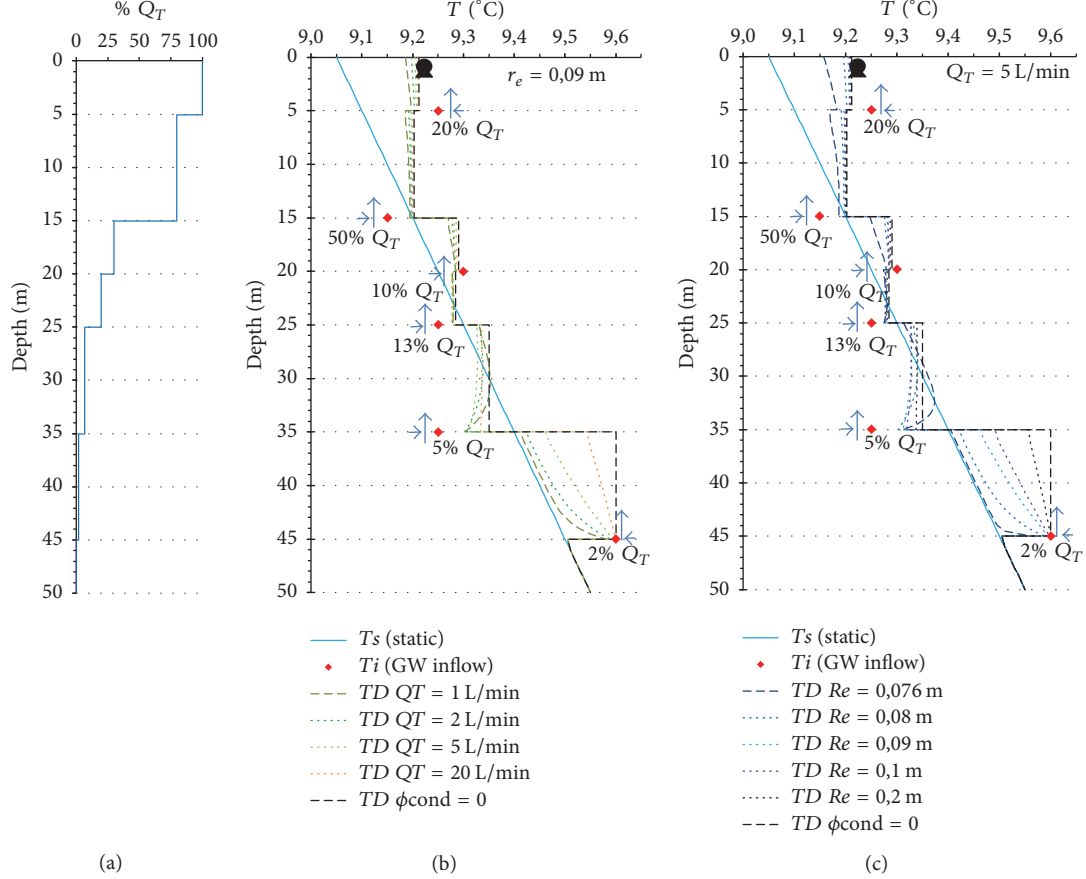


FIGURE 4: Dynamic depth-temperature profiles modelled with the heat budget.

pumping conditions favor heat conduction (i.e., lower total discharge in Figure 4(b) or lower  $r_e$  values in Figure 4(c)).

As  $T_D$  profiles are derived from both advection and conduction heat fluxes, the shape of the temperature profiles does not directly (graphically) reflect the water flow distribution in the wellbore. In Figures 4(b) and 4(c), temperature profiles do not mimic the shape of water flow distribution in the wellbore. Even when conduction is neglected ( $T_D \phi_{\text{cond}} = 0$  in Figures 4(b) and 4(c)), the resulting  $T_D$  profiles still do not directly reflect water flow distribution in the wellbore. Another important characteristic to note is that when conduction is (or becomes) negligible in this case,  $T_D(z)$  profiles are entirely controlled by the distribution of inflows into the wellbore, independently of the total discharge rate.

$T_D$  profiles appear to be extremely sensitive to very low groundwater inflows into the wellbore, especially at the bottom intervals for this example, where the total flow of water remains low. In this example, the bottom inflow,  $q$  (45 m), would be detectable for flows as low as 0.02 L/min (e.g., in Figure 4(b), where  $q(45 \text{ m}) = 2\% \text{ of } Q_T = 1 \text{ L/min}$ , with medium conduction,  $r_e = 0.091 \text{ m}$ ) or as low as 0.1 L/min (e.g., in Figure 4(c), where  $q(45 \text{ m}) = 2\% \text{ of } Q_T = 5 \text{ L/min}$ , with intense conduction,  $r_e = 0.076 \text{ m}$ ).

As  $T_D(z)$  profiles depend on the temperature of each inflow, the range for each  $T_i(z)$  could be qualitatively estimated by visualizing the cooling (e.g.,  $T_i(z) < T_D(z)$ ) or

warming (e.g.,  $T_i(z) > T_D(z)$ ) of the water column where steps in the profile occur.

The influence of heat conduction fluxes could become less important than heat advection with increasing pumping time and/or with increasing water flow rates in the borehole. In Figure 4(b) (representing increasing pumping rates),  $T_D$  profiles become dominated by heat advection for  $Q_T(35 \text{ m}) > 1.4 \text{ L/min}$  (e.g., 7% of  $Q_T = 20 \text{ L/min}$  at depths shallower than 35 m). In Figure 4(c) (representing increasing pumping time; e.g., increasing  $r_e$ , with  $Q_T = 5 \text{ L/min}$ ),  $T_D$  profiles become dominated by heat advection as soon as  $r_e > 0.081 \text{ m}$  for  $Q_T(35 \text{ m}) > 0.35 \text{ L/min}$  (e.g., 7% of  $Q_T = 5 \text{ L/min}$  at depths shallower than 35 m). It is important to note that a radius of influence of  $r_e = 0.081 \text{ m}$  represents a temperature front due to pumping that radially penetrates only 6 mm into the aquifer ( $r_i = 0.075 \text{ m}$  in this case).

Another way to look at the respective influences of advection and conduction fluxes at the borehole scale is given in Figure 5, which provides a comparison of advection and conduction fluxes calculated at the borehole scale using (2) and (4). Advection heat flux in the wellbore is related to flow and to the cooling or warming of the water ( $\Delta T$ ) due to inflowing groundwater. Conduction heat flux between the borehole wall (at  $T_D$ ) and the aquifer (at  $T_S = T_A$ ) varies logarithmically with the propagation distance ( $x = r_e - r_i$ ) of the temperature offset ( $T_D - T_S$ ) into the aquifer.

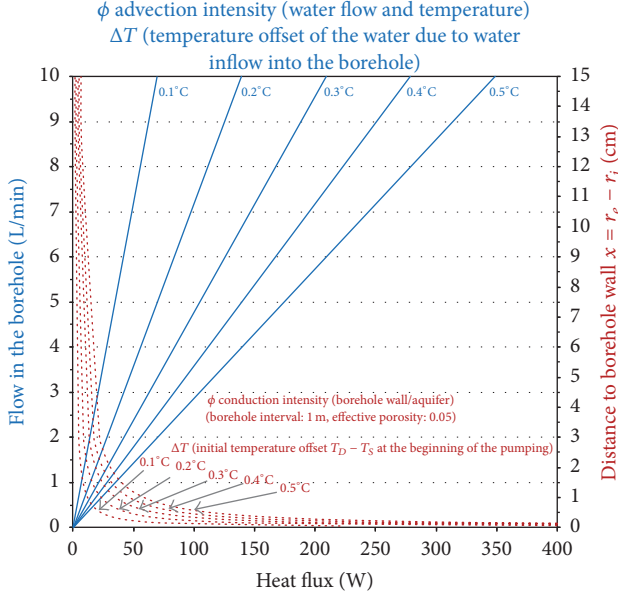


FIGURE 5: Comparison of advection and conduction heat fluxes at the borehole scale.  $\Phi_{\text{advection}} = f$  (total flow rate, temperature offset due to groundwater inflow) and  $\Phi_{\text{conduction}} = f$  (distance of radial temperature propagation into the aquifer,  $T_D - T_S$  offset).

Conduction flux is therefore intense at the beginning of the pumping ( $r_e \approx r_i$ ) and fades with pumping duration (i.e., with increasing  $r_e$ ). Interpretation of Figure 5 indicates that conduction flux is higher than advection flux when flow rates are less than 1 L/min and when temperature propagation is less than approximately 1.5 cm into the aquifer ( $r_e = 0.09$  m;  $r_i = 0.075$  m). Conversely, if water flow is greater than 1 L/min in the borehole, with increasing pumping duration (i.e.,  $x > 1.5$  cm), advection fluxes become higher than conduction.

**4.1.2. Potential of a High-Resolution Temperature Probe to Be Used as a Flowmeter.** A relevant question is whether passive temperature measurements could directly reflect the water flow distribution in the wellbore. This question is investigated in this section by modelling depth-temperature dynamic profiles with the heat budget, with  $T_i(z)$ ,  $q_i(z)$ , and  $r_e$  as variables. The fitting procedure consists of minimizing the root mean square error (RMSE) of  $T_D$  (see (6)), where  $T_{\text{Dreference}}(z)$  represents the observed temperature-depth profiles,  $T_{\text{Dmodel}}(z)$  represents the modelled temperature-depth profiles,  $D_{\text{total}}$  is the total depth of the wellbore, and  $dz$  is the vertical resolution of the heat budget.  $D_{\text{total}}/dz$  represents the number of  $T_{\text{Dmodel}}(z)$  calculated with the heat budget.

$$\text{RMSE } T_D = \sqrt{\frac{\sum (T_{\text{Dmodel}}(z) - T_{\text{Dreference}}(z))^2}{D_{\text{total}}/dz}}. \quad (6)$$

In this example, the fitting procedure has 13 variables ( $6T_i(z)$ ,  $6q_i(z)$ , and  $r_e$ ) and is constrained by  $100T_D(z)$  observations (well depth of 50 m, with a vertical resolution of  $dz = 0.5$  m). To avoid divergence of the iterative procedure,  $T_i(z)$  variables were initialized and constrained for each water inflow. Inflow

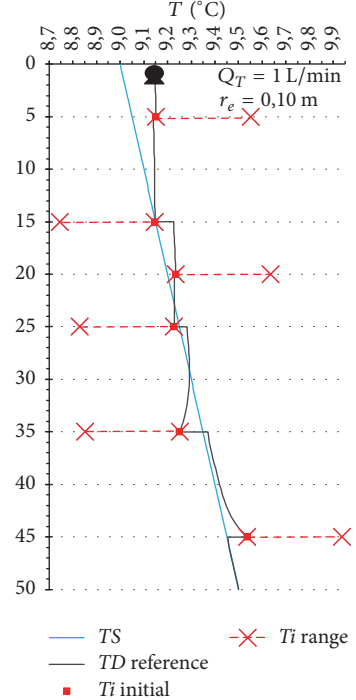


FIGURE 6: Example of  $T_i(z)$  initialization prior to  $T_D(z)$  modelling with the heat budget.

temperatures  $T_i(z)$  were initialized at  $T_{\text{Dreference}}(z)$  ( $T_{\text{initial}}$  in Figure 6) and constrained within the range of  $T_i(z) = T_{\text{Dreference}}(z) \pm \Delta T$  ( $T_{\text{range}}$  in Figure 6). The temperature range is logically anchored depending on the cooling or warming of the  $T_D$  profile resulting from inflows. For the situation wherein the water column is cooling (because of cold inflow), the range is set to  $T_{\text{Dreference}}(z) - \Delta T < T_{\text{range}} < T_{\text{Dreference}}(z)$  and vice versa for a warming situation ( $T_{\text{Dreference}}(z) < T_{\text{range}} < T_{\text{Dreference}}(z) + \Delta T$ ). In this example,  $\Delta T$  was arbitrarily set to  $0.4^\circ\text{C}$ , but a large possible range over which  $T_i(z)$  may vary is permitted before the fitting procedure converges. Water inflow intensities were all initialized at very low flows ( $q_i(z) = 0.0001$  L/min) and constrained so that the total modelled discharge must be equal to the total reference discharge. Finally, conduction in the borehole is initialized as being intense ( $r_e = 0.076$  m) and constrained within the possible range (i.e.,  $r_e > r_i$ ).

For modelling, two reference  $T_{\text{Dreference}}$  profiles were generated using the conceptual model (as described at the beginning of Section 4.1), with conduction set to  $r_e = 0.10$  m and total pumping rates of 1 L/min (Figure 7) and 20 L/min (Figure 8).

The fitting procedure very efficiently models  $T_D(z)$  in both cases. As shown in Figures 7 and 8,  $T_{\text{Dreference}}$  and  $T_{\text{Dmodel}}$  appear graphically superimposed. Numerically, some discrepancies remain, but the RMSE remains low in both cases ( $\text{RMSE } T_D \approx 10^{-4}$ ). The fitting procedure adequately models the whole system at a low discharge rate ( $Q_T = 1$  L/min, Figure 7), associated with low error for each variable;  $T_i(z)$  ( $\text{RMSE } T_i = 1.2 \times 10^{-5}^\circ\text{C}$ ),  $q_i(z)$  ( $\text{RMSE } q_i = 1.8 \times 10^{-3}$  L/min), and  $\Delta r_e = 8.7 \times 10^{-4}$  m ( $\Delta r_e = r_{\text{emodel}} - r_{\text{ereference}}$ ). At a higher

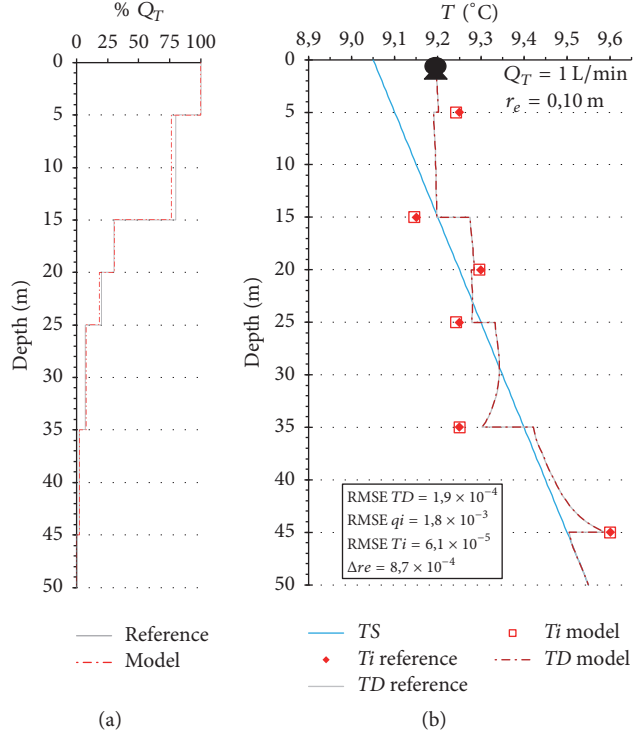


FIGURE 7: Results of  $T_D(z)$  modelling with the heat budget at  $Q_T = 1 \text{ L/min}$ . (a) Flow-depth distribution; (b) dynamic temperature profiles ( $T_D(z)$ ) and temperatures of inflows ( $T_i(z)$ ).

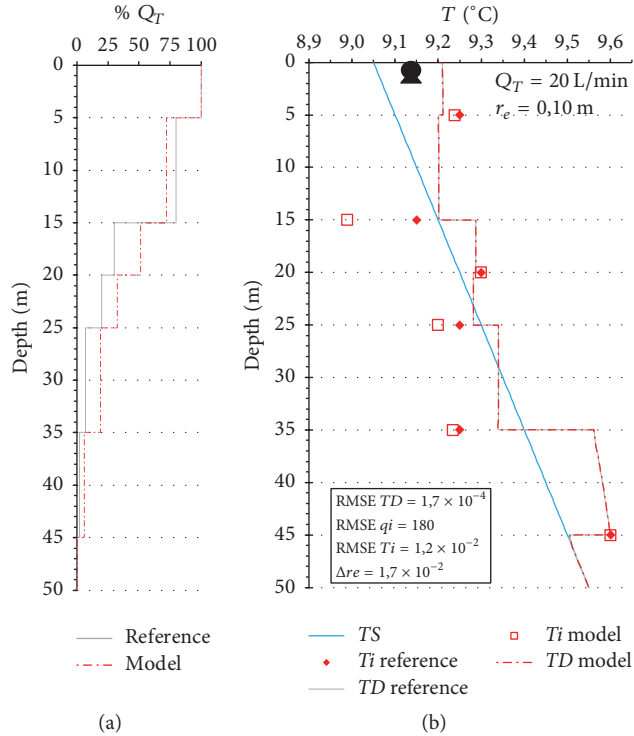


FIGURE 8: Results of  $T_D(z)$  modelling with the heat budget at  $Q_T = 20 \text{ L/min}$ . (a) Flow-depth distribution; (b) dynamic temperature profiles ( $T_D(z)$ ) and temperatures of inflows ( $T_i(z)$ ).

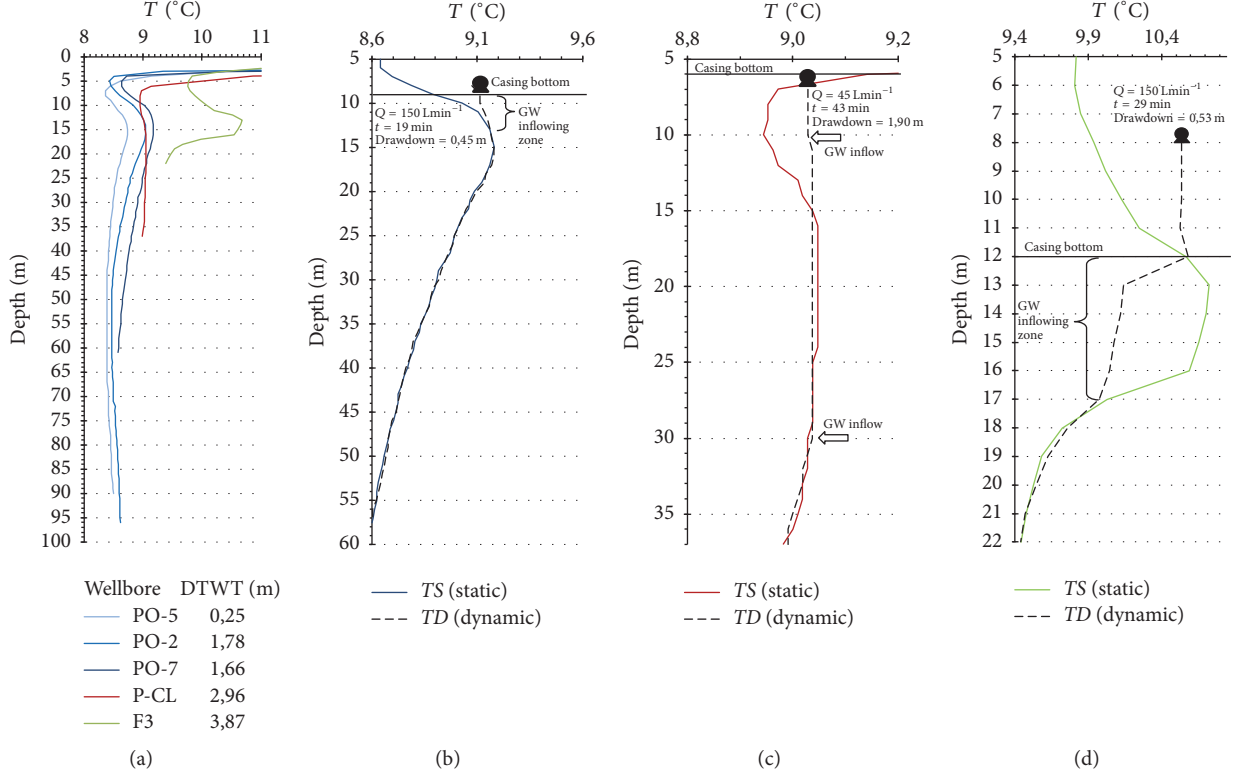


FIGURE 9: Temperature profiles in June 2016 for all wells under static conditions (a) and under static and dynamic conditions for wells PO-7 (b), P-Cl (c), and F3 (d).

discharge rate ( $Q_T = 20 \text{ L/min}$ , Figure 8), errors for modelled variables increase, with RMSE  $T_i = 1.2 \times 10^{-2} \text{ °C}$ , RMSE  $q_i = 180 \text{ L/min}$ , and  $\Delta r_e = 1.7 \times 10^{-2} \text{ m}$ . The ability of the model to converge to accurate variable values depends on the degree of curving for the  $T_D(z)$  profiles. The more the profile is curved along the entire profile due to the dominant influence of conduction over advection, the easier the fitting procedure can converge within a narrow, accurate range for the variables  $T_i$ ,  $q_i$ , and  $r_e$ . Even a very slight influence of conduction would theoretically induce a slight curvature in  $T_D(z)$ , so that the model can theoretically always be solved. However, with the diminishing influence of conduction, the preciseness (and complexity) of the fitting procedure has to proportionally increase to still obtain the narrowest and most accurate range of solutions for the variables. At the other extreme, if there is no conduction at all, the model can still perfectly converge to fit the  $T_D(z)$  profiles, but an infinity of solutions is possible for each pair of  $T_i(z)$  and  $q_i(z)$  associated with the inflows. This is because, without conduction, any variation in  $T_i(z)$  could be numerically compensated by  $q(z)$  to give the same perfectly square  $T_D(z)$  profiles that are observed after mixing.

#### 4.2. Field Applications

**4.2.1. Qualitative Interpretation of Field Depth-Temperature Profiles.** PO-2, PO-5, and PO-7 temperature logs under static conditions (Figure 9(a)) were taken on the same day and represent typical static temperature profiles not influenced

by ambient flows. Heat pulse flowmeter tests [43] were performed for well PO-7 under static conditions and did not allow the detection of water circulation in the borehole (the minimum velocity resolution of the device is 0.113 L/min). As PO-2, PO-5, and PO-7 temperature profiles have the same symmetrical curving, it is inferred that ambient flows are so low, if there are any at all, that they do not significantly impact the temperature profiles of these three wells. The corresponding  $T_s$  profiles of the three wells differ by 0.1–0.5 °C, which may be explained by different local recharge rates, the nature and thickness of the unconsolidated sediments, or differences in land cover. These discrepancies are not considered further in this work, which focuses rather on borehole logging to characterize active hydraulic fractures.  $T_s$  profiles for wells PO-2, PO-5, and PO-7 are therefore considered to be representative of typical  $T_A$  profiles of southern Quebec: (1) the seasonal variation in soil temperature (from the atmospheric signal) propagates from the land surface down to 15 m depth. The minimum temperature, near 5 m depth, corresponds to the cold temperature signal of winter 2015–2016, which has propagated into the subsurface; (2) from 15 m to 50–60 m, temperatures decrease with depth. This inverse gradient can be explained by the climatic warming in Canada over the last 150–200 years [44]; and (3) deeper than 50–60 m, which corresponds to the transition zone to the normal geothermal gradient, temperatures increase with depth.

Static and dynamic temperature logs of the three pumped wells are superimposed in Figure 9. The PO-7 temperature

log under dynamic conditions (Figure 9(b)) was taken after 19 min of pumping with a discharge rate of 150 L/min. Static and dynamic temperature profiles differ near the surface, down to 13 m depth, and are nearly identical below this depth (i.e.,  $T_S = T_D$ ). This indicates that the productivity of this 52 m screened well essentially originates from an only 4 m-long productive interval in the upper part of the well.

For well P-Cl, the static temperature log (Figure 9(a)) already suggests the presence of ambient flow between 15 and 30 m, because the constant temperature within this interval differs from the expected curved  $T_A$  profile. Although the direction and intensity of ambient flows could not be determined at this stage, the  $T_S$  profile already reveals that an ambient flow of water at 9.04°C is circulating between one or more fractured intervals located in the 15–30 m depth range. The P-Cl dynamic  $T_D$  profile, taken after 40 min of pumping with a discharge rate of 45 L/min, confirms the information revealed by the  $T_S$  profile but also indicates that the main productive zone must be located near 30 m depth, because its inflow temperature (9.04°C) completely resets the temperature of the water circulating upward along the entire length of the borehole. Other small water inflows from 10 m to 30 m depth may be possible, but as no temperature variation is distinguishable in this interval, the main inflow must be located at approximately 30 m depth.

The  $T_S$  profile for well F3 (Figure 9(d)) also suggests the presence of ambient flows, because between 12 and 17 m the profile is overcurved compared to what would be expected from the influence of  $T_A$  alone. This suggests that more than two active fracture zones are likely located within the interval between 12 and 17 m, thus creating a complicated temperature pattern. Ambient flows between these active fractures create this anomalous temperature interval. In F3, the  $T_D$  profile (Figure 9(d)) was taken after 29 min of pumping with a discharge rate of 150 L/min. As  $T_S$  and  $T_D$  coincide below 17 m, no active fracture is expected to be present below this depth. Joint analysis of passive and dynamic logs qualitatively reveals the following: (1) the first active fracture zone is located between 16 and 17 m depth and initiates water flow into the borehole, with a bottom inflow temperature of 10.00°C; (2) between 16 and 13 m depth, one single qualitative interpretation is not possible. The temperature gradient retains the same orientation and intensity between each measurement. This could either indicate that warmer water is inflowing ( $T_i > T_D$ ) or that temperature reequilibration by conduction occurs between the borehole and a warmer aquifer neighboring the borehole ( $T_S > T_D$ ) or a combination of these two scenarios. And, finally, (3) between 12 and 13 m, the slope of the dynamic log increases strongly, which can only be explained by warmer water inflow ( $T_i > T_D$ ), which increases substantially.

**4.2.2. Quantitative Borehole Investigation: Temperature Logging, Flow Metering, and Televiwing.** Flowmeter logging in boreholes PO-7 and F3 was performed with pumping rates as high as possible, depending on the productivity of the given well, in order to maximize water velocities in the boreholes. Different pumping rates were tested on each of the wells (results not shown in this article), with no measurable

variation in well inflow distribution found to result with depth. The PO-7 televiwing results are presented in Figures 10(a) and 10(b), and the flowmeter log is presented in Figure 10(c). The flowmeter log revealed that 10% of total inflows originate from a low-fractured interval, located between 12 and 13 m. A discrete fracture is visible at 10.5 m and alone accounts for 74% of the total productivity of the well. The remaining 16% of the inflow originates from a joint or fracture located at 9.6 m depth and from other small fractures located above this and down to the base of the casing. For well F3 (televiwing in Figures 11(a) and 11(b); flowmeter log in Figure 11(c)), small conduits are identifiable through televiwing at 16.5 m depth. Flowmeter measurements show that these conduits account for approximately 7% of the total well productivity. No other water inflow is identifiable through the flowmeter results until above 14 m depth. Televiwing also revealed information about the thickness of strongly fractured banks that alternate with unfractured dolomite intervals. Based on flowmeter results where flow increases, fractured zones from 14 to 13.7 m, 13.4 to 12.8 m, and 12.6 to 12.3 m account for approximately 3, 31, and 46% of the total transmissivity of well F3, respectively. The remaining 13% of the transmissivity likely originates from fractures located near the base of the casing. For wells PO-7 and F3, the distribution of hydraulic conductivities for each productive fractured interval are given in Figures 10(d) and 11(d), respectively, and have been calculated using (1). It should be noted that the spinner flowmeter provided highly valuable hydrogeological information here, with a high vertical resolution (5 cm in this work), and was obtained relatively quickly (i.e., less than half an hour to log a 60 m deep well).

Temperature logs under static and dynamic conditions are presented in Figures 10(e) and 11(e) for wells PO-7 and F3, with close-ups of depth intervals where water inflow occurs and influences  $T_D(z)$  profiles. The full-depth scale temperature logs are presented in Figure 9. The heat budget (see (5)) was partially used in this applied case, because the measurement resolution ( $dz = 1$  m) for the available data is insufficient to perform the full fitting procedure presented in Section 4.1.2. Also, at the time of measurement, high discharge rates were set to maximize the sensitivity of the flowmeter, while the thermal fitting procedure would instead require low discharge rates to favor conduction (Section 4.1.2). Nevertheless, the heat budget was applied for wellbore PO-7, to calculate mean inflow temperatures (Figure 10(e)), with flow distribution intervals known from flow metering. Given high flow rates and pumping times, conduction was set to low intensity ( $r_e = 1$  m). For PO-7, calculated  $T_i(z)$  were all warmer than  $T_S(z)$  at a 13 m depth, indicating that pumping-induced drainage might all originate from very surficial and warmer horizons, above 5 m depth ( $T_S(z)$  profile in Figure 9(a)), influenced by the previous summer's signal propagation within the subsurface. For well F3,  $T_i(z)$  can be calculated for very high inflow intervals (12 to 13 m, 13 to 14 m, and 16 to 17 m), with respective  $q_i(z)$  measured with the flowmeter (model 1 in Figure 11(e)). For two other intervals (14 to 15 m and 15 to 16 m), flow metering did not reveal any increase in flow, resulting in the nondetection of inflows

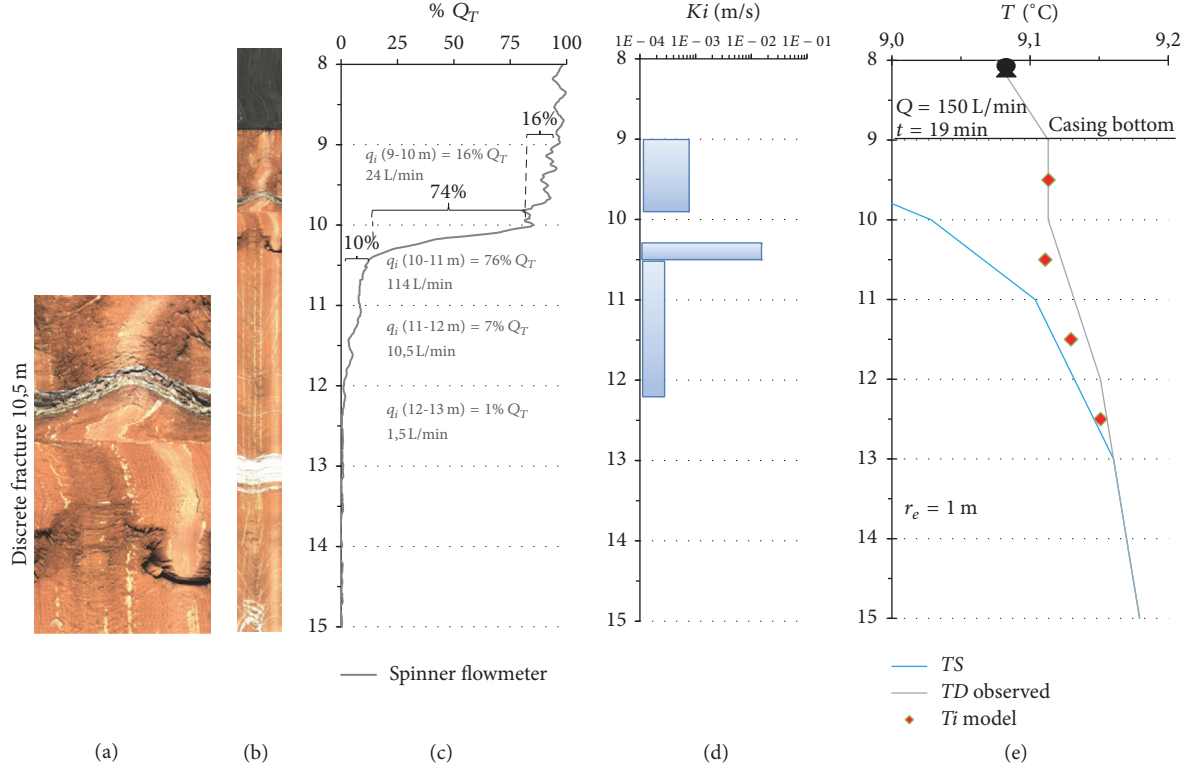


FIGURE 10: Borehole PO-7 logging results: (a) televiewing close-up of the most productive fracture, (b) televiewing log, (c) flow distribution obtained by flowmeter, (d) vertical distribution of hydraulic conductivities obtained by flowmeter, and (e) temperature profiles under static and dynamic conditions and temperature of groundwater inflows calculated with the heat budget.

within these intervals. However,  $T_D(z)$  profiles between 14 and 16 m show significant temperature increases. As total advection flow in the water column is already high above 16 m depth (10.5 L/min), increasing temperature between 16 and 14 m cannot be explained by conduction reequilibration towards  $T_S(z)$ . Examples are given in Figure 11(e) (model 1), representing modelled  $T_D(z)$  for various conduction intensities, but with no inflows between 14 and 16 m depth. In this case,  $T_D(z)$  modelled between 14 and 16 m could not fit the observed  $T_D(z)$  at any conduction intensity without introducing inflows at this interval. The heat budget fitting procedure was then applied to all intervals, including inflows to the 14 to 15 m and 15 to 16 m intervals (model 2 in Figure 11(e)). Conduction intensity in the latter model (2) was arbitrarily set to  $r_e = 1$  m, a value that lowers the influence of conduction, given that the pumping time of the experiment is 29 min. With model 2 (Figure 11(e)), warm inflows,  $T_i(14-15\text{ m}) = 10.70^\circ\text{C}$  and  $T_i(16-17\text{ m}) = 10.51^\circ\text{C}$ , were estimated, corresponding with  $q(14-15\text{ m}) = 0.69 \text{ L/min}$  and  $q(15-16\text{ m}) = 0.75 \text{ L/min}$ . These calculated values are not very accurate, because the fitting procedure is poorly constrained, with a limited temperature observation (resolution of only  $dz = 1\text{ m}$ ). In this case, warmer  $T_i(z)$  could lead to even lower  $q_i(z)$  while still perfectly fitting  $T_D(z)$ . Nevertheless, the most relevant information here is that the combination of temperature measurements (even at a resolution of  $0.01^\circ\text{C}$ ) and heat budget analysis allows the occurrence of very low

inflows to be inferred among the much higher productive intervals characterizing wellbore F3. Discussion linking the  $T_i(z)$  values of well F3 to the depth at which groundwater is drained during pumping is provided in Section 4.2.3 through more detailed experiments and analysis.

**4.2.3. Inference of Groundwater Origin from Transient Temperature Logging and Heat Budget Application.** Two temperature logs were obtained for well F3, in June and November 2016. In Figure 12(a),  $T_s$  measured in June 2016 showed a colder water interval from 5 to 11 m depth (influenced by cold air temperature at the ground surface for winter 2015-2016), followed by a warmer zone from 11 to 17 m (influenced by warm air temperature at the ground surface for summer 2015).  $T_s$  measured in November 2016 showed the influence of summer 2016 from the top of the water table until 12 to 13 m depth and likely a smoothed downward propagation of the summer 2015 signal below 17 m. Figures 12(b) and 12(c) present  $T_s$  and  $T_D$  for June and November 2016, respectively, along with  $T_i$  for each pumping time and discharge rate.  $T_i$  values were calculated using the heat budget at the borehole scale (see (5)) for the most productive intervals identified by flow metering (Section 4.2.2) to be 70, 23, and 7% of the total transmissivity of well F3 for the 12 to 13 m, 13 to 14 m, and 16 to 17 m depth intervals, respectively.

For both June and November logs,  $T_i$  profiles already differ from  $T_s$  shortly after the beginning of pumping. These

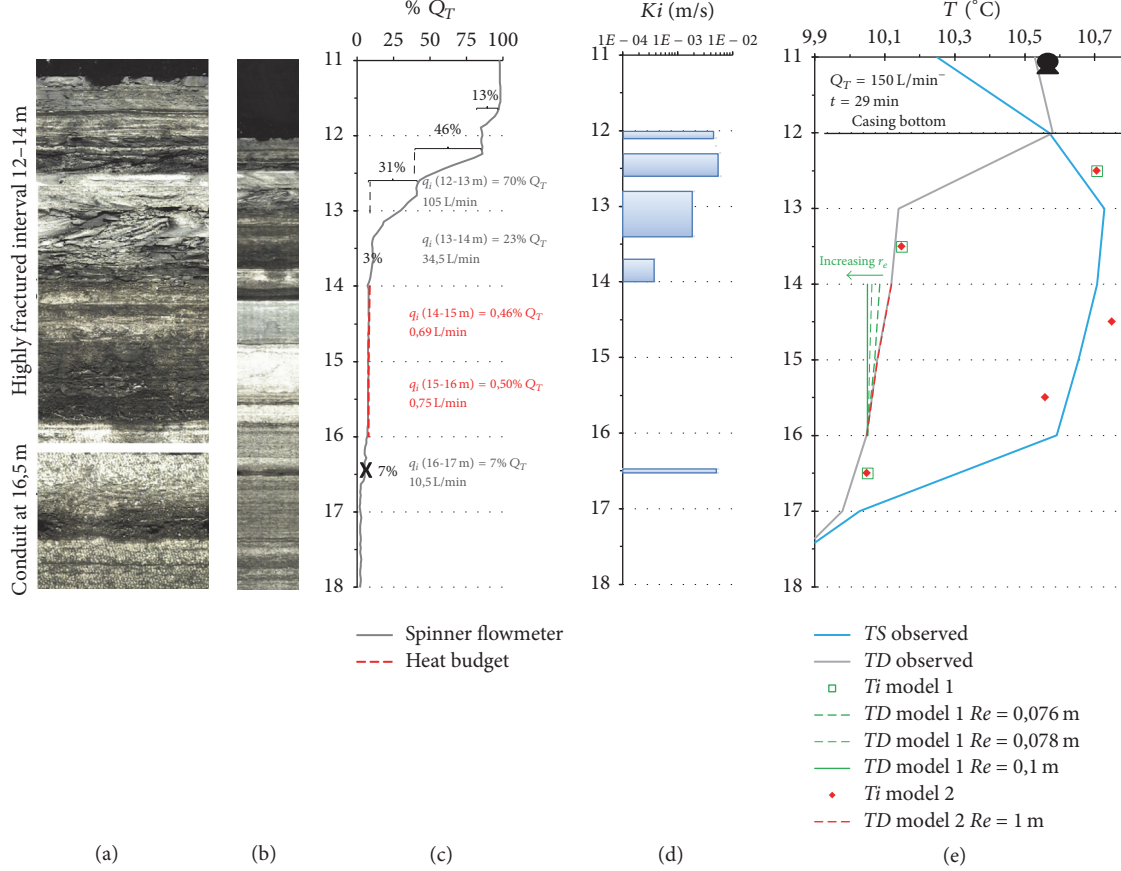


FIGURE 11: Borehole F3 logging results: (a) televiewer close-up of productive intervals, (b) televiewer log, (c) flow distribution obtained by flowmeter and flow calculated with the heat budget between 14 and 16 m depth, (d) vertical distribution of hydraulic conductivities obtained by flowmeter, and (e) temperature profiles under static and dynamic conditions and temperature of groundwater inflows calculated with the heat budget.

discrepancies suggest that, soon after pumping began,  $T_i$  patterns are influenced by inflows originating from active fracture networks in equilibrium with  $T_A$ . This also indicates that ambient flows (between 12 and 17 m depth) imposing the  $T_S$  profiles around the borehole mask the  $T_A$  profile.  $T_i$  temperatures then appear to be very rapidly controlled by the temperatures within drained horizons, the temperatures of which depend on the seasonal  $T_A$  signal. In June (Figure 12(b)),  $T_i$  is warmest in the 12 to 13 m interval and must drain the warmer horizon influenced by summer 2015 (13 to 16 m depth), because temperatures for over- and underlying intervals are colder.  $T_i$  for the two lower inflow intervals (13 to 14 and 16 to 17 m depth) are colder and, with respect to the  $T_S$  profiles for June, could drain colder horizons either above 11 m depth or below 17 m depth. However, analysis together with the November profiles (Figure 12(c)) shows that  $T_i$  from 13 to 14 and 16 to 17 m depth must drain cold water originating from below 17 m, because intervals above 11 m depth are warmer and cannot explain such cold temperatures. Although the interpretation of temperature inflow patterns in Figures 12(b) and 12(c) remains difficult, one key piece of information provided is that all  $T_i$  values become cooler as pumping duration increases, independently of the season.

This suggests that cold water originates from horizons deeper than 17 m depth.

The evolution of inflow temperatures,  $T_i(z)$ , in well F3 during pumping in November is presented in Figure 13. The temperature range from the beginning to the end of pumping is comparable for every depth interval. This common cooling of all inflows with time suggests that all inflows drain stratified fractured horizons and have comparable orientations. It can be noted that, even after 150 min of pumping at high discharge rates (150 L/min at the final stage), none of the inflow temperatures reaches a plateau. This means that temperature equilibration by conduction between flowing groundwater and the aquifer has not yet reached a thermal steady state along the flow path from the origin of aquifer drainage to the wellbore. Even if it is not quantified here, this suggests rather long conduits or channelized flow paths. In such a case, the reequilibration of the water temperature by heat conduction would take longer, because surface exchange with the aquifer is low. Conversely, thermal conduction equilibration occurring in a highly homogeneously fractured aquifer (or even a porous medium) would reach a steady state much faster, as the water/aquifer surface exchange is much higher. Compared to the two other fractured intervals,

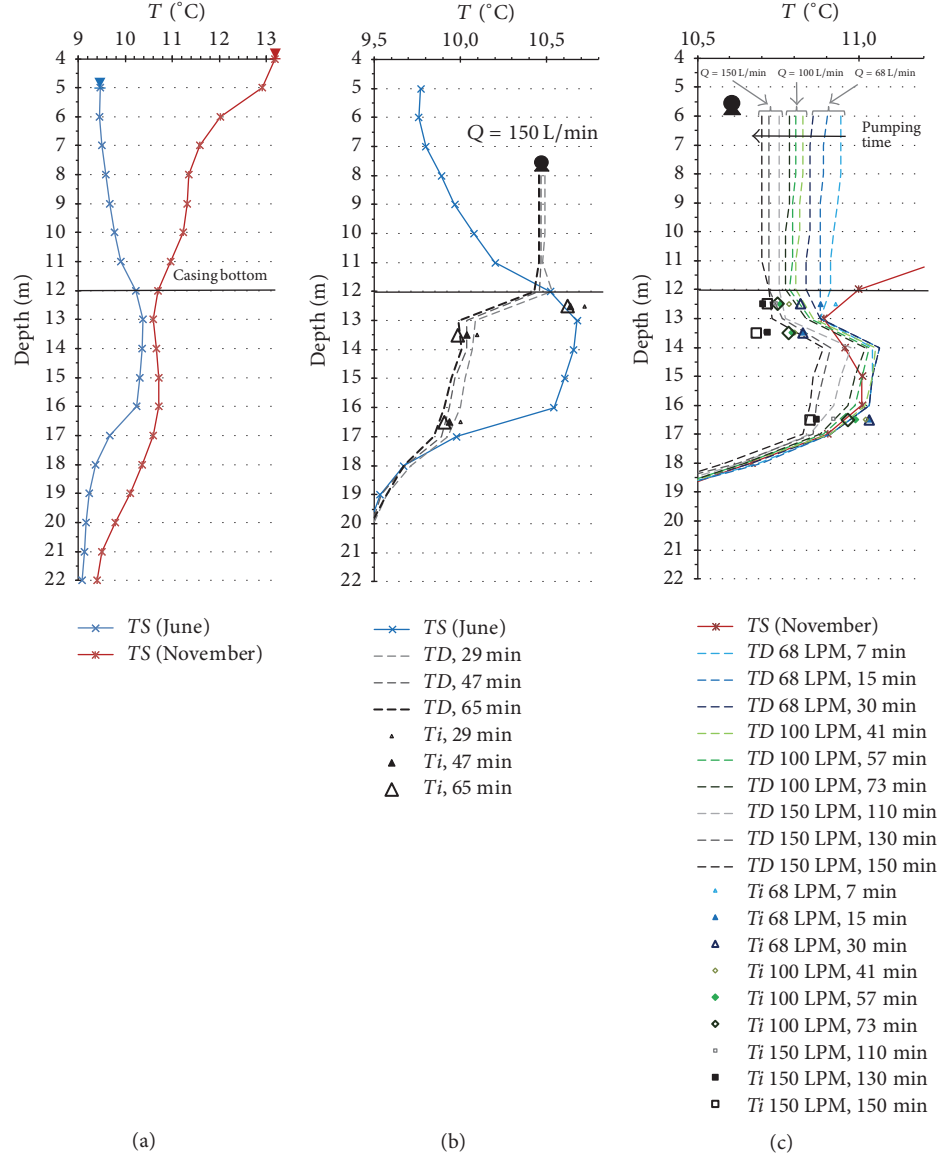


FIGURE 12: Temperature profiles in well F3: static conditions for June and November 2016 (a); static and dynamic conditions with several discharge rates and pumping durations for June (b) and November (c).  $T_i$  are the mean inflow temperatures calculated using the borehole-scale heat budget.

the increasing cooling rate of the lower interval (16 to 17 m depth) appears to coincide slightly better with the increase in pumping rate. Such a proportional thermal response may also indicate that the bottom inflow (16.5 m depth) would be the most channelized of all inflows, responding faster to advection changes, because of the lesser influence of conduction.

## 5. Discussion

### 5.1. Qualitative Interpretation of Depth-Temperature Profiles

**5.1.1. Utility of Temperature Profiles to Infer the Occurrence and Position of Water Inflows into the Wellbore.** Under static conditions, temperature profiles are rather complex close to

the surface. In the typical Quebec context shown in Figure 9(a),  $T_A$  profiles are characterized by two inflection points, and temperature in the top 15 m varies quite substantially and rapidly with the seasons. However, ambient water flows into the borehole may be detected using passive temperature logging by the interruption of the smoothed shape of these profiles. Temperature logs for the three wells studied here under static conditions allowed the presence or absence of ambient water circulation in the borehole to be inferred and if detected (for wells P-Cl and F3), allowed the intervals where active fractures are present to be rapidly determined. In general, if two or more hydraulically active fractures intercept a borehole at different depths, even a small hydraulic gradient between them would induce ambient flows into

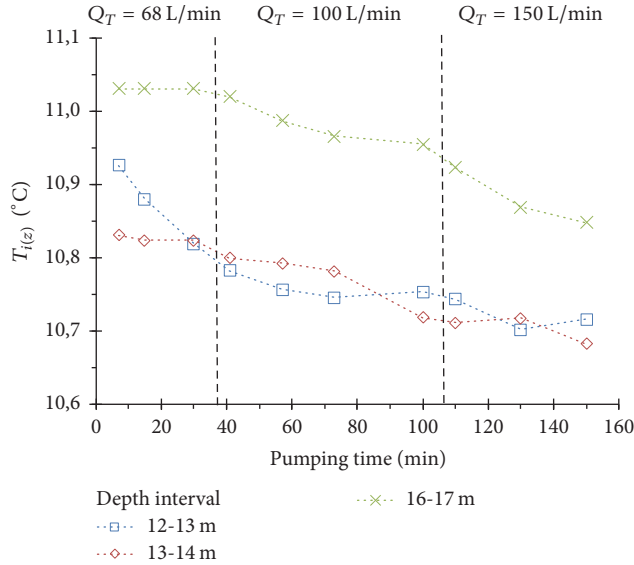


FIGURE 13: Evolution of main inflow temperatures ( $T_i(z)$ ) in well F3 during November 2016 pumping.

the borehole. As even small ambient flows are detectable by anomalous temperatures, logging under static conditions is a very efficient technique with which to identify productive fractured intervals in boreholes. Even if fractured zones are only identified qualitatively with static temperature logs, this remains very efficient, because the information on productive intervals could only otherwise be obtained by using more costly or sophisticated measurements (e.g., flow metering, packer testing, and tracers).

Under pumping conditions, temperature logging allows information obtained under static conditions to be either reinforced or clarified. Dynamic temperature profiling presents a portrait of water inflow solicited from hydraulically active fractures by pumping. In general, as shown theoretically in Figure 4 and in applied cases in Figure 9, the position of water inflows due to pumping should be easily identifiable in a first reading of high-resolution temperature profiles. However, if the temperature of a water inflow is very similar to the temperature of water flowing in the wellbore, the occurrence of the inflow cannot easily be detected by a single temperature log, even if the inflow intensity is high. Nevertheless, even a slight temperature shift would still be detectable through the use of high-resolution temperature probes ( $0.001^\circ\text{C}$ ). Such a high sensitivity may be further enhanced with the implementation of pumping procedures that favor heat conduction (i.e., low total discharge, temperature logging from the beginning of pumping). Theoretical examples of this are given in Figure 4 for inflows at 5 and 20 m depths, and applied examples for well F3 are given in Figure 11, where interpretation of  $T_D$  profiles between 14 and 16 m suggests the occurrence of very low inflows, which are not detectable by flow metering.

#### 5.1.2. Utility of Temperature Logging to Reveal the Occurrence of Low Flows in the Wellbore.

High-resolution temperature profiling appears to be extremely sensitive and to reveal very low groundwater inflows into boreholes. Even low pumping flow rates present a great advection potential, such that even a slight change in inflow temperature with pumping time would induce a detectable variation in the slope of the temperature profile, thus making low rates of inflow detectable. Such sensitive detection could even be applied to the low flows associated with the lowest productivity zone in a well during pumping (theoretical example in Figure 4 and applied examples in Figures 9, 10, and 11). However, in such cases, the detection of low inflows is enhanced within intervals of the borehole where the total flow of water remains low. If the pump is placed at the top of the borehole, the location of the lowermost active fracture could be more clearly defined, because it is located at the beginning of the divergence between static and dynamic temperature logs. However, the position of the pump can be adapted to allow low flow detection for different inflow distributions with the depth. If the pump is placed at the top of the well, small inflows located in the lower part of the borehole become much harder to detect if high inflow is present higher in the borehole. This issue could be addressed by performing two pumping tests, one with the pump placed at the bottom of the borehole and one with the pump placed at the top of the borehole. As mentioned in the previous paragraph, low flow, ultimately associated with only a slight  $T_D$  shift, should become visible even at low pumping rates by using a temperature sensor that has a high enough resolution, or by adapting pumping conditions so as to reveal them. The high sensitivity of temperature to low flows is of particular interest to reveal ambient (very low) flows when they occur in wells (i.e., Figures 9(c) and 9(d)). Ambient flows are usually not easily detectable without sophisticated instrumentation and delicate device operation, for instance, in the case of heat pulse flow meters.

**5.1.3. Interpretability of Temperature Profiles against Water Flow Distributions in the Wellbore.** Inferring flow distribution from temperature profiles is not straightforward. Processes that shape temperature profiles are complex, and temperature profiles will therefore not directly (graphically) reflect the water flow distribution in the wellbore. In the context of fractured aquifers, fractures can be oriented in a complex manner, so that the temperature of water discharging into the borehole can be quite randomly distributed with depth. None of the theoretical (Figure 4) or applied (Figures 9, 10, and 11) examples allows the water flow distribution in the wellbore to be directly inferred just from a simple reading of passive temperature logs. Temperature profiles do not mimic the water flow distribution in the wellbore, because implied heat fluxes are defined by both heat advection and conduction fluxes. Even when heat advection dominates over heat conduction ( $\phi_{\text{adv.}} \gg \phi_{\text{cond.}}$ ), heat advection fluxes rely on both flow intensity and the associated temperature (see (2)), so that the resulting temperature profiles will not directly reflect the water flow distribution in the wellbore. Therefore, without using a heat budget, the interpretation of temperature profiles does not allow inflow intensities into the wellbore to be quantified.

**5.1.4. Inferring the Temperature Range of Water Flowing into the Wellbore.** As depth-temperature profile shifts depend on the temperature of inflows, the temperature range for each inflow could at least be estimated by visualizing the cooling (e.g.,  $T_i(z) < T_D(z)$ ) or the warming (e.g.,  $T_i(z) > T_D(z)$ ) of the water column where steps are seen in the profile. An example of a theoretical  $T_i$  range is given in Figure 6, which served to initiate  $T_D(z)$  modelling in Section 4.1.2. This logical interpretation provides a valid range in applied cases (Figures 9, 10, and 11), without performing a heat budget calculation.

**5.2. Potential of and Limitations to Quantitative Interpretation Using the Heat Budget at the Borehole Scale.** Numerical models are able to assess the thermal response of hydrogeological systems extremely well [31]. However, these sophisticated models are generally very time-consuming to generate. At the borehole scale, the use of an analytical heat budget may complement numerical modelling or could even represent a very good and fast alternative for different types of quantitative investigation, as discussed below.

**5.2.1. Temperature Probes to Infer the Origin of Groundwater Drained from the Aquifer.** If a wellbore is logged for both passive high-resolution temperature and flow metering, the temperature of inflows can easily be calculated using the heat budget (Section 3.3). The determination of the inflow temperatures during pumping provides precious information regarding the origin of the groundwater drained from the fractured aquifer. Inflow temperatures are controlled by heat conduction occurring between groundwater flowing along flows paths and the aquifer neighboring the water-channeling fractures. Except for large conduits, such as in karsts, flow velocities and fracture apertures are generally rather small, such that the large specific surface allows for large conductive fluxes. As water flow converges towards a well, advection fluxes become denser. This implies that, with increasing distance from the well, conductive heat flux between the aquifer and flowing water would eventually dominate over heat advection, while, closer to the well, advection should eventually dominate over conduction. Therefore, with increasing distance from the well, the temperature of circulating water tends to be in equilibrium with  $T_A$ . With sufficient pumping duration and intensity, the temperature of water discharging into the borehole ( $T_i$ ) will approach the temperature in the region of the aquifer where water enters the fractured network ( $T_A$ ). If fractures are discrete conduits, the extent from their origin to the borehole may represent relatively long distances. However, if a fracture network is distributed, with small apertures, its thermal advection and conduction behaviour would be equivalent to a porous medium. In this latter case, it is inferred that  $T_i$  would be in equilibrium with  $T_A$  within few meters of the borehole.

**5.2.2. Potential of Temperature Probes as Integrated Quantitative Tools for Wellbore Investigation.** The simultaneous use of temperature measurements and heat budget fitting procedures may, in certain conditions, provide quantitative information about both the temperature and the intensity of

inflows. Theoretical examples presented in this work (Section 4.1.2) suggest that if highly curved depth-temperature dynamic profiles are obtained, a fitting procedure using the heat budget would be capable of quantifying both temperature and intensity of inflows. From a measurement perspective, the success of such a fitting procedure is dependent on the resolution the temperature probe ( $^{\circ}\text{C}$ ) and on the vertical interval ( $dz$ ) between temperature measurements. For fractured aquifers, the number and the distribution of temperature measurements must exceed those of the hydraulically active fractures. Only a few fractures would be adequately constrained by just a few temperature measurements, whereas if numerous fractures are involved, the number of temperature measurements required would consequently increase. From a field work perspective, such temperature modelling would more successfully characterize wellbores presenting discrete active fractures, or active fractured intervals that are at least clearly separated by nonproductive intervals. In these contexts, low discharge pumping rates should be preferred over high rates, in order to favor curved depth-temperature profiles. It is, however, assumed that, in many applied cases, the complexity of inflow distribution in wellbores would not allow a complete inflow characterization with only high-resolution temperature measurements and a heat budget. Nevertheless, even in such cases, the use of passive temperature logging and a heat budget would still be highly complementary to flow metering for characterizing very low inflows that would not otherwise be detected, or to calculate the temperature of inflows.

## 6. Conclusions

A difficult and often incompletely resolved task for hydrogeologists is to assess the origin and directions of groundwater flow paths in heterogeneous media. Far from being systematically used, some borehole logging techniques allow the distribution of aquifer hydraulic properties to be described with depth. High-resolution temperature logging has great potential to contribute to such assessments. In some cases, the temperature probe could act as a very sensitive flowmeter in fractured aquifers. Temperature logging is done very quickly, and temperature profiles efficiently identify productive sections in boreholes, so as to infer where they originate from within the aquifer. With measurements made under pumping conditions, and using some simple analytical heat budgets, temperature logs are among the rare techniques that permit inference on the origin of groundwater that is drained into the borehole. Furthermore, this information is collected without injecting and/or monitoring any anthropogenic tracer into the aquifer. Data acquired from temperature logging concurrent with other borehole logging techniques remains of great interest for improving the quality of hydrogeological applications. Such information would help to constrain flow and transport numerical models during both their construction and their calibration, to then delineate wellhead protection areas, identify subsurface flow paths of contaminated sites, and inform other water management issues where vertical aquifer stratification needs to be considered, in terms of both hydrogeochemistry and groundwater age distribution.

## Conflicts of Interest

The authors declare that there are no conflicts of interest regarding the publication of this paper.

## Acknowledgments

This research was supported by the Natural Sciences and Engineering Research Council of Canada (NSERC), in partnership with Envir'Eau-Puits Inc., which also kindly provided access to the experimental sites.

## References

- [1] G. De Marsily, F. Delay, J. Gonçalvès, P. Renard, V. Teles, and S. Violette, "Dealing with spatial heterogeneity," *Hydrogeology Journal*, vol. 13, no. 1, pp. 161–183, 2005.
- [2] D. Schulze-Makuch, D. A. Carlson, D. S. Cherkauer, and P. Malik, "Scale dependency of hydraulic conductivity in heterogeneous media," *Groundwater*, vol. 37, no. 6, pp. 904–919, 1999.
- [3] R. Raghavan, "Some observations on the scale dependence of permeability by pumping tests," *Water Resources Research*, vol. 42, no. 7, Article ID W07402, 2006.
- [4] T. Ouellet, R. Lefebvre, D. Marcotte, A. Boutin, V. Blais, and M. Parent, "Hydraulic conductivity heterogeneity of a local deltaic aquifer system from the kriged 3D distribution of hydrofacies from borehole logs, Valcartier, Canada," *Journal of Hydrology*, vol. 351, no. 1-2, pp. 71–86, 2008.
- [5] J. Perrin, B. L. Parker, and J. A. Cherry, "Assessing the flow regime in a contaminated fractured and karstic dolostone aquifer supplying municipal water," *Journal of Hydrology*, vol. 400, no. 3-4, pp. 396–410, 2011.
- [6] M. Nastev, M. M. Savard, P. Lapcevic, R. Lefebvre, and R. Martel, "Hydraulic properties and scale effects investigation in regional rock aquifers, south-western Quebec, Canada," *Hydrogeology Journal*, vol. 12, no. 3, pp. 257–269, 2004.
- [7] M.-A. Carrier, R. Lefebvre, C. Rivard et al., "Portrait des ressources en eau souterraine en Montérégie Est, Québec, Canada," Projet réalisé conjointement par l'INRS, la CGC, l'OBV Yamaska et l'IRDA dans le cadre du Programme d'acquisition de connaissances sur les eaux souterraines INRS R-1433, 2013.
- [8] M. Larocque, S. Gagné, D. Barnetche et al., "Projet de connaissance des eaux souterraines du bassin versant de la zone Nicolet et de la partie basse de la zone Saint-François - Rapport scientifique," Rapport déposé au ministère du Développement durable, de l'Environnement et de la Lutte contre les changements climatiques, 2015.
- [9] M. Larocque, S. Gagné, L. Tremblay, and G. Meyzonnat, "Projet de connaissance des eaux souterraines du bassin versant de la rivière Bécancour et de la MRC de Bécancour - Rapport scientifique," Rapport déposé au ministère du Développement durable, de l'Environnement, de la Faune et des Parcs, 2013.
- [10] USGS, "Determining Age and Vertical Contribution of Ground Water Pumped from Wells in a Small Coastal River Basin," Tech. Rep. 2005-1032, 2005.
- [11] J. L. Libby and G. A. Robbins, "An unsteady state tracer method for characterizing fractures in bedrock wells," *Groundwater*, vol. 52, no. 1, pp. 136–144, 2014.
- [12] S. Pistre, S. Marliac, H. Jourde, and P. Bidaux, "New combined log and tracer test interpretation method for identifying transfers in fissured aquifers," *Groundwater*, vol. 40, no. 3, pp. 232–241, 2002.
- [13] M. Barahona-Palomo, M. Riva, X. Sanchez-Vila, E. Vazquez-Sune, and A. Guadagnini, "Quantitative comparison of impeller-flowmeter and particle-size-distribution techniques for the characterization of hydraulic conductivity variability," *Hydrogeology Journal*, vol. 19, no. 3, pp. 603–612, 2011.
- [14] K. Miyakawa, K. Tanaka, Y. Hirata, and M. Kanauchi, "Detection of hydraulic pathways in fractured rock masses and estimation of conductivity by a newly developed TV equipped flowmeter," *Engineering Geology*, vol. 56, no. 1-2, pp. 19–27, 2000.
- [15] F. Paillet, "Borehole flowmeter applications in irregular and large-diameter boreholes," *Journal of Applied Geophysics*, vol. 55, no. 1-2, pp. 39–59, 2004.
- [16] A. E. Hess, "Identifying hydraulically conductive fractures with a slow-velocity borehole flowmeter," *Canadian Geotechnical Journal*, vol. 23, no. 1, pp. 69–78, 1985.
- [17] M. P. Anderson, "Heat as a ground water tracer," *Groundwater*, vol. 43, no. 6, pp. 951–968, 2005.
- [18] G. Ferguson and A. D. Woodbury, "The effects of climatic variability on estimates of recharge from temperature profiles," *Groundwater*, vol. 43, no. 6, pp. 837–842, 2005.
- [19] M. Taniguchi, D. R. Williamson, and A. J. Peck, "Disturbances of temperature-depth profiles due to surface climate change and subsurface water flow: 2. An effect of step increase in surface temperature caused by forest clearing in southwest Western Australia," *Water Resources Research*, vol. 35, no. 5, pp. 1519–1529, 1999.
- [20] W. S. Keys and R. F. Brown, "The use of temperature logs to trace the movement of injected water," *Groundwater*, vol. 16, no. 1, pp. 32–48, 1978.
- [21] R. A. Renken, K. J. Cunningham, A. M. Shapiro et al., "Pathogen and chemical transport in the karst limestone of the Biscayne aquifer: 1. Revised conceptualization of groundwater flow," *Water Resources Research*, vol. 44, no. 8, Article ID W08429, 2008.
- [22] M. O. Saar, "Review: geothermal heat as a tracer of large-scale groundwater flow and as a means to determine permeability fields," *Hydrogeology Journal*, vol. 19, no. 1, pp. 31–52, 2011.
- [23] G. Ferguson, "Heterogeneity and thermal modeling of ground water," *Groundwater*, vol. 45, no. 4, pp. 485–490, 2007.
- [24] D. J. Irvine, C. T. Simmons, A. D. Werner, and T. Graf, "Heat and Solute Tracers: How Do They Compare in Heterogeneous Aquifers?" *Groundwater*, vol. 53, no. 1, pp. 10–20, 2015.
- [25] M. V. Klepikova, T. Le Borgne, O. Bour, M. Dentz, R. Hochreutener, and N. Lavenant, "Heat as a tracer for understanding transport processes in fractured media: theory and field assessment from multiscale thermal push-pull tracer tests," *Water Resources Research*, vol. 52, no. 7, pp. 5442–5457, 2016.
- [26] M. Chatelier, S. Ruelle, O. Bour, G. Porel, and F. Delay, "Combined fluid temperature and flow logging for the characterization of hydraulic structure in a fractured karst aquifer," *Journal of Hydrology*, vol. 400, no. 3-4, pp. 377–386, 2011.
- [27] T. Le Borgne, F. Paillet, O. Bour, and J.-P. Caudal, "Cross-borehole flowmeter tests for transient heads in heterogeneous aquifers," *Groundwater*, vol. 44, no. 3, pp. 444–452, 2006.
- [28] P. E. Pehme, B. L. Parker, J. A. Cherry, J. W. Molson, and J. P. Greenhouse, "Enhanced detection of hydraulically active fractures by temperature profiling in lined heated bedrock boreholes," *Journal of Hydrology*, vol. 484, pp. 1–15, 2013.
- [29] V. F. Bense, T. Read, O. Bour et al., "Distributed Temperature Sensing as a downhole tool in hydrogeology," *Water Resources Research*, vol. 52, no. 12, pp. 9259–9273, 2016.

- [30] M. V. Klepikova, T. Le Borgne, O. Bour, and P. Davy, "A methodology for using borehole temperature-depth profiles under ambient, single and cross-borehole pumping conditions to estimate fracture hydraulic properties," *Journal of Hydrology*, vol. 407, no. 1-4, pp. 145–152, 2011.
- [31] M. V. Klepikova, T. Le Borgne, O. Bour, K. Gallagher, R. Hochreutener, and N. Lavenant, "Passive temperature tomography experiments to characterize transmissivity and connectivity of preferential flow paths in fractured media," *Journal of Hydrology*, vol. 512, pp. 549–562, 2014.
- [32] M. J. Drury and A. M. Jessop, "The effect of a fluid-filled fracture on the temperature profile in a borehole," *Geothermics*, vol. 11, no. 3, pp. 145–152, 1982.
- [33] S. Ge, "Estimation of groundwater velocity in localized fracture zones from well temperature profiles," *Journal of Volcanology and Geothermal Research*, vol. 84, no. 1-2, pp. 93–101, 1998.
- [34] Y. Globensky, "Géologie des Basses-Terres du Saint-Laurent," Tech. Rep. MM85-02, Direction Générale de l'exploitation Géologique et Minérale, Québec, Canada, 1987.
- [35] M. Larocque and G. Meyzonnat, "Projet de connaissance des eaux souterraines de la zone de Vaudreuil-Soulanges - Rapport scientifique," Rapport déposé au ministère du Développement durable, de l'Environnement et de la Lutte contre les changements climatiques, 2015.
- [36] Terraplus, QL 40 SFM, bidirectionnal spinner flowmeter, User guide, Richmond Hill, ON, Canada, 2014.
- [37] Terraplus, Matrix Borehole Logging System, User guide, Richmond Hill, ON, Canada, p. 2, 2014.
- [38] Terraplus, QL-40 OBI, optical borehole imager, User guide, Richmond Hill, ON, Canada, p. 2, 2014.
- [39] F. Barbecot, C. Marlin, E. Gibert, and L. Dever, "Hydrochemical and isotopic characterisation of the Bathonian and Bajocian coastal aquifer of the Caen area (northern France)," *Applied Geochemistry*, vol. 15, no. 6, pp. 791–805, 2000.
- [40] J.-A. Corcho Alvarado, F. Barbecot, and R. Purtschert, "Ambient vertical flow in long-screen wells: a case study in the Fontainebleau Sands Aquifer (France)," *Hydrogeology Journal*, vol. 17, no. 2, pp. 425–431, 2008.
- [41] A. Faghri, Y. Zhang, and J. R. Howell, *Advanced Heat and Mass Transfer*, Global Digital Press, Missouri, MO, USA, 2010.
- [42] B. L. Kurylyk and D. J. Irvine, "Analytical solution and computer program (FAST) to estimate fluid fluxes from subsurface temperature profiles," *Water Resources Research*, vol. 52, no. 2, pp. 725–733, 2016.
- [43] Terraplus, HFP-2293, heat-pulse Flowmeter probe, User guide, Richmond Hill, ON, Canada, p. 2, 2014.
- [44] C. Gosselin and J.-C. Mareschal, "Recent warming in north-western Ontario inferred from borehole temperature profiles," *Journal of Geophysical Research: Solid Earth*, vol. 108, no. 9, 2003.

## Research Article

# Material Exchange and Migration between Pore Fluids and Sandstones during Diagenetic Processes in Rift Basins: A Case Study Based on Analysis of Diagenetic Products in Dongying Sag, Bohai Bay Basin, East China

W. Meng,<sup>1,2</sup> J. H. Zeng<sup>ID, 1,2</sup> Z. Cao,<sup>1,2</sup> G. Q. Song,<sup>3</sup> Y. S. Wang,<sup>3</sup> J. L. Teng,<sup>1,2</sup> and Z. Guo<sup>1,2</sup>

<sup>1</sup>State Key Laboratory of Petroleum Resources and Prospecting, Beijing, China

<sup>2</sup>College of Geosciences, China University of Petroleum, Beijing, China

<sup>3</sup>Shengli Oilfield Branch Company, Sinopec, Dongying, China

Correspondence should be addressed to J. H. Zeng; zengjh@cup.edu.cn

Received 30 June 2017; Revised 15 December 2017; Accepted 28 December 2017; Published 15 February 2018

Academic Editor: Jet-Chau Wen

Copyright © 2018 W. Meng et al. This is an open access article distributed under the Creative Commons Attribution License, which permits unrestricted use, distribution, and reproduction in any medium, provided the original work is properly cited.

The exchange and migration of basin materials that are carried by pore fluids are the essence of diagenesis, which can alter physical properties of clastic rocks as well as control formation and distribution of favorable reservoirs of petrolierous basins. Diagenetic products and pore fluids, resulting from migration and exchange of basin materials, can be used to deduce those processes. In this study, 300 core samples from 46 wells were collected for preparation of casting thin sections, SEM, BSE, EDS, inclusion analysis, and isotope analysis in Dongying Sag, Bohai Bay Basin, East China. Combined with geochemical characteristics of pore fluids and geological background of the study area, the source and exchange mechanisms of materials in the pore fluids of rift basins were discussed. It was revealed that the material exchange of pore fluids could be divided into five stages. The first stage was the evaporation concentration stage during which mainly  $\text{Ca}^{2+}$ ,  $\text{Mg}^{2+}$ , and  $\text{CO}_3^{2-}$  precipitated as high-Mg calcites. Then came the shale compaction stage, when mainly  $\text{Ca}^{2+}$  and  $\text{CO}_3^{2-}$  from shale compaction water precipitated as calcites. The third stage was the carboxylic acid dissolution stage featured by predominant dissolution of plagioclases, during which  $\text{Ca}^{2+}$  and  $\text{Na}^+$  entered pore fluids, and Si and Al also entered pore fluids and then migrated as clathrates, ultimately precipitating as kaolinites. The fourth stage was the organic  $\text{CO}_2$  stage, mainly characterized by the kaolinization of K-feldspar as well as dissolution of metamorphic lithic fragments and carbon cements. During this stage,  $\text{K}^+$ ,  $\text{Fe}^{2+}$ ,  $\text{Mg}^{2+}$ ,  $\text{Ca}^{2+}$ ,  $\text{HCO}_3^-$ , and  $\text{CO}_3^{2-}$  entered pore fluids. The fifth stage was the alkaline fluid stage, during which the cementation of ferro-carbonates and ankerites as well as illitization or chloritization of kaolinites prevailed, leading to the precipitation of  $\text{K}^+$ ,  $\text{Fe}^{2+}$ ,  $\text{Mg}^{2+}$ ,  $\text{Ca}^{2+}$ , and  $\text{CO}_3^{2-}$  from pore fluids.

## 1. Introduction

Pore fluids mainly refer to all fluids that occupy and pass through the pore space of sedimentary basins [1, 2]. During the burial process, basin materials could be loaded and redistributed by pore fluids. Those processes could lead to regularly distributed diagenetic products in basins [3]. Formation and evolution of diagenetic products could result in preservation or destruction of primary pores as well as formation and transformation of secondary pores, which could significantly influence the formation and occurrence of effective reservoirs in the deep part of petrolierous basins

[4–16]. Previous studies mainly highlighted evolution of physical properties of clastic rocks and primarily investigated diagenetic facies and sequences based on sedimentological and petrological analyses [11, 17–26]. However, insufficient attention was paid to the nature of diagenesis, namely, the exchange and migration of basin materials loaded by pore fluids. Meanwhile, many controversies arose concerning the formation mechanism of secondary pores, which further obscured prediction of distribution of secondary pores and effective reservoirs [5, 14, 23, 27–34]. Therefore, it should be critical to figure out the mechanism of basin material exchange and migration during the diagenetic process so as to

analyze the formation and distribution of diagenetic products and favorable sandstone reservoirs.

During diagenetic process, matrix of clastic rocks could be transformed or dissolved, and materials might partly or totally enter into pore fluids as ions or complexes. Solutes (ions or complexes) carried by pore fluids could be deposited as cements under appropriate geological conditions. In these processes, compositions of clastic rocks and chemical properties of pore fluids could be changed. These changes could be used to infer material exchange and migration mechanisms during diagenesis.

## 2. Geological Setting

Dongying Sag is a subtectonic unit in the southeastern of Jiyang Depression, Bohai Bay Basin (Figure 1) [35]. It can be further subdivided into six secondary tectonic zones, known as Northern Steep Slope Zone, Lijin Subsag, Minfeng Subsag, Central Anticline Zone, Niuzhuang Subsag, and Southern Gentle Slope Zone (Figure 1) [35].

There are mainly three sets of successions in the Dongying Sag, namely, Paleogene, Neogene, and Quaternary. The Paleogene mainly comprises Kongdian (Ek), Shahejie (Es), and Dongying (Ed) Formations; the Neogene Guantao (Ng) and Minghuazhen (Nm) Formations; and the Quaternary Pingyuan (Qp) Formation (Zhai and He 1993) [36]. There is a main regional unconformity serving as the boundary between Ed and Ng Formations (Figure 2) (Zhai and He 1993) [35, 36]. Shahejie Formation can be subdivided into four members, namely, Es4, Es3, Es2, and Es1, from base to top [36]. This study focused on the Es4 and Es3 members.

Es4 consists of gray and dark-gray mudstones, gypsum and halite, interbedded nearshore subaqueous fan sandstones, and sublacustrine fan sandstones deposited in semi-deep and deep lacustrine environments, which are mainly located in the Northern Steep Slope Zone. The lower sub-member of Es3 (Es<sup>3</sup>) was deposited in semideep and deep lacustrine environments, dominated by lacustrine oil shales, dark-gray mudstones, calcareous mudstones, and subaqueous (sublacustrine) fan sandstones in terms of lithology. The middle submember of Es3 (Es<sup>2</sup>) consists of gray to dark-gray mudstones, calcareous mudstones, subaqueous (sublacustrine) fan sandstones, and delta sandstones deposited in semideep and deep lacustrine environments. The upper submember of Es3 (Es<sup>1</sup>) is dominated by deltaic sandstones.

## 3. Samples and Methods

A total of 1472 thin sections were collected, which were prepared from the Es core samples in the Dongying Sag by Geological Scientific Research Institute of China Sinopec Shengli Oilfield Company, where 1423 data about Es formation water chemical composition were also collected.

A total of 300 blue epoxy resin-impregnated thin sections were prepared for diagenesis analysis using the Es drill cores of 46 wells in Dongying Sag. This study focused on the type, occurrence, content, and contact metasomatic relationship of diagenetic products. With at least 300 points, estimations of component contents by point accounting can be more

reliable with a standard deviation less than 5.5%. 40 out of 300 samples were implemented with EBSD, SEM, and EDX analysis in order to investigate chemical characteristics of authigenic kaolinites and carbon cements. 34 out of 300 samples showed only one type of carbon cements, and they were selected for analysis of  $\delta^{13}\text{C}_{\text{V-PDB}}/\text{\textperthousand}$  and  $\delta^{18}\text{O}_{\text{V-PDB}}/\text{\textperthousand}$ . The collection of carbon cements from these samples was taken at the Institute of Mineral Resources and Regional Geology of Hebei Province, while the measurement of  $\delta^{13}\text{C}_{\text{V-PDB}}/\text{\textperthousand}$  and  $\delta^{18}\text{O}_{\text{V-PDB}}/\text{\textperthousand}$  was completed using Gas Isotope Ratio Mass Spectrometry (MAT 253) at Chinese Academy of Geological Sciences. Fluid inclusion analysis was carried out on 14 samples, which were prepared as doubly polished sections with approximate thicknesses of 100 mm for fluid inclusion petrographic analysis and thermometric measurement. Microthermometry of aqueous inclusions was conducted using calibrated Linkam-350, during which the homogenization temperature (Th) was obtained by cycling and Th measurements were completed with a heating rate of 10°C/min when the temperature was lower than 70°C, and 5°C/min when the temperature exceeded 70°C. The precision of measured Th was within  $\pm 1^\circ\text{C}$ . A total of 592 data concerning bulk rock and clay mineral analyses were collected from Geological Scientific Research Institute of China Sinopec Shengli Oilfield Company, which were mainly to identify the distribution of contents of different clay minerals.

## 4. Results

**4.1. Detrital Composition of Es Sandstones.** Es sandstones in Dongying Sag are medium to fine grained arkoses and lithic arkoses (av.  $\text{Q}_{47.4}\text{F}_{33.8}\text{L}_{18.7}$ ; Figure 3). They are poorly to moderately sorted and subangular, with the matrix content of 1.7–13.6%. It was revealed by thin section observation that the quartz grains in those sandstones (av. 39.8%) were mainly monocrystalline quartz (av. 39.0%) and, less commonly, polycrystalline quartz (av. 0.8%). Es3 sandstones had the highest content of quartz grains (av. 43.2%), while Es1 sandstones had the lowest (av. 39.5%). The feldspar particles in those sandstones (av. 15.1%) were mainly K-feldspar (av. 9.0%) and, less commonly, plagioclase (av. 6.1%). Es1 sandstones had the highest content of feldspar particles (av. 20.2%), while Es3 sandstones had the lowest (av. 12.2%). The content range of lithic fragments in those sandstones was relatively large, 1.7–53.2%. Lithic fragments in Es sandstones were all dominated by metamorphic lithic fragments. The difference is that the amount of igneous and sedimentary lithic fragments was relatively higher in the Es1 and Es2 sandstones, but relatively lower in Es3 and Es4 sandstones (Table 1).

During the burial process, the interaction between pore fluids and grains in sandstones could result in the changes of type and content of clastic particles. In the sandstones with depth less than 3200 m, the content of quartz particles increased significantly, and the content of feldspar grains decreased dramatically, with the increase of depth. However, such trend was opposite in sandstones with depth more than 3200 m. Moreover, it was found that the content of lithic fragments kept relatively unchanged until the depth reached 2800 m, after which it sharply decreased with depth

TABLE I: Modal composition (maximum, minimum, and average) of 1472 samples from the Es sandstones of Dongying Sag.

	Es1 Minimum (%)	Es1 Maximum (%)	Mean (%)	Minimum (%)	Maximum (%)	Mean (%)	Minimum (%)	Maximum (%)	Mean (%)	Es3 Minimum (%)	Maximum (%)	Mean (%)	Es4 Maximum (%)	Mean (%)	Es Mean (%)
<i>Detrital composition</i>															
Monocrystalline quartz	26.2	59.0	38.5	16.0	61.8	39.4	24.0	69.6	42.5	21.8	43.4	39.5	39.0		
Poly-crystalline quartz	0.8	1.2	1.0	0.2	1.9	0.9	0.2	3.6	0.7	0.4	0.9	0.6	0.8		
K-feldspar	1.7	26.5	10.4	1.0	25.9	10.5	1.0	16.5	7.4	5.8	16.4	7.7	9.0		
Plagioclase	1.5	19.2	9.3	1.2	18.5	4.3	1.0	19.8	4.8	4.3	17.4	5.0	6.1		
Volcanic lithic fragments	0.4	9.3	2.9	0.2	29.6	3.3	0.2	12.9	1.2	0.4	7.2	3.1	2.6		
Metamorphic lithic fragments	1.4	15.0	3.3	0.7	38.5	4.1	0.7	12.5	8.1	2.6	27.7	4.4	5.5		
Sedimentary lithic fragments	0.2	3.5	1.7	0.3	23.3	2.2	0.2	23.4	2.2	0.4	3.8	1.6	1.9		
Mica	0.1	0.3	0.5	0.4	0.9	0.5	0.3	2.4	0.7	0.0	0.0	0.0	0.4		
Charcoal debris	0.2	0.9	0.5	0.3	4.6	1.1	0.3	6.5	1.5	0.4	1.5	0.5	0.9		
Clay matrix	0.9	11.9	3.6	0.2	12.8	3.4	0.4	9.6	2.2	0.7	12.6	5.0	3.3		
Micritic matrix	0.9	6.9	2.1	0.4	4.5	1.2	0.2	3.3	1.4	0.0	0.0	0.0	1.4		
<i>Diagenetic minerals</i>															
Calcites	2.8	33.0	5.2	0.2	28.6	3.1	0.2	28.3	1.7	0.5	3.1	1.2	2.8		
Dolomites	0.0	0.7	0.4	1.5	18.5	2.2	0.3	22.8	1.6	0.4	7.5	3.4	1.9		
Ferrocalcites	0.0	1.8	0.9	0.0	27.5	3.1	0.3	31.3	6.2	0.7	8.4	2.6	3.2		
Ankerites	0.0	3.3	1.6	0.0	22.6	3.7	0.4	25.9	4.0	0.5	9.8	6.2	3.9		
Authigenic quartz	0.0	0.0	0.0	0.4	1.8	0.8	0.2	3.4	1.1	0.4	3.5	1.0	0.7		
Pyrites	0.0	2.6	1.8	0.0	5.0	1.3	0.4	4.5	1.3	0.2	6.7	2.5	1.7		
Authigenic kaolinites	0.0	0.0	0.0	0.0	3.9	2.7	0.4	9.4	3.2	0.0	1.6	0.3	1.6		
Fe-oxide	0.0	0.0	0.0	0.0	1.5	0.2	0.4	5.8	0.7	0.7	4.2	2.6	0.9		
Authigenic chlorites	0.0	1.3	0.7	0.0	2.3	0.4	0.0	4.6	1.3	0.6	5.7	3.2	1.4		
Authigenic illites	0.0	0.0	0.0	0.0	0.0	0.0	0.0	3.2	1.1	0.1	4.3	2.5	0.9		
Siderite	0.0	0.0	0.0	0.4	6.4	1.1	0.0	2.1	0.2	0.0	0.0	0.0	0.3		
<i>Porosity</i>															
Primary pore	15.0	20.5	13.9	5.4	17.3	7.2	0.0	7.3	0.5	0.0	6.2	0.7	5.6		
Feldspars dissolution pores	0.0	2.6	1.2	0.0	7.5	3.6	0.0	5.3	1.8	0.0	4.2	2.0	2.2		
Carbonate dissolution pores	0.0	0.0	0.0	0.0	2.1	0.4	0.0	10.5	2.2	0.0	8.9	4.3	1.7		
Fractures	0.0	0.9	0.5	0.0	1.2	0.7	0.0	1.3	0.5	0.0	1.7	0.2	0.5		

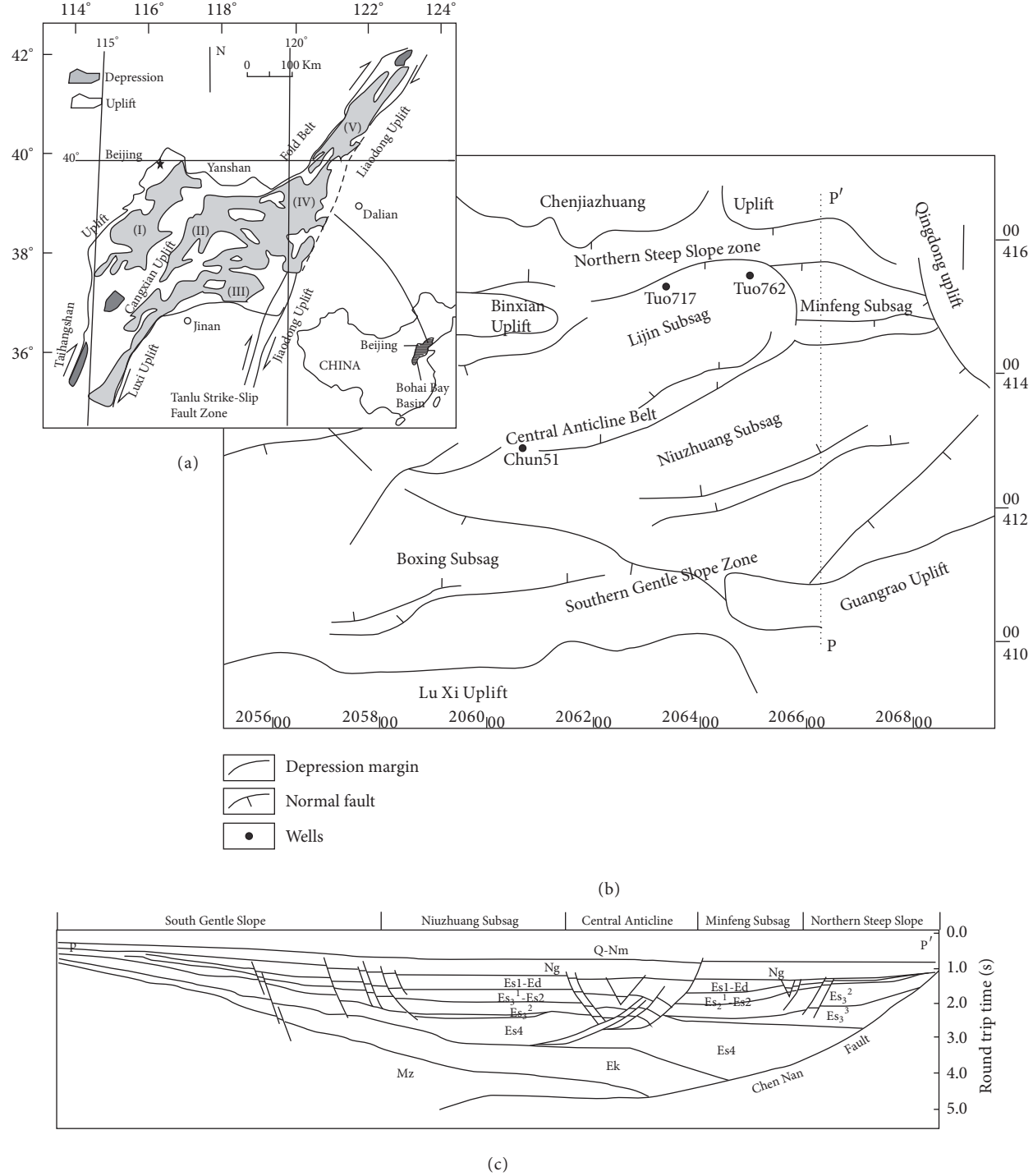


FIGURE 1: Location map and cross section of the study area. (a) Location map of the study area showing the subtectonic units of the Bohai Bay Basin, namely, Jizhong Depression (I), Huanghua Depression (II), Jiayang Depression (III), Bozhong Depression (IV), and Liaohe Depression (V). (b) Structural map of the Dongying Sag. (c) N-S cross section (P'-P) of the Dongying Sag showing the various tectonic-structural zones and key stratigraphic intervals [35].

(Figure 4). In addition, in the depth less than 2800 m, the proportion of different lithic fragments in total lithic fragments was relatively constant, which, however, changed when the depth reached 2800 m. To be specific, the proportion of igneous lithic fragments increased with depth, while

that of metamorphic lithic fragments decreased (Figure 4). Similarly, the proportion of anorthose grains in total feldspar grains declined with depth, while that of K-feldspar grains increased, when the depth was less than 2800 m (Figure 4). However, in sandstones with depth from 2800 m to 3200 m,

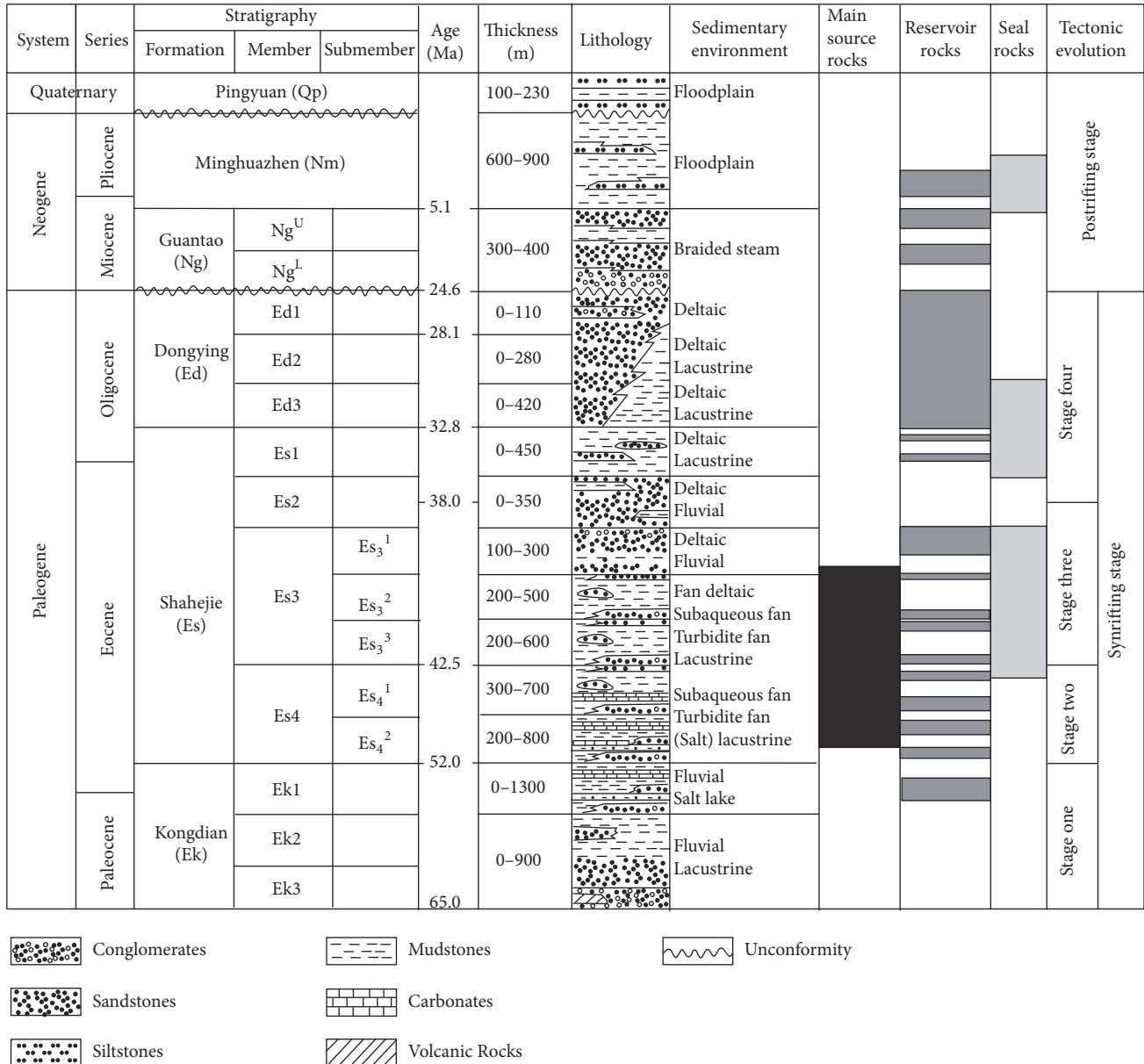


FIGURE 2: Generalized Cenozoic-Quaternary stratigraphy of the Dongying Sag (modified from [35]).

the trend was opposite, which meant increasing anorthose grains and decreasing K-feldspar grains with depth. As for the sandstones buried deeper than 3200 m, contents of anorthose and K-feldspar rarely changed (Figure 4).

**4.2. Chemical Characteristics of Formation Water in Dongying Sag.** The major elements of formation water were found to change regularly with depth in Dongying Sag. The contents of  $\text{Na}^+$  and  $\text{K}^+$  increased in the depth ranges of 2200 m–2500 m and 2800 m–3400 m, respectively, reaching the maximum at the depth of 3400 m and then slightly declining. The content of  $\text{Cl}^-$  increased with depth from 2200 m, achieving the maximum and remaining stable after the depth exceeded 2500 m. The content of  $\text{Ca}^{2+}$  greatly increased with depth

in the range of 2200 m–3200 m, reaching the maximum at 3200 m and then dropping greatly with depth. The content of  $\text{HCO}_3^-$  increased in the range of 2500 m–3000 m, achieving the maximum at 3000 m and then decreasing greatly with depth. The content of  $\text{CO}_3^{2-}$  increased with depth after the depth exceeded 2800 m (Figure 5).

**4.3. Morphological, Geochemical, and Distribution Features of Diagenetic Products in Es Sandstones.** Pore fluids in Es sandstones experienced multiphase material exchange and migration, leading to the formation and evolution of diagenetic products. These diagenetic products mainly included carbonate cements; quartz cements; aluminosilicate minerals such as kaolinite, illite, and chlorite; opaque minerals such

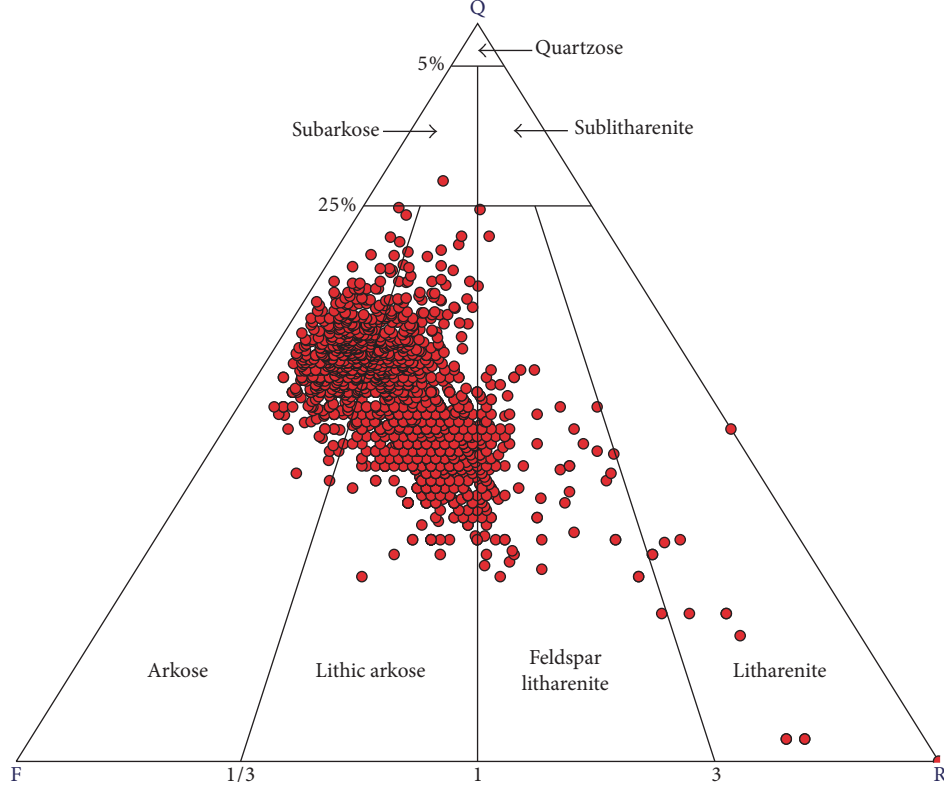


FIGURE 3: Detrital composition of sandstone samples of 1472 samples from the Es sandstones in Dongying Sag.

as pyrite; dissolution pores of unstable particles (feldspar and lithic fragments) and carbonate cements. The contents of different diagenetic products varied greatly in the sandstones of different members of Es. The contents of carbonate cements were relatively higher in Es3 and Es4 sandstones (av. 13.5% and av. 13.4%, resp.), while that in Es1 sandstones was relatively lower (av. 8.1%). The carbonate cements in Es1 sandstones were mainly calcite; those in Es2 sandstones calcite, dolomite, ferrocalcite, and ankerite; those in Es3 sandstones mainly ferrocalcite and ankerite; and those in Es4 sandstones mainly dolomite and ankerite. Quartz cements were mainly observed in sandstones of Es2, Es3, and Es4, with rare observations of them in Es1 sandstones. Authigenic kaolinites were mainly found in Es2 and Es3 sandstones, while few of them were observed in sandstones of Es1 and Es4. Feldspar dissolution pores were predominantly in sandstones of Es2, Es3, and Es4, and they were most developed in Es3 sandstones. Es3 and Es4 sandstones were main hosts to carbonate cement dissolution pores, and Es4 sandstones had the largest amount of carbonate cement dissolution pores (Table 1).

**4.3.1. Distribution and Geochemical Features of Carbonate Cements with Different Morphologies.** There were mainly four stages of carbonate cements with different morphologies in the study area. Carbonate cements of the first stage (Cc1) were generally isopachous on the surface of particles (Figures 6(a) and 6(b)), occurring in sandstones with depth ranging from 1700 m to 3600 m (Figure 7). They were only observed

in a few sandstone samples. Carbonate cements of the second stage (Cc2) were mainly medium-coarse crystalline calcite, filling the primary pores which were not obviously affected by compaction. This type of carbonate cements was generally on the outer side of Cc1 (Figures 6(a), 6(b), and 6(c)), and they usually occurred in sandstones with depth ranging from 1700 m to 3600 m, concentrated in the depth range of 1700–2800 m. From 2800 m to 3600 m, Cc2 was obviously dissolved (Figure 7). Carbonate cements of the third stage (Cc3) filled in residual primary pores after compaction as well as feldspar dissolution pores (Figures 6(e) and 6(f)). They generally occurred in the sandstones with depth ranging from 2000 m to 3600 m, concentrated in the range of 2100 m to 2700 m. The content of Cc3 decreased greatly with depth once the depth reached 2700 m (Figure 7). Carbonate cements of the fourth stage (Cc4) were euhedral fine crystalline ferrocalcites and ankerites, lying on the outer part of kaolinization feldspar or secondary pores dissolved by Cc3 (Figures 6(g) and 6(h)). They were mainly found in the sandstones with the depth over 3100 m, and their content increased greatly with depth (Figure 7).

Cc1 was mainly micritic high-Mg calcite ( $\text{CaCO}_3$  71–79%;  $\text{MgCO}_3$  15–23%;  $\text{FeCO}_3$  2–5%;  $\text{MnCO}_3$  0–2%) (Figure 8). It was difficult to obtain isotope data from Cc1, due to its low content. Cc2 was mainly calcite ( $\text{CaCO}_3$  91–100%;  $\text{MgCO}_3$  0–5%;  $\text{FeCO}_3$  0–5%;  $\text{MnCO}_3$  0–2%) (Figure 8), with  $\delta^{13}\text{C}_{\text{V-PDB}}/\text{\textperthousand}$  values from +1.60‰ to +3.50‰ (av. 2.76‰) and  $\delta^{18}\text{O}_{\text{V-PDB}}/\text{\textperthousand}$  values from -12.40‰ to -9.10‰ (av. -10.33‰) (Figure 9). The chemical composition of Cc3

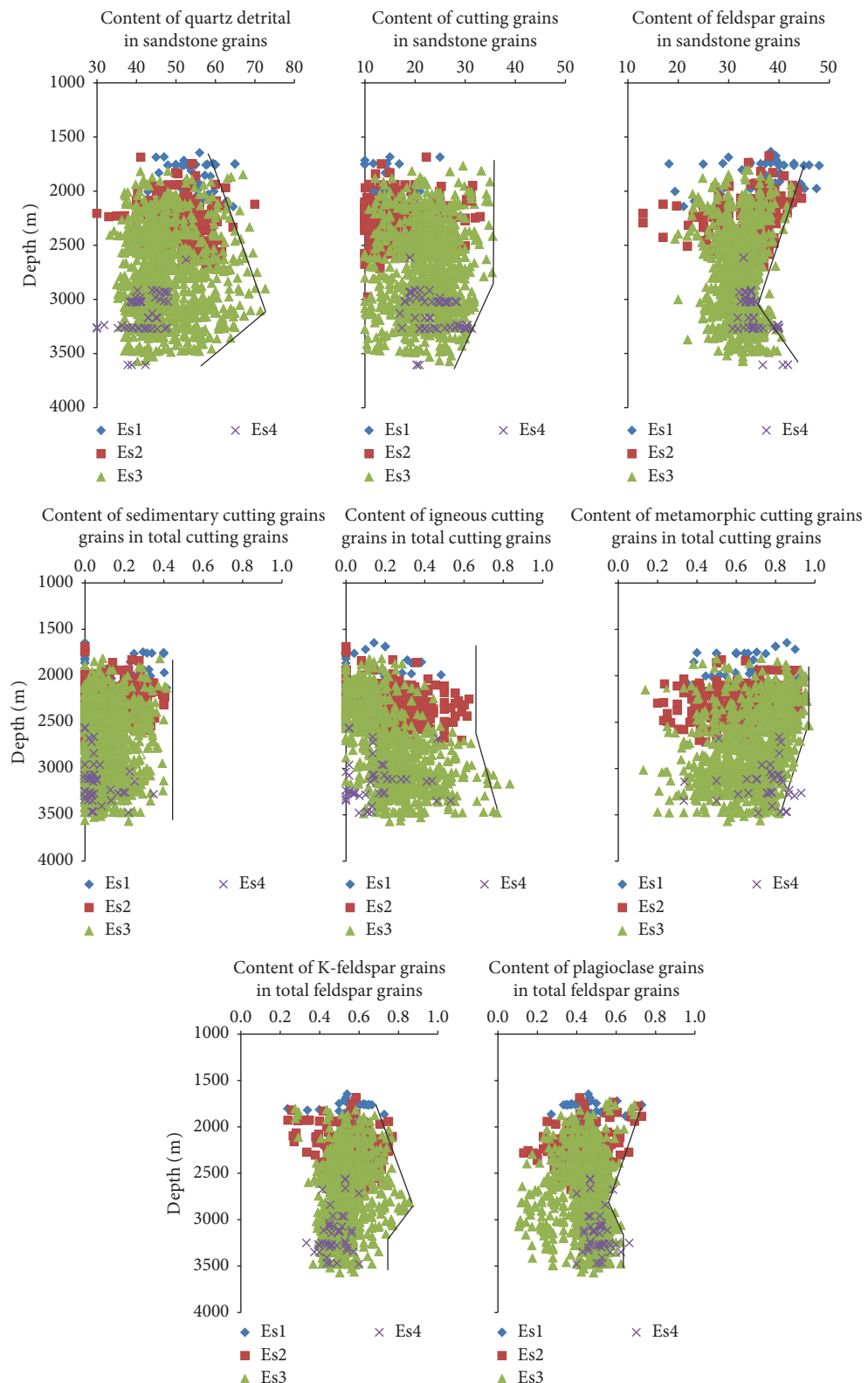


FIGURE 4: The content changes of different grains in sandstones of Es in Dongying Sag.

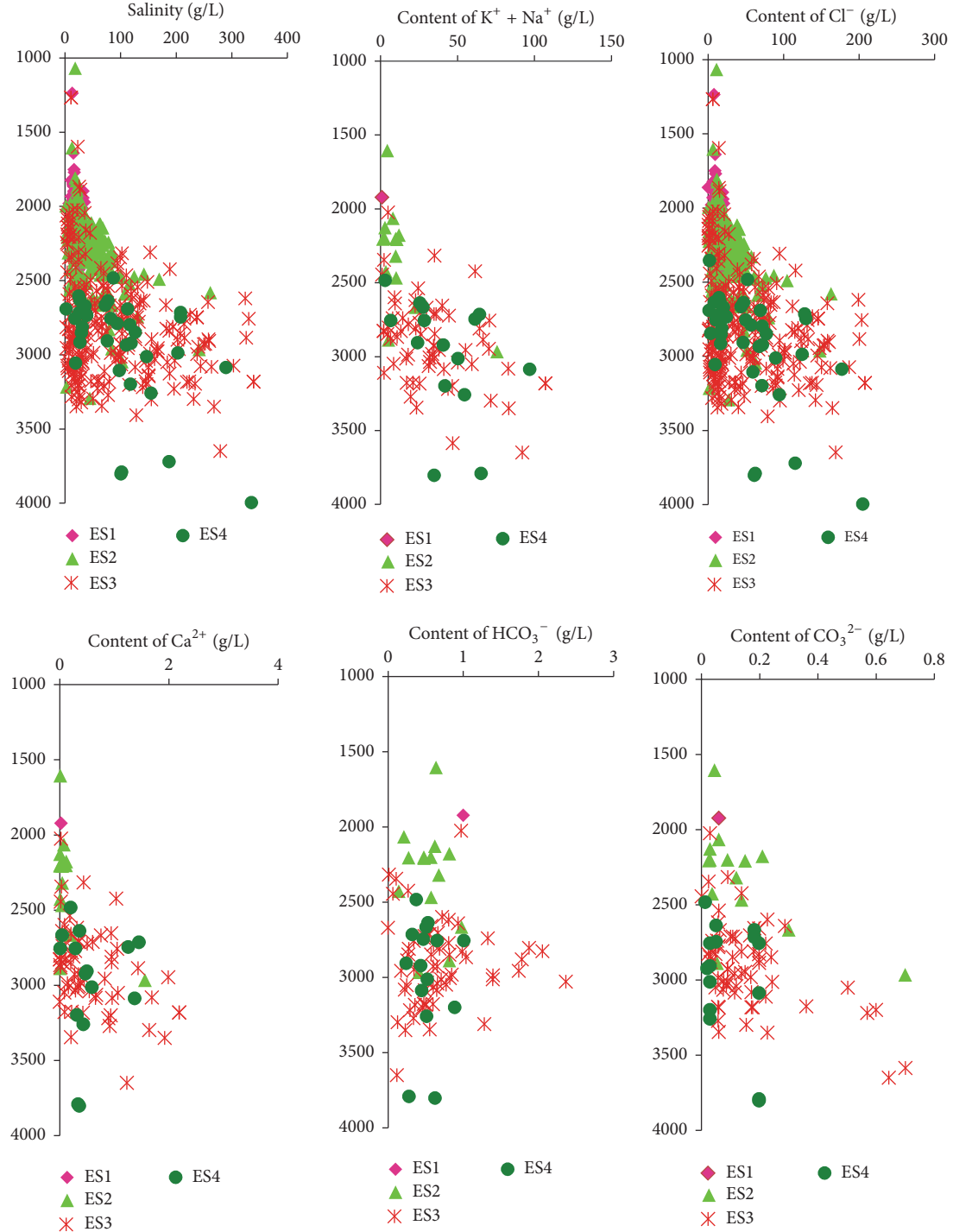


FIGURE 5: Changes of chemical characteristics of formation water with depth in Dongying Sag.

was complicated ( $\text{CaCO}_3$  43–97%;  $\text{MgCO}_3$  0–54%;  $\text{FeCO}_3$  1–11%;  $\text{MnCO}_3$  0–4%) (Figure 8), and it had a relatively wide range of  $\delta^{13}\text{C}_{\text{V-PDB}}/\text{\textperthousand}$  values from  $-6.60\text{\textperthousand}$  to  $+4.30\text{\textperthousand}$  (av.  $1.03\text{\textperthousand}$ ) and  $\delta^{18}\text{O}_{\text{V-PDB}}/\text{\textperthousand}$  values from  $-13.90\text{\textperthousand}$  to  $-5.10\text{\textperthousand}$  (av.  $-11.00\text{\textperthousand}$ ) (Figure 9). Cc4 had higher contents of Fe and Mn ( $\text{CaCO}_3$  38–83%;  $\text{MgCO}_3$  3–53%;  $\text{FeCO}_3$  6–14%;  $\text{MnCO}_3$  0–7%) (Figure 8), with the  $\delta^{13}\text{C}_{\text{V-PDB}}/\text{\textperthousand}$  values from

$-6.40\text{\textperthousand}$  to  $-3.30\text{\textperthousand}$  (av.  $-4.85\text{\textperthousand}$ ), and  $\delta^{18}\text{O}_{\text{V-PDB}}/\text{\textperthousand}$  values from  $-15.90\text{\textperthousand}$  to  $-13.50\text{\textperthousand}$  (av.  $-14.70\text{\textperthousand}$ ) (Figure 9).

**4.3.2. Distribution of Quartz Cementation with Different Morphologies and Fluid Inclusions.** Three types of quartz cementation could be identified according to the morphology, respectively, in forms of quartz overgrowth, micro- to

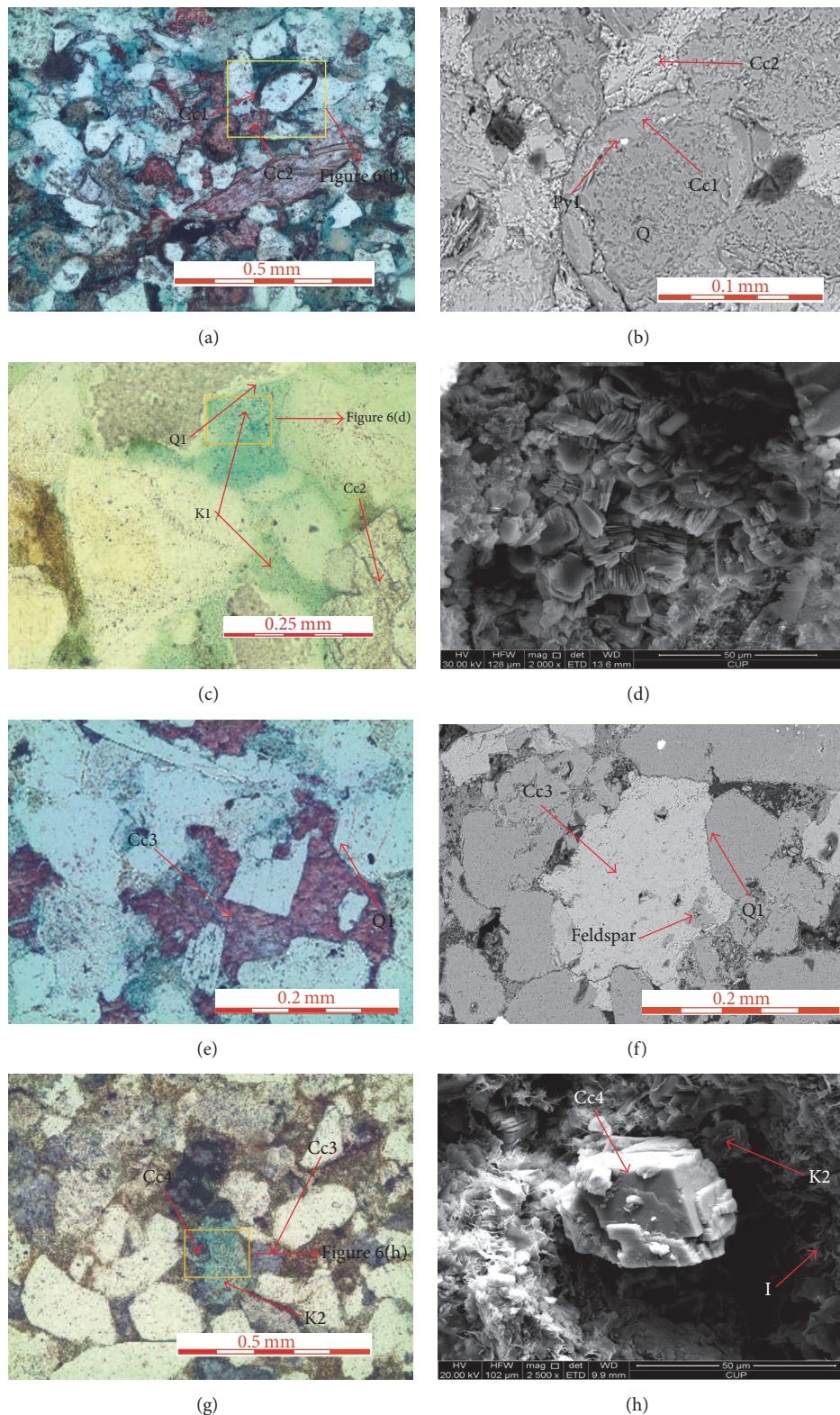


FIGURE 6: Morphological features of diagenetic products in Es of Dongying Sag. ((a) Well Shi127 2180.8 m, micritic high-Mg calcite (Cc1) and medium-coarse calcites (Cc2); (b) Well Shi127 2180.8 m, local amplification of (a), Cc1, Cc2, and Pyl; (c) Well Xin 154 2960.50 m, Cc2 partly filled in primary pores and the outer part was filled by K1; (d) Well Xin 154, 2960.50 m, local amplification of (c); (e) Well Niu110, 3004.80, dissolution of Cc3 and fillings in the outer of Q1; (g) Well FS1, 4322.40 m, Cc4 occurred in the outer of kaolinization feldspar (K2); (h) Well FS1, 4322.40 m, local amplification of (g)).

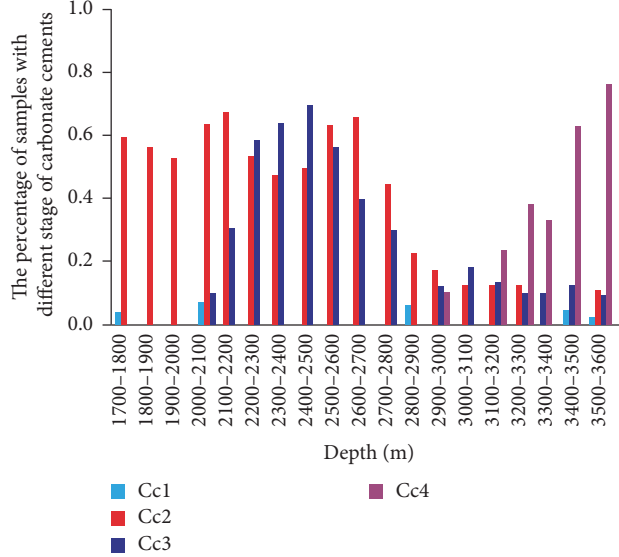


FIGURE 7: The distribution of carbonate cements with different morphological features in sandstone of Es in Dongying Sag.

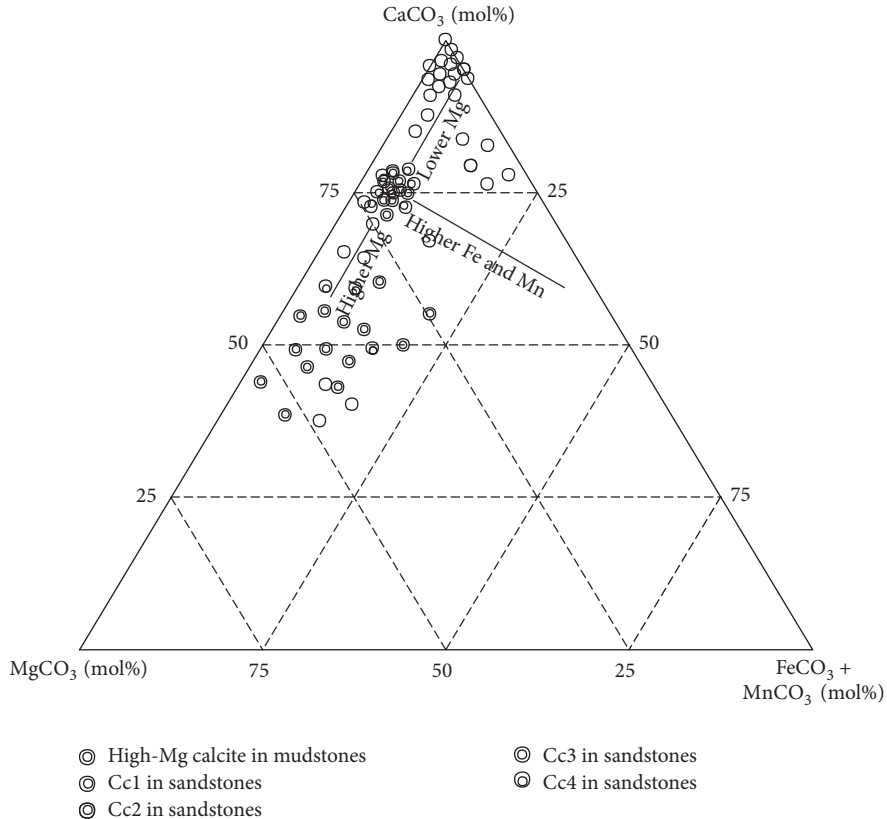


FIGURE 8: Geochemical characteristics of carbonate cements with different morphologies in Es of Dongying Sag.

mega-crystalline pore-filling quartz cements, and fracture-filling quartz cements (Figure 10). The first stage of quartz cements (Q1) was mainly in forms of quartz overgrowth, and the outer part was filled by Cc3 (Figures 6(e), and 6(f),

13(a), 13(b), and 13(c)). Q1 had a depth ranging from 2000 m to 3600 m, mainly concentrated in 2500–3600 m (Figure 11). The second stage of authigenic quartz (Q2) was mainly euhedral quartz and fracture-filling quartz, filled in the outer

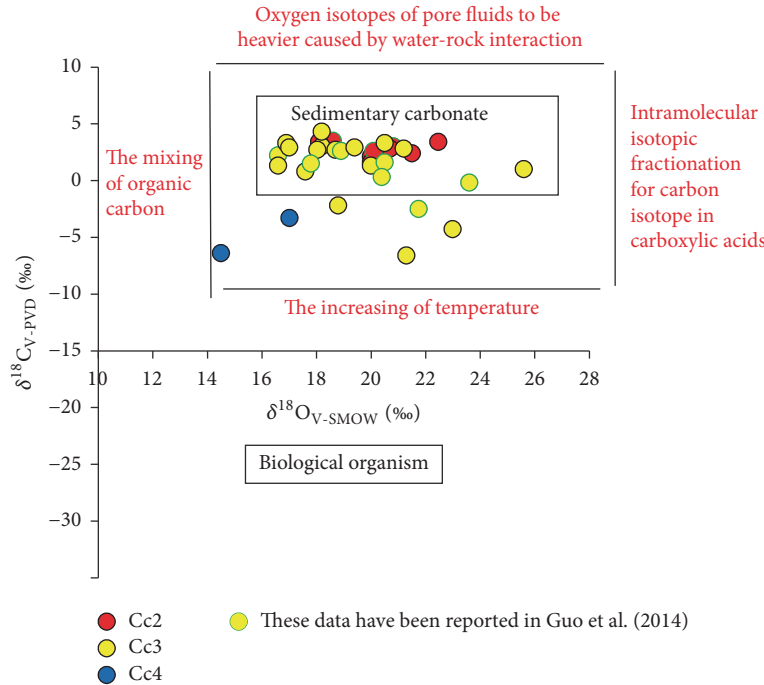


FIGURE 9: Isotope characteristics of carbonate cements with different morphologies in Es sandstones, Dongying Sag [37–46].

part or cutting Q1 (Figures 10(a) and 10(b)). Q2 was in a depth ranging from 2500 m to 3600 m and was mainly concentrated in 2900 m–3600 m (Figure 11).

The homogenization temperature of inclusions in Q1 ranged from 70°C to 115°C and that in Q2 from 110°C to 130°C (Figures 10(a), 10(b), and 12).

**4.3.3. Distribution and Geochemical Features of Authigenic Kaolinites with Different Morphologies.** The morphological features of authigenic kaolinites were comprehensively studied by thin section observation and SEM analysis. The authigenic kaolinites in the study area could be classified into two categories based on their morphologies. The first kind of authigenic kaolinite (K1) was featured by predominant scallop-shape under the microscope (Figures 6(c), 13(a), and 13(c)) as well as single crystals characterized by closely packed, thin complete pseudohexagonal flakes under SEM. The wormlike or book-like aggregation of K1 (Figures 6(d), 13(b), and 13(d)) was mainly in feldspar dissolution pores and residual primary pores which had been partially filled by Cc2 (Figure 6(c)). K1 intergrew with quartz overgrowth (Q1) (Figure 13(b)), and it could be replaced by illites (Figure 13(g)). K1 had a wide range of distribution from 1700 m to 3600 m and was mainly concentrated in the range of 2600 m to 3200 m (Figure 14). Under microscopes, the second kind of authigenic kaolinite (K2) was mainly distributed on the surface of feldspar particles, showing disordered scales, and the aggregate of K2 presented in the shape of feldspar particles (Figures 6(g) and 13(e)). Under SEM, single crystals of K2 were flake-shaped, thin, and loosely arranged. These crystals had curved edges and imperfect forms (Figure 13(f)). K2 was mainly in dissolution pores within Cc3, with the outer side filled by Cc4 (Figures

6(g) and 6(h)). Part of K2 intergrew with authigenic quartz (Q2). K2 was mainly in the range of 2600 m to 3600 m and was mainly concentrated in the range of 2900–3200 m (Figure 14).

K1 mainly contained three elements, namely, Al, Si, and O, while K2 had additional trace elements such as K (av. 1.01%) and Fe (av. 1.89%) (Table 2).

**4.3.4. Morphological and Distribution Characteristics of Other Water-Rock Reaction Products.** In the sandstones with depth less than 3200 m, contents of illite (less than 5%) and chlorite (less than 2%) were relatively low and stable, while that of kaolinite increased significantly with depth (Figure 15). However, when the burial depth reached 3200 m, the contents of illite and chlorite began to increase with depth, while that of kaolinites dropped (Figure 15), which was attributed to the transformation of kaolinites into illite and chlorite as observed under SEM (Figures 6(h), 13(g)).

There were mainly two kinds of authigenic pyrites in Es sandstones, Dongying Sag. The first kind of pyrites (Pyl) occurred as single particles in the inner side of Cc1 (Figure 6(b)), while the other kind (Py2) occurred as frambooids around Cc4 (Figure 13(h)).

## 5. Discussion

**5.1. Formation Timing and Diagenetic Sequence of Major Diagenetic Products.** The  $\delta^{18}\text{O}_{\text{smow}}/\text{‰}$  value of carbonate cements was controlled by formation temperatures and  $\delta^{18}\text{O}_{\text{smow}}/\text{‰}$  values of pore fluids. It was necessary to firstly determine  $\delta^{18}\text{O}_{\text{smow}}/\text{‰}$  values of pore when using  $\delta^{18}\text{O}_{\text{smow}}/\text{‰}$  value of carbonate cements to calculate the formation

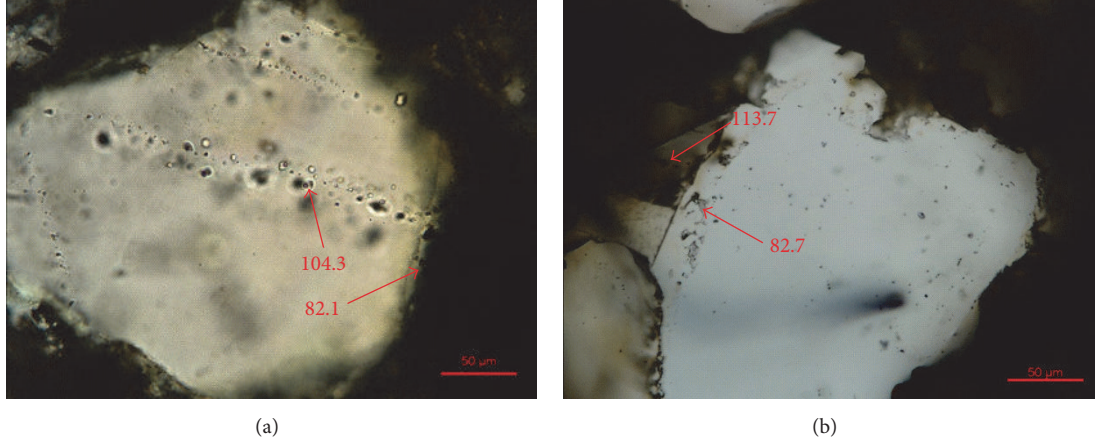


FIGURE 10: *The inclusion characteristics of authigenic quartz in Dongying Sag. ((a) Well Y67, 2960.50 m; (b) Well S126, 3450.4 m).*

TABLE 2: Element component characteristics of authigenic kaolinites in Es of Dongying Sag.

Well ID	Depth (m)	Type	O	Element content percentage (mol%)			
				Al	Si	K	Fe
S 126	3386.40	K1	60.15	18.38	21.47	—	—
S 126	3386.40	K1	60.37	18.22	21.41	—	—
S 126	3428.60	K1	52.99	21.16	25.85	—	—
S 126	3428.60	K1	56.62	19.51	23.87	—	—
X 154	2935.90	K1	58.34	18.87	22.79	—	—
N 105	3096.20	K1	56.61	20.24	23.15	—	—
H 159	2960.30	K1	68.16	13.79	18.05	—	—
S 126	3513.1	K1	55.02	20.14	24.84	—	—
S 126	3450.40	K1	65.32	16.02	18.66	—	—
S 128	3452.40	K1	51.47	21.51	27.02	—	—
S 126	3450.40	K2	48.13	19.94	27.70	2.23	2.00
S 126	3450.40	K2	50.80	19.61	28.28	0.52	0.78
S 126	3450.40	K2	50.55	13.47	31.95	1.20	2.84
N 105	3096.20	K2	56.90	15.58	25.13	0.76	1.63
N 105	3096.20	K2	51.08	20.97	27.19	0.76	—
N 105	3096.20	K2	49.41	22.03	28.07	0.49	—
S 126	3513.1	K2	55.00	20.44	23.02	0.68	0.86
S 126	3513.1	K2	53.64	18.30	25.27	1.63	1.16
S 127	3451.40	K2	48.95	20.63	28.01	0.95	1.46
S 130	3454.40	K2	47.52	21.64	27.50	—	3.34
S 131	3455.40	K2	52.62	18.50	25.05	0.87	2.96

temperature [37, 48]. During diagenetic process, material exchanges between particles and pore fluids (mainly feldspar dissolution) led the  $\delta^{18}\text{O}_{\text{smow}}/\text{\textperthousand}$  value of pore fluids to be heavier [35, 39, 43]. The  $\delta^{18}\text{O}_{\text{smow}}/\text{\textperthousand}$  value of pore water at eodiagenetic stage was about  $-4.8\text{\textperthousand}$ , which became heavier, reaching about  $-3\text{\textperthousand}$  due to significant feldspar dissolution [35, 49]. In other words, Cc1 and Cc2, which were clearly anterior to feldspar dissolution, precipitated from pore fluids with  $\delta^{18}\text{O}_{\text{smow}}/\text{\textperthousand}$  value of  $-4.8\text{\textperthousand}$  (Figures 6(a), 6(b), and 6(c)), while Cc3 and Cc4, which were clearly posterior to

feldspar dissolution, precipitated from pore fluids with  $\delta^{18}\text{O}_{\text{smow}}/\text{\textperthousand}$  value of  $-3\text{\textperthousand}$  (Figures 6(e), 6(f), 6(g), and 6(h)). The chemical composition of Cc1 was similar to micritic high-Mg calcite formed during syndiagenetic stage in shales (Figure 8). Thus, it could be deduced that Cc1 should be formed during syndiagenetic stage as well. The  $\delta^{18}\text{O}_{\text{V-PDB}}/\text{\textperthousand}$  values of Cc2 ranged from  $-12.40\text{\textperthousand}$  to  $-8.20\text{\textperthousand}$ , indicating the formation temperature range of Cc2 to be  $33.2\text{--}58.1^\circ\text{C}$ . The  $\delta^{18}\text{O}_{\text{V-PDB}}/\text{\textperthousand}$  value of Cc3 ranged from  $-13.90\text{\textperthousand}$  to  $-5.10\text{\textperthousand}$ , suggesting the formation temperature range of Cc3

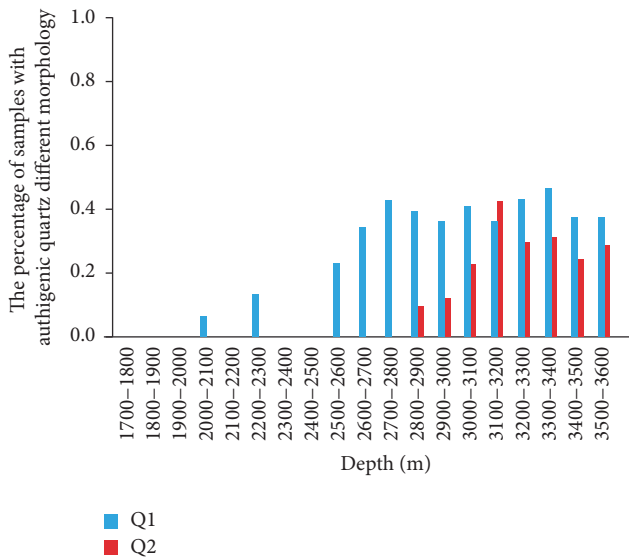


FIGURE 11: The distribution of authigenic quartz with different morphological features in sandstone of Es in Dongying Sag.

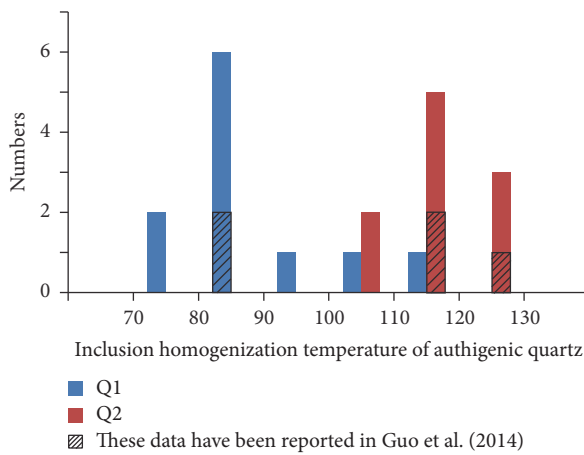


FIGURE 12: The homogenization temperature of inclusion of authigenic quartz with different morphological features in sandstones of Es, Dongying Sag.

to be 50.0–115.2°C. Similarly, the  $\delta^{18}\text{O}_{\text{V-PDB}}/\text{\textperthousand}$  of Cc4 ranged from -15.90‰ to -13.50‰, implying the formation temperature range of Cc3 to be 130–170°C [37, 48].

The homogenization temperatures of brine inclusions in Q1 and Q2, respectively, ranged from 70°C to 115°C and from 110°C to 130°C (Figures 10(a), 10(b), and 12).

K1, which was posterior to cementation of Cc1 and Cc2 and prior to Cc3, generally presented as intergrowth of Q1 (Figures 6(c), 6(h), and 13(b)), indicating the formation temperature range of K1 to be 70–115°C. K2, which was posterior to cementation of Cc3 and anterior to Cc4, generally occurred as intergrowth of K2, implying the formation temperature of K1 to range from 115°C to 130°C.

Chlorite and illite were synchronous with or posterior to Cc4 and were concentrated in depth more than 3200 m

(>140°C), suggesting that they were the latest diagenetic products (Figure 6(h), and 15).

Pyl was generally associated with Cc1 (Figure 6(b)) and Py2 with Cc4 (Figure 13(h)).

Finally, the diagenetic sequence of sandstones in Es, Dongying Sag, was concluded as shown in Figure 16.

## 5.2. Material Sources of Main Diagenetic Products

**5.2.1. Material Sources of Carbonate Cements.** Cc1 could be directly precipitated out from sedimentary waters during syndiagenetic stage [51]. The  $\delta^{13}\text{C}_{\text{PDB}}/\text{\textperthousand}$  and  $\delta^{18}\text{O}_{\text{PDB}}/\text{\textperthousand}$  values of Cc2 in sandstones ranged from 1.60‰ to 3.50‰ and from -12.4‰ to -8.2‰, respectively, indicating Cc2 to be typical lacustrine carbonate cements (Figure 9). Cc2 mainly occurred in sandstones which were proximal to sand-shale interfaces [52–55]. Formation temperatures of Cc2 were within the range of 33.2–58.1°C, which corresponded to the depth range of 500–1000 m [50]. In this depth range, the porosity of mudstones declined from 60% to 10–20% because of compaction, leading to discharge of a large amount of sedimentary water into sandstones [13, 53, 55–58].  $\text{Ca}^{2+}$  and  $\text{CO}_3^{2-}$  were rich in those fluids, and they were main material sources for Cc2.

The  $\delta^{13}\text{C}_{\text{PDB}}/\text{\textperthousand}$  and  $\delta^{18}\text{O}_{\text{PDB}}/\text{\textperthousand}$  values of Cc3 in sandstones mainly ranged from -6.6‰ to 4.3‰ and from -13.9‰ to -5.1‰, respectively, which indicated the influence of organic carbon on part of Cc3 (Figure 9). The chemical composition of Cc3 was complex (Figure 8). Vertically, Cc3 was mainly concentrated in transitional areas of normal-pressure and overpressure zones (Figure 7; [59]). Laterally, distribution of Cc3 was controlled by main faults [59]. All of these proved that hydrothermal fluids that flowed through the faults provided part of the material sources for Cc3. Formation temperatures of Cc3 ranged from 50.0°C to 115.2°C, in the range of which carboxylic acids were formed and expelled from organic matters into mudstones [13, 60]. The presence of carboxylic acids led to dissolution of plagioclases (mainly Ca-feldspars and Na-feldspars) and also caused the entrance of  $\text{Ca}^{2+}$  and  $\text{Na}^+$  into pore fluids (Figures 4, 6(f), and 5). During this time, no obvious dissolution of Cc1 and Cc2 occurred (Figure 6(c), Figure 7; [61]). The  $\text{Ca}^{2+}$ ,  $\text{Mg}^{2+}$ , and  $\text{CO}_3^{2-}$  (partly influenced by organic carbon) in hydrothermal fluids and  $\text{Ca}^{2+}$  (dissolved by Ca-feldspar) and  $\text{CO}_3^{2-}$  (sedimentary carbon) in formation water were material sources for Cc3 [59, 62, 63].

The  $\delta^{13}\text{C}_{\text{PDB}}/\text{\textperthousand}$  and  $\delta^{18}\text{O}_{\text{PDB}}/\text{\textperthousand}$  values of Cc4 in sandstones ranged from -6.4‰ to -3.3‰ and from -15.9‰ to -13.5‰, respectively, indicating the significant influence of organic carbon on Cc4 (Figure 9). Cc4 was mainly concentrated in sandstones with depth over 3200 m (Figure 7). At this depth (corresponding temperature > 120°C), cracking of carboxylic acids and organic matters resulted in a large amount of  $\text{CO}_2$ , which was transformed to  $\text{CO}_3^{2-}$  in the following diagenetic processes [13, 27, 35, 50, 54, 60]. Carbonate cements (mainly Cc2 and Cc3) were dissolved obviously, leading to the entrance of  $\text{Ca}^{2+}$  and  $\text{CO}_3^{2-}$  into pore fluids (Figures 6(e), and 7; [64]). The dissolution of metamorphic

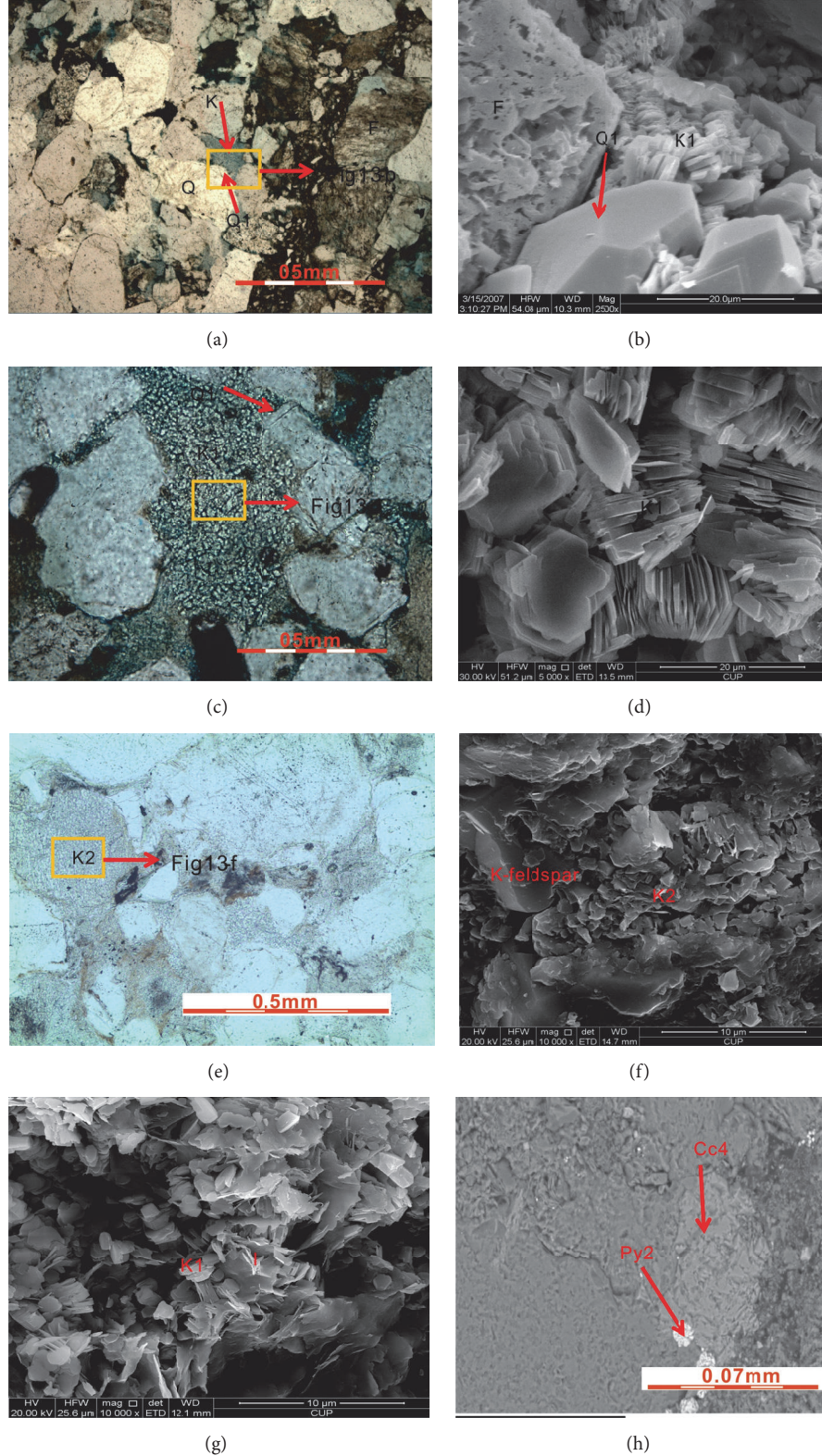


FIGURE 13: Morphological features of diagenetic products in Es of Dongying Sag. ((a) Well He 142, 3064.83 m, wormlike authigenic kaolinites (K1) intergrew with quartz overgrowths; (b) Well He 142, 3064.83 m, local amplification of (a), K1 intergrew with quartz overgrowths; (c) Well Xin 154, 2938.56 m, K1 filled in secondary pores; (d) Well Xin 154, 2938.56 m, local amplification of (c), wormlike authigenic kaolinite (K1); (e) Well N105, 3096.2 m, disordered authigenic kaolinite distributed on the surface of K-feldspars (K2); (f) Well N105, 3096.2 m, local amplification of (e); (g) Well XX161, 3272.5 m, illitization of K1 and K2; (h) Well S106, 3398.70 m, Cc4 and Py2).

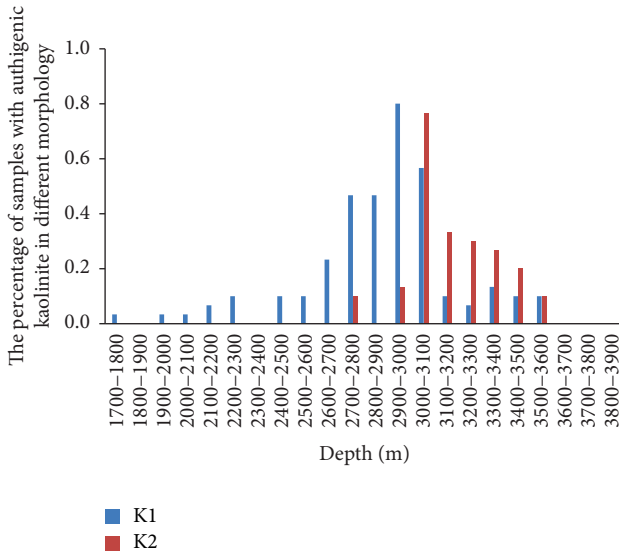


FIGURE 14: The distribution of authigenic kaolinites with different morphologies in Es sandstone of Dongying Sag [47].

lithic fragments promoted the entrance of  $\text{Fe}^{2+}$  and  $\text{Mg}^{2+}$  into pore fluids (Figure 4). All of these materials were the sources for precipitation of Cc4.

**5.2.2. Material Sources of Authigenic Quartz.** Precipitation of authigenic quartz occurred in the diagenesis process (Figure 16) as the concentration of  $\text{SiO}_2$  (aq) (<100 ppm) in lake waters was too low for authigenic quartz [11]. There were no external sources of free  $\text{SiO}_2$  for sandstones of Es in Dongying Sag [35]. However, quartz dissolution at grain contacts and dissolution or transformation of feldspars in sandstones could be possible internal source for authigenic quartz. Contact relationships of Es sandstones were mainly point contact, with a small proportion of line contact (Figures 6(a), 6(c), 13(a), and 13(c)). No much free  $\text{SiO}_2$  (aq) was released during this process. Therefore, the depth distribution range of authigenic quartz was identical to that of feldspar (Figures 4 and 11). In the thin sections and SEM, dissolution and transformation of feldspars associated with authigenic quartz could be identified (Figure 13(b)). Therefore, the most likely source of authigenic quartz might be the internal dissolution and transformation of feldspars.

**5.2.3. Material Sources of Authigenic Kaolinites.** The concentrations of  $\text{SiO}_2$  (aq) (<100 ppm) and  $\text{Al}^{3+}$  (<10 ppm) were too low to be effective material source for authigenic kaolinites [11]. However, there were a lot of authigenic kaolinites in the sandstone reservoirs of Es in Dongying Sag. Vertically, the content of authigenic kaolinites was negatively correlated with feldspar content (Figures 4 and 14; [35, 47, 65]). In other words, the dissolution of aluminosilicate minerals (mainly feldspars) was important material source for authigenic kaolinites [9, 66–71].

K1 was featured by perfect crystal forms and exclusive Al, Si, and O ions, indicating those authigenic kaolinites to be

precipitated directly from pore fluids [72, 73]. High content of K1 often appeared in samples with no or little feldspar dissolution, while low content of K1 was common in samples with a large amount of feldspar dissolution [74], which indicated the significant amount of free  $\text{Si}^{4+}$  and  $\text{Al}^{3+}$  which are released by dissolution of feldspar and then migration in pore fluids during the formation of K1. In the deep burial environment, pore fluids flowed slowly, dissolving only a small amount of free  $\text{Si}^{4+}$  and  $\text{Al}^{3+}$ . Therefore, it was hard for silicon and aluminum to migrate in the form of  $\text{Si}^{4+}$  and  $\text{Al}^{3+}$  [75–77]. Considering the formation temperature (60–115°C) of K1, which was suitable for formation and preservation of carboxylic acids, it was suggested that complex reaction between carboxylic acids and cations of  $\text{Si}^{4+}$  and  $\text{Al}^{3+}$  could induce the dissolution of feldspars [27, 35, 78]. The  $\text{Si}^{4+}$  and  $\text{Al}^{3+}$  migrated over long distances in the form of clathrates and precipitated as authigenic kaolinite (K1) in the proper geological environment.

K2 was featured by imperfect crystal forms and more other ions (like Fe and K) besides Al, Si, and O, which indicated these authigenic kaolinites to be products of feldspar transformation [72, 73]. Pore fluids rich in  $\text{CO}_2$  led to the occurrence of a large amount of  $\text{H}^+$  and  $\text{HCO}_3^-$  in pore fluids at the depth of 2800–3200 m (Figure 5). Under this situation, K-feldspar particles were totally or partly transformed into K2 and Q2 [5, 61].

**5.2.4. Material Sources of Other Water-Rock Reaction Products.** In the depth range of 2800–3200 m, kaolinization of K-feldspars and dissolution of metamorphic lithic fragments led to concentration of  $\text{K}^+$ ,  $\text{Fe}^{2+}$ , and  $\text{Mg}^{2+}$  in pore fluids. At the same time, a large amount of  $\text{H}^+$  was consumed. All of these led authigenic kaolinites (K1 and K2) to be unstable [56, 79]. Once the depth was above 3200 m (130°C), K1 and K2 were partly or totally transformed into illites and chlorites (Figures 6(h), 13(g), and 15).

**5.3. Material Exchanges between Pore Fluids and Rocks during Diagenetic Processes.** The material exchange between pore fluids and rocks was mainly controlled by geochemical and physical properties of pore fluids. During diagenetic processes, fluids, which were recharged by mudstones and flowed along faults, could lead to obvious changes of properties of pore fluids. Based on analyses of changes of detrital composition, geochemical features of pore fluids, and material sources of diagenetic products in Es of Dongying Sag, this study divided the material exchanges during diagenetic processes in rift basins into five stages.

**Stage 1.** Certain amounts of  $\text{Ca}^{2+}$ ,  $\text{Mg}^{2+}$ ,  $\text{Fe}^{3+}$ ,  $\text{CO}_3^{2-}$ , and  $\text{SO}_4^{2-}$  were existent in lake waters of the Paleogene in Dongying Sag [51, 80, 81]. During syngenetic stage, evaporation of lake water led to concentration of ions, and they precipitated as a small amount of micritic high-Mg calcite [51, 54, 81–83]. At the same time, activities of sulfate-reducing bacteria led to the change of  $\text{Fe}^{3+}$  and  $\text{SO}_4^{2-}$  to  $\text{Fe}^{2+}$  and  $\text{S}^{2-}$ , respectively. Part of  $\text{Fe}^{2+}$  entered into crystal lattices of Cc1 as

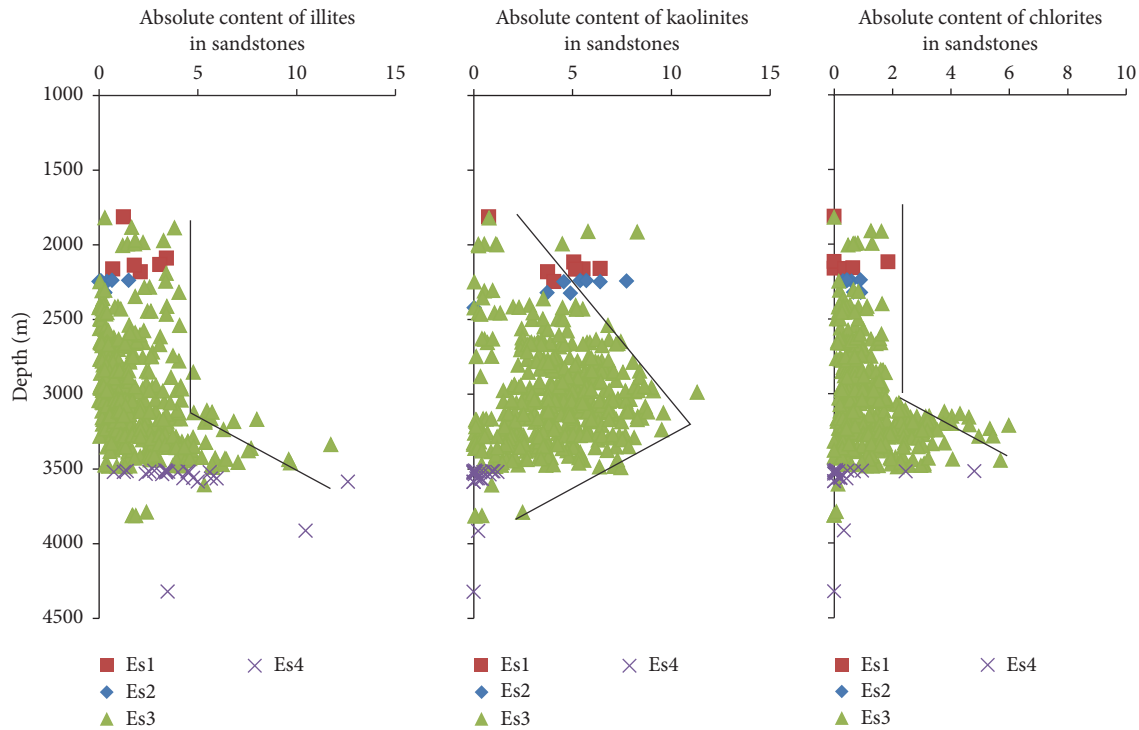


FIGURE 15: The content changes of clay minerals in Es sandstones from Dongying Sag.

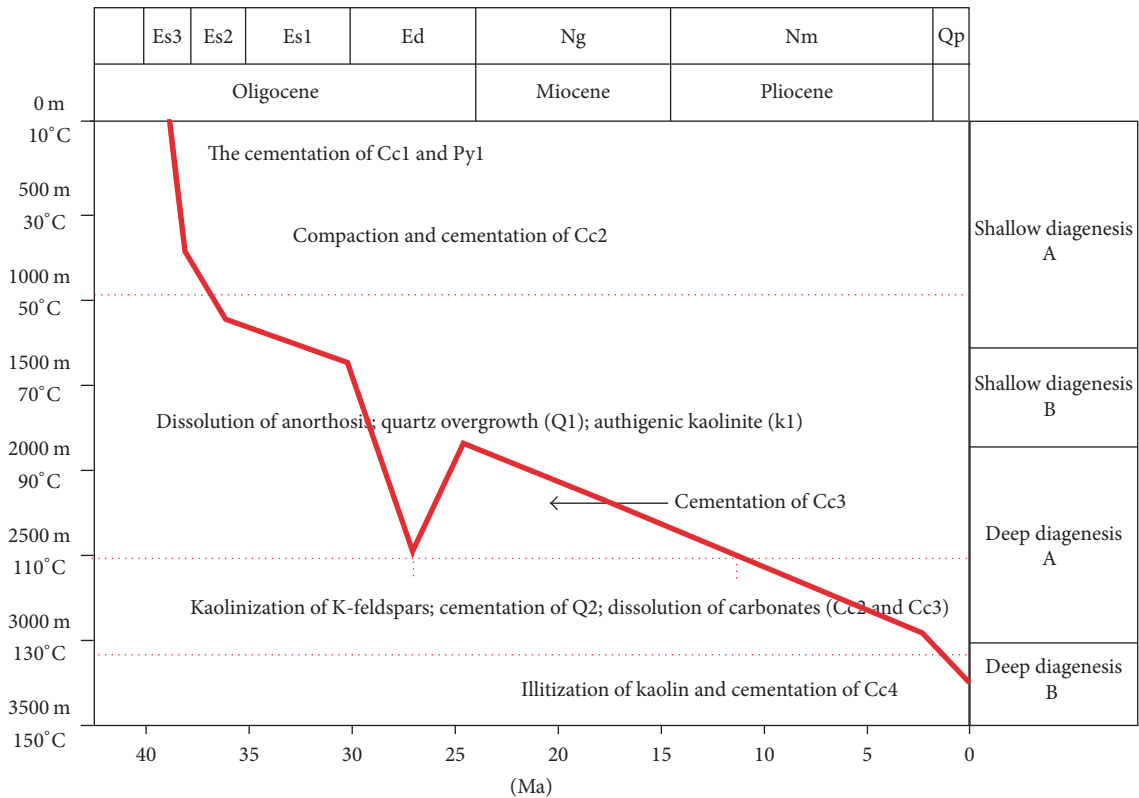


FIGURE 16: The diagenetic sequence of Es in Dongying Sag (paleogeothermal data was based on [50]; burial history was based on [47]).

heteroatom, while the remaining part was combined with  $S^{2-}$ , precipitating as Pyl associated with Ccl. In this stage, mainly  $Mg^{2+}$ ,  $Ca^{2+}$ ,  $CO_3^{2-}$ ,  $Fe^{2+}$ , and  $SO_4^{2-}$ , which originated from lake waters, entered sandstones in the forms of Ccl and Pyl.

*Stage 2.* In the depth range of 500–1000 m (paleotemperature of 30–50°C), concentrated compaction waters rich in  $Ca^{2+}$  and  $CO_3^{2-}$  entered into sandstones from mudstones, resulting in the formation of Cc2 in sandstones close to the sandstone-mudstone interfaces. During this stage,  $Ca^{2+}$  and  $CO_3^{2-}$  from compaction waters entered into sandstones and precipitated as Cc2.

*Stage 3.* In the depth range of 1250–2800 m (paleotemperature of 60–120°C), waters rich in carboxylic acids enter into sandstones from mudstones, leading to dissolution of plagioclases. In this process,  $Na^+$  and  $Ca^{2+}$  entered into pore fluids and were well preserved.  $Si^{4+}$  and  $Al^{3+}$  were complexed with carboxylic acids, and these complexes migrated in pores and then precipitated as K1 and Q1 in the proper geological conditions. In this stage, activation of faults could cause the blend of hydrothermal fluids (upwelling through faults, rich in  $Mg^{2+}$ ,  $Ca^{2+}$ , and partly organic source  $CO_3^{2-}$ ) and formation waters (in place, rich in  $Ca^{2+}$ ), leading to the precipitation of Cc3.

*Stage 4.* In the depth range of 2800–3200 m (paleotemperature of 120–140°C),  $CO_2$  with organic sources, formed by cracking of organic matters and carboxylic acids, entered the pore fluids and was preserved as  $H_2CO_3$  ( $HCO_3^-$ ). The presence of organic source  $H_2CO_3$  ( $HCO_3^-$ ) led to the transformation of K-feldspars and the dissolution of Cc2, Cc3, and metamorphic lithic fragments. During transformation of K-feldspars, a large amount of  $K^+$  entered into pore fluids and was well preserved. The dissolution of Cc2 and Cc3 led to the entrance of a large amount of sedimentary source  $Ca^{2+}$  and  $CO_3^{2-}$  into pore fluids, which were then well preserved. The dissolution and transformation of metamorphic lithic fragments led to the entrance of  $Fe^{2+}$  and  $Mg^{2+}$  into pore fluids and subsequently good preservation (Figure 5). The transformation of K-feldspars led to the formation of K2 and Q2. In this process,  $K^+$ ,  $Ca^{2+}$ ,  $CO_3^{2-}$ ,  $Mg^{2+}$ ,  $Fe^{2+}$ , and  $Mn^{2+}$  entered pore fluids.

*Stage 5.* In the depth above 3200 m (paleotemperature above 140°C), less or no formation of organic  $CO_2$  resulted in the transformation of pore fluids into alkaline. In this depth range, the contents of  $Na^+$ ,  $K^+$ ,  $Ca^{2+}$ , and  $HCO_3^-$  significantly declined (Figure 5), which might be due to the precipitation of Cc4 as well as illitization and chloritization of K. During this process, because of declining of  $H^+$ ,  $HCO_3^{2-}$  transformed to  $CO_3^{2-}$ . This caused  $CO_3^{2-}$  (dissolution of Cc2 and Cc3, organic source  $CO_3^{2-}$ ),  $Ca^{2+}$ ,  $Mg^{2+}$ ,  $Fe^{2+}$ , and  $Mn^{2+}$  to precipitate as Cc4. Concentration of  $K^+$  and declining of  $H^+$  contributed to the transformation of K1 and K2 into illites, while concentration of  $Mg^{2+}$  and  $Fe^{2+}$  as well as declining of  $H^+$  led to the transformation of K1 and K2 into chlorites. In this process,  $CO_3^{2-}$ ,  $Ca^{2+}$ ,  $Mg^{2+}$ ,  $Fe^{2+}$ ,  $Mn^{2+}$ , and  $K^+$  entered sandstones in the forms of Cc4, illites, and chlorites.

## 6. Conclusions

The material exchange of pore fluids in rift basins could be divided into five stages. The first stage was the near surface evaporation concentration stage, during which  $Ca^{2+}$ ,  $Mg^{2+}$ , and  $CO_3^{2-}$  in lake waters precipitated as high-Mg calcites (Ccl), mainly caused by evaporation. The second stage was the shale compaction stage, during which  $Ca^{2+}$  and  $CO_3^{2-}$  from shale compaction waters precipitated as calcites (Cc2), mainly caused by compaction of shales. The third stage was the carboxylic acid dissolution stage, during which dissolution of plagioclases (by carboxylic acid) occurred. During this stage,  $Ca^{2+}$  and  $Na^+$  entered into pore fluids as ions, while  $Si^{4+}$  and  $Al^{3+}$  entered into pore fluids and migrated as clathrates, ultimately precipitating as kaolinites (K1) and quartz overgrowth (Q1). Partly, the upwelling of hydrothermal fluids caused by active faults led to the precipitation of carbon cements (Cc3). Those processes were mainly caused by carboxylic acids and upwelling of hydrothermal fluids. The fourth stage was the organic  $CO_2$  stage, which was featured by the kaolinization of K-feldspar, formation of organic  $CO_2$ , and dissolution of metamorphic lithic fragments and carbon cements (mainly Cc2 and Cc3). During this stage,  $K^+$ ,  $Fe^{2+}$ ,  $Mg^{2+}$ ,  $Ca^{2+}$ ,  $HCO_3^-$ , and  $CO_3^{2-}$  entered into pore fluids, driven by formation of organic  $CO_2$ . The fifth stage was the alkaline fluid stage, which was characterized by the cementation of ferro-carbonates and ankerite as well as illitization or chloritization of kaolinites. During this stage,  $K^+$ ,  $Fe^{2+}$ ,  $Mg^{2+}$ ,  $Ca^{2+}$ , and  $CO_3^{2-}$  precipitated from pore fluids and entered into sandstones, caused by declining concentration of  $H^+$ .

## Conflicts of Interest

The authors declare that they have no conflicts of interest.

## Acknowledgments

This study was financially supported by the National Science and Technology Special Grant (no. 2016ZX05006001) and National Natural Science Foundation of China (no. 41172128). The authors also appreciate Shengli Oilfield Company of Sinopec for providing core samples and other geological data of Dongying Sag.

## References

- [1] M. C. Li, J. Li, Y. J. Wan, Z. Y. Deng, and X. Q. Du, "Fluids in the sedimentary basin," *Acta Petrolei Sinica*, vol. 04, pp. 13–17, 2001, [In Chinese with English abstract].
- [2] J. H. Zeng, "Geofluids Flow and Hydrocarbon Accumulation in Sedimentary Basin," *Marine Origin Petroleum Geology*, vol. 01, pp. 37–42, 2005, [In Chinese with English abstract].
- [3] X. N. Xie, J. M. Cheng, and Y. L. Meng, "Basin fluid flow and associated diagenetic processes," *Acta Sedimentologica Sinica*, vol. 05, pp. 863–871, 2009, [In Chinese with English abstract].
- [4] S. T. Paxton, J. O. Szabo, J. M. Ajdukiewicz, and R. E. Klimenidis, "Construction of an intergranular volume compaction curve for evaluating and predicting compaction and porosity

- loss in rigid-grain sandstone reservoirs,” *AAPG Bulletin*, vol. 86, no. 12, pp. 2047–2067, 2002.
- [5] S. J. Huang, H. W. Wu, J. Liu, L. C. Shen, and C. G. Huang, “Generation of secondary porosity by meteoric water during time of subaerial exposure: An example from Yanchang Formation sandstone of Triassic of Ordos Basin,” *Earth Science*, vol. 04, pp. 419–424, 2003, [In Chinese with English abstract].
- [6] M. A. K. El-ghali, H. Mansurbeg, S. Morad, I. Al-Aasm, and G. Ajdanlisky, “Distribution of diagenetic alterations in fluvial and paralic deposits within sequence stratigraphic framework: evidence from the Petrohan Terrigenous Group and the Svidol Formation, Lower Triassic, NW Bulgaria,” *Sedimentary Geology*, vol. 190, no. 1-4, pp. 299–321, 2006.
- [7] M. P. Verma, “Qrtzgeotherm: An ActiveX component for the quartz solubility geothermometer,” *Computers & Geosciences*, vol. 34, no. 12, pp. 1918–1925, 2008.
- [8] A. Berger, S. Gier, and P. Krois, “Porosity-preserving chlorite cements in shallow-marine volcaniclastic sandstones: Evidence from cretaceous sandstones of the sawan gas field, Pakistan,” *AAPG Bulletin*, vol. 93, no. 5, pp. 595–615, 2009.
- [9] K. Bjørlykke, M. Ramm, and G. C. Saigal, “Sandstone diagenesis and porosity modification during basin evolution,” *Geologische Rundschau*, vol. 78, no. 1, pp. 243–268, 1989.
- [10] K. Bjørlykke, “Fluid flow in sedimentary basins,” *Sedimentary Geology*, vol. 86, no. 1-2, pp. 137–158, 1993.
- [11] K. Bjørlykke and J. Jahren, “Open or closed geochemical systems during diagenesis in sedimentary basins: Constraints on mass transfer during diagenesis and the prediction of porosity in sandstone and carbonate reservoirs,” *AAPG Bulletin*, vol. 96, no. 12, pp. 2193–2214, 2012.
- [12] G. Yuan, Y. Cao, T. Yang et al., “Porosity enhancement potential through mineral dissolution by organic acids in the diagenetic process of clastic reservoir,” *Earth Science Frontiers*, vol. 20, no. 5, pp. 207–219, 2013.
- [13] G.-H. Yuan, Y.-C. Cao, Z.-Z. Jia, Y.-Z. Wang, and T. Yang, “Research progress on anomalously high porosity zones in deeply buried clastic reservoirs in petrolierous basin,” *Natural Gas Geoscience*, vol. 26, no. 1, pp. 28–42, 2015.
- [14] X. Q. Ding, M. M. Han, S. N. Zhang, M. Y. Fu, and Y. L. Wan, “Roles of meteoric water on secondary porosity of siliciclastic reservoirs,” *International Geology Review*, vol. 60, pp. 145–158, 2014, [In Chinese with English abstract].
- [15] A. Putnis, “Transient porosity resulting from fluid-mineral interaction and its consequences,” *Reviews in Mineralogy and Geochemistry*, vol. 80, no. 1, pp. 1–23, 2015.
- [16] Z. Cao, G. Liu, Y. Kong et al., “Lacustrine tight oil accumulation characteristics: Permian Lucaogou Formation in Jimusaer Sag, Junggar Basin,” *International Journal of Coal Geology*, vol. 153, pp. 37–51, 2016.
- [17] M. H. Liu and C. L. Zhao, “Review of the studies on oil and gas reservoirs,” *Journal of China University of Petroleum*, vol. 15, pp. 115–124, 1991, [In Chinese with English abstract].
- [18] P. Luo, Y. N. Qiu, A. L. Jia, and X. S. Wang, “The Present Challenges of Chinese Petroleum Reservoir Geology and Research Direction,” *Acta Sedimentologica Sinica*, vol. 21, pp. 142–147, 2003, [In Chinese with English abstract].
- [19] S. N. Ehrenberg, P. H. Nadeau, and Ø. Steen, “A megascale view of reservoir quality in producing sandstones from the offshore Gulf of Mexico,” *AAPG Bulletin*, vol. 92, no. 2, pp. 145–164, 2008.
- [20] S. N. Ehrenberg, P. H. Nadeau, and Ø. Steen, “Petroleum reservoir porosity versus depth: Influence of geological age,” *AAPG Bulletin*, vol. 93, no. 10, pp. 1281–1296, 2009.
- [21] C.-L. Ye, G.-D. Zheng, and J. Zhao, “Research review of Water-Rock interactions in reservoir rocks,” *Bulletin of Mineralogy Petrology and Geochemistry*, vol. 29, no. 1, pp. 89–97, 2010.
- [22] J. M. Ajdukiewicz and R. H. Lander, “Sandstone reservoir quality prediction: the state of the art,” *AAPG Bulletin*, vol. 94, no. 8, pp. 1083–1091, 2010.
- [23] T. R. Taylor, M. R. Giles, L. A. Hathon et al., “Sandstone diagenesis and reservoir quality prediction: models, myths, and reality,” *AAPG Bulletin*, vol. 94, no. 8, pp. 1093–1132, 2010.
- [24] R. C. Tobin, T. McClain, R. B. Lieber et al., “Reservoir quality modeling of tight-gas sands in Wamsutter field: integration of diagenesis, petroleum systems, and production data,” *AAPG Bulletin*, vol. 94, no. 8, pp. 1229–1266, 2010.
- [25] J. Lai, G. Wang, Y. Ran, Z. Zhou, and Y. Cui, “Impact of diagenesis on the reservoir quality of tight oil sandstones: The case of Upper Triassic Yanchang Formation Chang 7 oil layers in Ordos Basin, China,” *Journal of Petroleum Science and Engineering*, vol. 145, pp. 54–65, 2016.
- [26] Z. Cao, G. D. Liu, W. Meng, P. Wang, and C. Y. Yang, “Origin of different chlorite occurrences and their effects on tight clastic reservoir porosity,” *Journal of Petroleum Science Engineering*, pp. 384–392, 2017.
- [27] R. C. Surdam and P. Yin, “Organic Acids and Carbonate Stability, the Key to Predicting Positive Porosity Anomalies,” in *Organic Acids in Geological Processes*, Pittman E. D. and M. D. Lewan, Eds., pp. 398–448, Springer, Berlin, Germany, 1994.
- [28] S. M. C. D. Anjos, L. F. D. Ros, R. S. D. Souza, C. M. D. A. Silva, and C. L. Sombra, “Depositional and diagenetic controls on the reservoir quality of Lower Cretaceous Pendência sandstones, Potiguar rift basin, Brazil,” *AAPG Bulletin*, vol. 84, 2000.
- [29] P. Gouze and A. Coudrain-Ribstein, “Chemical reactions and porosity changes during sedimentary diagenesis,” *Applied Geochemistry*, vol. 17, no. 1, pp. 39–47, 2002.
- [30] J. M. Ketzer, M. Holz, S. Morad, and I. S. Al-Aasm, “Sequence stratigraphic distribution of diagenetic alterations in coal-bearing, paralic sandstones: evidence from the Rio Bonito Formation (early Permian), southern Brazil,” *Sedimentology*, vol. 50, no. 5, pp. 855–877, 2003.
- [31] S. J. Huang, K. K. Huang, L. W. Feng, H. P. Tong, L. H. Liu, and X. H. Zhang, “Mass exchanges among feldspar, kaolinite and illite and their influences on secondary porosity formation in clastic diagenesis—a case study on the Upper Paleozoic, Ordos Basin and Xujiahe Formation, Western Sichuan Depression,” *Geochimica*, vol. 38, pp. 498–506, 2009, [In Chinese with English abstract].
- [32] H. Mansurbeg, M. A. K. El-ghali, S. Morad, and P. Plink-Björklund, “The impact of meteoric water on the diagenetic alterations in deep-water, marine siliciclastic turbidites,” *Journal of Geochemical Exploration*, vol. 89, no. 1-3, pp. 254–258, 2006.
- [33] B. S. Yu and X. Y. Lai, “Dissolution of calcite cement and its contribution to the secondary pores of reservoir in the kela2 gas field in the Tarim basin,” *Journal of Mineralogy and Petrology*, vol. 26, pp. 74–79, 2006, [In Chinese with English abstract].
- [34] Z. Cao, G. Liu, H. Zhan et al., “Pore structure characterization of Chang-7 tight sandstone using MICP combined with N<sup>2</sup> GA techniques and its geological control factors,” *Scientific Reports*, vol. 6, Article ID 36919, 2016.
- [35] G. Yuan, J. Gluyas, Y. Cao et al., “Diagenesis and reservoir quality evolution of the Eocene sandstones in the northern Dongying Sag, Bohai Bay Basin, East China,” *Marine and Petroleum Geology*, vol. 62, pp. 77–89, 2015.

- [36] Y. Li, J. G. Cai, and J. M. Liu, "High-resolution sequence stratigraphy of paleogene in Dongying Depression," *Acta Sedimentologica Sinica*, vol. 20, pp. 212-213, 2002, [In Chinese with English abstract].
- [37] I. Friedman and O'Neil Jr, "Compilation of stable isotope fractionation factors of geochemical interest," in *in. Data of Geochemistry*, M. Fleischer, Ed., p. 114, Geological Survey, USA, 6 edition, 1977.
- [38] P. Deines, "The isotopic composition of reduced organic carbon," in *in. Handbook of Environmental Isotope Geochemistry*, P. Fritz and J. C. Fontes, Eds., pp. 329–406, Elsevier, Amsterdam, The Netherlands, 1980.
- [39] S. M. Savin, "Oxygen and hydrogen isotope effects in low-temperature mineral-water interactions," in *In : Handbook of environmental isotope geochemistry*, P. Fritz and J. C. Fontes, Eds., pp. 283–327, Elsevier, Amsterdam, The Netherlands, 1980.
- [40] K. Kelts and M. Talbot, "Lacustrine Carbonates as Geochemical Archives of Environmental Change and Biotic/Abiotic Interactions," in *Large Lakes*, Brock/Springer Series in Contemporary Bioscience, pp. 288–315, Springer Berlin Heidelberg, Berlin, Heidelberg, 1990.
- [41] J. Veizer, D. Ala, K. Azmy et al., "  $^{87}\text{Sr}/^{86}\text{Sr}$ ,  $\delta^{13}\text{C}$  and  $\delta^{18}\text{O}$  evolution of Phanerozoic seawater," *Chemical Geology*, vol. 161, no. 1, pp. 59–88, 1999.
- [42] D. Ala, K. Azmy, P. Bruckschen et al., "  $^{87}\text{Sr}/^{86}\text{Sr}$ ,  $\delta^{13}\text{C}$  and  $\delta^{18}\text{O}$  evolution of Phanerozoic seawater," *Chemical Geology*, vol. 161, no. 1, pp. 1586–1586, 1999.
- [43] M. Fayek, T. M. Harrison, M. Grove, K. D. McKeegan, C. D. Coath, and J. R. Boles, "In situ stable isotopic evidence for protracted and complex carbonate cementation in a petroleum reservoir, north coles levee, san joaquin basin, California, U.S.A," *Journal of Sedimentary Research*, vol. 71, no. 3, pp. 444–458, 2001.
- [44] S. G. Franks, R. F. Dias, K. H. Freeman et al., "Carbon isotopic composition of organic acids in oil field waters, San Joaquin Basin, California, USA," *Geochimica et Cosmochimica Acta*, vol. 65, no. 8, pp. 1301–1310, 2001.
- [45] S. Liu, S. Huang, Z. Shen, Z. Lü, and R. Song, "Diagenetic fluid evolution and water-rock interaction model of carbonate cements in sandstone: An example from the reservoir sandstone of the Fourth Member of the Xujiahe Formation of the Xiaoquan-Fenggu area, Sichuan Province, China," *Science China Earth Sciences*, vol. 57, no. 5, pp. 1077–1092, 2014.
- [46] B. Wu, A. Wei, C. Liu et al., "Stable isotope tracing on the formation of white sandstone in Yan'an Group, northern Ordos Basin, and its geological significance," *Earth Science Frontiers*, vol. 22, no. 3, pp. 205–214, 2015.
- [47] S. X. Shao, J. H. Zeng, S. W. Zhang et al., "Types , characteristics and origin of kaolinite in sandstone reservoir of Shahejie Formation, Dongying Sag," *Acta Sedimentologica Sinica*, vol. 33, pp. 1204–1216, 2015, [In Chinese with English abstract].
- [48] A. Matthews and A. Katz, "Oxygen isotope fractionation during the dolomitization of calcium carbonate," *Geochimica et Cosmochimica Acta*, vol. 41, no. 10, pp. 1431–1438, 1977.
- [49] C. L. Liu, "Carbon and oxygen isotopic compositions of lacustrine carbonates of the Shahejie Formation in the Dongying depression and their paleolimnological significance," *Acta Sedimentologica Sinica*, vol. 16, pp. 109–114, 1998, [In Chinese with English abstract].
- [50] N. Qiu, S. Li, and J. Zeng, "Thermal history and tectonic-thermal evolution of the Jiyang depression in the Bohai Bay Basin, East China," *Acta Geologica Sinica*, vol. 78, no. 2, pp. 263–269, 2004.
- [51] X. C. Lu, W. X. Hu, Q. Fu et al., "Study of salinity evolution of geofluids during syngensis and diagenesis using composition of carbonate minerals," *Acta Sedimentologica Sinica*, vol. 16, pp. 120–126, 1998, [In Chinese with English abstract].
- [52] J. H. Zeng, J. L. Peng, N. S. Qiu, and Z. Q. Zhu, "Carbonate dissolution-precipitation in sandstone-shale contact and its petroleum geological meanings," *Natural Gas Geoscience*, vol. 06, pp. 760–764, 2006, [In Chinese with English abstract].
- [53] S. Zhang, L. Zhang, S. Zhang, Q. Liu, R. Zhu, and Y. Bao, "Formation of abnormal high pressure and its application in the study of oil-bearing property of lithologic hydrocarbon reservoirs in the Dongying Sag," *Chinese Science Bulletin*, vol. 54, no. 23, pp. 4468–4478, 2009.
- [54] J. Guo, J. H. Zeng, G. Q. Song, Y. W. Zhang, X. J. Wang, and W. Meng, "Characteristics and Origin of Carbonate Cements of Shahejie Formation of Central Uplift Belt in Dongying Depression," *Earth Science*, vol. 39, pp. 565–576, 2014, [In Chinese with English abstract].
- [55] Y. W. Zhang, J. H. Zeng, X. Gao, and S. Y. Zhou, "Distribution characteristics and main controlling Factors of carbonate cements in the paleogene reservoirs in Dongying Depression," *Journal of Jilin University*, vol. 39, pp. 16–22, 2009, [In Chinese with English abstract].
- [56] H. O. Cookenboo and R. M. Bustin, "Pore water evolution in sandstones of the Groundhog Coalfield, northern Bowser Basin, British Columbia," *Sedimentary Geology*, vol. 123, no. 1–2, pp. 129–146, 1999.
- [57] N. R. Goultby, C. Sargent, P. Andras, and A. C. Aplin, "Compaction of diagenetically altered mudstones – Part 1: Mechanical and chemical contributions," *Marine and Petroleum Geology*, vol. 77, pp. 703–713, 2016.
- [58] J. Zhao, "Laws of mudstone compaction on the west slope of the Songliao Basin," *Oil and Gas Geology*, vol. 31, pp. 486–492, 2010, [In Chinese with English abstract].
- [59] Y. J. Han, S. He, G. Q. Song et al., "Origin of carbonate cements in the overpressured top seal and adjacent sandstones in Dongying depression," *Petroleum Processing Section*, vol. 33, pp. 385–393, 2012, [In Chinese with English abstract].
- [60] R. C. Surdam, L. J. Crossey, E. S. Hagen, and H. P. Heasler, "Organic-inorganic interactions and sandstone diagenesis," *The American Association of Petroleum Geologists Bulletin*, vol. 73, no. 1, pp. 1–23, 1989.
- [61] D. K. Zhong, X. M. Zhu, and J. G. Cai, "Vertical distribution of secondary pores in Paleogene sandstones in Zhanhua Depression," *Oil and Gas Geology*, vol. 24, pp. 286–290, 2003, [In Chinese with English abstract].
- [62] G. R. Davies and L. B. Smith Jr, "Structurally controlled hydrothermal dolomite reservoir facies: an overview," *AAPG Bulletin*, vol. 90, no. 11, pp. 1641–1690, 2006.
- [63] B. J. Wang, S. He, and J. Wang, "Hydrochemistry field origin and its coupling relationship with overpressure system , Dongying depression," *Journal of China University of Petroleum*, vol. 36, pp. 54–64, 2012, [In Chinese with English abstract].
- [64] R. Shiraki and T. L. Dunn, "Experimental study on water-rock interactions during CO<sub>2</sub> flooding in the Tensleep formation, Wyoming, USA," *Applied Geochemistry*, vol. 15, no. 3, pp. 265–279, 2000.
- [65] Y. Zhang, J. Zeng, Z. Qu, and J. Chen, "Development characteristics and genetic mechanism of authigenic kaolinite in

- sandstone reservoirs of the Dongying Sag, Bohai Bay Basin," *Oil and Gas Geology*, vol. 36, no. 1, pp. 73–79, 2015.
- [66] Q. P. Che and H. B. Sun, "Authigenic kaolinite origin analysis of paleogene sandstone reservoirs in Niuju area," *Journal of Changchun University of science and Technology*, vol. 25, pp. 306–309, 1995, [In Chinese with English abstract].
- [67] J. Y. Gu and B. He, "Study on triassic fin delta sedimentation and reservoir in Lunnan Area Tarim basin," *Acta Sedimentologica Sinica*, vol. 12, pp. 54–62, 1994, [In Chinese with English abstract].
- [68] X. Y. Zhao, "The conditions for formation of kaolinite subgroup in Tarim Basin," *Xinjiang Petroleum Geology*, vol. 24, pp. 419–423, 2003, [In Chinese with English abstract].
- [69] H. Y. Zou, F. Hao, G. D. Liu, and C. Sui, "Genesis of authigenic kaolinite and gas accumulation in Bashijiqike Fm sandstone in Kuqa thrust belt," *Oil and Gas Geology*, vol. 26, pp. 786–791, 2005, [In Chinese with English abstract].
- [70] J. Cao, Y. J. Zhang, H. u. WX et al., "Developing characteristics of kaolinite in central Junggar Basin and their effect on the reservoir quality," *Acta Mineralogica Sinica*, vol. 25, pp. 367–373, 2005, [In Chinese with English abstract].
- [71] X. Chen, J. Zhong, J. Yuan, K. Nie, and Y. Yang, "Development and formation of Paleogene kaolinite, Bonan subsag," *Shiyu Kantan Yu Kaifa/Petroleum Exploration and Development*, vol. 36, no. 4, pp. 456–462, 2009.
- [72] H. Irwin and A. Hurst, "Applications of geochemistry to sandstone reservoir studies," *Geological Society, London, Special Publications*, vol. 12, pp. 127–146, 1983.
- [73] W. J. Fu and W. B. Liu, "Study on the alteration of feldspar from clastic rock in Tarim Basin," *Acta Sedimentologica Sinica*, pp. 84–89, 1996, [In Chinese with English abstract].
- [74] J. H. Zeng, "Effect of fluid-rock interaction on porosity of reservoir rocks in Tertiary System, Dongying Sag," *Shiyu Xuebao/Acta Petrolei Sinica*, vol. 22, no. 4, p. 39, 2001.
- [75] J. Tóth, "Cross-formational gravity-flow of groundwater: A mechanism of the transport and accumulation of petroleum (the generalized hydraulic theory of petroleum migration)," in *Problems of petroleum migration*, I. Roberts and R. J. Cordell, Eds., pp. 121–167, AAPG Studies in Geology, USA, 1980.
- [76] M. Zha, "The dynamic models and numerical simulation of secondary petroleum migration in compactional flow basins an example from the Dong Ying Depression," *Acta Sedimentologica Sinica*, vol. 15, pp. 86–90, 1997, [In Chinese with English abstract].
- [77] K. Bjørlykke, "Relationships between depositional environments, burial history and rock properties. Some principal aspects of diagenetic process in sedimentary basins," *Sedimentary Geology*, vol. 301, pp. 1–14, 2014.
- [78] E. H. Oelkers and J. Schott, "Experimental study of anorthite dissolution and the relative mechanism of feldspar hydrolysis," *Geochimica et Cosmochimica Acta*, vol. 59, no. 24, pp. 5039–5053, 1995.
- [79] J. S. Jahren and P. Aagaard, "Compositional variations in diagenetic chlorites and illites, and relationships with formation-water chemistry," *Clay Minerals*, vol. 24, no. 2, pp. 157–170, 1989.
- [80] C. L. Liu, H. Q. Zhao, and P. X. Wang, "Water Chemistry of the Paleogene Dongying Lake: Evidence from Fossil Assemblages and Shell Isotopes," *Acta Geoscientia Sinica*, vol. 23, pp. 237–242, 2002, [In Chinese with English abstract].
- [81] Z. H. Chen, M. Zha, and Q. Jin, "Mineral elemental response to the evolution of terrestrial Brine faulted-basin: a case study in the Paleogene of Well Haoke-1, Dongying Sag," *Acta Sedimentologica Sinica*, vol. 26, pp. 925–932, 2008, [In Chinese with English abstract].
- [82] B. N. Popp and B. H. Wilkinson, "Holocene lacustrine ooids from Pyramid lake, Nevada," in *Coated Grains*, T. Peryt, Ed., pp. 141–153, Springer-Verlag, Berlin, Germany, 1983.
- [83] P. A. Sandberg, "New interpretations of Great Salt Lake ooids and of ancient non-skeletal carbonate mineralogy," *Sedimentology*, vol. 22, no. 4, pp. 497–537, 1975.

## Research Article

# Predicting Erosion-Induced Water Inrush of Karst Collapse Pillars Using Inverse Velocity Theory

Banghua Yao,<sup>1,2,3</sup> Zhongwei Chen<sup>2,4</sup> Jianping Wei,<sup>1,3</sup> Tianhang Bai,<sup>4</sup> and Shumin Liu<sup>1</sup>

<sup>1</sup>School of Safety Science and Engineering, Henan Polytechnic University, Jiaozuo, Henan 454000, China

<sup>2</sup>State Key Laboratory of Mining Disaster Prevention and Control Co-Founded by Shandong Province and the Ministry of Science and Technology, Shandong University of Science and Technology, Shandong 266590, China

<sup>3</sup>Collaborative Innovation Center of Coal Work Safety, Henan Province, Jiaozuo 454000, China

<sup>4</sup>School of Mechanical and Mining Engineering, The University of Queensland, Brisbane, QLD 4072, Australia

Correspondence should be addressed to Zhongwei Chen; zhongwei.chen@uq.edu.au

Received 28 July 2017; Accepted 16 November 2017; Published 28 January 2018

Academic Editor: Tianchiyi Yeh

Copyright © 2018 Banghua Yao et al. This is an open access article distributed under the Creative Commons Attribution License, which permits unrestricted use, distribution, and reproduction in any medium, provided the original work is properly cited.

Although the impact of Karst Collapse Pillars (KCPs) on water inrush has been widely recognized and studied, few have investigated the fluid-solid interaction, the particles migration inside KCPs, and the evolution feature of water inrush channels. Moreover, an effective approach to reliably predict the water inrush time has yet to be developed. In this work, a suite of fully coupled governing equations considering the processes of water flow, fracture erosion, and the change of rock permeability due to erosion were presented. The inverse velocity theory was then introduced to predict the water inrush time under different geological and flow conditions. The impact of four different controlling factors on the fracture geometry change, water flow, and inrush time was discussed in detail. The results showed that the inverse velocity theory was capable of predicting the occurrences of water inrush under different conditions, and the time of water inrush had a power relationship with the rock heterogeneity, water pressure, and initial particle concentration and an exponential relationship with the initial fracture apertures. The general approach developed in this work can be extended to other engineering applications such as the tunneling and tailing dam erosion.

## 1. Introduction

Groundwater inrush in coal mines has caused thousands of fatalities across many countries, such as the USA, Russia, Poland, Canada, Australia, Germany, Great Britain, India, and especially China [1]. As mining activities progress further deeper underground, there have been an increasing number of water outburst incidents occurring annually largely due to the impact of some key geological structures such as Karst Collapse Pillars (KCPs), as illustrated in Figure 1 [2, 3]. As a special geological structure, KCPs commonly exist at more than twenty coal fields in the northern China, such as Shanxi province (see Figure 2) [4].

The existence of the geological structure usually functions as an underground water flow path, thus posing a great threat to the mining production safety [3, 5]. According to the statistics, the most serious water disasters in Chinese coal mines were all directly caused by water inrushes associated

with the KCPs under the Permo-Carboniferous coal seams located at northern China [6, 7]. Take Fangezhuang coal mine of Kuiluan Group, for instance, during the accident in 1984, the maximum water inflow associated with KCPs reached  $2,053 \text{ m}^3/\text{min}$ , resulting in the mine and other three neighboring mines submerged in a very short time, and caused a direct capital loss of around US\$90 million [8]. Thus, better understanding of the mechanism of water inrush has both economic and safety benefits.

Significant number of investigations have been performed to explore water inrush mechanism of KCPs using single or combined methods of theoretical analysis and numerical simulation as well as experimental studies. For instance, based on the elastic thick plate theory, Tang et al. [4] developed a mechanical model for water inrush of KCPs. Bai et al. [9] established a mechanical model-plug model, which was used to describe the behavior of water seepage flow in coal-seam-floor containing KCPs. Furthermore, the variable

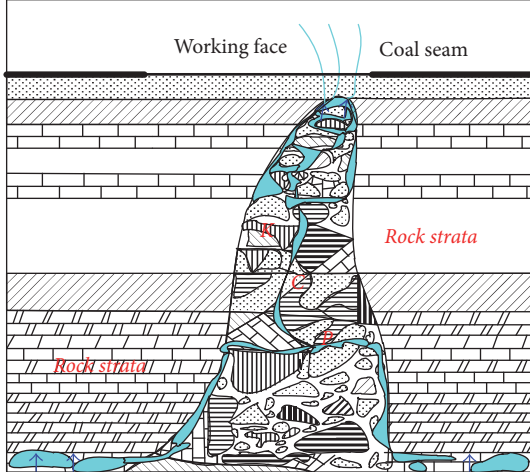


FIGURE 1: Illustration of a Karst Collapse Pillar: front view of a typical cone shaped KCP (not to scale) [23] and different shapes of rock layers represent different types of rocks.

mass dynamics and nonlinear dynamics were introduced, and the seepage properties of KCPs associated with particles migration were investigated using numerical simulation [3]. Ma and Bai [10] numerically studied the impacts of mining-induced damage on KCPs and the surrounding rocks and on the formation of the fracture zone and analyzed mining-induced KCP groundwater inrush risk. This work was later extended to study the effect of coal mining operations on KCPs related groundwater inrush using FLAC<sup>3D</sup>, and the shear stress, damage zone, and their effects on seepage field development were also discussed [11]. Yao [12] experimentally studied the evolution of the crushed rock mass seepage properties under different particle sizes and stresses and analyzed particle migration feature and the KCPs water inrush mechanism. Moreover, there are also some experimental studies focused on the permeability change of the KCPs to investigate water inrush mechanisms [13–15].

Recent studies on the water inrush mechanism of KCPs have consistently revealed that complex interactions exist between the evolution of fractures and porosity in solids, water transport, and rock solid particles migration, which accompanies the erosion phenomenon [3, 12]. Significant progress on the understanding of this complex process has been made. For example, the reaction of aqueous solutions mineral components and its impact on water flow were investigated, and a model for porosity change was established [16]. Vardoulakis et al. [17] studied the piping and surface erosion effects based on mass balance, particles migration, and Darcy's law. The dissolution of fracture surfaces due to water-rock interactions with variable fracture apertures over time was also studied, and a depth-averaged model of fracture flow and reactive transport that explicitly calculated local dissolution-induced alterations in fracture apertures were presented [18]. Habib et al. [19] numerically investigated the erosion rate correlations of a pipe protruding from an abrupt pipe contraction problem.

Despite the significant progress in understanding KCPs water inrush mechanism and water prevention technology over the past several decades [20–22], most investigations were carried out with respect to structure failure, and few have investigated this issue by integrating the solid-fluid interaction and particles migration due to erosion. Water inflow rate, as probably the only direct measuring data in the field, has yet to be directly used in the literature to predict the precise time of water inrush. An effective method to predict water inrush does not appear to be available neither. In this work, a set of fully coupled governing equations for KCPs water inrush will be developed by incorporating the fractures and porosity evolution for KCPs, particles migration, and water seepage process. The governing equations will then be implemented into COMSOL Multiphysics software. The heterogeneity of rocks in KCPs will be determined using the Weibull distribution, and the parameters including porosity, seepage, particle concentration, and water inflow as well as seepage channels evolution law will be obtained accordingly. This numerical model will be then used to investigate the water flow characteristics with erosion. Based on the inverse velocity theory, the corresponding water inrush times for different flow conditions will also be discussed in detail.

## 2. Development of a Fully Coupled Theoretical Model

**2.1. Selection of Microstructure Model of KCPs.** A KCP typically consists of three parts: solid rock matrix, fluids, and infilling particles. The intact rock blocks form a rock mass, which is filled with fluids, for example, water, and infilling materials such as solid particles (Figure 3). As the permeability of rock blocks is generally very low, the interrock fractures provide the main passages for water flow. This structure matches the characteristics of the dual porosity model, where the rocks are considered as consisting of matrixes and fractures. A numbers of different dual porosity models have been developed including the Warren-Root, Kazemi et al., and de Swaan models [24–26], but the Warren-Root model, as shown in Figure 4, was widely accepted as a proper model to represent such rock structure. As such, in this work, the Warren-Root model is selected to examine the processes of particle migration and the evolution of the fractures aperture and porosity.

### 2.2. Governing Equations

**2.2.1. Assumptions.** In order to establish a fully coupled theoretical model that integrates particles migration, seepage, and fracture and porosity evolution in KCPs under erosion effects, the following assumptions have been made:

- (1) The fluid and particles in KCPs are incompressible.
- (2) The suspended particles share the velocity field with the fluid.
- (3) As the internal structure of KCPs is generally very loose and the rock mass surrounding the KCPs is

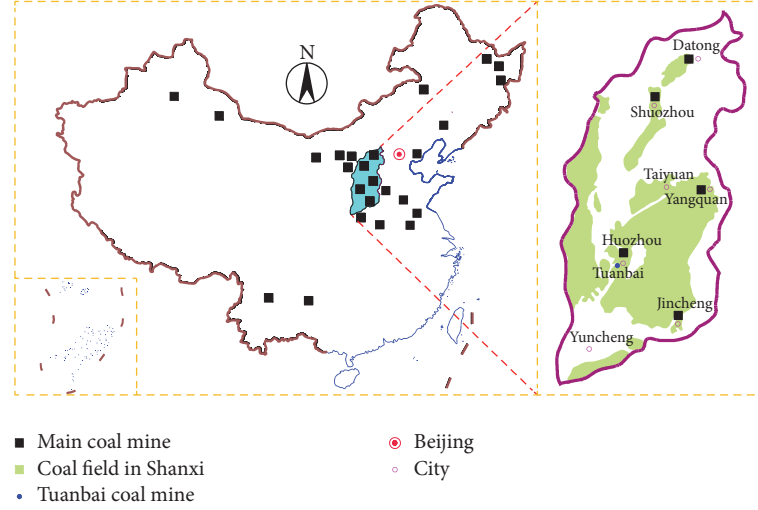


FIGURE 2: The distribution of major coal mines in China and the coal fields in Shanxi province.

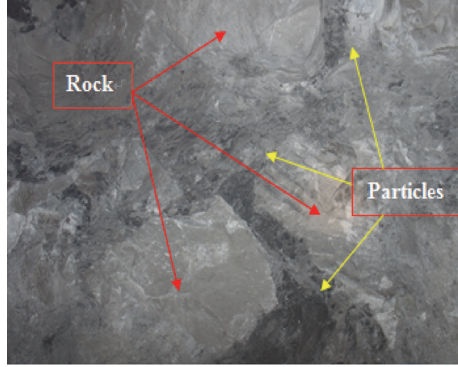


FIGURE 3: Rock and infilling material (particles) in a KCP.

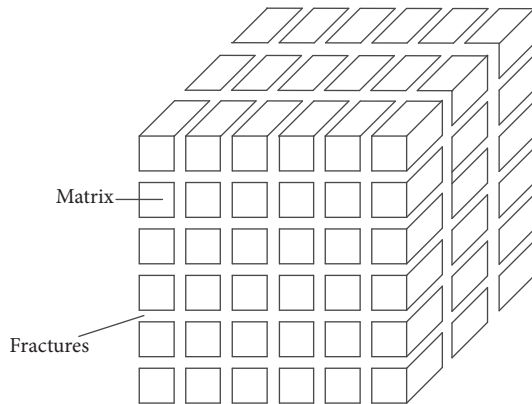


FIGURE 4: Sketch of the Warren-Root Model [24].

- generally competent, the impact of the change in the effective stress on KCP's permeability is insignificant.
- (4) The impact of erosion on the permeability change is in proportion to the change of particle concentration in the fluid.

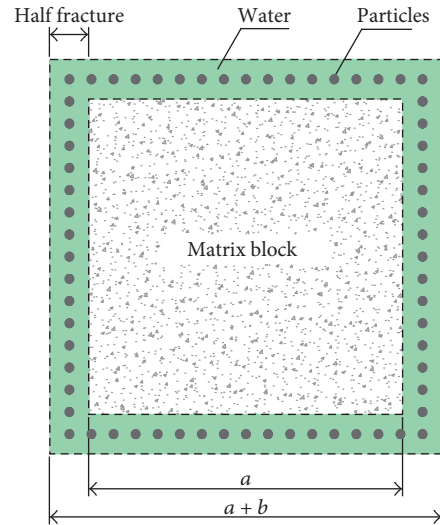


FIGURE 5: Sketch of a representative element of a typical KCP.

**2.2.2. Definition.** Based on the aforementioned assumptions, a representative element for a typical KCP microstructure is shown in Figure 5. The length  $L$  (m) and volume  $V$  ( $\text{m}^3$ ) of the element are expressed as

$$\begin{aligned} L &= a + b, \\ V &= (a + b)^3, \end{aligned} \quad (1)$$

where  $a$  (m) is the length of the matrix and  $b$  (m) is the aperture of the fracture.

The total voidage  $\varphi$  (%) of an element is written as [28]

$$\varphi = \frac{(a + b)^3 - a^3}{(a + b)^3} + \phi \cong \frac{3b}{a} + \phi, \quad (2)$$

where  $\phi$  (%) is the matrix porosity. It should be noted that  $b \ll a$ .

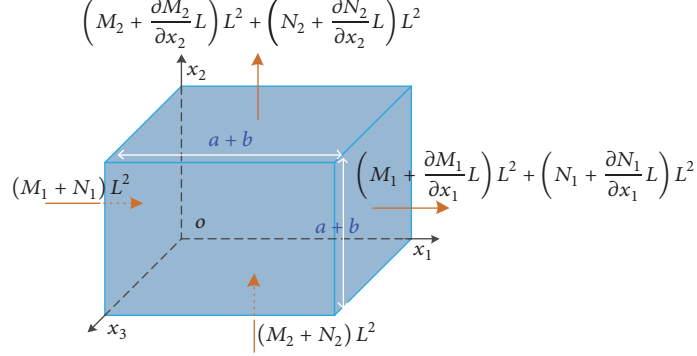


FIGURE 6: Illustration of a three-dimensional characteristic element in a KCP.  $M_i$  and  $N_i$  are mass change of solids due to convection and diffusion, respectively, defined as  $M_i = C\rho_s q_i$ ,  $N_i = -D(\partial(C\varphi\rho_s)/\partial x_i)$ .

**2.2.3. Mass Conservation Equations for Particles.** In order to study the migration characteristics of the infilling particles, the dynamic mass conservation equations for particles were calculated based on a three-dimensional representative element, as illustrated in Figure 6.

Infilling particles migration inside a representative element under erosion effects is affected by both convection and processes. The average seepage velocity of an element can be defined as  $\vec{q}_i$  (m/s). For the convection and diffusion process, in the direction of  $x_i$  ( $i = 1, 2, 3$ ), the mass losses of particles flowing out of the element in a unit time can be calculated by (3) and (4), respectively:

$$\frac{\partial(C\rho_s q_i)}{\partial x_i} V, \quad (3)$$

$$-\frac{\partial}{\partial x_i} \left[ D \frac{\partial(C\varphi\rho_s)}{\partial x_i} \right] V, \quad (4)$$

where  $C$  (%) is the particle concentration (i.e., particle saturation),  $\rho_s$  (kg/m<sup>3</sup>) denotes the density of solid particles, and  $D$  (m<sup>2</sup>/s) illustrates the particles diffusion coefficient.

In the direction of  $x_i$ , the mass flowing into the element due to the convection-diffusion should be expressed as

$$\frac{\partial M_i}{\partial x_i} V + \frac{\partial N_i}{\partial x_i} V \quad (i = 1, 2, 3). \quad (5)$$

For the element, the total mass flowing can be expressed as the summation of the three directions:

$$\sum_{i=1}^3 \left( \frac{\partial M_i}{\partial x_i} V + \frac{\partial N_i}{\partial x_i} V \right). \quad (6)$$

Under the effects of erosion, the mass loss of the element in a unit time can be summarized as

$$-\frac{\partial}{\partial t} (C\varphi\rho_s) V + \dot{m} V, \quad (7)$$

where  $\dot{m}$  (kg/m<sup>3</sup>/s) is the particle mass that migrates into the fluid from a unit element in a unit time and  $\dot{m}$  is written as

$$\dot{m} = \frac{\partial\varphi}{\partial t} \rho_s. \quad (8)$$

According to the mass conservation law, for the unit element, (6) and (7) are equivalent, giving the mass conservation equation for particles as

$$-\frac{\partial}{\partial t} (C\varphi\rho_s) V + \dot{m} V = \sum_{i=1}^3 \left( \frac{\partial M_i}{\partial x_i} V + \frac{\partial N_i}{\partial x_i} V \right). \quad (9)$$

Substituting (2) into (9) yields

$$\begin{aligned} & \left[ \frac{3}{a} \frac{\partial(bC)}{\partial t} + \frac{\partial(C\phi)}{\partial t} \right] + \nabla \cdot (C\vec{q}) - \nabla \\ & \cdot \left\{ D \nabla \cdot \left[ C \left( \frac{3b}{a} + \phi \right) \right] \right\} = \left( \frac{3}{a} \frac{\partial b}{\partial t} + \frac{\partial \phi}{\partial t} \right). \end{aligned} \quad (10)$$

As particle sizes are normally several orders of magnitude smaller than the fracture aperture, the diffusion effect can be neglected. Equation (10) can therefore be simplified into

$$\left[ \frac{3}{a} \frac{\partial(bC)}{\partial t} + \frac{\partial(C\phi)}{\partial t} \right] + \nabla \cdot (C\vec{q}) = \left( \frac{3}{a} \frac{\partial b}{\partial t} + \frac{\partial \phi}{\partial t} \right). \quad (11)$$

**2.2.4. Water Mass Conservation Equations.** For the water flow, the mass flowing out of the element in the direction of  $x_i$  ( $i = 1, 2, 3$ ) can be expressed as

$$\frac{\partial[(1-C)\rho_f q_i]}{\partial x_i} V \quad (i = 1, 2, 3), \quad (12)$$

where  $\rho_f$  (kg/m<sup>3</sup>) denotes the density of the fluid. The mass loss of the fluid in the element in a unit time can be calculated as

$$-\frac{\partial}{\partial t} [(1-C)\varphi\rho_f] V. \quad (13)$$

By combining (2), (3), (12), and (13), the mass conservation equation for water flow can be derived as

$$\begin{aligned} & \left\{ \frac{3}{a} \frac{\partial[b(1-C)]}{\partial t} + \frac{\partial[(1-C)\phi]}{\partial t} \right\} + \nabla \cdot [(1-C)\vec{q}] \\ & = 0. \end{aligned} \quad (14)$$

**2.2.5. Evolution of the Fracture Aperture and Porosity.** Rock porosity plays an important role in determining rock permeability, so full understanding of its evolution is essential to study the seepage characteristics of KCPs. Sakthivadivel and Irmay [29] investigated the erosion problem for porous media by using both experimental and theoretical methods. Vardoulakis et al. [17] summarized the studies on porous media erosion, and according to that study, the evolution of fracture aperture and permeability was affected by the porosity and particles concentration as well as the seepage velocity. The following equations have been developed to determine the evolution of fracture aperture and porosity [17]:

$$\begin{aligned}\frac{\partial b}{\partial t} &= \lambda_1 \rho_s (b_{\max} - b) C |q|, \\ \frac{\partial \phi}{\partial t} &= \lambda_2 \rho_s (\phi_{\max} - \phi) C |q|,\end{aligned}\quad (15)$$

where  $\lambda_1$  and  $\lambda_2$  are constant,  $|q| = \sqrt{q_1^2 + q_2^2 + q_3^2}$  is the absolute value of the seepage velocity (m/s), and  $b_{\max}$  and  $\phi_{\max}$  illustrate the maximum value that fracture aperture and porosity can reach under fluid erosion.

Equations (15) indicate that the porosity evolution is proportional to the particle concentration, as well as the seepage velocity.

**2.2.6. Water Seepage.** Fluid transport in porous media is normally described by Darcy's law, which is derived (a) from balance of momentum for the fluid phase and (b) from a constitutive equation for the fluid-solid interaction force (i.e., the seepage force) [30]. In general, the balance of linear momentum for the fluid phase has the form [31]

$$-\frac{\partial p}{\partial x_i} = -\frac{\eta}{k} q_i + \rho_f \frac{\partial}{\partial t} \left( \frac{q_i}{\varphi} \right), \quad (16)$$

where  $p$  denotes the pore pressure (Pa),  $\eta$  is the dynamic viscosity of the fluid (Pa·s), and  $k$  illustrates the permeability of the volumetric element ( $\text{m}^2$ ). For this study, the flow velocity is relatively low; thereby, the acceleration term can be neglected, giving

$$\vec{q} = -\frac{k}{\eta} (\nabla p + \rho_f g \nabla z), \quad (17)$$

where  $\vec{q}$  is the Darcy velocity (m/s) and  $\nabla z$  is the unit vector in the direction of gravity. For fractured porous media,  $k$  is the sum of fracture permeability and porosity permeability ( $\text{m}^2$ ), which can be expressed as [32]

$$k = k_m + k_f = k_{m0} \left( \frac{\phi_m}{\phi_{m0}} \right)^3 \left( \frac{1 - \phi_{m0}}{1 - \phi_m} \right)^2 + \frac{b^3}{12a}, \quad (18)$$

in which  $k_m = k_{m0}(\phi_m/\phi_{m0})^3((1 - \phi_{m0})/(1 - \phi_m))^2$  and  $k_f = b^3/12a$  represent the porosity permeability and fracture permeability, respectively.

Equations (2), (11), (14), (15), and (17) together with (18) compose the coupled processes of water transport of KCPs

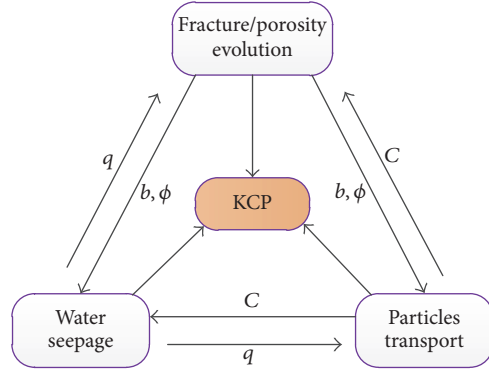


FIGURE 7: Coupling process among each physics.

under erosion effects, as illustrated in Figure 7. The above governing equations will be implemented into COMSOL Multiphysics next to understand water inrush mechanism in KCPs, to evaluate water inrush risks, and to predict water inrush time under different rock and flow conditions. There are six unknowns with equations, so the set of governing equations can provide a unique solution.

In petroleum engineering, generally there is a critical velocity associated with sand production in oil and gas reservoirs. However, for the particle movements in KCPs, the critical velocity was not considered because (1) the sizes of the infilling particles are significantly smaller than the fracture apertures ( $\mu\text{m}$  versus mm); (2) the movement of the eroded materials does not require a critical pressure gradient (or flow velocity) for most KCP infilling materials are soluble to water forming diluted solution, and (3) the fluid flow inside KCPs is generally much greater than the critical velocity of around 0–7.7 mm/s for the particle size of 1–10  $\mu\text{m}$  [33, 34].

**2.3. Inverse Velocity Theory.** The inverse velocity theory was originally proposed by Fukuzono [35] based on experimental studies. This theory was initially used to predict the failure time of a solid material that experiences slow continuous deformation (i.e., creep). When the reciprocal of the deformation velocity (i.e., the inverse velocity) is plotted as a function of time, its value approaches zero as the velocity increases asymptotically towards failure. The trend line of the inverse velocity intersects with the abscissa which represents time, and the intersectional point can predict the time of failure. There are three types of trend line, namely, concave, linear, and convex, as shown in Figure 8.

The following equation is used to define the envelope:

$$V^{-1} = [A(\alpha - 1)]^{1/(\alpha-1)} (t_f - t)^{1/(\alpha-1)}, \quad (19)$$

where  $V$  is the inverse velocity (m/s),  $A$  and  $\alpha$  are constants,  $t_f$  is the time of failure, and  $t$  is the time of cutoff or the most recent time of the monitoring data. The inverse velocity curve is concave when  $\alpha < 2$ , and it is linear when  $\alpha = 2$ , while it is convex when  $\alpha > 2$ . Fukuzono [35] indicated that a linear fit could provide a reasonable prediction of failure time.

The inverse velocity theory has been successfully used in soils, rocks, and other materials and has been proved to be

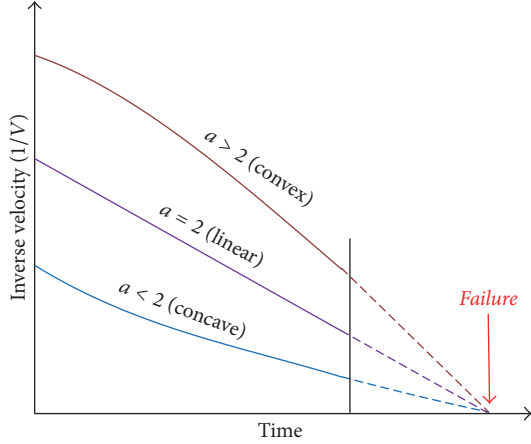


FIGURE 8: Inverse velocity trend lines to predict the time of failure [27].

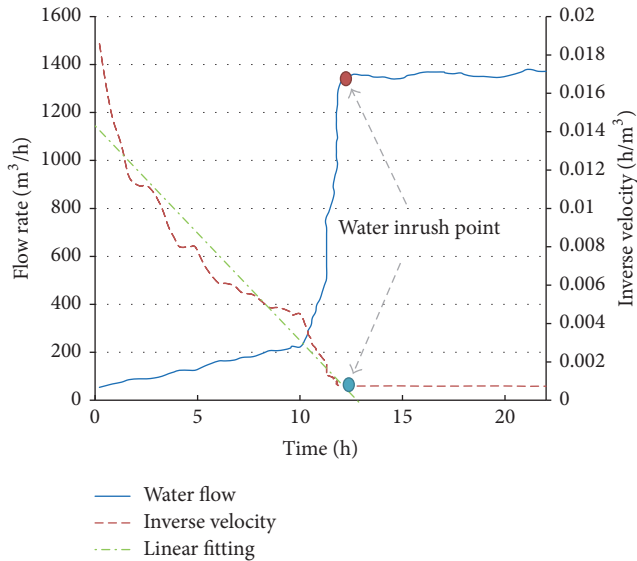


FIGURE 9: Verification of the inverse velocity theory in predicting water inrush.

reliable in estimating the failure time using the linear fitting curve [36, 37]. Therefore, in this work, this theory (i.e., inverse fluid flow velocity) is adopted as the first attempt to predict water inrush in KCPs.

In order to verify the applicability of theory to water inrush, the field monitoring data from Yao et al. [38] and Bai [39] was used, and the comparison of inrush time between real data and predicted time using inverse velocity theory was conducted. The results were plotted in Figure 9. It can be seen that the predicted inrush time matches the actual water inrush time very well, which proves that this theory can be used to predict water inrush for KCPs.

### 3. Numerical Model Implementation

**3.1. Background of the Coal Mine.** In this section, a case study was conducted based on the hydrogeological conditions of

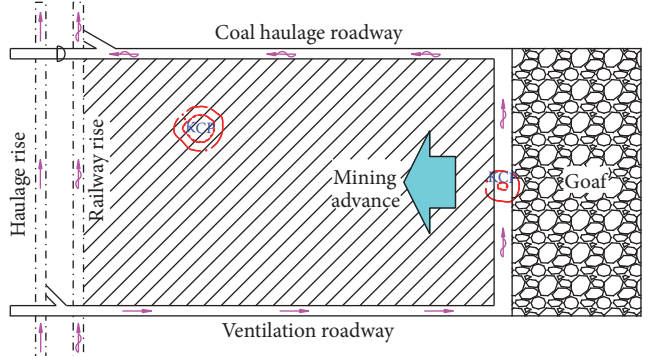


FIGURE 10: Illustration of number 10-106 longwall panel and KCP in Tuanbai coal mine of Shanxi province, China.

the Tuanbai Coal mine, which is affiliated with Huozhou Coal Electricity Group of China. The mine is located in Tuanbai County, Linfen City, Shanxi Province, as marked in blue in Figure 2. The mining operation is current extracting number 10 coal seam at approximately 300 m depth. To date, 97 KCPs have been found during the mining operations at this seam. These KCPs included rock blocks of different sizes, and in most cases, mud infillings and sizes of KCPs varied from tens to hundreds of meters. In addition, some had low level of compaction and cementation and relatively high infiltration capabilities.

Since the distance between number 10 coal seam and the Ordovician limestone was only about 35 m (as illustrated in Figure 13(a)), the mining operation is being carried out under pressure from the Ordovician limestone water of the floor. The water pressure was found to be about 2 MPa. This mine has suffered a number of water inrush accidents associated with the KCPs. For instance, one accident occurred on the belt roadway of the first longwall panel in 2007, with a water flow rate of nearly 470  $m^3/h$ . In addition, there were a number of water inrush accidents on longwall panels such as 10-106 as shown in Figure 10, 10-112 and 10-114 at a rate of range from 40  $m^3/h$  to 150  $m^3/h$  in 2010, resulting in the submergence of the longwall panels. Later investigation of these incidents revealed that all were directly caused by the KCPs, which acted as water channels, with the confined water serving as the source.

**3.2. Characterisation of the Infilling Materials.** In KCPs, the composition of the infillings and their particle size distribution (PSD) have been found to be highly relevant to the migration of the particles. For this reason, two samples (i.e., sample 1 and sample 2) were collected from the Tuanbai coal mine, and the X-ray diffraction phase analysis (composition analysis) was carried out on the infilling materials of the KCPs as well as the PSD characteristics. The results are shown in Figures 11 and 12.

The composition analysis (as shown in Figure 11) indicated that the infilling materials mainly included kaolinites, quartz, illite, smectite mixed layers, small quantities of feldspars, montmorillonites, chlorites, calcites, siderites, and

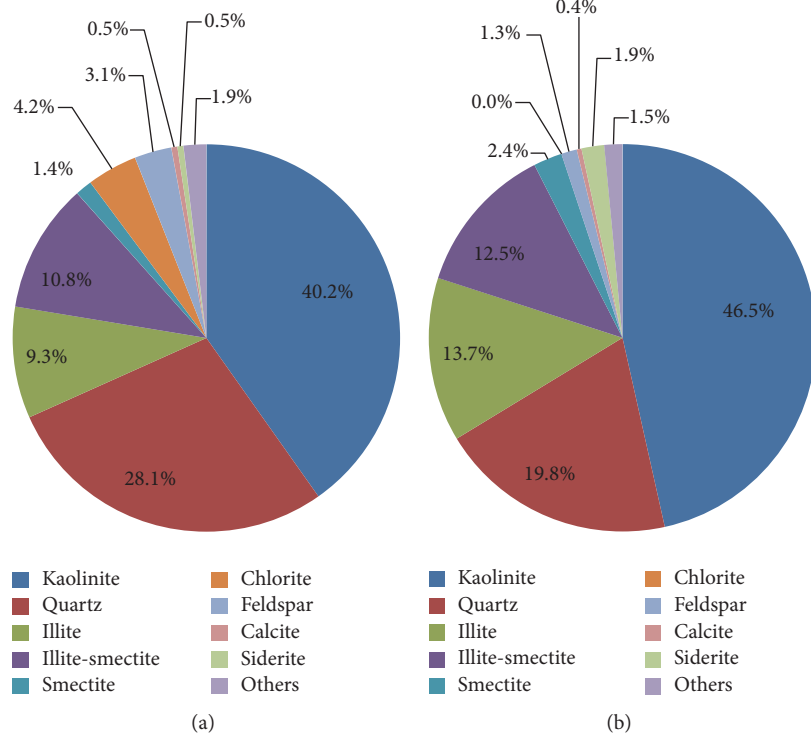


FIGURE 11: (a) Mineral components of infilling materials for Sample 1; and (b) mineral components of infilling materials for Sample 2.

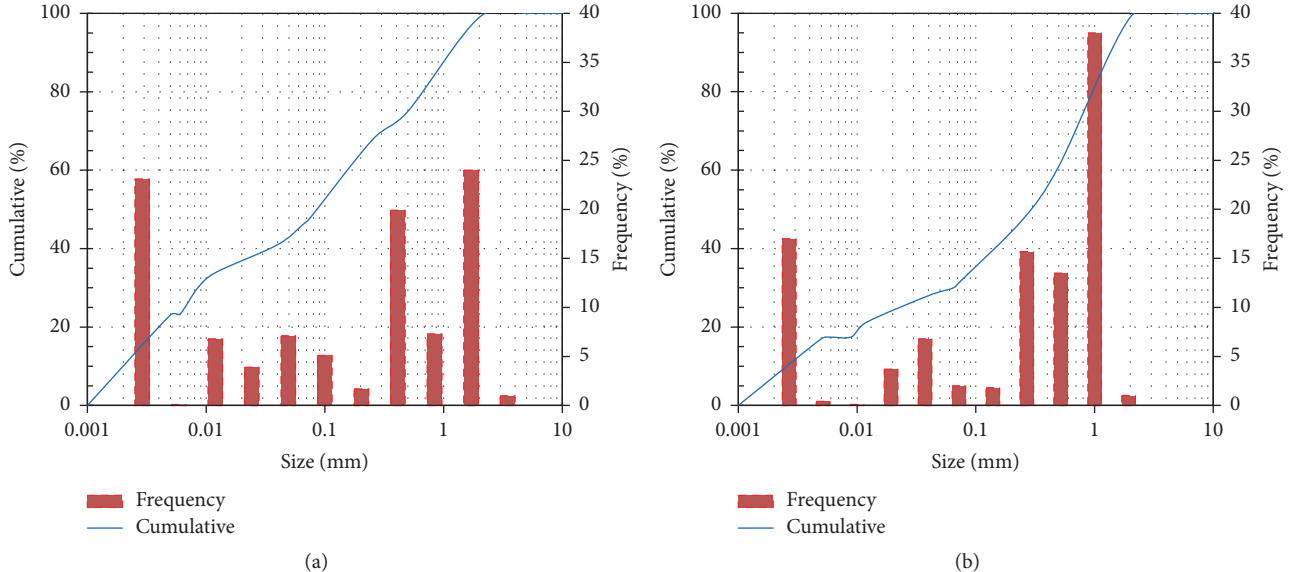


FIGURE 12: Particle size distribution (PSD) of infilling materials: (a) Sample 1; (b) Sample 2.

other mineral compositions. The PSD results (Figure 12) showed that the particle sizes varied from  $1\text{ }\mu\text{m}$  to a few mm for both Samples 1 and 2, with majority spanning from  $10\text{ }\mu\text{m}$  to  $1\text{ mm}$ . This could be a result of long-term weathering, but the weak and unfavorable rock properties observed in the field indicate that KCPs are very fractured and loose in structure, with low strength, high permeability, being prone to water erosion, and the water inrush risks.

**3.3. Numerical Model Setup.** Although diverse in geometry, KCPs are usually presented similarly to a dome shape [9]. Each of these approximates a 3D axisymmetric model, which can be simplified as a 2D symmetrical model.

In this work, according to the lithology of the mine, the bottom diameter, top diameter, and height are 15 m, 10 m, and 20 m, respectively (as shown in Figure 13). The pressure at the water inlet on the lower boundary was 2.0 MPa and the

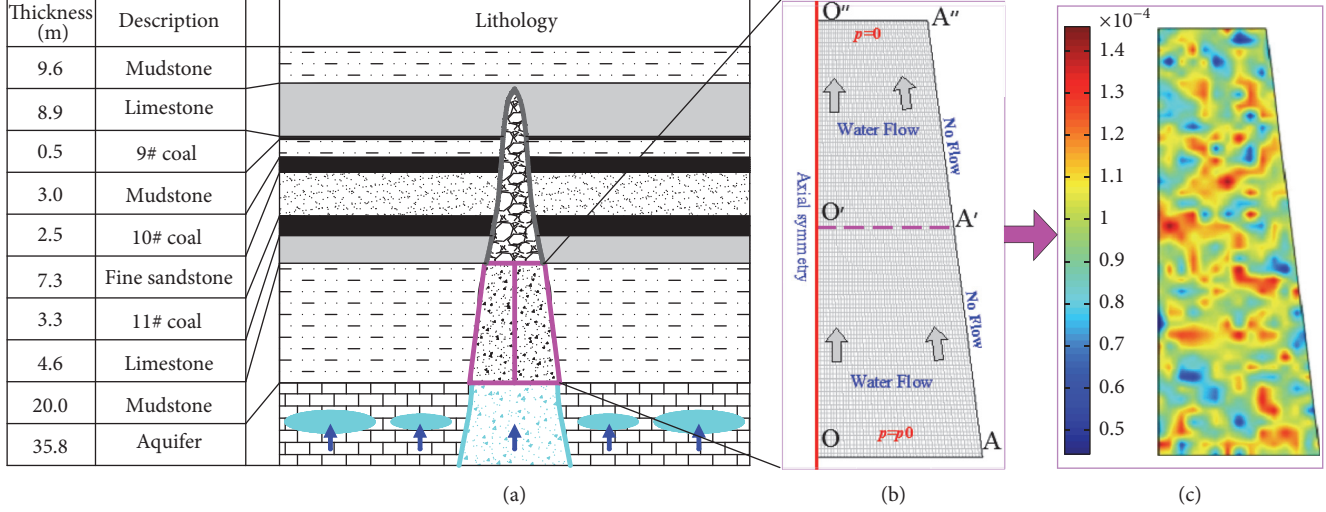


FIGURE 13: Model geometry and setup: (a) illustration of KCP and rock strata; (b) 2D simulation model; and (c) distribution of aperture opening based on Weibull function.

pressure at the water outlet on the top was 0.1 MPa; initial water pressure in the model was 0.1 MPa; initial particle volume concentration was 0.01; initial average fracture aperture  $\bar{b}_0$  was 0.1 mm; and initial porosity  $\phi_0$  was 10%. The main parameters of the model were all determined according to the relevant references [3, 12], in which the studies were conducted on the same seam. Other used parameters are listed in Table 1. The model was divided into 5,000 grids using mapped mesh method embedded in the COMSOL software. The shape of the grids is rectangular.

Heterogeneity has been determined to be a prominent feature of rock. There are currently various approaches to obtaining the characteristics of the heterogeneous distribution of rock materials. For example, digital core techniques and mathematical statistics methods have both been utilized. Previous studies have shown that the heterogeneity of rock can be described by the Weibull distribution [40–42]. Thus, the Weibull distribution was selected in this study due to its effectiveness and great simplicity to obtain the heterogeneous distribution of fracture apertures of the KCPs. The distribution probability density equation was as follows:

$$f(b) = \frac{m}{b_0} \left( \frac{b}{b_0} \right)^{m-1} \exp \left[ -\left( \frac{b}{b_0} \right)^m \right], \quad (20)$$

where  $b$  indicates the fracture aperture,  $b_0$  denotes the initial fracture aperture, and  $m$  is the uniformity index. The larger  $m$  represents, the higher level of uniformity. The fracture aperture distribution obtained by the numerical generation method is shown in Figure 13(c).

Based on this model geometry, (9), (11), (14), (15), (17), and (18) will be solved simultaneously to investigate the dynamic change of water flow behaviors and the associated inrush risk under different flow conditions.

## 4. Results and Analysis

In order to analyze the characteristics of seepage at different times, in this study, six different moments were selected (i.e.,  $14 \times 10^3$ ,  $15 \times 10^3$ ,  $16 \times 10^3$ ,  $17 \times 10^3$ ,  $17.5 \times 10^3$ , and  $18 \times 10^3$  s). The specific results will be discussed below.

**4.1. Distribution of the Fracture Apertures.** Figure 14 illustrates the spatial changes of the fracture apertures at different times. Figure 15 shows the evolution of fracture apertures along O-O'' and O'-A' lines as marked in Figure 13(b), and the average fracture aperture-time curve was plotted in Figure 16. The results show the following:

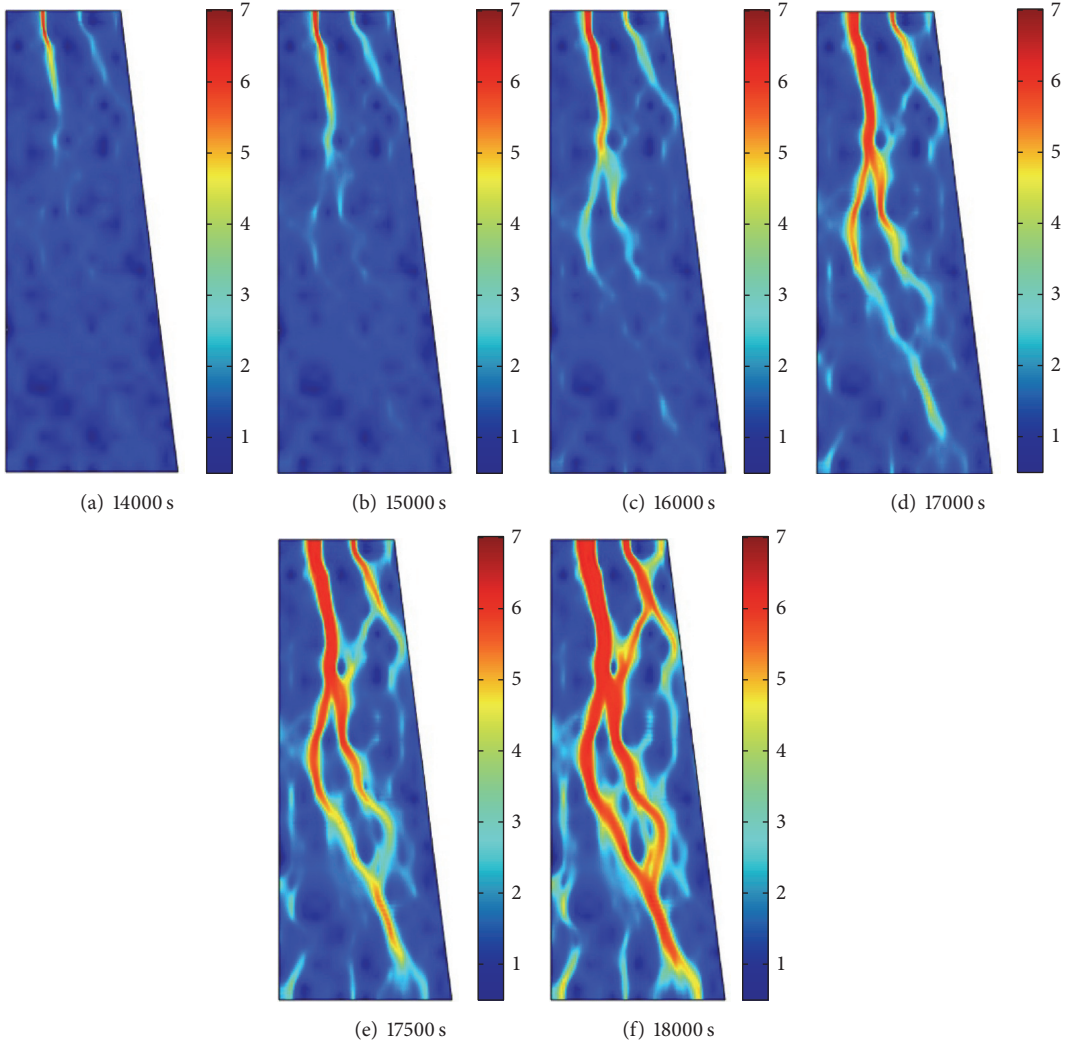
(1) The fracture aperture gradually increases under the effects of the erosion. However, the increase rate is higher in the upper part of the model than in the lower part. This is likely because the upper outlet boundary is narrower than the bottom inlet boundary, giving rise to higher flow velocity. Such higher velocity causes more significant erosion, and consequently the fracture aperture change is faster.

(2) As the infiltration continues, the average fracture aperture increases by approximately 200%, from 0.1 mm to nearly 0.3 mm (Figure 16). At the initial stage, the fracture is subject to random distribution, with minor difference in the apertures. However, the variation diverges under the effects of the erosion. The fractures with smaller initial apertures become slowly enlarged by approximately 20%, while those with larger apertures continuously increase by more than 200%. As the fractures gradually dilate and interconnect with each other, a number of dominant seepage channels are formed, as illustrated in Figure 14(f).

**4.2. Distribution of Water Seepage Velocity.** The seepage velocities (i.e., Darcy velocity) in the model domain and along O-O'' and O'-A' lines were shown in Figures 17 and

TABLE 1: Input parameters for the numerical simulation.

$\rho_s/(\text{kg/m}^3)$	$\eta/(\text{Pa}\cdot\text{s})$	$k_{m0}/(\text{m}^2)$	$\phi_0$	$\bar{b}_0/(\text{m})$	$a$	$\lambda_1/(\text{m}^{-1})$	$\lambda_2/(\text{m}^{-1})$	$m$	$C_0$
2000	$10^{-3}$	$10^{-12}$	0.1	0.0001	0.01	0.01	0.01	6	0.01

FIGURE 14: The spatial distribution of aperture  $b$  ( $10^{-4}$  m) at different times.

18, respectively. The predicted failure time using the inverse velocity theory was plotted in Figure 19. The key observations include the following:

(1) As shown in Figure 17, the changes in the flow velocity are consistent with the distribution of the fractures (Figure 14), and more fracture aperture changes are observed at the locations where higher seepage velocities take place. As shown in Figure 18, at  $1.4 \times 10^4$  s, the minimum and maximum seepage velocities were approximately  $3.5 \times 10^{-6}$  m/s and  $4.11 \times 10^{-5}$  m/s. At  $1.8 \times 10^4$  s, these two figures increased by 20% and 200%, to  $4.2 \times 10^{-6}$  m/s and  $1.25 \times 10^{-3}$  m/s, respectively.

(2) There was a continuous increase in flow rate at the outlet, from approximately  $3.7 \text{ m}^3/\text{h}$  initially, to approximately  $100 \text{ m}^3/\text{h}$  at  $1.8 \times 10^4$  s, increased by nearly 30 times. However, its increase showed a nonlinear trend, likely due to the fact

that the increase rate was relatively slow in the initial stage but accelerated gradually until the water inrush occurred. Figure 19 was generated according to the inverse velocity theory, and the results showed that the water inrush would occur at  $1.85 \times 10^4$  s for this particular flow condition. The trend has been reflected by the change in flow velocity shown in Figure 17. The figure shows that shortly before the inrush, the flow channels rapidly connected together and formed a main channel, resulting in a surge in water flow.

**4.3. Distribution of the Particle Concentrations.** Particle concentration is directly related to the erosion rate. Higher particle concentration indicates more severe erosion, which is more likely to result in greater fracture aperture change.

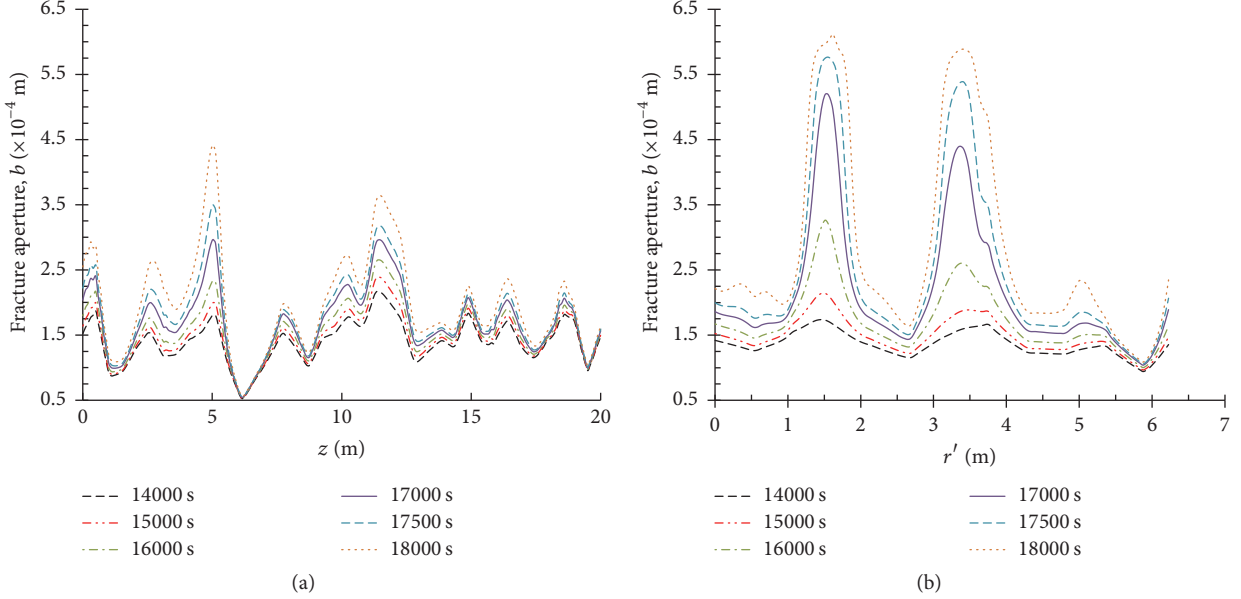


FIGURE 15: Evolution of fracture aperture along the lines of (a)  $O-O''$  axis and (b)  $O'-A'$  axis.

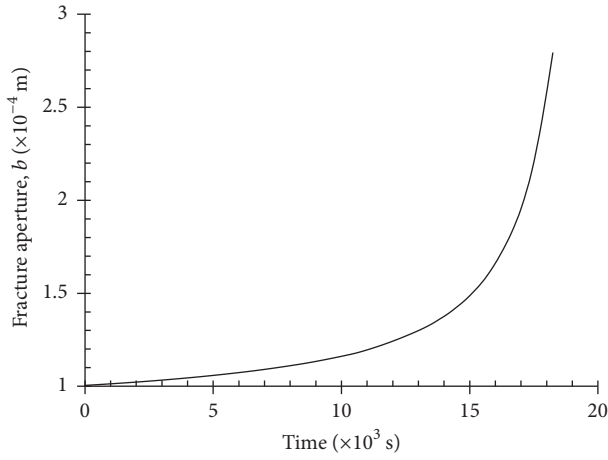


FIGURE 16: Change of average fracture aperture with time.

Figure 20 shows the evolution of the average particle concentration along  $O-O''$  and  $O'-A'$  lines. The average particle concentration and particle loss rate was plotted in Figure 21.

Figure 20 plots the spatial distribution of the particle concentrations for the whole model at different times. Results show that the particle concentration gradually increases from the bottom upwards. This is because, under the effects of the erosion, increasing amount of particles migrated into the water and gradually moved upwards through the fractures and pores. This is consistent with the change in the particle concentration at different locations, as shown in Figure 21.

Results in Figure 22 are well in line with the results shown in Figure 18. For example, at the beginning, the particle loss rate is relatively low; however, the rate constantly increases over time and culminates at the inrush. This is due to the fact

that, along with the increases in the seepage velocities, the erosion effects on the solid particles are constantly intensified, which results in frequent migration and substantial particle loss.

**4.4. Sensitivity Analyses.** The outburst processes were affected or controlled by various factors, including the spatial heterogeneity of lithology of the KCPs, water pressure, absolute aperture, and distribution of the fractures, distribution law of concentration of the karst particles, and their sensitivity to water erosion. Based on the newly developed coupling model, this work further examined the water and particle migration characteristics in the KCPs under different hydrological and geological conditions, as well as the variations in the inrush occurrences. The scenarios to be studied are summarized in Table 2.

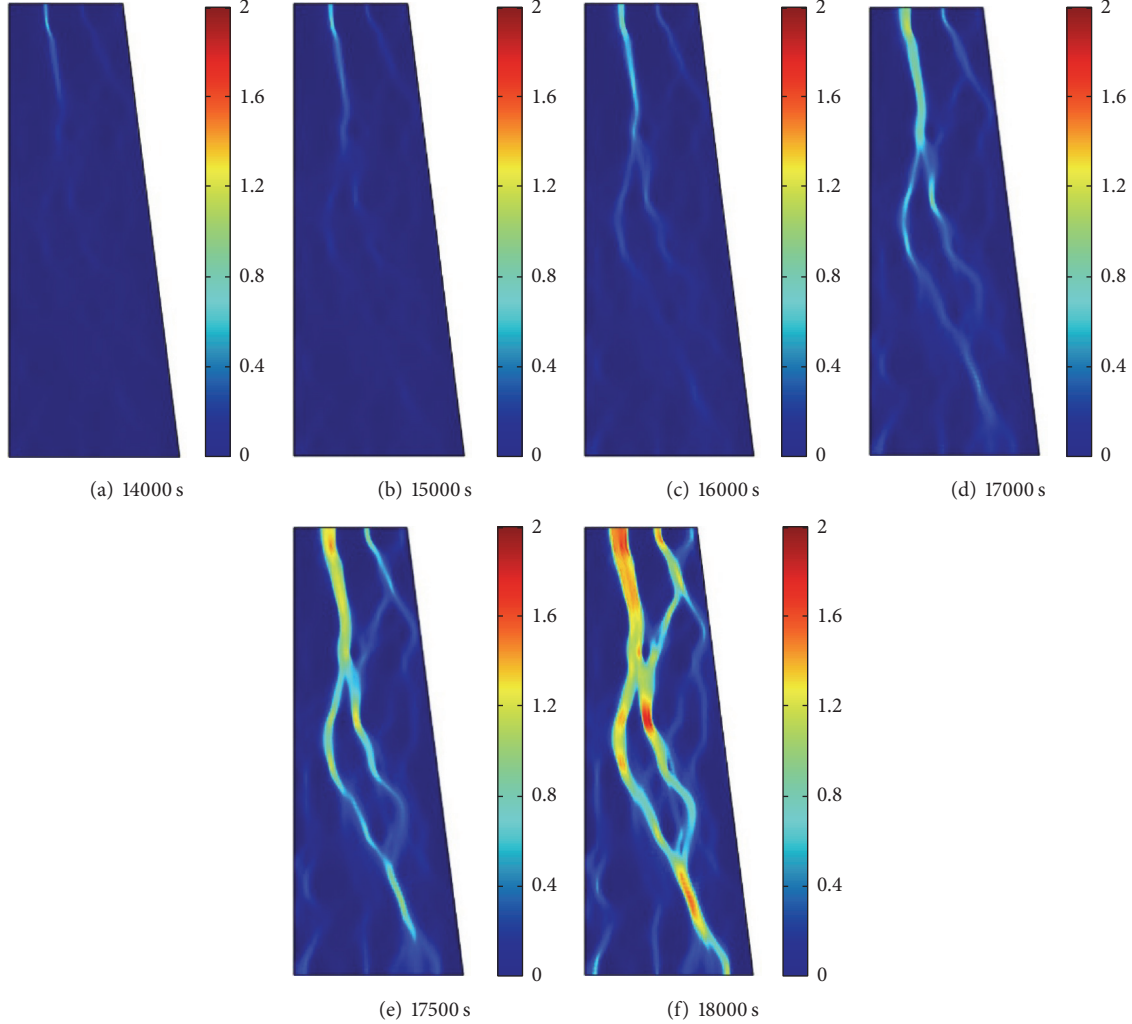
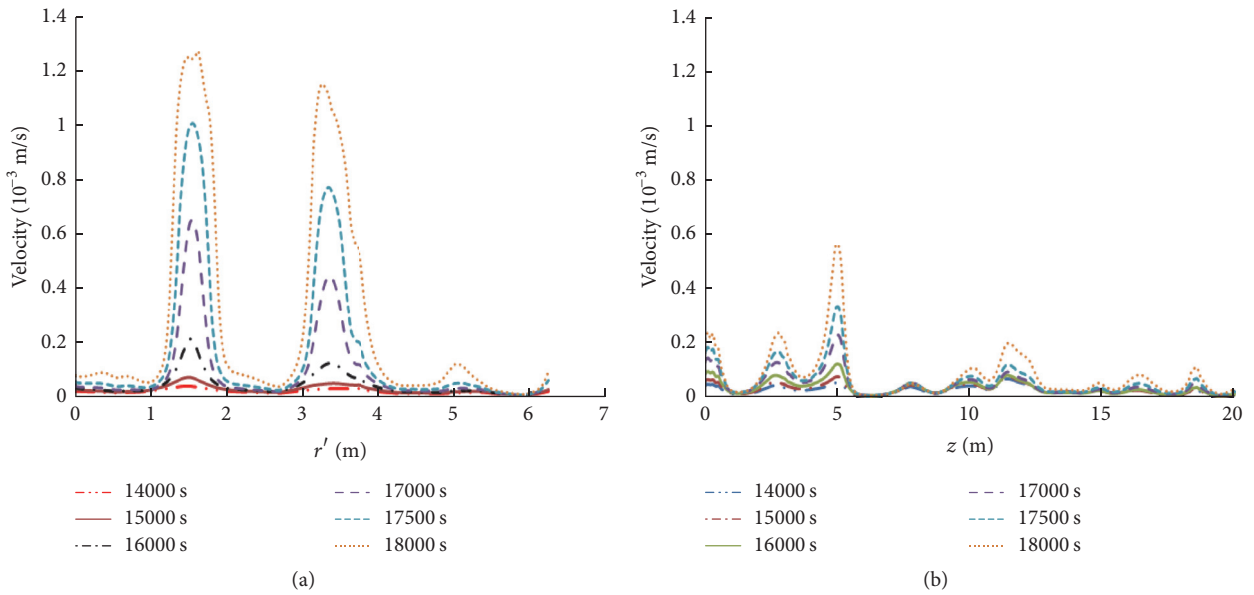
FIGURE 17: The change of seepage velocity ( $10^{-3}$  m/s) in a KCP.

FIGURE 18: Evolution of seepage velocity along the lines of (a) O-O'' axis and (b) O'-A' axis.

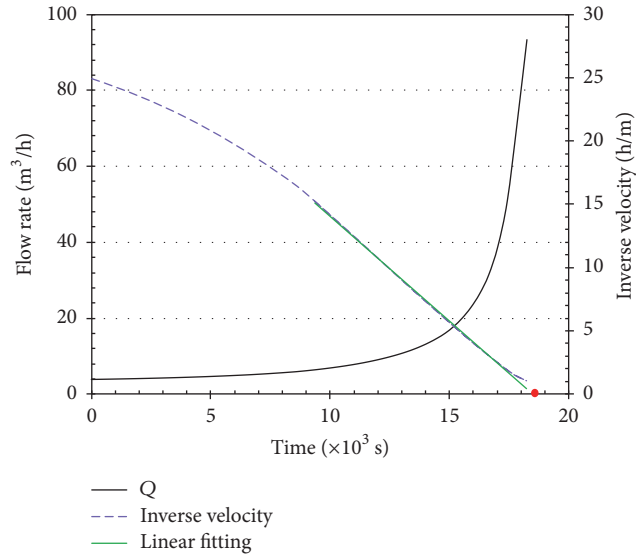


FIGURE 19: Water flow rate along the bottom surface of the numerical model.

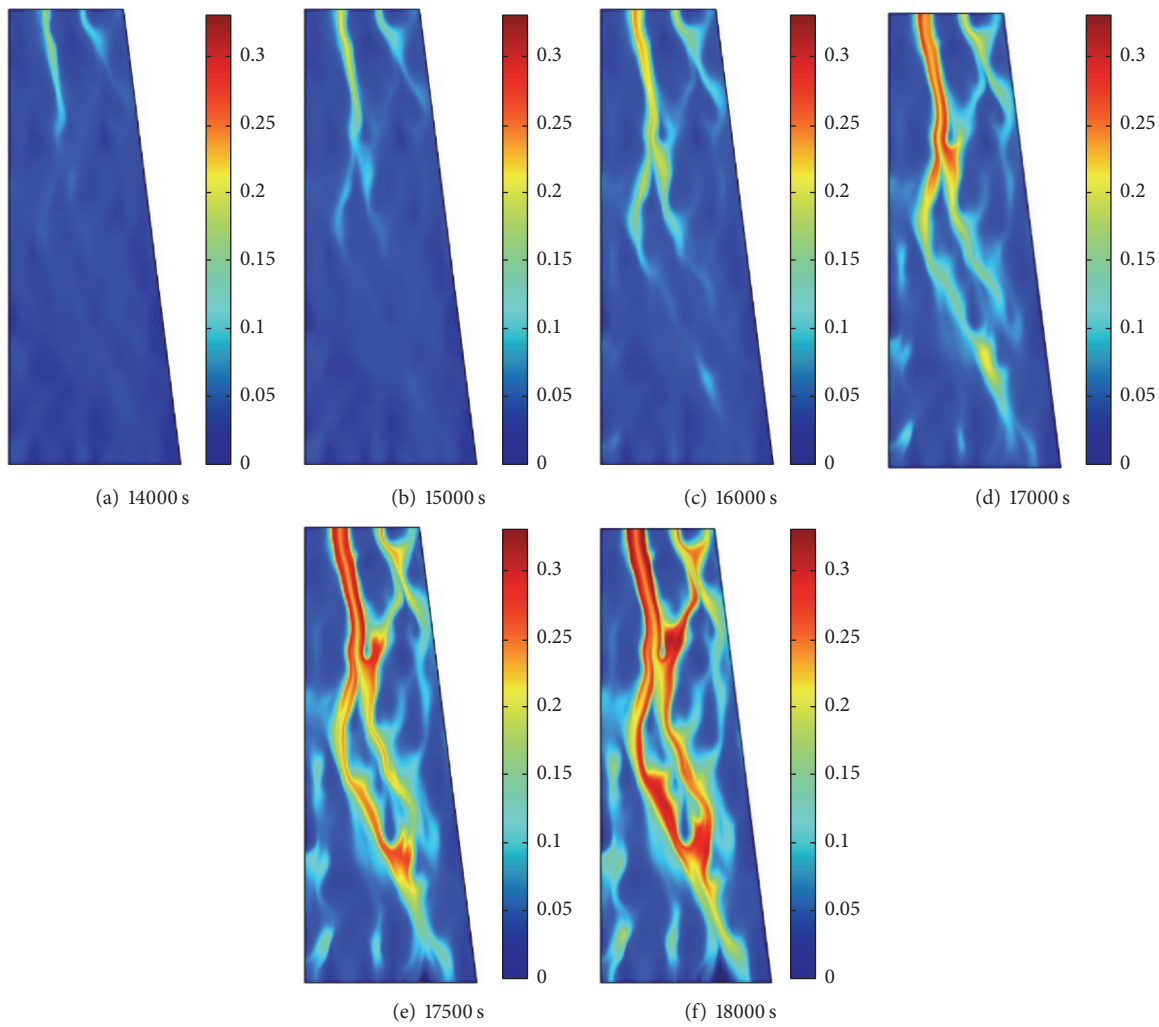


FIGURE 20: Change of particles concentration in a KCP.

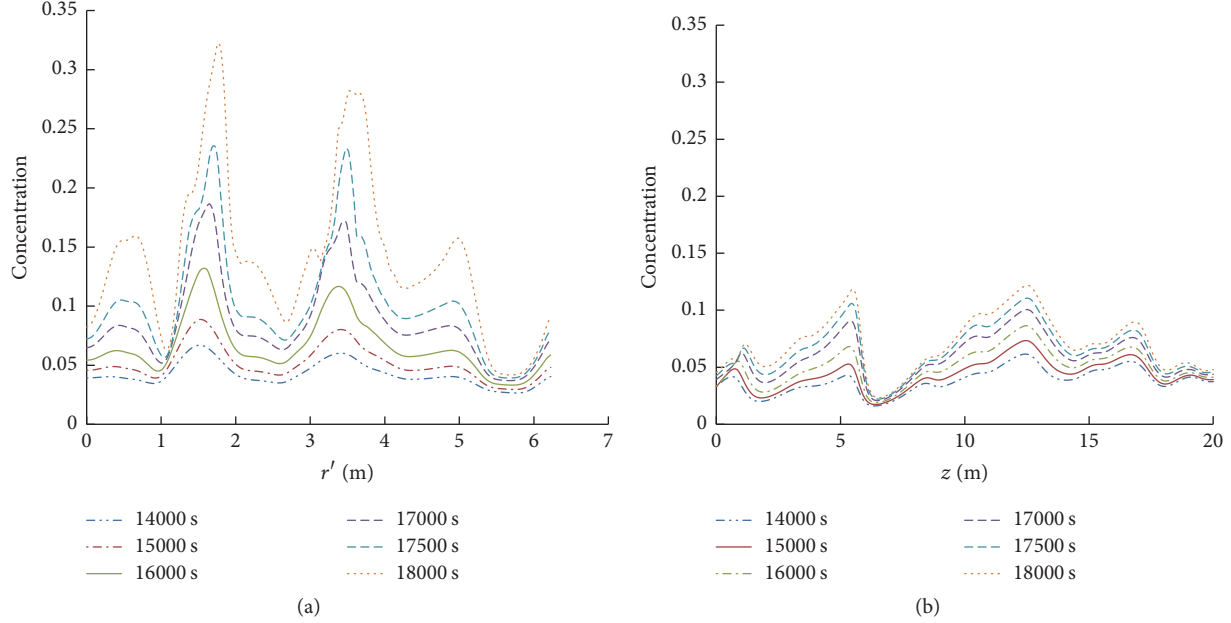


FIGURE 21: Evolution of particle concentration along the lines of (a)  $O-O''$  axis and (b)  $O'-A'$  axis.

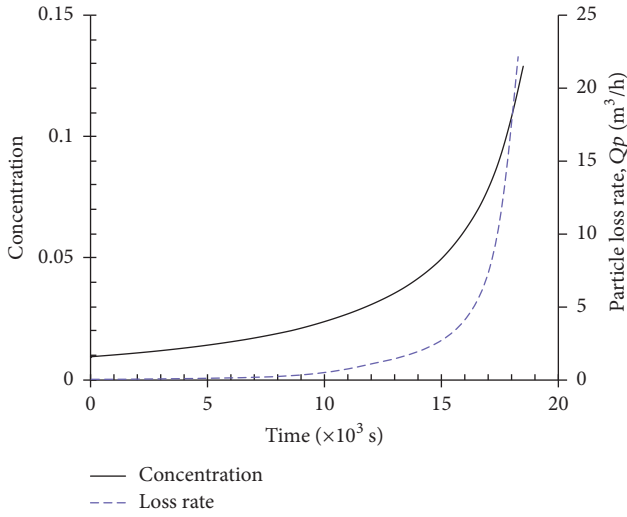


FIGURE 22: Evolution of average particle volumetric concentration and particle loss rate.

**4.4.1. Impact of Heterogeneity on Fracture Evolution.** Figure 23 illustrates the distribution law of the fractures, seepage velocities, and particle volume concentrations under identical flow pressures, but different fracture distribution conditions, at  $17.5 \times 10^3$  seconds. The results show that more interconnected fractures are developed along with the increase in  $m$  values. For example, when  $m = 4$ , there are only two interconnected fractures. However, as  $m$  value increases, an increasing number of fractures were generated and interconnected. In the fourth case ( $m = 10$ ), three interconnected fractures were generated. This finding indicates that the homogeneity can accelerate the propagation of the fractures. An increase in

TABLE 2: List of simulation scenarios.

Parameter	Value
$m = 4$	
Weibull distribution coefficient (-)	
$m = 6$	
$m = 8$	
$m = 10$	
$p = 1.0$	
Water pressure (MPa)	
$p = 2.0$	
$p = 3.0$	
$p = 4.0$	
$C_0 = 0.005$	
Initial particle concentration (%)	
$C_0 = 0.01$	
$C_0 = 0.02$	
$C_0 = 0.05$	
$b = 0.75$	
Fracture aperture ( $\times 10^{-4}$ m)	
$b = 1.0$	
$b = 1.25$	
$b = 1.5$	

flow velocity and particle concentration with increasing  $m$  values was also observed, as shown in Figures 23(b) and 23(c).

**4.4.2. Prediction of Water Inrush under Different Conditions.** The analysis and prediction of the occurrences of water inrush in KCPs, based on the changes in seepage, are essential for the safety of mining processes. Some researchers have adopted catastrophe theories to predict the occurrences of water inrush. However, an approach that can be used to predict water inrush based on water flow has yet to be found in the literature. This study presents the first attempt to resolve this challenge by applying the inverse velocity theory,

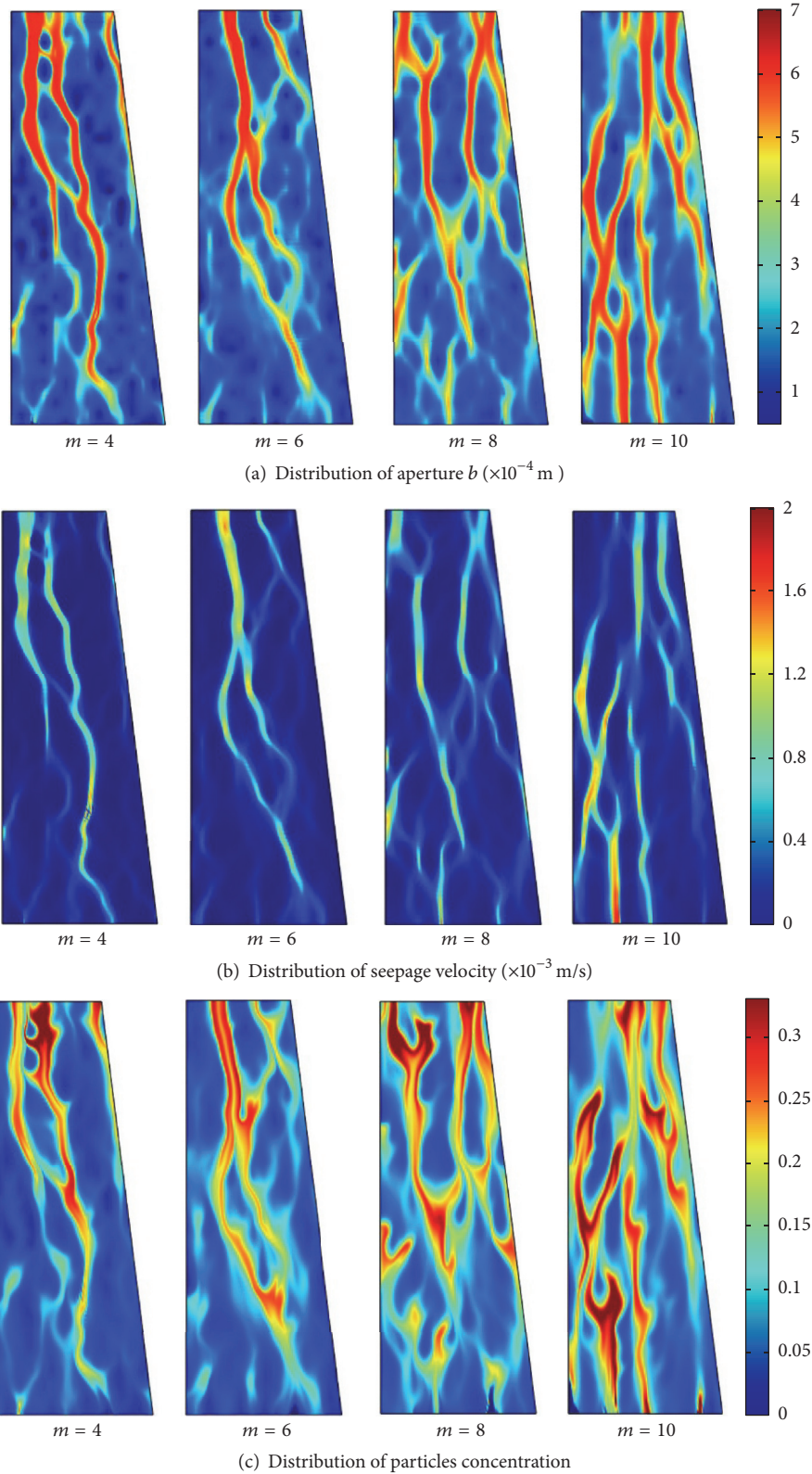


FIGURE 23: Distribution of fracture, seepage velocity, and particle concentration at different Weibull distribution conditions. (a) Impact of Weibull distribution on fractures evolution; (b) impact of Weibull distribution on water velocity evolution; (c) impact of Weibull distribution on particle concentration evolution.

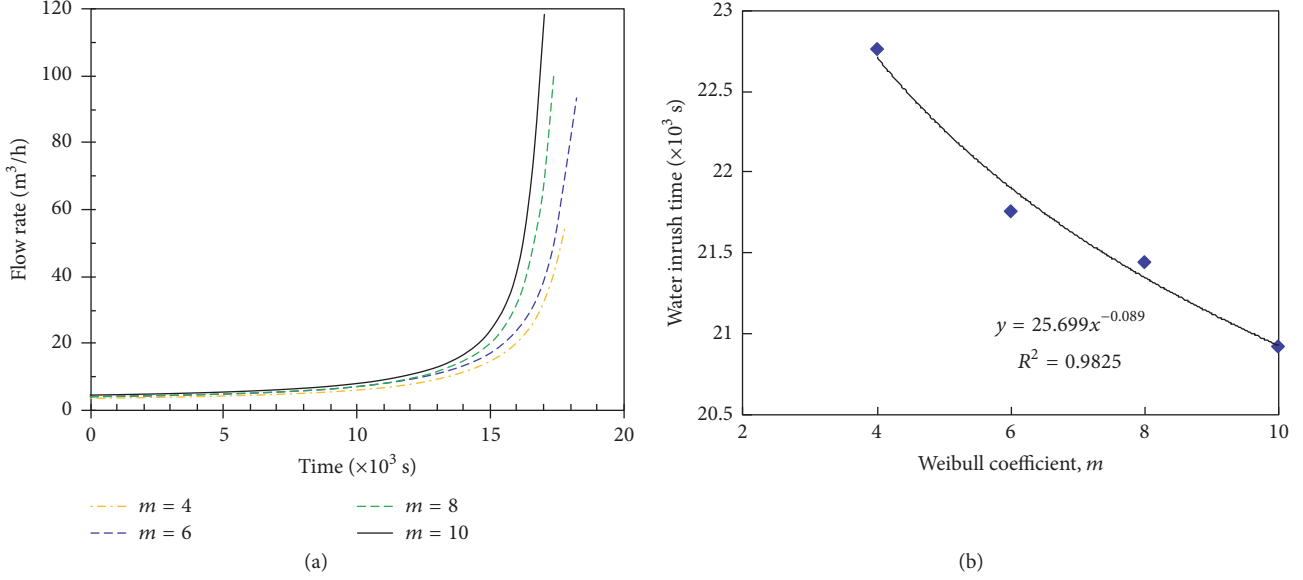


FIGURE 24: Impact of heterogeneity on water flow rate (a) and inrush time (b).

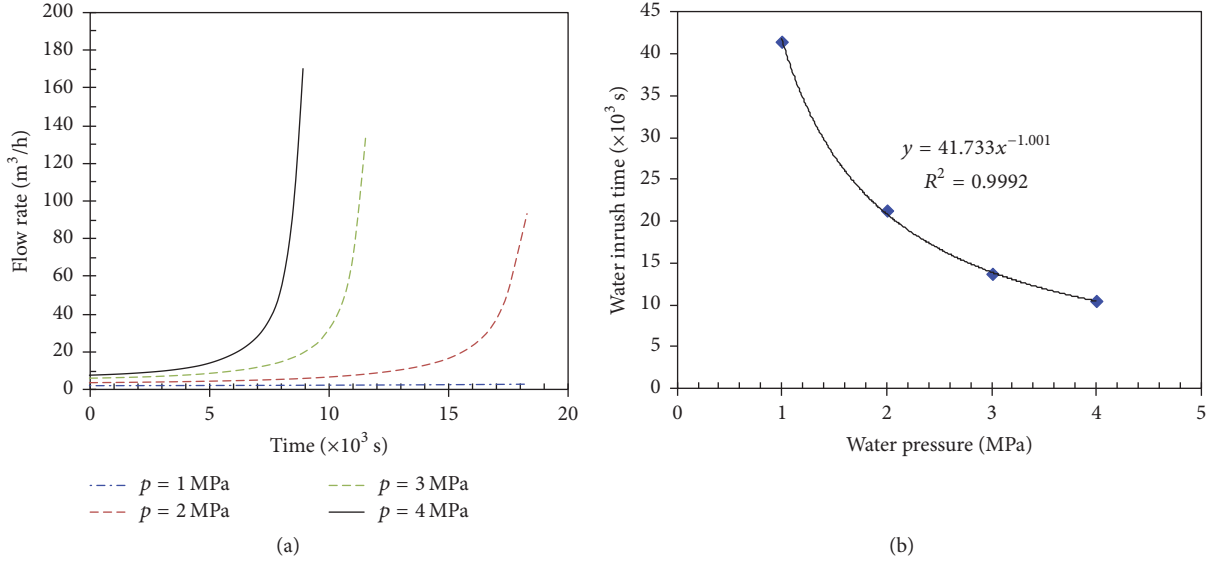


FIGURE 25: Impact of aquifer water pressure on water flow rate (a) and inrush time (b).

which has been widely approved effective in many fields such as slope stability prediction. The relevant results and analyses are shown in Figure 24–Figure 27.

As shown in Figure 24, water flow rate exhibits a non-linear increase, and as the value of  $m$  increases, the seepage rate accelerates gradually. For example, at  $t = 1.5 \times 10^4 \text{ s}$ , the seepage rate was approximately  $15 \text{ m}^3/\text{h}$  for  $m = 4$ , while it jumped to  $25 \text{ m}^3/\text{h}$  for  $m = 10$ . Results from Figure 24(b) show that water inrush occurs sooner for a greater  $m$  value. In other words, the inrush occurs earlier as the heterogeneity increases. The water inrush time follows the power function. This is due to the fact that the water is more prone to flowing through the existing fractures (which indicates a higher

permeability) in the heterogeneous structure. Nevertheless, due to the heterogeneous distribution of the aperture, the fractures cannot be easily interconnected, which hampers the formation of the seepage channels. In regard to the homogeneous rock strata, since the flow of water was dominantly controlled by the pressure gradient, the fractures generated during the process of erosion could be easily interconnected, and as a result the water inrush occurred sooner.

Figure 25 illustrates the impact of the initial KCP's water pressure on the flow rates and water inrush time. It can be seen that, as the pressure increases, the changes in the flow rates accelerate. For example, for  $p = 2 \text{ MPa}$ , the flow rate was only approximately  $5 \text{ m}^3/\text{h}$ , and it increased to  $30 \text{ m}^3/\text{h}$  when

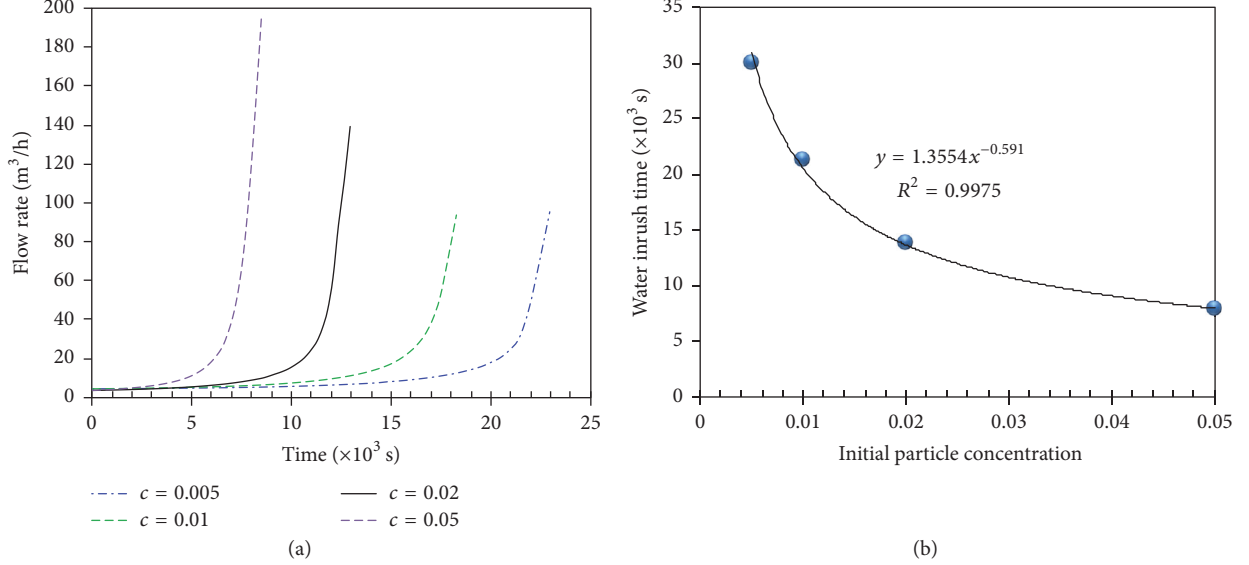


FIGURE 26: Impact of initial particle concentration on water flow rate (a) and inrush time (b).

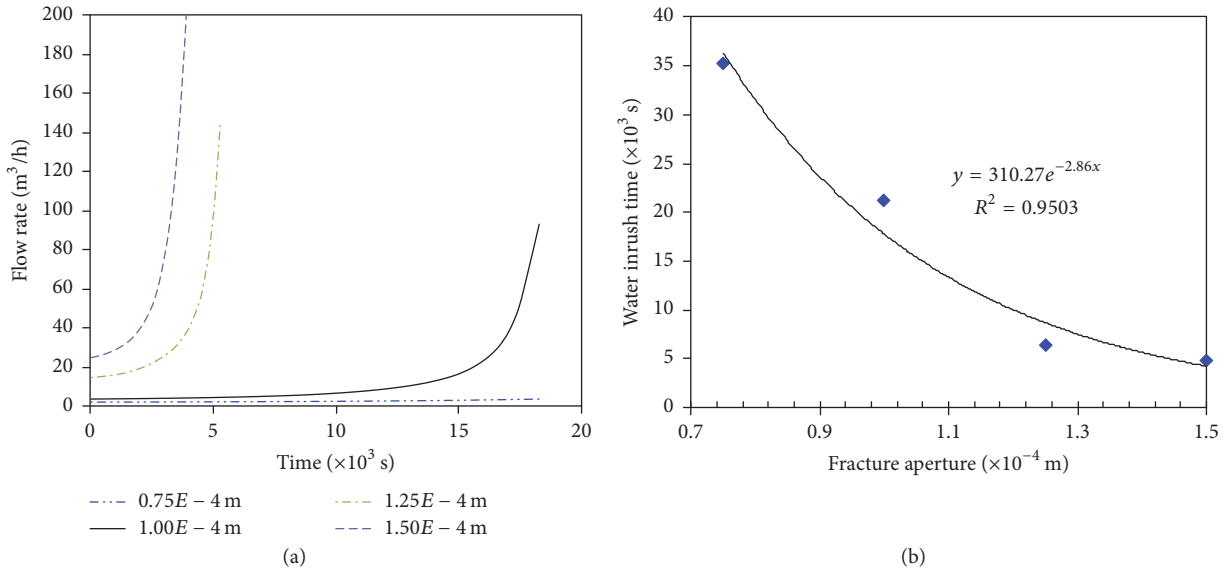


FIGURE 27: Impact of absolute aperture on water flow rate (a) and inrush time (b).

$p = 3 \text{ MPa}$ . In addition, with increasing the aquifer water pressure, the water inrush time was also brought forward, as shown in Figure 25(a). The outburst time was approximately  $t = 4.0 \times 10^4 \text{ s}$  for  $p = 1 \text{ MPa}$ , while only  $1.0 \times 10^4 \text{ s}$  for  $p = 4 \text{ MPa}$ . The relationship between the time of the inrush occurrences and the aquifer water pressure follows the power function, as illustrated in Figure 25.

For varying initial particle concentrations, the evolution of both the water flow rate change and the water inrush time shows a similar trend to that of different aquifer water pressures. The flow rate accelerates with increasing initial particle concentration, and consequently the water inrush occurs earlier, as shown in Figure 26. The outburst times also show a power function to the initial particle concentration.

The initial average fracture aperture also shows significant impact on water flow behavior. For instance, results from Figure 27 clearly illustrate that the flow rate increases with increasing initial average fracture aperture. Please note that the inrush time follows an exponential function to the initial average fracture aperture.

These numerical results can be explained by the fact that the initial seepage velocity is expected to be higher for the modelling cases with the higher initial aquifer pressure, initial fracture aperture, and/or initial particle concentration. The higher flow velocity would intensify the erosion of the fractures, enhance the permeability, and thereby accelerate the migration of the particles and interconnection of seepage channels, which causes water inrush.

## 5. Conclusions

In this study, a systematic approach was established to investigate the impact of controlling factors on water flow behavior for KCPs and to predict water inrush time by introducing the inverse velocity theory. In this approach, a suite of governing equations was developed to couple all the physics involved in this complex process, including water flow, rock erosion, and change in rock microstructure. These equations were then implemented into a finite element software COMSOL Multiphysics to simulate the fully coupled process. Based on this numerical model, a series of sensitivity studies were conducted, and some important findings have been drawn:

- (i) Water flow rate increases with increasing aquifer pressure, initial particle concentration, and fracture opening. This results in an increase in the permeability and finally an acceleration of the migration of the particles and interconnection of the seepage channels. This finding suggests the grouting of the KCPs could be an effective measure to mitigate water inrush risk.
- (ii) The inverse velocity theory was successfully applied to analyze the occurrences of water inrush under different conditions. The results show that the time of inrush has a power relationship to the rock heterogeneity, water pressure, and initial particle concentration and follows an exponential relationship to the initial fracture apertures.

The framework developed from this work not only helps enhance coal mining operations safety by better understanding and predicting water inrush risks, so that proper mitigation measures can be put in place timely. It can also be extended to other fields such as tunneling, backfill paste piping, tailing dam erosion, and other engineering applications, which are likely to encounter time-dependent erosion or deformation, or water inrush issues.

Please be noted that there are a number of other stochastic methods available in the literature that can be used to illustrate rock heterogeneity, such as the Monte-Carlo method or First-Order approach. The differences of these methods on the results of water inrush prediction may be worth comparing in the near future.

## Conflicts of Interest

The authors declare that they have no conflicts of interest.

## Acknowledgments

This project is supported by the National Natural Science Foundation of China (nos. 51304072, 51774110), the Program for Innovative Research Team in University of Ministry of Education of China (IRT\_16R22), and the Postdoctoral Science Foundation of China (2017M612398).

## References

- [1] D. Ma, X. Miao, H. Bai et al., "Effect of mining on shear sidewall groundwater inrush hazard caused by seepage instability of the penetrated karst collapse pillar," *Natural Hazards*, vol. 82, no. 1, pp. 73–93, 2016.
- [2] H. Keqiang, Y. Guangming, and L. Yaoru, "Palaeo-karst collapse pillars in northern China and their damage to the geological environments," *Environmental Geology*, vol. 58, no. 5, pp. 1029–1040, 2009.
- [3] B. Yao, J. Wei, D. Wang, D. Ma, and Z. Chen, "Numerical study on seepage property of karst collapse columns under particle migration," *CMES: Computer Modeling in Engineering & Sciences*, vol. 91, no. 2, pp. 81–100, 2013.
- [4] J. Tang, H. Bai, B. Yao, and Y. Wu, "Theoretical analysis on water-inrush mechanism of concealed collapse pillars in floor," *Mining Science and Technology*, vol. 21, no. 1, pp. 57–60, 2011.
- [5] Y. Chen, M. Yi, C. Chen, and C. Yu, "Bernstein polynomials method for fractional convection-diffusion equation with variable coefficients," *Computer Modeling in Engineering & Sciences*, vol. 83, no. 6, pp. 639–653, 2012.
- [6] J. Zhang and B. Shen, "Coal mining under aquifers in China: A case study," *International Journal of Rock Mechanics and Mining Sciences*, vol. 41, no. 4, pp. 629–639, 2004.
- [7] D. Ma, H. Bai, X. Miao, H. Pu, B. Jiang, and Z. Chen, "Compaction and seepage properties of crushed limestone particle mixture: an experimental investigation for Ordovician karst collapse pillar groundwater inrush," *Environmental Earth Sciences*, vol. 75, no. 1, article 11, p. 14, 2016.
- [8] S. Yin, J. Zhang, and D. Liu, "A study of mine water inrushes by measurements of in situ stress and rock failures," *Natural Hazards*, vol. 79, no. 3, pp. 1961–1979, 2015.
- [9] H. Bai, D. Ma, and Z. Chen, "Mechanical behavior of groundwater seepage in karst collapse pillars," *Engineering Geology*, vol. 164, pp. 101–106, 2013.
- [10] D. Ma and H. Bai, "Groundwater inflow prediction model of karst collapse pillar: a case study for mining-induced groundwater inrush risk," *Natural Hazards*, vol. 76, no. 2, pp. 1319–1334, 2015.
- [11] D. Ma, H. Bai, and Y. Wang, "Mechanical behavior of a coal seam penetrated by a karst collapse pillar: mining-induced groundwater inrush risk," *Natural Hazards*, vol. 75, no. 3, pp. 2137–2151, 2015.
- [12] B. Yao, *Research on variable mass fluid-solid coupling dynamic theory of broken rockmass and application*, China University of Mining and Technology, Xuzhou, China, 2012.
- [13] D. Ma, X. Miao, H. Bai et al., "Impact of particle transfer on flow properties of crushed mudstones," *Environmental Earth Sciences*, vol. 75, no. 7, article 593, 2016.
- [14] D. Ma, H. Bai, Z. Chen, and H. Pu, "Effect of particle mixture on seepage properties of crushed mudstones," *Transport in Porous Media*, vol. 108, no. 2, pp. 257–277, 2015.
- [15] B. Zhang, H. Bai, and K. Zhang, "Seepage characteristics of collapse column fillings," *International Journal of Mining Science and Technology*, 2015.
- [16] P. Ortoleva, J. Chadam, E. Merino, and A. Sen, "Geochemical self-organization II; the reactive-infiltration instability," *American Journal of Science*, vol. 287, no. 10, pp. 1008–1040, 1987.
- [17] I. Vardoulakis, M. Stavropoulou, and P. Papanastasiou, "Hydro-mechanical aspects of the sand production problem," *Transport in Porous Media*, vol. 22, no. 2, pp. 225–244, 1996.
- [18] R. L. Detwiler and H. Rajaram, "Predicting dissolution patterns in variable aperture fractures: Evaluation of an enhanced depth-averaged computational model," *Water Resources Research*, vol. 43, no. 4, Article ID W04403, 2007.

- [19] M. A. Habib, H. M. Badr, R. Ben-Mansour, and M. E. Kabir, "Erosion rate correlations of a pipe protruded in an abrupt pipe contraction," *International Journal of Impact Engineering*, vol. 34, no. 8, pp. 1350–1369, 2007.
- [20] H. T. Xiao and H. Y. Xu, "In situ permeability measurements to establish the influence of slice mining on floor rocks," *International Journal of Rock Mechanics and Mining Sciences*, vol. 37, no. 5, pp. 855–860, 2000.
- [21] H. Guo, D. P. Adhikary, and M. S. Craig, "Simulation of mine water inflow and gas emission during longwall mining," *Rock Mechanics and Rock Engineering*, vol. 42, no. 1, pp. 25–51, 2009.
- [22] R. Zhang, Z. Jiang, H. Zhou, C. Yang, and S. Xiao, "Groundwater outbursts from faults above a confined aquifer in the coal mining," *Natural Hazards*, vol. 71, no. 3, pp. 1861–1872, 2014.
- [23] B. Yao, F. Du, E. Li, and X. Wang, "Mechanical model of karst collapse columns water inrush and its application," *Electronic Journal of Geotechnical Engineering*, vol. 19, pp. 1665–1675, 2014.
- [24] J. Warren and P. Root, "The behavior of naturally fractured reservoirs," *SPE Journal*, vol. 3, no. 3, pp. 245–255, 2013.
- [25] H. Kazemi, M. S. Seth, and G. W. Thomas, "The interpretation of interference tests in naturally fractured reservoirs with uniform fracture distribution," *SPE Journal*, vol. 9, no. 4, pp. 463–472, 1969.
- [26] A. de Swaan O., "Analytical solutions for determining naturally fractured reservoir properties by well testing," *SPE Journal*, vol. 16, no. 3, pp. 117–122, 1976.
- [27] N. D. Rose and O. Hungr, "Forecasting potential rock slope failure in open pit mines using the inverse-velocity method," *International Journal of Rock Mechanics and Mining Sciences*, vol. 44, no. 2, pp. 308–320, 2007.
- [28] J. R. Fanchi, *Petroleum Engineering Handbook, Volume 1: General Engineering*, Society of Petroleum Engineers, 2006.
- [29] R. Sakthivadivel and S. Irmay, *A Review of Filtration Theories*, Hydraulic Engineering Laboratory, College of Engineering, University of California, Berkeley, Calif, USA, 1996.
- [30] C. Wang, P. Zhai, Z. Chen, J. Liu, L. Wang, and J. Xie, "Experimental study of coal matrix-cleat interaction under constant volume boundary condition," *International Journal of Coal Geology*, vol. 181, pp. 124–132, 2017.
- [31] S. Irmay, "On the theoretical derivation of Darcy and Forchheimer formulas," *Eos, Transactions, American Geophysical Union*, vol. 39, no. 4, pp. 702–707, 1958.
- [32] C. H. Lee and I. W. Farmer, "A simple method of estimating rock mass porosity and permeability," *International Journal of Mining and Geological Engineering*, vol. 8, no. 1, pp. 57–65, 1990.
- [33] C. Nalluri, A. K. El-Zaemey, and H. L. Chan, "Sediment transport over fixed deposited beds in sewers - An appraisal of existing models," *Water Science and Technology*, vol. 36, no. 8-9, pp. 123–128, 1997.
- [34] P. Novak and C. Nalluri, "Sediment transport in smooth fixed bed channels," *Journal of the Hydraulics Division*, vol. 101, no. 9, pp. 1139–1154, 1975.
- [35] T. Fukuzono, "A new method for predicting the failure time of a slope," in *Proceedings of the In 4th International Conference and Field Workshop on Landslides*, Tokyo, Japan, 1985.
- [36] C. R. J. Kilburn and D. N. Petley, "Forecasting giant, catastrophic slope collapse: lessons from Vajont, Northern Italy," *Geomorphology*, vol. 54, no. 1-2, pp. 21–32, 2003.
- [37] B. Voight, "A method for prediction of volcanic eruptions," *Nature*, vol. 332, no. 6160, pp. 125–130, 1988.
- [38] B. Yao, X. Mao, J. Wei, and D. Wang, "Study on coupled fluid-solid model for collapse columns considering the effect of particle transport," *Zhongguo Kuangye Daxue Xuebao/Journal of China University of Mining and Technology*, vol. 43, no. 1, pp. 30–35, 2014.
- [39] H. Bai, *Seepage Characteristics of Top Stratum of Ordovician System and Its Application Study as Key Aquifuge*, China University of Mining & Technology, Xuzhou, China, 2008.
- [40] C. A. Tang, L. G. Tham, P. K. K. Lee, T. H. Yang, and L. C. Li, "Coupled analysis of flow, stress and damage (FSD) in rock failure," *International Journal of Rock Mechanics and Mining Sciences*, vol. 39, no. 4, pp. 477–489, 2002.
- [41] W. C. Zhu and C. A. Tang, "Micromechanical model for simulating the fracture process of rock," *Rock Mechanics and Rock Engineering*, vol. 37, no. 1, pp. 25–56, 2004.
- [42] T. H. Yang, L. G. Tham, C. A. Tang, Z. Z. Liang, and Y. Tsui, "Influence of heterogeneity of mechanical properties on hydraulic fracturing in permeable rocks," *Rock Mechanics and Rock Engineering*, vol. 37, no. 4, pp. 251–275, 2004.

## Research Article

# A Novel Boundary-Type Meshless Method for Modeling Geofluid Flow in Heterogeneous Geological Media

Jing-En Xiao, Cheng-Yu Ku , Chih-Yu Liu, and Wei-Chung Yeih 

*Department of Harbor and River Engineering, National Taiwan Ocean University, Keelung, Taiwan*

Correspondence should be addressed to Cheng-Yu Ku; chkst26@email.ntou.edu.tw

Received 3 July 2017; Accepted 18 December 2017; Published 16 January 2018

Academic Editor: Shujun Ye

Copyright © 2018 Jing-En Xiao et al. This is an open access article distributed under the Creative Commons Attribution License, which permits unrestricted use, distribution, and reproduction in any medium, provided the original work is properly cited.

A novel boundary-type meshless method for modeling geofluid flow in heterogeneous geological media was developed. The numerical solutions of geofluid flow are approximated by a set of particular solutions of the subsurface flow equation which are expressed in terms of sources located outside the domain of the problem. This pioneering study is based on the collocation Trefftz method and provides a promising solution which integrates the T-Trefftz method and F-Trefftz method. To deal with the subsurface flow problems of heterogeneous geological media, the domain decomposition method was adopted so that flux conservation and the continuity of pressure potential at the interface between two consecutive layers can be considered in the numerical model. The validity of the model is established for a number of test problems. Application examples of subsurface flow problems with free surface in homogenous and layered heterogeneous geological media were also carried out. Numerical results demonstrate that the proposed method is highly accurate and computationally efficient. The results also reveal that it has great numerical stability for solving subsurface flow with nonlinear free surface in layered heterogeneous geological media even with large contrasts in the hydraulic conductivity.

## 1. Introduction

Numerical approaches to the simulation of various subsurface flow phenomena using the mesh-based methods such as the finite difference method or the finite element method are well documented in the past [1–5]. Differing from conventional mesh-based methods, the meshless method has the advantages that it does not need the mesh generation. The meshless method has attracted considerable attention in recent years because of its flexibility in solving practical problems involving complex geometry in subsurface flow problems [6–9]. Chen et al. [10] conducted a comprehensive review of mesh-free methods and addressed that mesh-free methods have emerged into a new class of computational methods with considerable success. Subsurface flow problems are usually governed by second-order partial differential equations. Problems involving regions of irregular geometry are generally intractable analytically. For such problems, the use of numerical methods, especially the boundary-type meshless method, to obtain approximate solutions is advantageous.

Several meshless methods have been reported, such as the Trefftz method [11–16], the method of fundamental solutions [7, 17–19], the element-free Galerkin method [20], the reproducing kernel particle method [21, 22], the meshless local boundary integral equation method [23, 24], and the meshless local Petrov-Galerkin approach [25]. Proposed by Trefftz in 1926 [16], the Trefftz method is probably one of the most popular boundary-type meshless methods for solving boundary-value problems where approximate solutions are expressed as a linear combination of functions automatically satisfying governing equations. According to Kita and Kamiya [12], Trefftz methods are classified as either direct or indirect formulations. Unknown coefficients are determined by matching boundary conditions. Li et al. [14] provided a comprehensive comparison of the Trefftz method, collocation, and other boundary methods, concluding that the collocation Trefftz method (CTM) is the simplest algorithm and provides the most accurate solutions with optimal numerical stability.

To solve subsurface flow problems with the layered soil in heterogeneous porous media, the domain decomposition

method (DDM) [26] is adopted because the DDM is natural from the physics of the problem to deal with different values of hydraulic conductivity in subdomains. The DDM can be divided into overlapping domain decomposition and nonoverlapping domain decomposition methods. In overlapping domain decomposition methods, the subdomains overlap by more than the interface. In nonoverlapping methods, the subdomains intersect only on their interface. One may need to use the DDM which decomposes the problem domain into several simply connected subdomains and to use the numerical method in each one. In this study, we adopted the nonoverlapping method to deal with the seepage problems of layered soil profiles. The problems on the subdomains are independent, which makes the DDM suitable for describing the layered soil in heterogeneous porous media.

The subsurface flow problem with a free surface is a nonlinear problem in which nonlinearities arise from the nonlinear boundary characteristics [27]. Such nonlinearities are handled in the numerical modeling using iterative schemes [28]. Techniques for solving problems with nonlinear boundary conditions have been investigated. Typically, the methods, such as the Picard method or Newton's method, are iterative in that they approach the solution through a series of steps. Since the computation of the subsurface flow problem with a free surface has to be solved iteratively, the location of the boundary collocation points and the source points must be updated simultaneously with the moving boundary. Solving subsurface flow with a nonlinear free surface in layered heterogeneous soil is generally much more challenging. In addition, the convergence problems often arise from nonlinear phenomena. A previous study [28] indicates that the Picard scheme is a simple and effective method for the solution of nonlinear and saturated groundwater flow problems. Therefore, we adopted the Picard scheme to find the solution of the nonlinear free surface.

In this paper, we proposed a novel boundary-type meshless method. This pioneering study is based on the collocation Trefftz method and provides a promising solution which integrates the T-Trefftz method and F-Trefftz method for constructing its basis function using one of the particular solutions which satisfies the governing equation and allows many source points outside the domain of interest. To the best of the authors' knowledge, the pioneering work has not been reported in previous studies and requires further research. Two important phenomena in subsurface flow modeling were explored in this study using the proposed method. We first adopted the domain decomposition method integrated with the proposed boundary-type meshless method to deal with the subsurface flow problems of heterogeneous geological media. The flux conservation and the continuity of pressure potential at the interface between two consecutive layers can be considered in the numerical model. Then, we attempted to utilize the proposed method to solve the geofluid flow with free surface in heterogeneous geological media.

The validity of the model is established for a number of test problems, including the investigation of the basis function using two possible particular solutions and the comparison of the numerical solutions using different particular solutions and the method of fundamental solutions.

Application examples of subsurface flow problems with free surface were also carried out.

## 2. Solutions to the Subsurface Flow Equation in Cylindrical Coordinates

Consider a three-dimensional domain  $\Omega$  enclosed by a boundary  $\Gamma$ . The steady-state subsurface flow equation can be expressed as

$$\nabla^2 h = 0 \quad \text{in } \Omega, \quad (1)$$

with

$$\begin{aligned} h &= f \quad \text{on } \Gamma_D, \\ h_n &= \frac{\partial h}{\partial n} \quad \text{on } \Gamma_N, \end{aligned} \quad (2)$$

where  $n$  denotes the outward normal direction,  $\Gamma_D$  denotes the boundary where the Dirichlet boundary condition is given, and  $\Gamma_N$  denotes the boundary where the Neumann boundary condition is given. Equation (1) is also known as the Laplace equation. In this study, we adopted the cylindrical coordinate system. In the cylindrical coordinate system, the Laplace governing equation can be written as

$$\frac{\partial^2 h}{\partial \rho^2} + \frac{1}{\rho} \frac{\partial h}{\partial \rho} + \frac{1}{\rho^2} \frac{\partial^2 h}{\partial \theta^2} + \frac{\partial^2 h}{\partial z^2} = 0, \quad (3)$$

where  $\rho$ ,  $\theta$ , and  $z$  are the radius, polar angle, and altitude in the three-dimensional cylindrical coordinate system.  $h$  is the unknown function to be solved. Considering a two-dimensional domain in the polar coordinate, the Laplace governing equation can be written as

$$\frac{\partial^2 h}{\partial \rho^2} + \frac{1}{\rho} \frac{\partial h}{\partial \rho} + \frac{1}{\rho^2} \frac{\partial^2 h}{\partial \theta^2} = 0, \quad (4)$$

where  $\rho$  and  $\theta$  are the radius and polar angle in the two-dimensional polar coordinate system. For the Laplace equation, the particular solutions can be obtained using the method of separation of variables. The particular solutions of (4) include the following basis functions:

$$1, \ln \rho, \rho^\nu \cos(\nu\theta), \rho^\nu \sin(\nu\theta), \rho^{-\nu} \cos(\nu\theta), \rho^{-\nu} \sin(\nu\theta), \quad (5)$$

$$\nu = 1, 2, 3, \dots$$

The definition of the particular solution in this study is in a wide sense which is to satisfy the homogenous or the nonhomogenous differential equations with or without part of boundary conditions. If we adopt the solution of a boundary value problem and enforce it to exactly satisfy the partial differential equation with the boundary conditions at a set of points, this leads to the CTM.

The CTM belongs to the boundary-type meshless method which can be categorized into the T-Trefftz method and F-Trefftz method. The T-Trefftz method introduces the T-complete functions where the solutions can be expressed as a linear combination of the T-complete functions automatically

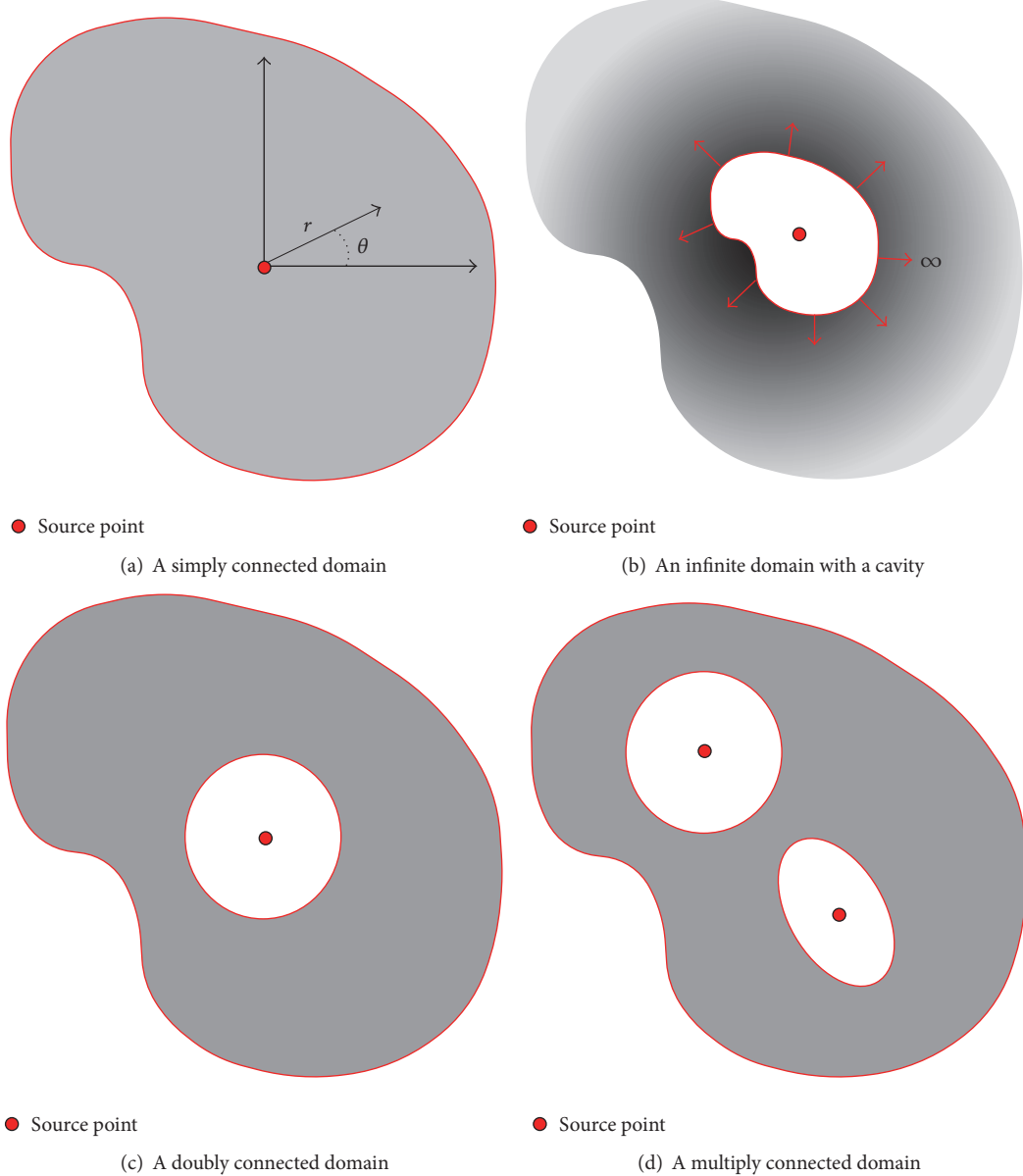


FIGURE 1: Illustration of four different types of domain in the CTM.

satisfying governing equations. On the other hand, the F-Trefftz method constructs its basis function space by allowing many source points outside the domain of interest. The solutions are approximated by a set of fundamental solutions which are expressed in terms of sources located outside the domain of the problem. The T-Trefftz method and the F-Trefftz method both required the evaluation of a coefficient for each term in the series. The evaluation of coefficients may be obtained by solving the unknown coefficients in the linear combination of the solutions which are accomplished by collocation imposing the boundary condition at a finite number of points.

The CTM begins with the consideration of T-complete functions. For indirect Trefftz formulation, the approximated solution at the boundary collocation point can be written

as a linear combination of the basis functions. For a simply connected domain or infinite domain with a cavity, as illustrated in Figures 1(a) and 1(b), one usually locates the source point inside the domain or the cavity and the number of source points is only one for in the CTM [29].

For the doubly and multiply connected domains with genus greater than one, as illustrated in Figures 1(c) and 1(d), one may locate many source points in the domain. Usually, at least one source point inside the cavity is required. If we considered a simply connected domain, the T-complete basis functions can be expressed as

$$h(\mathbf{x}) \approx \sum_{i=1}^M \mathbf{b}_i \mathbf{T}_i(\mathbf{x}), \quad (6)$$

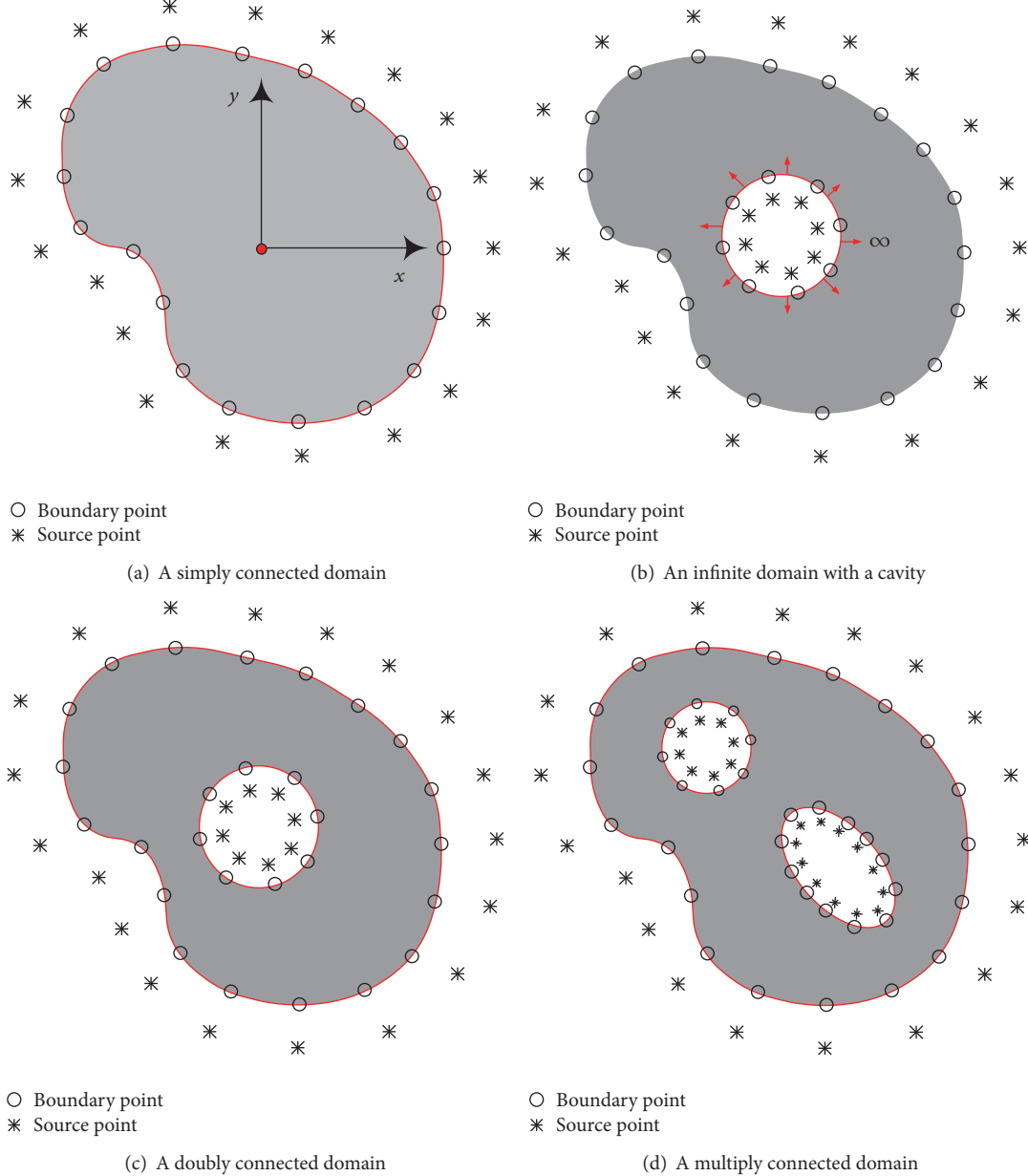


FIGURE 2: Illustration of four different types of domain in the MFS.

where  $\mathbf{b}_i = [A_0 \ A_i \ B_i]^T$  and  $\mathbf{T}_i(\mathbf{x}) = [\ln \rho \ \rho^i \cos(i\theta) \ \rho^i \sin(i\theta)]^T$ .  $\mathbf{x} \in \Omega$  and  $M$  is the order of the T-complete function for approximating the solution. For an infinite domain with a cavity as illustrated in Figure 1(b), one usually locates the source point inside the cavity, and the T-complete functions (negative T-complete set) include

$$\mathbf{T}_i(\mathbf{x}) = [\ln \rho \ \rho^{-i} \cos(i\theta) \ \rho^{-i} \sin(i\theta)]^T. \quad (7)$$

The accuracy of the solution for the CTM depends on the order of the basis functions. Usually, one may need to increase the  $M$  value to obtain better accuracy. However, the ill-posed behavior also grows up with the  $M$  value.

On the other hand, there is another type of the Trefftz method, namely, the F-Trefftz method, or the so-called method of the fundamental solutions (MFS) [14]. Instead of using only one source point and increasing the order of basis function, the MFS allows many source points outside the domain of interest. The solutions are approximated by a set of fundamental solutions which are expressed in terms of sources located outside the domain of the problem. Figures 2(a), 2(b), 2(c), and 2(d) illustrate the collocation of the boundary and the source points for a simply connected domain, an infinite domain with a cavity, doubly connected domains, and a multiply connected domain, respectively.

The unknown coefficients in the linear combination of the fundamental solutions which are accomplished by

collocation imposing the boundary condition at a finite number of points can then be solved. Due to its singular free and meshless merits, the indirect type F-Trefftz method is commonly used. An approximation solution of the two-dimensional Laplace equation using the MFS can also be obtained as

$$h(\mathbf{x}) \approx \sum_{j=1}^N c_j F(\mathbf{x}, \mathbf{y}_j), \quad (8)$$

where  $\mathbf{x} \in \Omega$  and  $\mathbf{y}_j \notin \Omega$  and  $N$  is the number of source points which are placed outside the domain. The fundamental solution of Laplace equation can be expressed as

$$F(\mathbf{x}, \mathbf{y}_j) = -\frac{1}{2\pi} \ln(\rho_j). \quad (9)$$

$\rho_j$  is defined as the distance between the boundary point and source point, and  $\rho_j = |\mathbf{x} - \mathbf{y}_j|$ . Then we selected a finite number of collocation points over the boundary and imposed the boundary condition at boundary collocation points to determine the coefficients of  $\mathbf{b}_i$  and  $c_j$  for the CTM and the MFS, respectively.

For the conventional Trefftz method, the number of source points is only one. Theoretically, one may increase the accuracy by using a larger order of the basis functions [30]. Instead of using only one source point and increasing the order of basis functions, the MFS allows many source points but uses only one basis function, that is, the fundamental solution of the differential operator. One may be interested to investigate a method similar to the MFS which allows many source points but uses other basis functions.

In the following, we proposed a novel boundary-type meshless method. This pioneering study is based on the collocation Trefftz method and provides a promising solution which integrates the T-Trefftz method and F-Trefftz method for constructing its basis function using one of the particular solutions which satisfies the governing equation and allows many source points outside the domain of interest. Differing from the CTM and the MFS, the numerical solutions of the proposed method are approximated by a set of basis functions which are expressed in terms of source points located outside the domain. An approximation solution of the two-dimensional steady-state subsurface flow equation using the proposed method can be obtained as

$$h(\mathbf{x}) \approx \sum_{j=1}^O \mathbf{a}_j \mathbf{P}_j(\mathbf{x}, \mathbf{y}_j), \quad (10)$$

where  $\mathbf{x} \in \Omega$  is the spatial coordinate which is collocated on the boundary,  $\mathbf{y}_j \notin \Omega$  is the source point, and  $O$  is the number of source points which are placed outside the domain. The unknown coefficients can be expressed as  $\mathbf{a}_j = [a_j \ b_j]$ .  $\mathbf{P}_j(\mathbf{x}, \mathbf{y}_j)$  is the particular solution of Laplace equation. In this study, two different particular solutions of Laplace equation were adopted as the basis functions. Two possible particular solutions of Laplace equation can be expressed as

$$\begin{aligned} \mathbf{P}_j(\mathbf{x}, \mathbf{y}_j) &= [\rho_j^{-1} \cos \theta_j \ \rho_j^{-1} \sin \theta_j]^T, \\ \mathbf{P}_j(\mathbf{x}, \mathbf{y}_j) &= [\rho_j^{-2} \cos 2\theta_j \ \rho_j^{-2} \sin 2\theta_j]^T. \end{aligned} \quad (11)$$

The determination of the unknown coefficients for the proposed method is exactly the same with those in the MFS as described in previous section. We first selected a finite number of collocation points  $\mathbf{x}_k$  over the boundary such that

$$\sum_{j=1}^O \mathbf{a}_j \mathbf{P}_j(\mathbf{x}_k, \mathbf{y}_j) = g(\mathbf{x}_k), \quad k = 1, \dots, M, \quad (12)$$

where  $\mathbf{a}_j = [a_j \ b_j]$  are the constant coefficients to be solved, and  $g(\mathbf{x}_k)$  is the boundary condition imposed at boundary collocation points. Considering the boundary conditions, we have

$$Bh(\mathbf{x}) = g(\mathbf{x}), \quad (13)$$

where  $B = 1$  represents the Dirichlet boundary condition;  $B = \partial/\partial n$  represents the Neumann boundary condition. Applying Dirichlet and Neumann boundary conditions, we obtained

$$\begin{aligned} h(\mathbf{x}_k) &\approx \sum_{j=1}^O \mathbf{a}_j \mathbf{P}_j(\mathbf{x}_k, \mathbf{y}_j) = g(\mathbf{x}_k), \\ \frac{\partial h(\mathbf{x}_k)}{\partial n} &\approx \sum_{j=1}^O \mathbf{a}_j \frac{\partial}{\partial n} \mathbf{P}_j(\mathbf{x}_k, \mathbf{y}_j) = f(\mathbf{x}_k), \end{aligned} \quad (14)$$

where  $j = 1, \dots, O$  and  $\mathbf{x}_k \in \Gamma$ .  $f(\mathbf{x}_k)$  is the Neumann boundary condition imposed at boundary collocation points. The source points are on the artificial fictitious boundary, which are placed outside the domain to avoid the singularity of the solution at origin. The artificial fictitious boundary is often chosen as a circle with a radius. However, the position of source and collocation points may affect the accuracy. In order to determine the unknowns  $\mathbf{a}_j$ , collocating the numerical expansion of (12) at boundary conditions of (14) at  $M$  boundary collocation points yields the following equations:

$$\mathbf{A}\boldsymbol{\alpha} = \mathbf{b}, \quad (15)$$

where  $\mathbf{A}$  is a matrix which takes values of the solutions at the corresponding  $M$  collocation points and  $N$  source points,  $\boldsymbol{\alpha} = [\mathbf{a}_1, \mathbf{a}_2, \dots, \mathbf{a}_O]^T$  is a vector of unknown coefficients, and  $\mathbf{b}$  is a vector of function values at collocation points.

### 3. Validation of the Proposed Method

**3.1. Investigation of the Basis Function.** In this example, we adopted two possible particular solutions of Laplace equation as the basis functions. They are  $\mathbf{P}_{1j}$  and  $\mathbf{P}_{2j}$  where  $\mathbf{P}_{1j}(\mathbf{x}, \mathbf{y}_j) = [\rho_j^{-1} \cos \theta_j \ \rho_j^{-1} \sin \theta_j]^T$  and  $\mathbf{P}_{2j}(\mathbf{x}, \mathbf{y}_j) = [\rho_j^{-2} \cos 2\theta_j \ \rho_j^{-2} \sin 2\theta_j]^T$ , respectively. In this example, we verified the accuracy of the proposed method and also compared the numerical solution with the MFS. To compare the results with the analytical solution, we considered the subsurface flow problem with an exact solution.

For a two-dimensional simply connected domain  $\Omega$  enclosed by a boundary, the subsurface flow equation can

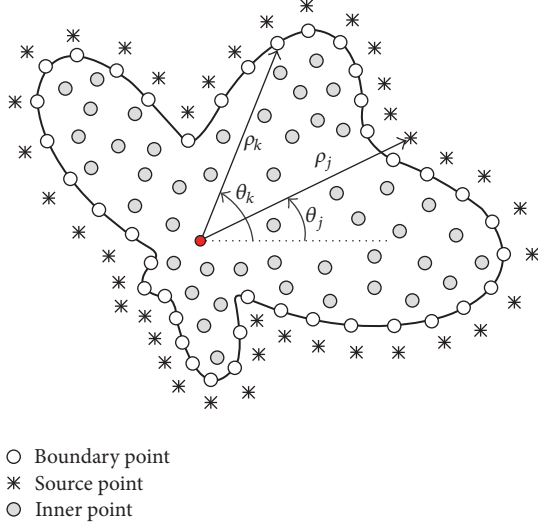


FIGURE 3: The collocation of boundary and source points.

be expressed as Laplace governing equation which can be expressed as

$$\nabla^2 h = 0 \quad \text{in } \Omega. \quad (16)$$

The two-dimensional object boundary under consideration is defined as

$$\Gamma = \{(x, y) \mid x = \rho(\theta) \cos \theta, y = \rho(\theta) \sin \theta\}, \quad (17)$$

where  $\rho(\theta) = 2(e^{(\sin \theta \sin 2\theta)^2} + e^{(\cos \theta \cos 2\theta)^2})$ ,  $0 \leq \theta \leq 2\pi$ .

The analytical solution can be found as

$$h = e^x \cos y + e^x \sin y. \quad (18)$$

The Dirichlet boundary condition is imposed on the amoeba-like boundary by using the analytical solution as shown in (18) for the problem.

Figure 3 shows the collocation point for the boundary and the source points. To obtain a promising result of the location of the source points for the proposed method in this study, a sensitivity study was first carried out. An algorithm similar to the study conducted by Chen et al. [31] was adopted with scaling of the artificial boundary with the domain size. Assuming the boundary collocation points can be described as a known parametric representation as follows:

$$\mathbf{x}_k = r_k (\cos \theta_k, \sin \theta_k), \quad k = 1, \dots, M. \quad (19)$$

The source points can also be described as a known parametric representation from the above equation:

$$\mathbf{y}_j = \eta r_j (\cos \theta_j, \sin \theta_j), \quad j = 1, \dots, N, \quad (20)$$

where  $\eta$  is the dilation parameter and is greater than one.  $\theta_k$  and  $\theta_j$  are the angles of the discretization of the boundary for boundary and source points, respectively.  $r_k$  and  $r_j$  are the radii which represent the scale of the domain size for boundary and source points, respectively. The sensitivity

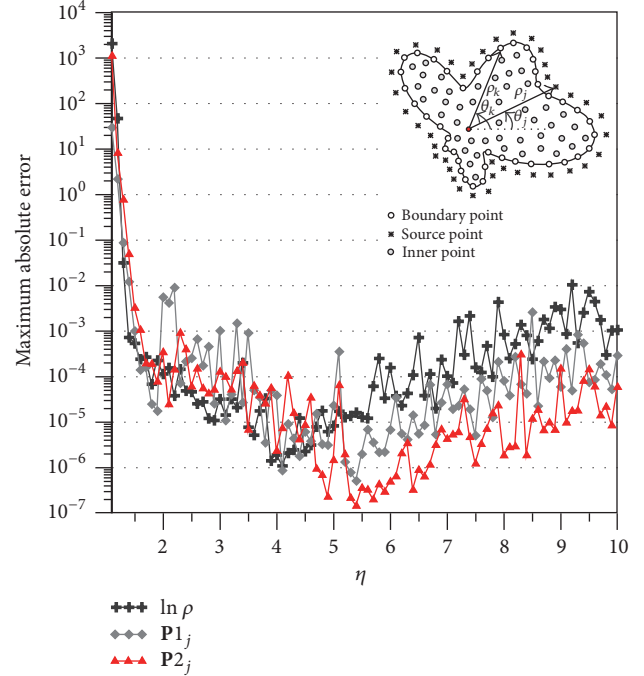


FIGURE 4: The accuracy of the maximum absolute error versus  $\eta$ .

example under investigation is in a simply connected domain. In this example, we investigated the accuracy by choosing locations of the source points through different  $\eta$  values using the MFS. Figure 4 shows that  $\eta = 4$  could be the satisfactory location of the source points.

Using  $\eta = 4$ , we conducted an example to clarify the approximate number of boundary collocation and the source points. For simplicity, we took the same number of the boundary points. To examine the accuracy, we collocated 1074 uniformly distributed inner points inside the domain, as shown in Figure 5. The maximum absolute error can then be found by evaluating the absolute error for each inner point.

Figure 5 depicted the computed results of the maximum absolute error versus the number of source points. It is well known that the linear algebraic equation systems may be ill-conditioned while the global basis functions were adopted. To clarify this issue, we investigated the condition number versus the number of source points. Figure 6 shows that the relationship of the condition number versus the number of source points for the proposed method and the MFS. For simplicity, we adopted the commercial program MATLAB backslash operator to solve the linear algebraic equation systems. It is found that the proposed method remains relatively high accuracy compared to the MFS in this example. The best accuracy can reach the order of  $10^{-8}$  while the number of source points is greater than 180. On the other hand, the best accuracy of the MFS can reach only about  $10^{-6}$  in the same example.

**3.2. Comparison of the Numerical Results.** Similar to the previous example, we verified the accuracy of the proposed

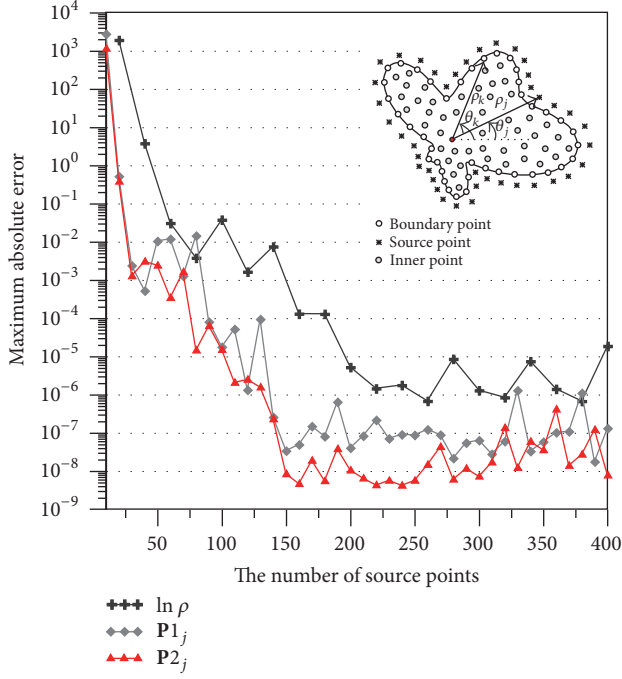


FIGURE 5: The accuracy of the maximum absolute error versus the number of source points.

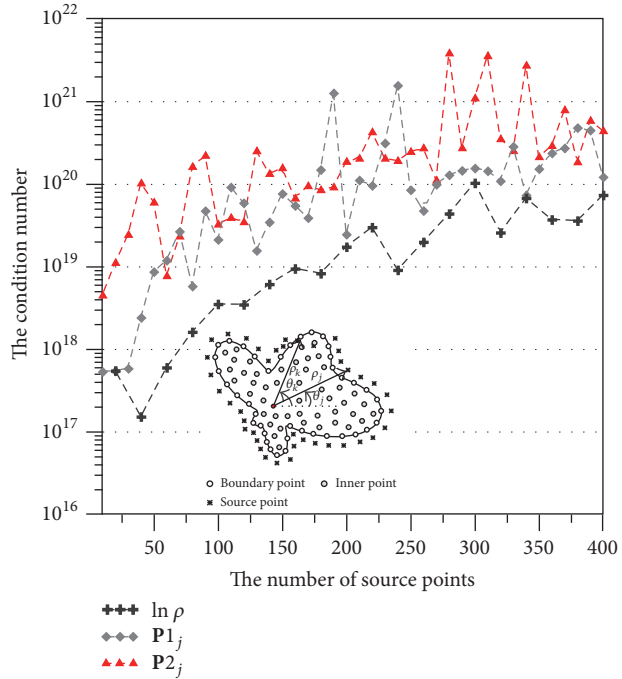
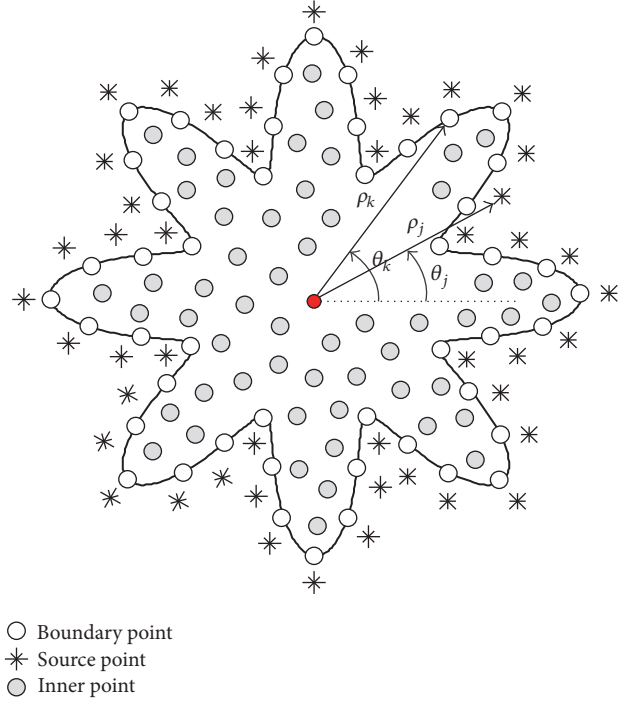


FIGURE 6: The condition number versus the number of source points.

method with the consideration of a complex star-like boundary. For a two-dimensional simply connected domain  $\Omega$  enclosed by a boundary, the subsurface flow equation can



be expressed as Laplace governing equation which can be expressed as

$$\nabla^2 h = 0 \quad \text{in } \Omega. \quad (21)$$

The two-dimensional object boundary under consideration is defined as

$$\Gamma = \{(x, y) \mid x = \rho(\theta) \cos \theta, y = \rho(\theta) \sin \theta\}, \quad (22)$$

where  $\rho(\theta) = 5(1 + (\cos(4\theta))^2)$ ,  $0 \leq \theta \leq 2\pi$ .

The analytical solution can be found as

$$h = (\sinh x + \cosh x)(\cos y + \sin y). \quad (23)$$

The Dirichlet boundary condition is imposed on the boundary by using the analytical solution as shown in (23) for the problem. Figure 7 shows the collocation point for the boundary and the source points. A sensitivity study using the MFS was first carried out and  $\eta = 3$  could be the satisfactory location of the source points, as shown in Figure 8. Also, to examine the accuracy, we collocated 3250 uniformly distributed inner points inside the domain, as shown in Figure 9. The maximum absolute error can then be found by evaluating the absolute error for each inner point.

Figure 9 depicted the computed results of the maximum absolute error versus the number of source points. Figure 10 shows the relationship of the condition number versus the number of source points for the proposed method and the MFS. It is found that the proposed method remains relatively high accuracy compared to the MFS in this example. The best

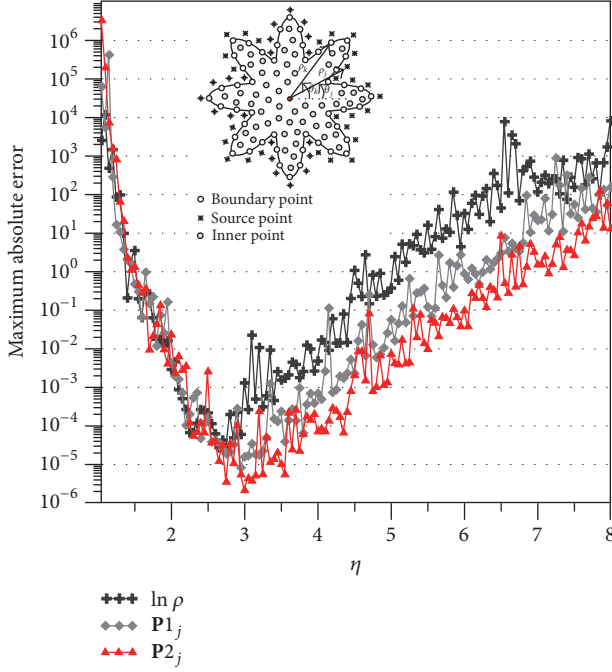


FIGURE 8: The accuracy of the maximum absolute error versus  $\eta$ .

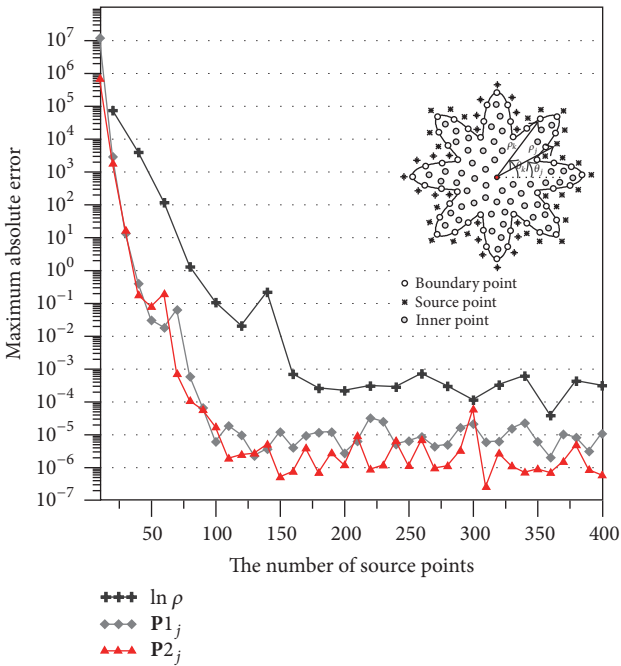


FIGURE 9: The accuracy of the maximum absolute error versus the number of source points.

accuracy can reach the order of  $10^{-6}$  while the number of source points is greater than 150. On the other hand, the best accuracy of the MFS can reach only about  $10^{-3}$  in the same example.

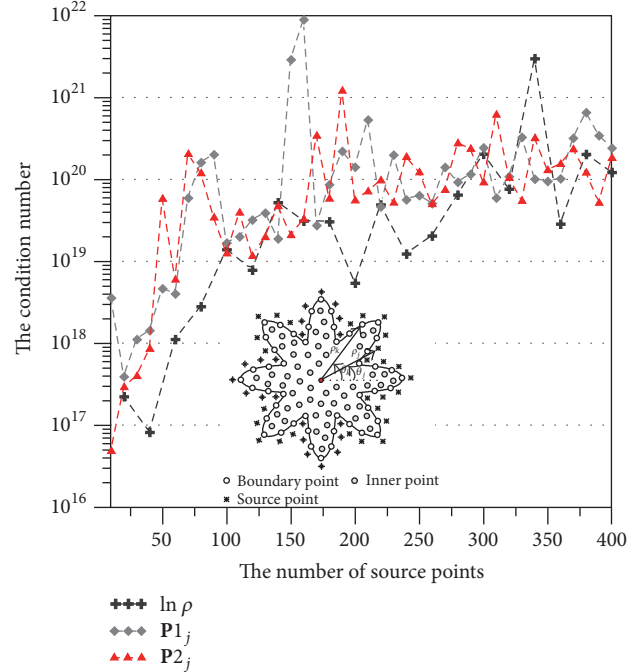


FIGURE 10: The condition number versus the number of source points.

#### 4. Application of the Proposed Method

**4.1. Modeling of Subsurface Flow with Free Surface.** The first application under investigation is a free surface seepage problem of a rectangular dam as depicted in Figure 11. The subsurface flow equation is the Laplace equation. The example with the upstream hydraulic head is 24 m, the downstream hydraulic head is 4 m, and the width of the rectangular dam is 16 m. The boundary conditions includes  $\Gamma_1$ ,  $\Gamma_2$ ,  $\Gamma_3$ ,  $\Gamma_4$ , and  $\Gamma_5$ , as depicted in Figure 11. In  $\Gamma_2$  and  $\Gamma_5$ , the Dirichlet boundary conditions are given as

$$\begin{aligned} h &= H_2 \quad \text{on } \Gamma_2, \\ h &= H_1 \quad \text{on } \Gamma_5. \end{aligned} \quad (24)$$

Based on the Bernoulli equation, we neglected the velocity head and the total head or the potential can be written as

$$h = Y(x) + \frac{p}{\gamma}, \quad (25)$$

where  $Y(x)$  is the elevation head,  $p$  is the pressure head, and  $\gamma$  is the unit weight of fluid. In  $\Gamma_3$  and  $\Gamma_4$ , the free surface boundaries are given as overspecified boundary conditions as

$$\frac{\partial h}{\partial n} = 0, \quad h = Y(x) \quad \text{on } \Gamma_3 \text{ and } \Gamma_4. \quad (26)$$

In  $\Gamma_1$ , the no-flow Neumann boundary condition to simulate the imperious boundary is given as

$$\frac{\partial h}{\partial n} = 0 \quad \text{on } \Gamma_1. \quad (27)$$

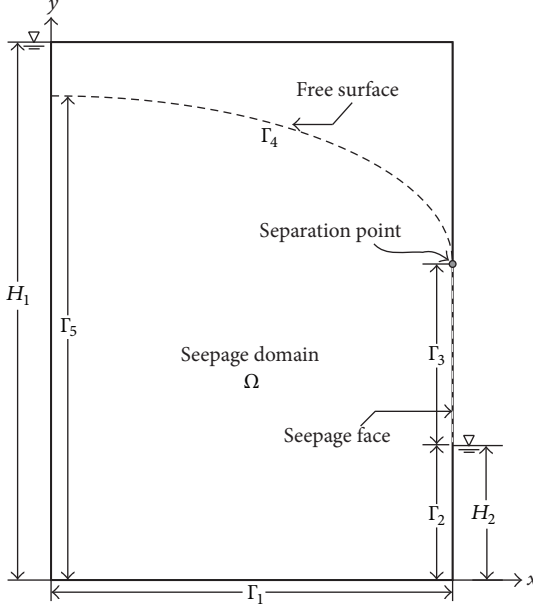


FIGURE 11: Subsurface flow with free surface through a rectangular dam.

Since  $h = Y(x)$  is unknown a priori which needs to be determined iteratively after the initial guess of the free surface, the proposed method adopted to find the location of free boundary is expressed in the following section.

The subsurface flow with a free surface is a nonlinear problem in which nonlinearities arise from the nonlinear boundary characteristics. Such nonlinearities are handled in the numerical modeling using iterative schemes. Typically, the methods, such as the Picard method or Newton's method, are iterative in that they approach the solution through a series of steps. In this study, the Picard method is adopted.

There are 16 boundary collocation nodes uniformly distributed in the initial guess of the moving boundary with the spacing of 1 m as shown in Figure 12. Figure 12 shows the computed results using the proposed method. There are 132 iterations to reach the stopping criterion using the Picard scheme. The numerical solutions of free surface were then compared with those obtained from Aitchison et al. [32, 33]. The separation point is the intersection of the free surface and the seepage face. The location of the separation point computed by this study is 13.19 m. It is found that the computed results agree closely with those from other methods.

**4.2. Free Surface Seepage Flow through Layered Heterogeneous Geological Media.** The previous examples have demonstrated that the proposed method can be used to deal with the subsurface flow with a free surface. Since the appearance of layered soil in heterogeneous geological media is much more common than homogeneous soil in nature, we further adopted the proposed method to deal with the subsurface flow problems of layered heterogeneous geological media using the DDM.

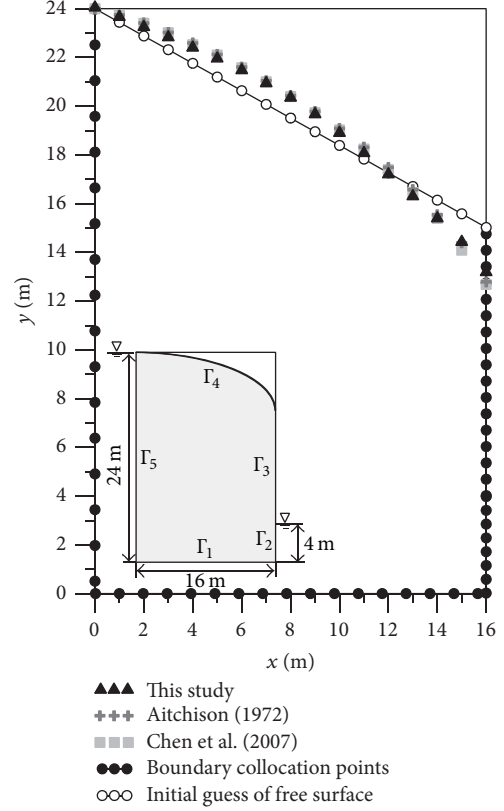


FIGURE 12: Result comparison of the computed free surface for a rectangular dam.

This example under investigation is a rectangular dam in layered soil as depicted in Figure 13. We considered the problem where the upstream hydraulic head is 10 m, the downstream hydraulic head is 2 m, and the height and the width of the rectangular dam are 10 m and 5 m, respectively. The boundary conditions including  $\Gamma_1, \Gamma_2, \dots, \Gamma_{10}$  are shown in Figure 13. At  $\Gamma_5$  and  $\Gamma_{10}$ , the Dirichlet boundary conditions are given as

$$\begin{aligned} h &= 10 \text{ m} & \text{on } \Gamma_5, \\ h &= 2 \text{ m} & \text{on } \Gamma_{10}. \end{aligned} \quad (28)$$

At  $\Gamma_3, \Gamma_4, \Gamma_8$ , and  $\Gamma_9$ , the free surface boundaries are given as overspecified boundary conditions as

$$\frac{\partial h}{\partial n} = 0, \quad h = Y(x) \quad \text{on } \Gamma_3, \Gamma_4, \Gamma_8, \Gamma_9. \quad (29)$$

At  $\Gamma_1$  and  $\Gamma_6$ , the no-flow Neumann boundary condition to simulate the imperious boundary is given as

$$\frac{\partial h}{\partial n} = 0 \quad \text{on } \Gamma_1, \Gamma_6. \quad (30)$$

To deal with the geofluid flow through layered heterogeneous geological media, the domain decomposition method was adopted. The solution continuity or compatibility between

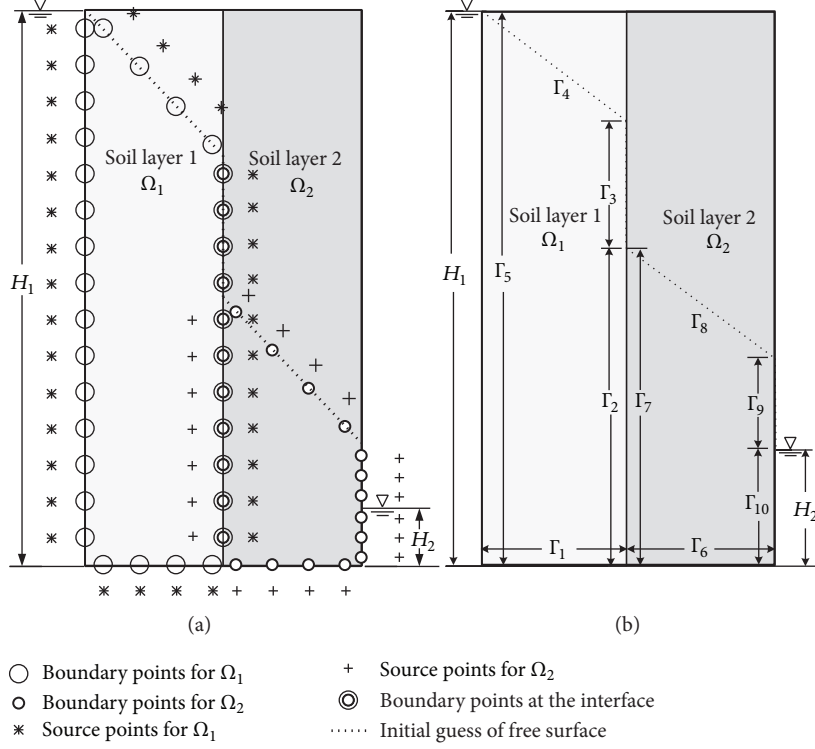


FIGURE 13: The collocation of boundary, source points (a) and configuration of boundary condition (b).

different subdomains was assured by remaining equal values of the pressure potential and the flux at the interface between subdomains. For instance, the free surface seepage flow through layered heterogeneous geological media as at  $\Gamma_2$  and  $\Gamma_7$ , the flux conservation, and the continuity of pressure potential at the interface between two consecutive layers have to ensure the solution continuity. Accordingly, the following additional boundary conditions must be given:

$$\begin{aligned} h|_{\Gamma_2} &= h|_{\Gamma_7} \quad \text{at } \Gamma_2, \Gamma_7, \\ k_1 \frac{\partial h}{\partial n}|_{\Gamma_2} &= k_2 \frac{\partial h}{\partial n}|_{\Gamma_7} \quad \text{at } \Gamma_2, \Gamma_7. \end{aligned} \quad (31)$$

There are two soil layers in this example. The values of the hydraulic conductivity for layer 1 and layer 2 are  $k_1$  and  $k_2$ , respectively, and  $k_1 = 0.1k_2$  and  $k_1 = 10^{-3}$  cm/s.

In this study, we adopted the nonoverlapping method to deal with the subsurface flow problems of layered soil profiles. The problems on the subdomains are independent, which makes the DDM suitable for describing the layered soil in heterogeneous porous media.

For the modeling of the layered soil, we split the domain into smaller subdomains in which subdomains were intersected only on the interface between soil layers, as shown in Figure 13. For example, there is a problem with two soil layers as shown in Figure 13. The hydraulic conductivities are  $k_1$  and  $k_2$  for soil layer 1 and soil layer 2, respectively. The boundary and source points were collocated in each subdomain. At the interface, the boundary collocation points on left and

right sides coincide with each other. The proposed method was then adopted to ensure that flux conservation and the continuity of pressure potential at the interface between two consecutive layers remain the same.

For the first subdomain, there are a total of 250 boundary collocation nodes where 50 boundary collocation nodes are uniformly distributed in the initial guess of the moving boundary. For the second subdomain, there are also a total of 250 boundary collocation nodes where 50 boundary collocation nodes are uniformly distributed in the initial guess of the moving boundary.

Figure 14 shows the computed results using the proposed method. There are 14 iterations to reach the stopping criterion using the Picard scheme. The numerical solutions of free surface were then compared with those obtained from previous studies [27, 34]. It is found that the computed results agree well with those from other methods.

**4.3. Modeling of Three-Dimensional Subsurface Flow Problem.** Because the basis function,  $P_j(\mathbf{x}, \mathbf{y}_j) = [\rho_j^{-2} \cos 2\theta_j \ \rho_j^{-2} \sin 2\theta_j]^T$ , is also the particular solution of the Laplace equation in three-dimensional cylindrical coordinate system, it implies that the basis function proposed in this study can also be used to solve the three-dimensional subsurface flow problems. Accordingly, the last example under investigation is a three-dimensional homogenous isotropic steady-state subsurface flow problem. For a three-dimensional simply connected domain  $\Omega$  enclosed by a

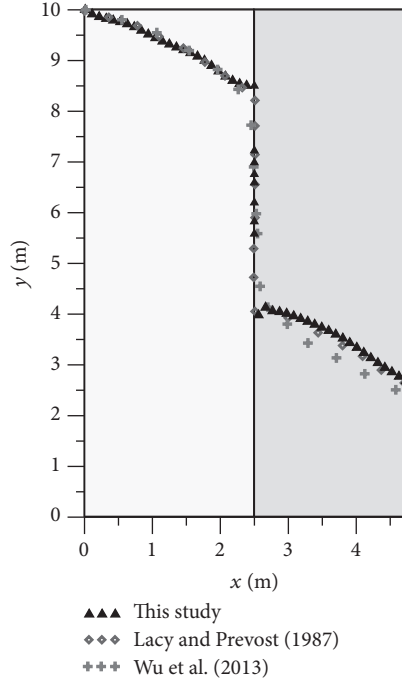


FIGURE 14: Comparison of free surface for a rectangular dam in layered heterogeneous geological media.

boundary as shown in Figure 15, the governing equation is expressed as

$$\nabla^2 h = 0 \quad \text{in } \Omega. \quad (32)$$

The boundary is defined as

$$\begin{aligned} \Gamma &= \{(x, y, z) \mid x = \rho(\theta) \cos \theta, y = \rho(\theta) \sin \theta \sin \phi, z \\ &= \rho(\theta) \sin \theta \cos \phi\}, \end{aligned} \quad (33)$$

where  $\rho(\theta) = e^{(\sin \theta \sin 2\theta)^2} + e^{(\cos \theta \cos 2\theta)^2}$ ,  $0 \leq \theta \leq 2\pi$ , and  $0 \leq z \leq 1$ .

The analytical solution of the problem is given as

$$h = xyz. \quad (34)$$

The Dirichlet boundary condition is imposed on the boundary by using the analytical solution as shown in (34) for the problem. Figure 15 shows the boundary collocation and the three-dimensional shape of the problem. A sensitivity study was first carried out and  $\eta = 80$  could be the satisfactory location of the source points, as shown in Figure 16. Also, to examine the accuracy, we collocated 889 uniformed distributed inner points inside the domain. The maximum absolute error can then be found by evaluating the absolute error for each inner point.

Figure 17 depicted the computed results of the maximum absolute error versus the number of source points. The best accuracy of the proposed method can reach the order of  $10^{-9}$  while the number of source points is greater than 350.

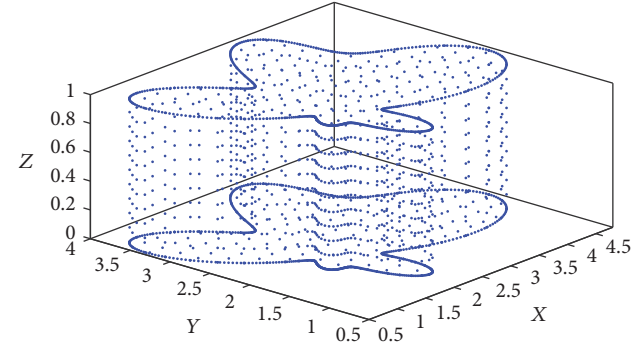


FIGURE 15: The boundary collocation points of three-dimensional subsurface flow problem.

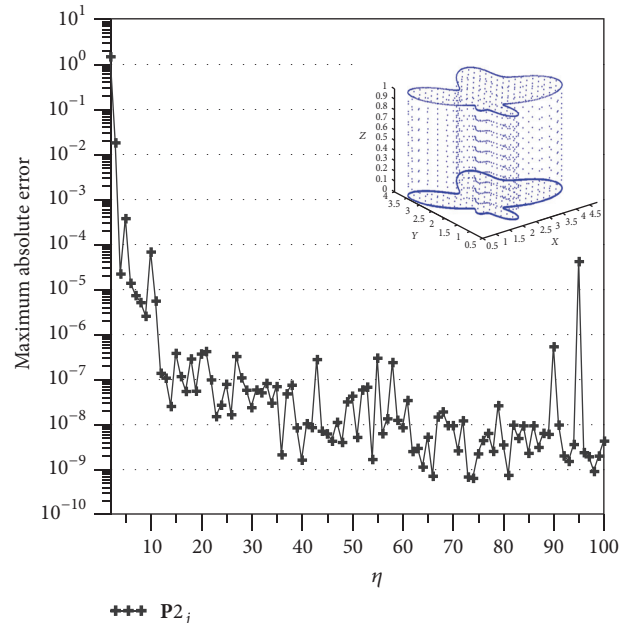


FIGURE 16: The accuracy of the maximum absolute error versus  $\eta$ .

## 5. Conclusions

This study has proposed a novel boundary-type meshless method for modeling geofluid flow in heterogeneous geological media. The numerical solutions of geofluid flow are approximated by a set of particular solutions of the subsurface flow equation which are expressed in terms of sources located outside the domain of the problem. To deal with the subsurface flow problems of heterogeneous geological media, the domain decomposition method was adopted. The validity of the model is established for a number of test problems. Application examples of subsurface flow problems with free surface were also carried out. The fundamental concepts and the construct of the proposed method are addressed in detail. The findings are addressed as follows.

In this study, a pioneering study is based on the collocation Trefftz method and provides a promising solution which integrates the T-Trefftz method and F-Trefftz method for constructing its basis function using one of the negative

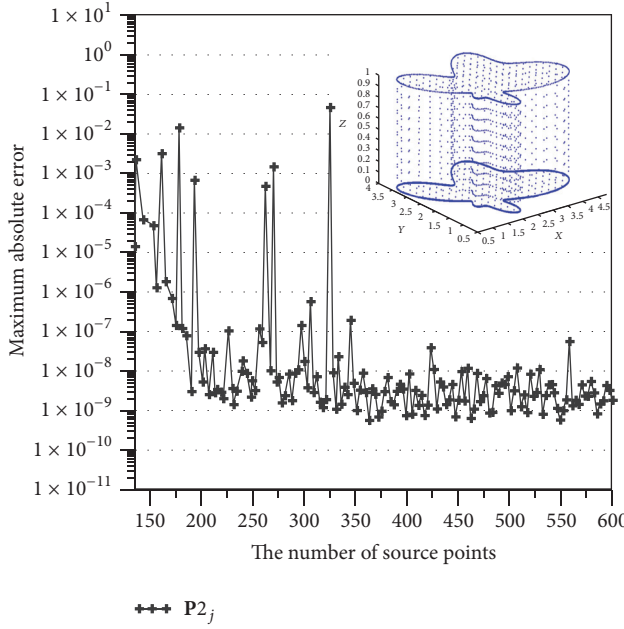


FIGURE 17: The accuracy of the maximum absolute error versus the number of source points.

particular solutions which satisfies the governing equation and allows many source points outside the domain of interest. The proposed method uses the same concept of the source points in the MFS, but the fundamental solutions can be replaced by the negative Trefftz functions. It may release one of the limitations of the MFS in which the fundamental solutions may be difficult to find.

It is well known that the system of linear equations obtained from the Trefftz method may also become an ill-posed system with the higher order of the terms. In this study, the proposed method integrates the collocation Trefftz method and the MFS which approximates the numerical solutions by superpositioning of the negative particular solutions as basis functions expressed in terms of many source points. As a result, only two Trefftz terms were adopted because many source points are allowed for approximating the solution. Meanwhile, the ill-posedness from adopting the higher order terms for the solution with only one source point in the collocation Trefftz method can be mitigated. In addition, results from the validation examples demonstrate that the proposed method may obtain better accuracy than the MFS.

The validity of the model is established for a number of test problems, including the investigation of the basis function using two possible particular solutions and the comparison of the numerical solutions using different particular solutions and the method of fundamental solutions. Application examples of subsurface flow problems with free surface were also carried out. Numerical results demonstrate that the proposed method is highly accurate and computationally efficient. This pioneering study demonstrates that the proposed boundary-type meshless method may be the first successful attempt for solving the subsurface flow with nonlinear free

surface in layered heterogeneous geological media which has not been reported in previous studies. Moreover, the application example depicted that the proposed method can be easily applied to the three-dimensional problems.

## Conflicts of Interest

The authors declare that there are no conflicts of interest regarding the publication of this paper.

## Acknowledgments

This study was partially supported by the Ministry of Science and Technology, Taiwan. The authors thank the Ministry of Science and Technology for the generous financial support.

## References

- [1] R. Allen and S. Sun, "Computing and comparing effective properties for flow and transport in computer-generated porous media," *Geofluids*, vol. 2017, Article ID 4517259, 2017.
- [2] M. H. Baziar and A. Graili, "A practical and efficient numerical scheme for the analysis of steady state unconfined seepage flows," *International Journal for Numerical and Analytical Methods in Geomechanics*, vol. 36, no. 16, pp. 1793–1812, 2012.
- [3] J. T. Chen, H.-K. Hong, and S. W. Chyuan, "Boundary element analysis and design in seepage problems using dual integral formulation," *Finite Elements in Analysis and Design*, vol. 17, no. 1, pp. 1–20, 1994.
- [4] J. Li and D. Brown, "Upscaled lattice boltzmann method for simulations of flows in heterogeneous porous media," *Geofluids*, vol. 2017, Article ID 1740693, 2017.
- [5] J. A. Liggett and L. F. Liu, *The Boundary Integral Equation Method for Porous Media Flow*, George Allen & Unwin, London, UK, 1983.
- [6] C.-Y. Ku, C.-L. Kuo, C.-M. Fan, C.-S. Liu, and P.-C. Guan, "Numerical solution of three-dimensional Laplacian problems using the multiple scale Trefftz method," *Engineering Analysis with Boundary Elements*, vol. 50, pp. 157–168, 2015.
- [7] W. Yeih, I.-Y. Chan, C.-Y. Ku, and C.-M. Fan, "Solving the inverse cauchy problem of the laplace equation using the method of fundamental solutions and the exponentially convergent scalar homotopy algorithm (ECSHA)," *Journal of Marine Science and Technology (Taiwan)*, vol. 23, no. 2, pp. 162–171, 2015.
- [8] C.-Y. Ku, "On solving three-dimensional laplacian problems in a multiply connected domain using the multiple scale trefftz method," *CMES: Computer Modeling in Engineering & Sciences*, vol. 98, no. 5, pp. 509–541, 2014.
- [9] C.-Y. Ku, "A novel method for solving ill-conditioned systems of linear equations with extreme physical property contrasts," *CMES. Computer Modeling in Engineering & Sciences*, vol. 96, no. 6, pp. 409–434, 2013.
- [10] J.-S. Chen, M. Hillman, and S.-W. Chi, "Meshfree methods: Progress made after 20 years," *Journal of Engineering Mechanics*, vol. 143, no. 4, Article ID 04017001, 2017.
- [11] C.-M. Fan, H.-F. Chan, C.-L. Kuo, and W. Yeih, "Numerical solutions of boundary detection problems using modified collocation Trefftz method and exponentially convergent scalar homotopy algorithm," *Engineering Analysis with Boundary Elements*, vol. 36, no. 1, pp. 2–8, 2012.

- [12] E. Kita and N. Kamiya, "Treffitz method: an overview," *Advances in Engineering Software*, vol. 24, no. 1-3, pp. 3–12, 1995.
- [13] E. Kita, N. Kamiya, and T. Iio, "Application of a direct Trefftz method with domain decomposition to 2D potential problems," *Engineering Analysis with Boundary Elements*, vol. 23, no. 7, pp. 539–548, 1999.
- [14] Z.-C. Li, T.-T. Lu, H.-Y. Hu, and A. H.-D. Cheng, *Trefftz and Collocation Methods*, WIT Press, Southampton, UK, 2008.
- [15] C.-S. Liu, "A modified Trefftz method for two-dimensional Laplace equation considering the domain's characteristic length," *CMES: Computer Modeling in Engineering & Sciences*, vol. 21, no. 1, pp. 53–65, 2007.
- [16] E. Trefftz, "Ein Gegenstück zum Ritzschen Verfahren," in *Proceedings of the 2nd International Congress for Applied Mechanics*, pp. 131–137, 1926.
- [17] V. D. Kupradze and M. A. Aleksidze, "The method of functional equations for the approximate solution of certain boundary value problems," *USSR Computational Mathematics and Mathematical Physics*, vol. 4, no. 4, pp. 82–126, 1964.
- [18] M. Katsurada and H. Okamoto, "The collocation points of the fundamental solution method for the potential problem," *Computers & Mathematics with Applications*, vol. 31, no. 1, pp. 123–137, 1996.
- [19] J. T. Chen, C. S. Wu, Y. T. Lee, and K. H. Chen, "On the equivalence of the Trefftz method and method of fundamental solutions for Laplace and biharmonic equations," *Computers & Mathematics with Applications. An International Journal*, vol. 53, no. 6, pp. 851–879, 2007.
- [20] T. Belytschko, Y. Y. Lu, and L. Gu, "Element-free Galerkin methods," *International Journal for Numerical Methods in Engineering*, vol. 37, no. 2, pp. 229–256, 1994.
- [21] W. K. Liu, S. Jun, and Y. F. Zhang, "Reproducing kernel particle methods," *International Journal for Numerical Methods in Fluids*, vol. 20, no. 8-9, pp. 1081–1106, 1995.
- [22] J.-S. Chen, C. Pan, C.-T. Wu, and W. K. Liu, "Reproducing kernel particle methods for large deformation analysis of non-linear structures," *Computer Methods Applied Mechanics and Engineering*, vol. 139, no. 1-4, pp. 195–227, 1996.
- [23] T. Zhu, J. Zhang, and S. N. Atluri, "Meshless numerical method based on the local boundary integral equation (LBIE) to solve linear and non-linear boundary value problems," *Engineering Analysis with Boundary Elements*, vol. 23, no. 5, pp. 375–389, 1999.
- [24] J. Sladek, V. Sladek, and S. N. Atluri, "Local boundary integral equation (LBIE) method for solving problems of elasticity with nonhomogeneous material properties," *Computational Mechanics*, vol. 24, no. 6, pp. 456–462, 2000.
- [25] H. Lin and S. N. Atluri, "Meshless local Petrov-Galerkin (MLPG) method for convection-diffusion problems," *CMES-Computer Modeling in Engineering & Sciences*, vol. 1, no. 2, pp. 45–60, 2000.
- [26] D.-L. Young, C.-M. Fan, C.-C. Tsai, and C.-W. Chen, "The method of fundamental solutions and domain decomposition method for degenerate seepage flownet problems," *Journal of the Chinese Institute of Engineers, Transactions of the Chinese Institute of Engineers, Series A/Chung-kuo Kung Ch'eng Hsueh Kan*, vol. 29, no. 1, pp. 63–73, 2006.
- [27] S. J. Lacy and J. H. Prevost, "Flow through porous media: A procedure for locating the free surface," *International Journal for Numerical and Analytical Methods in Geomechanics*, vol. 11, no. 6, pp. 585–601, 1987.
- [28] S. Mehl, "Use of Picard and Newton iteration for solving nonlinear ground water flow equations," *Groundwater*, vol. 44, no. 4, pp. 583–594, 2006.
- [29] W. Yeih, C.-S. Liu, C.-L. Kuo, and S. N. Atluri, "On solving the direct/inverse cauchy problems of laplace equation in a multiply connected domain, using the generalized multiple-source-point boundary-collocation Trefftz method & characteristic lengths," *CMC: Computer, Materials, & Continua*, vol. 17, no. 3, pp. 275–302, 2010.
- [30] C.-Y. Ku, J.-E. Xiao, C.-Y. Liu, and W. Yeih, "On the accuracy of the collocation Trefftz method for solving two- and three-dimensional heat equations," *Numerical Heat Transfer, Part B: Fundamentals*, vol. 69, no. 4, pp. 334–350, 2016.
- [31] C. S. Chen, A. Karageorghis, and Y. Li, "On choosing the location of the sources in the MFS," *Numerical Algorithms*, vol. 72, no. 1, pp. 107–130, 2016.
- [32] J. Aitchison, "Numerical treatment of a singularity in a free boundary problem," *Proceedings of the Royal Society A Mathematical, Physical and Engineering Sciences*, vol. 330, pp. 573–580, 1972.
- [33] J.-T. Chen, C.-C. Hsiao, Y.-P. Chiu, and Y.-T. Lee, "Study of free-surface seepage problems using hypersingular equations," *Communications in Numerical Methods in Engineering*, vol. 23, no. 8, pp. 755–769, 2007.
- [34] M. X. Wu, L. Z. Yang, and T. Yu, "Simulation procedure of unconfined seepage with an inner seepage face in a heterogeneous field," *Science China Physics, Mechanics & Astronomy*, vol. 56, no. 6, pp. 1139–1147, 2013.

## Research Article

# Characterization of Aquifer Multiscale Properties by Generating Random Fractal Field with Truncated Power Variogram Model Using Karhunen–Loève Expansion

Liang Xue,<sup>1,2</sup> Diao Li,<sup>1</sup> Cheng Dai,<sup>3</sup> and Tongchao Nan<sup>4</sup>

<sup>1</sup>Department of Oil-Gas Field Development, College of Petroleum Engineering, China University of Petroleum, Beijing 102249, China

<sup>2</sup>State Key Laboratory of Petroleum Resources and Engineering, China University of Petroleum, Beijing 102249, China

<sup>3</sup>State Key Laboratory of Shale Oil and Gas Enrichment Mechanisms and Effective Development, Sinopec Group, Beijing 100083, China

<sup>4</sup>Department of Hydrosciences, School of Earth Sciences and Engineering, Nanjing University, Nanjing 210093, China

Correspondence should be addressed to Tongchao Nan; tcnan@nju.edu.cn

Received 29 June 2017; Revised 31 October 2017; Accepted 28 November 2017; Published 19 December 2017

Academic Editor: Walter A. Illman

Copyright © 2017 Liang Xue et al. This is an open access article distributed under the Creative Commons Attribution License, which permits unrestricted use, distribution, and reproduction in any medium, provided the original work is properly cited.

The traditional geostatistics to describe the spatial variation of hydrogeological properties is based on the assumption of stationarity or statistical homogeneity. However, growing evidences show and it has been widely recognized that the spatial distribution of many hydrogeological properties can be characterized as random fractals with multiscale feature, and spatial variation can be described by power variogram model. It is difficult to generate a multiscale random fractal field by directly using nonstationary power variogram model due to the lack of explicit covariance function. Here we adopt the stationary truncated power variogram model to avoid this difficulty and generate the multiscale random fractal field using Karhunen–Loève (KL) expansion. The results show that either the unconditional or conditional (on measurements) multiscale random fractal field can be generated by using truncated power variogram model and KL expansion when the upper limit of the integral scale is sufficiently large, and the main structure of the spatial variation can be described by using only the first few dominant KL expansion terms associated with large eigenvalues. The latter provides a foundation to perform dimensionality reduction and saves computational effort when analyzing the stochastic flow and transport problems.

## 1. Introduction

Groundwater resources management and contamination prevention are the important issues to sustain the development of human society. One of the most challenging tasks to address these issues is to describe the heterogeneity of the hydrogeological parameters, such as hydraulic conductivity and porosity over scales. Many techniques have been devoted to obtain more information on the heterogeneity of the hydrogeological parameters in different scales, such as core samples analysis [1], direct push technology [2], and hydraulic tomography [3]. Due to the complex nature of the spatial distribution of these hydrogeological parameters, these parameters tend to be treated as random variables, and thus their spatial distribution can be quantitatively described using stochastic process [4, 5]. The governing equations

of groundwater flow and contaminant transport become stochastic partial differential equations. In this manner, the state variables, such as hydraulic head, velocity, and contaminant concentration, are predicted with uncertainty. The merit of the stochastic method is that it can produce the probabilistic distribution of the prediction. The best prediction (quantified by the first moment, i.e., mean) and the associated uncertainty (quantified by the second moment, variance/covariance) can be inferred from this distribution. Geostatistics was introduced to hydrogeology and became popular in numerical simulation of groundwater flow and solute transport [6–8]. The assumption underlying the traditional geostatistics [9] is that the spatial distribution of the hydrogeological property is statistically homogeneous; that is, the joint probability of hydrogeological parameters depends only on their relative locations, but not on the exact locations.

TABLE 1: Comparison of the existing methods to generate random fractal field.

Tool	Variogram type	Conditioning	Dimensionality reduction	Reference
GSLIB	Stationary	Yes	No	Deutsch and Journel, 1997
GSLIB-TPV	Stationary and nonstationary	Yes	No	Xue and Zhang, 2014; Xue et al., 2014
Spectral methods	Stationary and nonstationary	No	No	Heße et al., 2014
Fractal method	Stationary and nonstationary	No	No	Dieker, 2004
KL-TPV	Stationary and nonstationary	Yes	Yes	Current method

However, it is evident that the random hydrogeological field may manifest it as random fractals with statistically homogeneous increments [10–14]. Stochastic fractal models to characterize such random field include Gaussian-based fractional Brownian motion and fractional Gaussian noise [10, 12, 15], non-Gaussian-based fractional Levy motion or fractional Levy noise [13], and multifractals [16]. The Gaussian-based fractional Brownian motion model that can be characterized by power law variogram can be inferred from collected hydrogeological data, such as permeability or porosity, at several sites over diversified distance scales [12, 17]. The random field described using such model exhibits the self-affine scaling properties and thus can take the multiscale variation into account.

To analyze the scale-dependency of the random fractal field and investigate the effect of multiscale random fractals to the behavior of groundwater flow and contaminant transport, it requires generating the realizations of hydrogeological properties based on their stochastic characteristics. If measurements on the hydrogeological properties are directly available, the generated multiscale random fractal field should be further conditional on the measurement values. The most common method used to generate a Gaussian random field is sequential Gaussian simulation (SGSIM) due to the wide usage of geostatistical software library (GSLIB) developed by Deutsch and Journel [9]. Although power variogram model is included in GSLIB, it can not be used directly to generate a multiscale random fractals field. The traditional geostatistical method can only generate Gaussian random field with the assumption of stationarity or statistical homogeneity. Since the power variogram does not have a finite sill and integral scale and lacks an explicit form of covariance function, the SGSIM module in GSLIB does not have the support to use power variogram. The spectral method can be used to generate a multiscale random fractals field, which represents the random field in Fourier space and thus can be referred to as Fourier method [18]. The Fourier method has been improved to be a hierarchical method, such as the hybrid method [19] and Fourier-Wavelet method [20].

In this work, we adopt a truncated power variogram model proposed by Di Federico and Neuman [21] to generate the multiscale random fractal field that can be characterized by power variogram model. The truncated power variogram can describe the multiscale characteristics of the random field and can take measurement scale, observation scale, and

window scale into account. This model also has a reasonable hydrogeological interpretation, which states that the power law variogram behavior of log hydraulic conductivity random field can be considered as a weighted integral of infinite hierarchies of mutually uncorrelated stationary fields. After truncating the higher and/or lower frequency, the truncated power variogram models become stationary and have explicit forms of covariance functions. Each hierarchy is referred to as a mode in the spectra of such random field. Mathematically, it has been proved that each mode can be characterized by either the exponential or the Gaussian variogram. It renders two types of truncated power variogram: truncated power variogram with exponential modes (TpvE) and truncated power variogram with Gaussian modes (TpvG). We have modified the GSLIB code to incorporate these truncated power variogram models to generate random fractal field, both unconditional and conditional, using sequential Gaussian simulation method [22]. Other methods can also generate random fractal field, such as the spectral methods [23] and fractal method [24]. However, these existing methods do not have the capability to generate the conditional random field. The conditioning data of hydrogeological properties are usually available and they are critical components to improve the characterization of the targeted field. Therefore, it is necessary to take these hard data into account by the conditioning technique. The comparison of the existing methods to generate random fractal fields is listed in Table 1. Here in this work, an innovative method to generate the multiscale random fractal field is proposed by incorporating the truncated power variogram models with Karhunen–Loève (KL) expansion method. The advantage of the proposed method is that KL expansion has the capability to conduct the model dimensionality reduction. If it is further incorporated with polynomial chaos expansion on the state variables, such as hydraulic head in the single-phase flow problem [25], saturation in the multiphase problem [26], and contaminant transport problem [27], the computational cost to perform uncertainty analysis in the hydrological research can be greatly reduced. The proposed KL-based multiscale random fractal field generator provides the foundation to establish a high-efficiency stochastic analysis framework.

The rest of the paper is arranged as follows: the theoretical bases of truncated power variogram model and KL expansion are introduced in Section 2; the results of unconditional and conditional multiscale random fractal field generations and

the capability of KL expansion to perform dimensionality reduction are presented in Section 3; and the conclusions are drawn in Section 4.

## 2. Methodology

**2.1. Truncated Power Variogram Models.** The heterogeneous log hydraulic conductivity, denoted as  $Y$ , random fractal field with statistical homogeneous increments, can be described using power variogram model:

$$\gamma(s) = A_0 s^{2H}, \quad (1)$$

where  $A_0$  is a constant,  $H$  is Hurst coefficient ( $0 < H < 1$ ), and  $s$  is the lag distance.

The log hydraulic conductivity random field is self-affine since the power variogram function has the scaling property:

$$\gamma(rs) = r^{2H} \gamma(s), \quad (2)$$

where  $r$  is any positive constant ( $r > 0$ ).

The fractal dimension of the self-affine log hydraulic conductivity random field is

$$d = E + 1 - H, \quad (3)$$

where  $E$  is the Euclidean or topologic dimension.

Define the mode number  $n = 1/I$  representing the spatial frequency of random fluctuation (where  $I$  is the integral scale), integrate continuously over all the possible modes within the range  $[n_l, n_u]$ , and weight each mode with a factor of  $1/n$  [21],

$$\gamma(s, n_l, n_u) = \int_{n_l}^{n_u} \gamma(s, n) \frac{1}{n} dn, \quad (4)$$

where the lower and upper limits of mode number  $n_l$  and  $n_u$  correspond with the upper and lower limits of integral scale  $I_u$  and  $I_l$  due to the reciprocal relationship. The upper limit of integral scale  $I_u$  is proportional to the characterization length of window scale (e.g., the domain size of an aquifer), and the lower limit of integral scale  $I_l$  is proportional to the characterization length of data support or measurement scale (e.g., the size of the soil core). It can be noted that the truncated variogram  $\gamma(s, n_l, n_u)$  is a linear combination of the variogram  $\gamma(s, n)$  in each mode weighted by  $1/n$  (where  $n$  is always positive,  $n > 0$ ); therefore the property of truncated variogram  $\gamma(s, n_l, n_u)$  holds that of  $\gamma(s, n)$ ; that is,  $\gamma(s, n_l, n_u)$  is conditionally negative definite function if variogram function  $\gamma(s, n)$  (that can be in the form of exponential and Gaussian variogram as will be shown soon) is conditionally negative definite function. It also indicates that the corresponding truncated covariance function  $C(s, n_l, n_u)$  is positive definite if covariance function  $C(s, n)$  (here can be exponential and Gaussian covariance) is positive defined, since the truncated covariance function is stationary.

If each statistically homogeneous mode in an infinite hierarchy log hydraulic conductivity random field with uncorrelated spatial increments can be characterized by exponential variograms in terms of  $I$  integral scale,

$$\gamma(s, I) = \sigma^2(I) \left[ 1 - \exp\left(-\frac{s}{I}\right) \right], \quad (5)$$

where  $\sigma^2(I) = AI^{2H}$  is the variance of log hydraulic conductivity and  $A$  is a constant.

The consequent truncated power variogram model with exponential modes (TpvE) is

$$\gamma(s, I_l, I_u) = \gamma(s, I_u) - \gamma(s, I_l) \quad (6)$$

with the analytical form ( $0 < H \leq 0.5$ )

$$\begin{aligned} \gamma(s, I_m) = & \frac{AI_m^{2H}}{2H} \left[ 1 - \exp\left(-\frac{s}{I_m}\right) \right. \\ & \left. + \left(\frac{s}{I_m}\right)^{2H} \Gamma\left(1 - 2H, \frac{s}{I_m}\right) \right], \end{aligned} \quad (7)$$

where  $m = l, u$  and  $\Gamma(\cdot, \cdot)$  is the incomplete gamma function.

The corresponding covariance function of TpvE model is

$$C(s, I_l, I_u) = C(s, I_u) - C(s, I_l) \quad (8)$$

with the analytical form

$$\begin{aligned} C(s, I_m) = & \frac{AI_m^{2H}}{2H} \left[ \exp\left(-\frac{s}{I_m}\right) + \left(\frac{s}{I_m}\right)^{2H} \Gamma\left(1 - 2H, \frac{s}{I_m}\right) \right]. \end{aligned} \quad (9)$$

If each statistically homogeneous mode in an infinite hierarchy random field with uncorrelated spatial increments can be characterized by Gaussian variogram,

$$\gamma(s, I) = \sigma^2(I) \left[ 1 - \exp\left(-\frac{\pi s^2}{4I^2}\right) \right]. \quad (10)$$

The analytical form of truncated power variogram model with Gaussian modes (TpvG) is ( $0 < H \leq 1$ ):

$$\begin{aligned} \gamma(s, I_m) = & \frac{AI_m^{2H}}{2H} \left[ 1 - \exp\left(-\frac{\pi}{4} \frac{s^2}{I_m^2}\right) \right. \\ & \left. + \left(\frac{\pi}{4} \frac{s^2}{I_m^2}\right)^H \Gamma\left(1 - H, \frac{\pi}{4} \frac{s^2}{I_m^2}\right) \right]. \end{aligned} \quad (11)$$

The corresponding analytical form of TpvG covariance is

$$\begin{aligned} C(s, I_m) = & \frac{AI_m^{2H}}{2H} \left[ \exp\left(-\frac{\pi}{4} \frac{s^2}{I_m^2}\right) \right. \\ & \left. + \left(\frac{\pi}{4} \frac{s^2}{I_m^2}\right)^H \Gamma\left(1 - H, \frac{\pi}{4} \frac{s^2}{I_m^2}\right) \right]. \end{aligned} \quad (12)$$

If the lower limit  $\lambda_l$  approaches 0 (i.e., the point measurement scale) when the size of the log hydraulic conductivity measurement is so small that it can be treated as a point and the upper limit  $\lambda_u$  approaches infinity (i.e., infinitely large window scale or domain size), the truncated variogram models can also reduce the power variogram model (1) with the condition

$$A_0 = \frac{A\Gamma(1 - 2H)}{2H} \quad \text{for TpvE model,} \quad (13)$$

$$A_0 = \frac{A(\pi/4)^H \Gamma(1 - H)}{2H} \quad \text{for TpvG model.} \quad (14)$$

**2.2. KL Expansion of Stochastic Process.** The spatial distribution of hydrogeological variables, such as log hydraulic conductivity  $Y$ , can be treated as a stochastic process. The covariance function  $C(\mathbf{x}, \mathbf{y})$ , as in (9) for TpvE and in (12) for TpvG, of a zero-mean stochastic process,  $Y(\mathbf{x})$ , is bounded, symmetric, and positive definite, and it can be expanded as

$$C_Y(\mathbf{x}, \mathbf{y}) = \sum_{n=1}^{\infty} \lambda_n f_n(\mathbf{x}) f_n(\mathbf{y}), \quad (15)$$

where  $\mathbf{x}, \mathbf{y}$  is the spatial coordinate in a topological space  $\mathbf{D}$ , the lag distance  $s = |\mathbf{x} - \mathbf{y}|$ ,  $\lambda_n$  is the eigenvalue, and  $f_n(\mathbf{x})$  is eigenfunction.

The eigenfunctions are orthogonal and form a complete set. They satisfy the condition

$$\int_D f_n(\mathbf{x}) f_m(\mathbf{x}) d\mathbf{x} = \delta_{nm}, \quad (16)$$

where  $\delta_{nm}$  is the Kronecker delta function.

The KL expansion of the stochastic process can be expressed as

$$Y(\mathbf{x}) = \sum_{n=1}^{\infty} \xi_n \sqrt{\lambda_n} f_n(\mathbf{x}), \quad (17)$$

where  $\xi_n$  is the standard Gaussian random variable following the normal distribution  $N(0, 1)$ . The unconditional random field can be generated by using this equation by finding its eigenvalues and eigenfunctions with the stochastic characteristics known.

The eigenvalues and eigenfunctions of the covariance function can be solved from the Fredholm equation

$$\int_D C_Y(\mathbf{x}, \mathbf{y}) f(\mathbf{x}) d\mathbf{x} = \lambda f(\mathbf{y}). \quad (18)$$

If there are  $n_Y$  measurements  $Y_1(\mathbf{x}_1), Y_2(\mathbf{x}_2), \dots, Y_{n_Y}(\mathbf{x}_{n_Y})$ , it may require generating random field conditioning on these measurements. The generation of the conditional random field can be achieved by the conditional Kriging. The conditional Kriging mean and variance are, respectively,

$$E(Y(\mathbf{x}))^{(c)} = E(Y(\mathbf{x})) + \sum_{i=1}^{n_Y} \mu_i(\mathbf{x}) [Y(\mathbf{x}_i) - E(Y(\mathbf{x}))], \quad (19)$$

$$C_Y^{(c)}(\mathbf{x}, \mathbf{y}) = C_Y(\mathbf{x}, \mathbf{y}) - \sum_{i=1}^{n_Y} \mu_i(\mathbf{x}) C_Y(\mathbf{x}_i, \mathbf{y}),$$

where  $\mu_i(\mathbf{x})$  are weighting functions and the subscript  $c$  represents "conditional."

The weighting function can be computed by using the following Kriging equations:

$$\sum_{i=1}^{n_Y} \mu_i(\mathbf{x}) C_Y(\mathbf{x}_i, \mathbf{y}) = C_Y(\mathbf{x}, \mathbf{y}), \quad j = 1, 2, \dots, n_Y. \quad (20)$$

Since the set of eigenfunctions  $\{f_n(\mathbf{x})\}$  is complete, we can expand  $\mu_i(\mathbf{x})$  on the basis of  $\{f_n(\mathbf{x})\}$ ,

$$\mu_i(\mathbf{x}) = \sum_{k=1}^{\infty} \mu_{ik} f_k(\mathbf{x}), \quad (21)$$

where  $\mu_{ik}$  is the coefficients to be determined.

Substitute this expansion to Kriging equation (20), multiply  $f_m(\mathbf{x})$ , and integrate both sides with respect to  $\mathbf{x}$  over the domain  $D$ :

$$\sum_{i=1}^{n_Y} \mu_{im} C_Y(\mathbf{x}_i, \mathbf{y}) = \lambda_m f_m(\mathbf{y}). \quad (22)$$

Similar to unconditional case, the conditional eigenvalues  $\lambda_n^{(c)}$  and eigenfunctions  $f_n^{(c)}(\mathbf{x})$  of the conditional covariance functions  $C_Y^{(c)}(\mathbf{x}, \mathbf{y})$  can be solved from the following Fredholm equation:

$$\int_D C_Y^{(c)}(\mathbf{x}, \mathbf{y}) f^{(c)}(\mathbf{x}) d\mathbf{x} = \lambda^{(c)} f^{(c)}(\mathbf{y}). \quad (23)$$

To determine  $f_n^{(c)}(\mathbf{x})$ , we expand it in terms of unconditional eigenfunctions  $f_n(\mathbf{x})$  in a similar way to Kriging coefficients. Write the conditional eigenfunction as

$$f^{(c)}(\mathbf{x}) = \sum_{m=1}^M d_m f_m(\mathbf{x}). \quad (24)$$

Substituting this expression into (23), multiply  $f_m(\mathbf{y})$  and integrate it with respect to  $\mathbf{y}$  over  $D$ ,

$$\begin{aligned} & \sum_{k=1}^M (\lambda_m \delta_{km}) d_k - \sum_{k=1}^M \left( \sum_{i=1}^{n_Y} \mu_{ik} \lambda_m f_m(\mathbf{x}_i) \right) d_k \\ &= \sum_{k=1}^M (\lambda^{(c)} \delta_{km}) d_k. \end{aligned} \quad (25)$$

Write it in the matrix form

$$(\mathbf{A} - \lambda^{(c)} \mathbf{E}) \mathbf{d} = 0, \quad (26)$$

where the components of  $\mathbf{A} = (a_{km})_{M \times M}$ ,  $a_{km} = \lambda_m \delta_{km} - \sum_{i=1}^{n_Y} \mu_{ik} \lambda_m f_m(\mathbf{x}_i)$ , and  $\mathbf{E}$  is  $M \times M$  identity matrix. This equation indicates that the problem of finding the eigenvalues of conditional covariance function can be transformed into the problem of finding the eigenvalues of matrix  $\mathbf{A}$ .

After finding the eigenvalue of matrix  $\mathbf{A}$ ,  $\lambda^{(c)}$ , the corresponding eigenvector  $\mathbf{d}$  can be used to construct the conditional eigenfunction of the conditional covariance

$$f_n^{(c)}(\mathbf{x}) = \sum_{i=1}^M d_m f_i(\mathbf{x}). \quad (27)$$

Once the eigenvalue  $\lambda^{(c)}$  and eigenfunction  $f_n^{(c)}(\mathbf{x})$  of conditional covariance function are obtained, the conditional

log hydraulic conductivity random field can be generated using

$$Y(\mathbf{x}) = \sum_{n=1}^N z_n \sqrt{\lambda_n^{(c)}} f_n^{(c)}(\mathbf{x}), \quad (28)$$

where  $N$  is the number of terms required to generate the conditional random field and  $z_n \sim N(0, 1)$  is the standard Gaussian random variable.

### 3. Results and Discussion

**3.1. Equivalency Condition of Truncated Power Variogram and Power Variogram Models.** To investigate the equivalency of statistically homogeneous or stationary truncated power variogram models and nonstationary power variogram model with homogeneous increments, a set of different  $I_u$  values in the truncated power variogram models are used in the increasing order to compare with the corresponding power variogram model. The results obtained by TpvE and TpvG models are very similar to each other, and it may be redundant to show both results in this work. Due to the larger range of  $H$  parameter in the TpvG model and thus its flexibility (especially in the inverse modeling process when observation scale needs to be accounted for), only the results obtained by TpvG model is shown in this paper. The lower limit  $I_l$  approaching to 0 corresponds with a point scale measurement. In reality, most of the measurements, such as the permeability measurements of soil cores, satisfy this condition since its scale is much smaller than the scale of domain size. Therefore, we set  $I_l$  as 0 and vary  $I_u$  in an increasing order to show the equivalency of TpvG with power variogram within a prescribed finite range of lag distance. As shown in (1) and (11), the parameter set is  $\{A, H, I_u\}$  for TpvG model with a point measurement scale and  $\{A_0, H\}$  for power variogram model. The relationship of  $A$  and  $A_0$  is described by (14). Here, we set the parameter set of TpvG as  $\{A, H\} = \{0.02, 0.25\}$  and the corresponding parameter set for power variogram model is  $\{A_0, H\} = \{0.046, 0.25\}$  and then vary  $I_u$  from  $10^2$  to  $10^6$ . The obtained results are shown in Figure 1. It indicates that when  $I_u$  is small (e.g.,  $I_u = 10^2$ ), the TpvG model is associated with a finite sill and integral scale, which are 0.4 and 33.33, respectively. With the increasing of  $I_u$ , sill and integral scale increases. When  $I_u$  increases to  $10^5$  in this case, the TpvG model can approximate the power variogram model accurately in the range of the investigated lag distance.

**3.2. Unconditional Multiscale Random Fractal Field.** After determining the proper parameters for TpvG model to approximate the spatial distribution of multiscale random fractal field characterized by power variogram model (here we further increase  $I_u$  to  $10^6$  and the parameter set  $\{A, H, I_u\} = \{0.02, 0.25, 10^6\}$  in TpvG is used to ensure the sufficient accuracy to approximate the power variogram with parameter set  $\{A_0, H\} = \{0.046, 0.25\}$ ), a two-dimensional multiscale random fractals field can be generated by using KL expansion method with the TpvG model given by (12) as the covariance function. The procedures to generate the

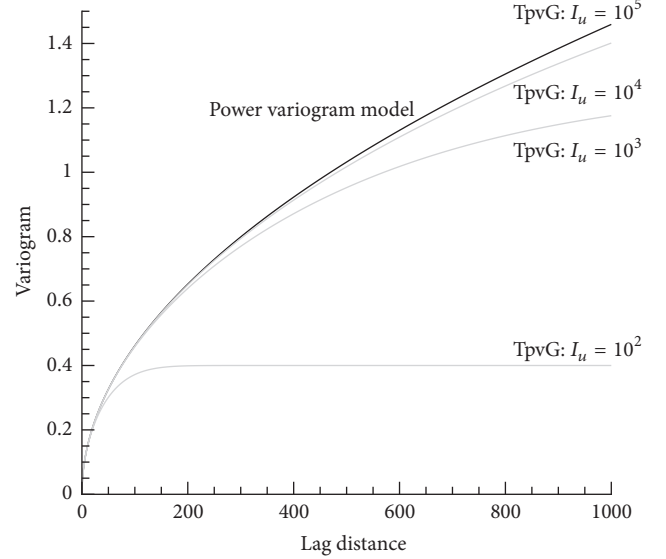


FIGURE 1: The equivalency of TpvG and power variogram models.

unconditional multiscale random fractal field are shown in Figure 2(a). In this case, the generated  $50 \times 50$  random multiscale fractal field is shown in Figure 3. As can be found in Figure 3, the upper region is associated with relative large values and the lower right region is associated with relative small values. To confirm the quality of the generated unconditional multiscale random fractal field, the sample variogram of the generated 2500 data values is used to compare with its theoretical counterpart. The sample variogram can be estimated using

$$\hat{\gamma}(s) = \frac{1}{2N_s} \sum_{(i,j) \in N_s} |\mathbf{x}_i - \mathbf{x}_j|^2, \quad (29)$$

where  $N_s$  is the number of pairs of samples  $i, j$  such that  $|\mathbf{x}_i - \mathbf{x}_j| = h$ . This task can be achieved by using the GAMV module in GSLIB code. As can be observed in Figure 4, the sample variogram model can reproduce the variogram structure of theoretical power variogram with parameter set  $\{A_0, H\} = \{0.046, 0.25\}$  very well, which justifies the quality of the generated multiscale random fractal field. Although not shown here, a series of similar tests with different power variogram model parameter values have also been performed. They include the cases when the Hurst coefficient  $0 < H < 0.5$  (indicating negatively correlated spatial increments),  $0.5 < H < 1$  (indicating a positively correlated spatial increments), and  $H = 0.5$  (indicating independent spatial increments). All the test results confirm that sample variograms can coincide well with their corresponding theoretical variograms.

**3.3. Capability of Dimensionality Reduction by Using KL Expansion.** One of the significant advantages to use KL expansion to generate the multiscale random fractal field is that it has the capability of reducing the dimensionality of the field in probabilistic space. This can be achieved by

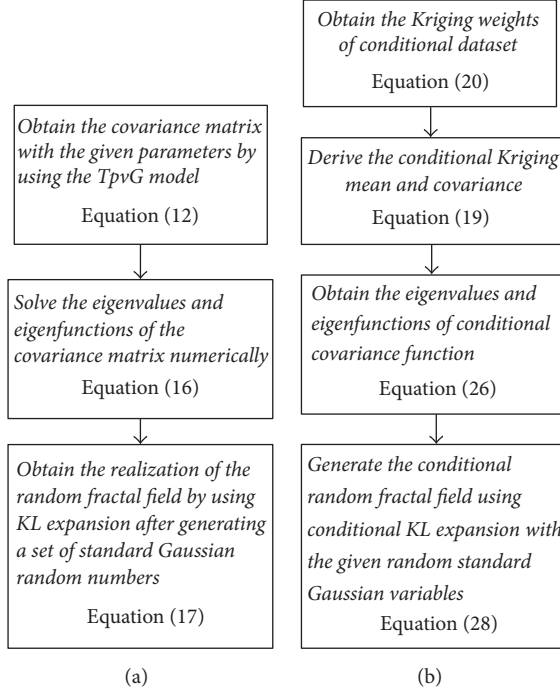


FIGURE 2: Flowchart to generate the random fractal fields: (a) unconditional; (b) conditional.

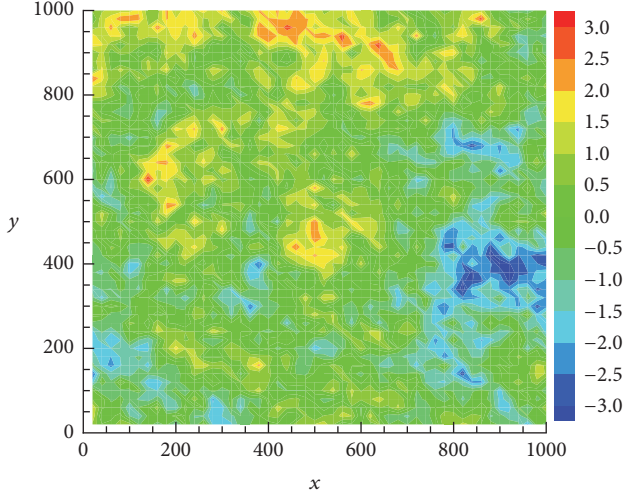


FIGURE 3: The generated unconditional multiscale random fractal field using KL expansion with the power variogram model parameters  $\{A_0, H\} = \{0.046, 0.25\}$ .

truncating out the expanded KL terms with small eigenvalues. The eigenvalues of covariance function are plotted in Figure 5. It can be found that the eigenvalues decrease dramatically with the increasing of the number of the remained terms after truncation. Approximately, all the eigenvalues are less than 1 after 200 terms. As stated in Chang and Zhang [28], each eigenvalue represents the energy and information content for each term to express the spatial variability of the random field. To determine the number of terms that needs to be retained

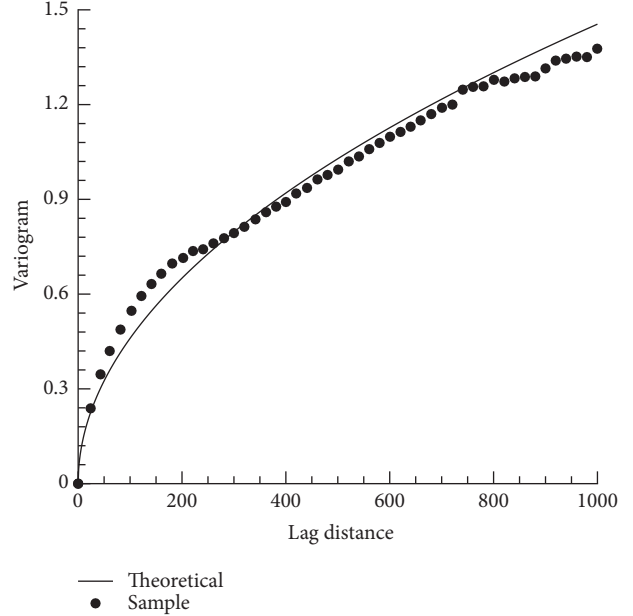


FIGURE 4: Comparison of the theoretical power variogram with parameters  $\{A_0, H\} = \{0.046, 0.25\}$  and its corresponding sample variogram.

to accurately represent the random field, Chang and Zhang [28] propose to define an energy criterion  $E_c$ :

$$E_c = \frac{\sum_{i=1}^{N_r} \lambda_i}{\sum_{i=1}^{\infty} \lambda_i} = \frac{\sum_{i=1}^{N_r} \lambda_i}{D\sigma^2}, \quad (30)$$

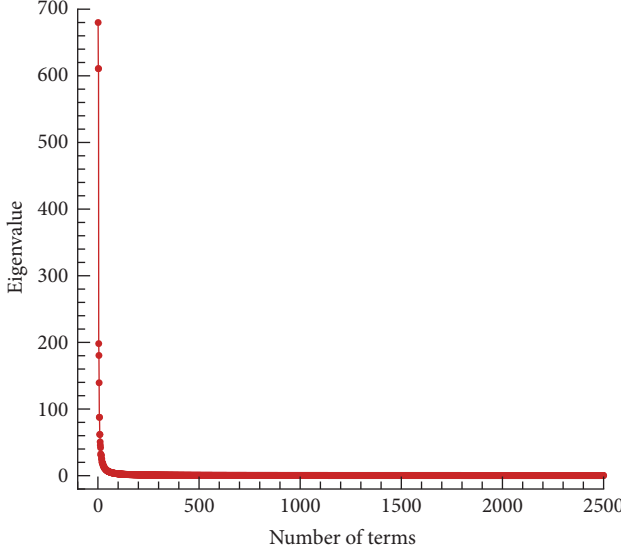


FIGURE 5: Eigenvalues of KL expansion.

TABLE 2: The relationship of energy criterion and number of retained terms.

$N_r$	$E_c$
10	53.42%
50	69.59%
100	74.83%
200	79.43%
500	85.16%
1000	90.07%
1500	93.74%
2000	97.02%
2500	100.00%

where  $N_r$  is the number of the retained terms,  $D$  is the domain size, and  $\sigma^2$  is the variance of the random field. The relationship of  $E_c$  and  $N_r$  is shown in Table 2. As can be observed in Table 2, the first 10 terms associated with large eigenvalues has already taken up to more than 50% of the total energy. To investigate how the number of the retained terms affects the generation of the multiscale random fractal field, a set of realizations of multiscale random fractal field are generated with different number of retained terms (e.g., 50, 100, 200, 500, 1000, and 1500) in KL expansion, as shown in Figure 6. It can be found that even only 50 leading terms, taking up to approximately 70% of the total energy, are retained in KL expansion during the generation of the multiscale random fractal field; the general pattern of the spatial variation can be captured. With the increasing of the number of the retained terms in KL expansion, the details of the heterogeneous characteristics become more and more revealed. When 1500 leading terms, corresponding to approximately 94% of the total energies, are retained in the KL expansion, the generated multiscale random fractal field is almost indistinguishable from that generated with full

KL expansion by comparing Figure 6(f) and Figure 3. This finding indicates that the heterogeneous characteristics of the random field are dominated by the leading KL expansion terms with large eigenvalues, which provides the foundation to conduct the dimensionality reduction. Since the small details of the heterogeneous characteristics may not affect the flow and transport characteristics dramatically, the KL expansion terms with small eigenvalues can be safely truncated to improve computational efficiency in the stochastic analysis of flow and transport. For example, it has been demonstrated that the mean and variance of hydraulic head obtained with only the first few leading KL expansion terms (e.g.,  $N_r = 6$  for a 1D case) is very close to those obtained from thousands of Monte Carlo simulation with full models [25]. Similar observations are also reported in Li et al. [26] and Liao and Zhang [27]. In a quantitative sense, if the polynomial chaos expansion (PCE) is used to construct a surrogate model for the state variables (e.g., hydraulic head) and KL expansion on the model parameter (e.g., log hydraulic conductivity), the number of model evaluation required to obtain the PCE coefficients is  $(N_r + p)!/N_r!p!$ , where  $p$  is the degree of PCE. For a given  $p$ , the number of model evaluation is greatly reduced when  $N_r$  decreases; hence the construction of surrogate model can be more efficient.

**3.4. Generation of Conditional Multiscale Random Fractal Field.** When direct measurement data are available, it may require generating the multiscale random fractal field that can be conditional on these measurements. To take the measurements into account, the procedures to generate the conditional random fractal field are shown in Figure 2(b), and the measurement values are obtained from a realization of the generated unconditional field to maintain the underlying random fractal characterizations. If there are 100 measurement data (the location of the measurements is shown in Figure 7(a)) collected from the unconditional multiscale random fractal field, the two generated conditional random fractal field can be depicted as shown in Figures 7(b) and 7(c). It can be observed that the generated values on the measurement locations honor the measurement values as shown in Figure 7(d), and the spatial correlation of the values on the unmeasured locations is governed by the given power variogram. Therefore, both the measurement values and the multiscale random fractal features can be represented in the generated unconditional field. With the aid of the generated multiscale random fractal field conditioning on the available measurements on the hydrogeological properties, the conditional stochastic analysis on flow and transport can be further performed.

**3.5. Advantages and Limitations of TPV Models in Simulating Real Fields.** This study is focused on random field generation, but it will be helpful to discuss when and how the proposed method can be used to characterize an aquifer based on the real observations. Due to the diversity and complexity of the geologic heterogeneity, there exists no versatile geostatistical model which works consistently well for all cases. Different models and tools have been developed to describe specific characteristics, for example, (non)stationarity, log-normal

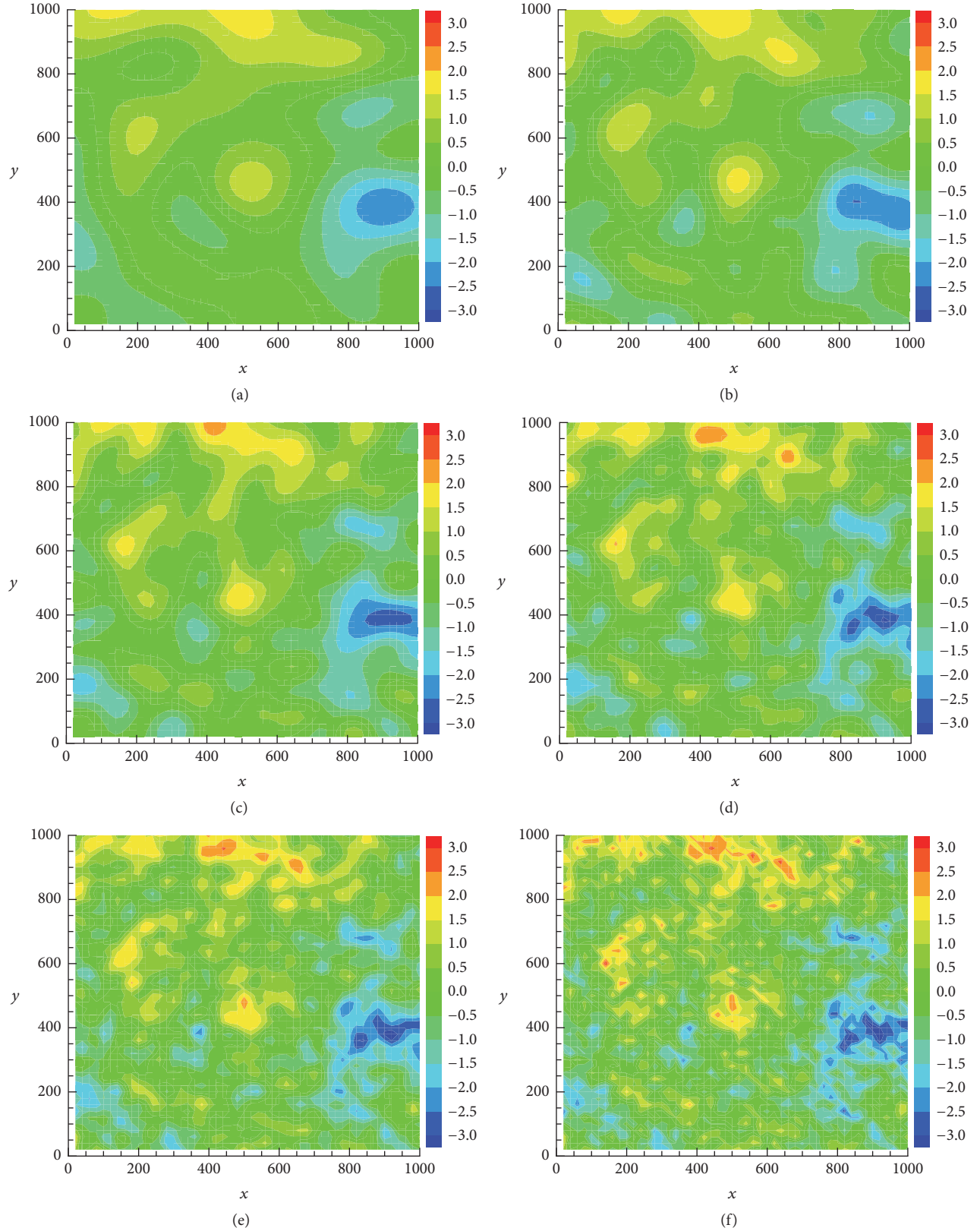


FIGURE 6: Generated multiscale random fractal field with different numbers of retained terms in KL expansion: (a) 50; (b) 100; (c) 200; (d) 500; (e) 1000; (f) 1500.

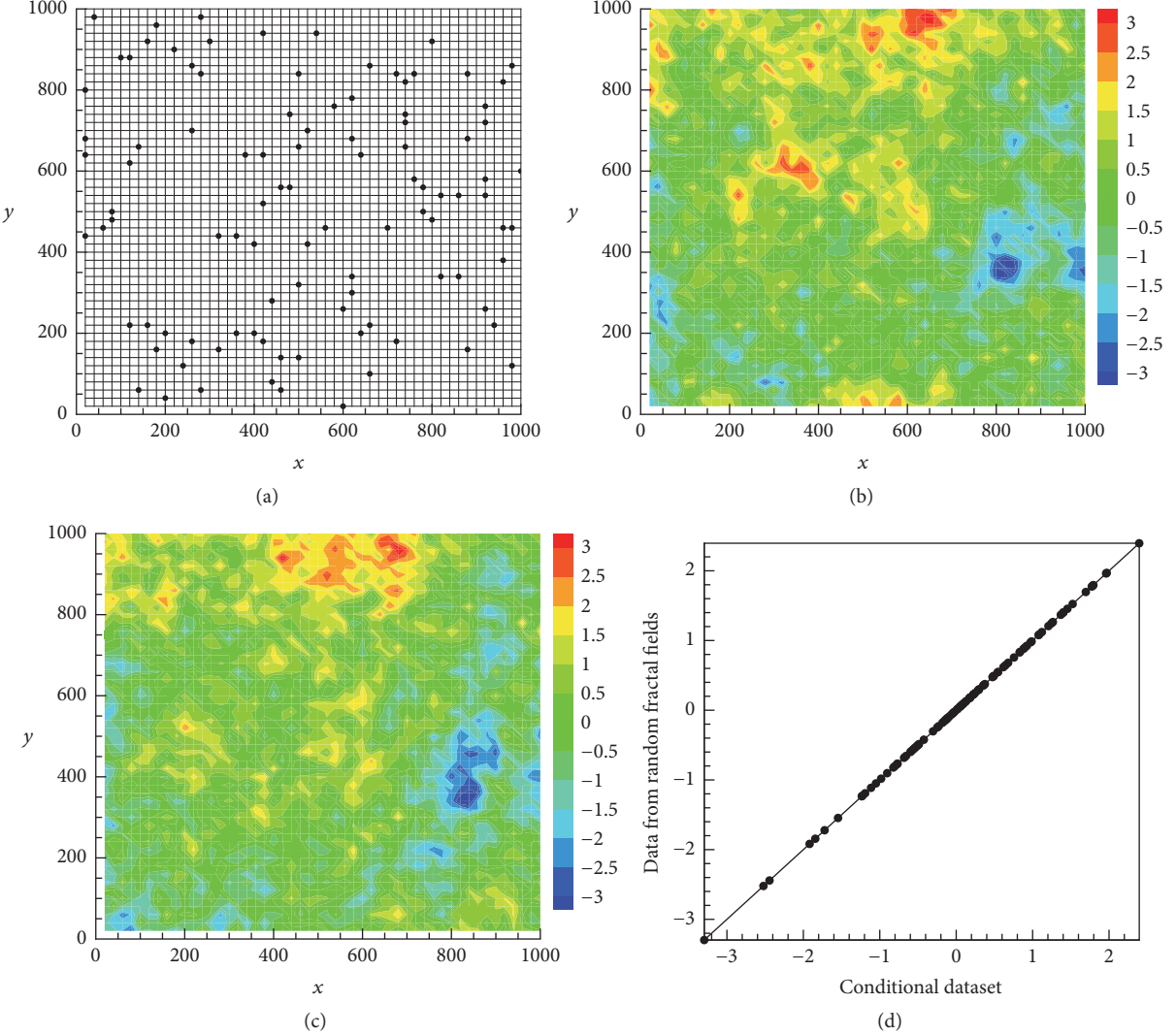


FIGURE 7: Conditional random fractal fields: (a) locations of the measurement data; (b) and (c) realizations of conditional random fractal fields; (d) comparison of measurements and generated values on the 100 measurement locations.

distribution, channeling, and self-similarity or fractal scaling [9, 21, 29]; [Carle and Fogg, 1996]. Compared to traditional geostatistical models employed in GSLIB, TPV models have some additional and unique merits. First, they can capture fractal scaling, a widely reported feature in real sediments, rocks, aquifers, and reservoirs ([30–37], among many others). Fractal scaling in many cases can be significant but cannot be described by traditional models. Second, unlike traditional models which are limited to stationarity assumption, TPV models are able to treat true fields as nonstationary in general and allow them to be stationary through upper cutoffs representing the impact of finite observation ranges or geologic homogeneity. That is, TPV models are compatible to both stationary fields and nonstationary fields, as demonstrated in Figures 1 and 4.

In the meanwhile, TPV models inherit the advantages of the traditional models; for example, they can take the

anisotropy, nested structures, and conditioning effect into account. In order to capture the property of geological layering in real fields, one may choose long correlation lengths in the horizontal directions and a much shorter one in the vertical direction. More specifically, the parameters  $H$  and/or  $I_u$  above can be anisotropic to reflect the anisotropy of geologic layering.

As discussed above, it may be unwise to expect a versatile tool to handle all the fields. TPV model has its limitations in certain circumstances. The main limitation is that TPV, as a member of two-point statistical tools, is weak in featuring apparently observed connectivity, branching, or channeling. At the present stage, to solve this problem one may also need postprocessing using tools like sequential indicator simulation or directly resort to multipoint statistics (MPS [29, 38]). Combining fractal scaling and connectivity will be a promising work in the future.

## 4. Conclusion

Traditional geostatistical method used to characterize the heterogeneity of the hydrogeological properties is assumed that the random field is statistically homogeneous or stationary. However, growing evidences show that the heterogeneity of the hydrogeological random field is a nonstationary stochastic process but with a statistically homogeneous increments. Such field can be characterized by random fractals with the spatial variation described by power variogram model. It can be used to characterize the multiscale effect of the random field. To investigate the scaling effect of the random fractals on the flow and transport, it is necessary to generate such random fractals field numerically. Since power variogram does not have a corresponding covariance function, we adopt the stationary truncated variogram models to approximate the power variogram model and combine these models with Karhunen–Loève (KL) expansion to generate the random fractal field.

The main findings in this work lead to the following conclusions:

- (1) The truncated power variogram model can approximate the power variogram model in the range of the investigation region when the upper limit of the integral scale is very large under the point measurement scale condition. The truncated power variogram model is stationary, which has an explicit form of the covariance function and can be used in the traditional geostatistical analysis based on the stationary assumption.
- (2) KL expansion is an effective way to generate random field by decomposing the covariance function into its eigenvalues and eigenfunctions. The multiscale random fractal field can be generated by combining the stationary truncated power variogram model with KL expansion.
- (3) The main structure of the spatial heterogeneity is characterized by the dominating terms in the KL expansion with relative large eigenvalues. The eigenvalues of the TpvG covariance function decreases rapidly, which provides a foundation to conduct dimensionality reduction by truncating out the KL expansion terms associated with small eigenvalues.
- (4) The conditional multiscale random fractal field can be generated by using the conditional Kriging techniques by solving the Kriging equations when the measurement data are available. The generated values of conditional multiscale random fractal field honor the measurement values on the measurement locations.

## Conflicts of Interest

The authors declare that they have no conflicts of interest.

## Acknowledgments

This work is funded by the National Natural Science Foundation of China (Grants nos. 41402199 and 41602250), National Science and Technology Major Project (Grants nos. 2016ZX05037003 and 2016ZX05060002), the Science Foundation of China University of Petroleum, Beijing (Grant no. 2462014YJRC038), China Postdoctoral Science Foundation (Grants nos. 2016M591353 and 2017M611782), the Science Foundation of Sinopec Group (Grant no. P16058), the independent research funding of State Key Laboratory of Petroleum Resources and Prospecting (Grant no. PRP/indep-4-1409), and China Geological Survey (Grant no. DD20160293).

## References

- [1] E. A. Sudicky, “A natural gradient experiment on solute transport in a sand aquifer: Spatial variability of hydraulic conductivity and its role in the dispersion process,” *Water Resources Research*, vol. 22, no. 13, pp. 2069–2082, 1986.
- [2] P. Dietrich and C. Leven, “Direct push-technologies,” in *Groundwater Geophysics*, R. Kirsch, Ed., pp. 347–366, Springer, Berlin, Germany, 2006.
- [3] S. J. Berg and W. A. Illman, “Three-dimensional transient hydraulic tomography in a highly heterogeneous glaciofluvial aquifer-aquitard system,” *Water Resources Research*, vol. 47, no. 10, Article ID W10507, 2011.
- [4] G. Dagan, *Flow and Transport in Porous Formations*, Springer, New York, NY, USA, 1989.
- [5] L. W. Gelhar, *Stochastic Subsurface Hydrology*, Prentice-Hall, Englewood Cliffs, NJ, USA, 1993.
- [6] J. P. Delhomme, “Spatial variability and uncertainty in groundwater flow parameters: A geostatistical approach,” *Water Resources Research*, vol. 15, no. 2, pp. 269–280, 1979.
- [7] R. J. Hoeksema and P. K. Kitanidis, “Prediction of transmissivities, heads, and seepage velocities using mathematical modeling and geostatistics,” *Advances in Water Resources*, vol. 12, no. 2, pp. 90–102, 1989.
- [8] R. A. Carlson and J. L. Osiensky, “Geostatistical analysis and simulation of nonpoint source groundwater nitrate contamination: A case study,” *Environmental Geosciences*, vol. 5, no. 4, pp. 177–186, 1998.
- [9] C. V. Deutsch and A. G. Journel, *GSLIB: Geostatistical Software Library and User’s Guide*, Applied Geostatistics Series, Oxford University Press, Oxford, UK, 2nd edition, 1997.
- [10] S. P. Neuman, “Universal scaling of hydraulic conductivities and dispersivities in geologic media,” *Water Resources Research*, vol. 26, no. 8, pp. 1749–1758, 1990.
- [11] L. W. Gelhar, C. Welty, and K. R. Rehfeldt, “A critical review of data on field-scale dispersion in aquifers,” *Water Resources Research*, vol. 28, no. 7, pp. 1955–1974, 1992.
- [12] F. J. Molz and G. K. Boman, “Further evidence of fractal structure in hydraulic conductivity distributions,” *Geophysical Research Letters*, vol. 22, no. 18, pp. 2545–2548, 1995.
- [13] S. Painter, “Evidence for non-Gaussian scaling behavior in heterogeneous sedimentary formations,” *Water Resources Research*, vol. 32, no. 5, pp. 1183–1195, 1996.
- [14] L. Tennekoorn, M. C. Boufadel, D. Lavallee, and J. Weaver, “Multifractal anisotropic scaling of the hydraulic conductivity,” *Water Resources Research*, vol. 39, no. 7, pp. 113–117, 2003.

- [15] J. Eggleston and S. Rojstaczer, "Inferring spatial correlation of hydraulic conductivity from sediment cores and outcrops," *Geophysical Research Letters*, vol. 25, no. 13, pp. 2321–2324, 1998.
- [16] M. C. Boufadel, S. Lu, F. J. Molz, and D. Lavalée, "Multifractal scaling of the intrinsic permeability," *Water Resources Research*, vol. 36, no. 11, pp. 3211–3222, 2000.
- [17] H. H. Liu and F. J. Molz, "Discrimination of fractional Brownian movement and fractional Gaussian noise structures in permeability and related property distributions with range analyses," *Water Resources Research*, vol. 32, no. 8, pp. 2601–2605, 1996.
- [18] F. Ruan and D. McLaughlin, "An efficient multivariate random field generator using the fast Fourier transform," *Advances in Water Resources*, vol. 21, no. 5, pp. 385–399, 1998.
- [19] P. R. Kramer, O. Kurbanmuradov, and K. Sabelfeld, "Comparative analysis of multiscale Gaussian random field simulation algorithms," *Journal of Computational Physics*, vol. 226, no. 1, pp. 897–924, 2007.
- [20] C. Cameron, "Relative efficiency of Gaussian stochastic process sampling procedures," *Journal of Computational Physics*, vol. 192, no. 2, pp. 546–569, 2003.
- [21] V. Di Federico and S. P. Neuman, "Scaling of random fields by means of truncated power variograms and associated spectra," *Water Resources Research*, vol. 33, no. 5, pp. 1075–1085, 1997.
- [22] L. Xue and D. Zhang, "A multimodel data assimilation framework via the ensemble Kalman filter," *Water Resources Research*, vol. 50, no. 5, pp. 4197–4219, 2014.
- [23] F. Heße, V. Prykhodko, S. Schlüter, and S. Attinger, "Generating random fields with a truncated power-law variogram: A comparison of several numerical methods," *Environmental Modeling and Software*, vol. 55, pp. 32–48, 2014.
- [24] T. Dieker, *Simulation of fractional Brownian motion [M.S. thesis]*, Department of Mathematical Sciences, University of Twente, Enschede, The Netherlands, 2004.
- [25] H. Li and D. Zhang, "Probabilistic collocation method for flow in porous media: Comparisons with other stochastic methods," *Water Resources Research*, vol. 43, pp. 6627–6632, 2007.
- [26] H. Li, H. Chang, and D. Zhang, "Stochastic collocation methods for efficient and accurate quantification of uncertainty in multiphase reservoir simulations," in *Proceedings of the SPE Reservoir Simulation Symposium 2009*, pp. 509–520, February 2009.
- [27] Q. Liao and D. Zhang, "Probabilistic collocation method for strongly nonlinear problems: 1. Transform by location," *Water Resources Research*, vol. 49, no. 12, pp. 7911–7928, 2013.
- [28] H. Chang and D. Zhang, "A comparative study of stochastic collocation methods for flow in spatially correlated random fields," *Communications in Computational Physics*, vol. 6, no. 3, pp. 509–535, 2009.
- [29] S. Strebelle, "Conditional simulation of complex geological structures using multiple-point statistics," *Mathematical Geology*, vol. 34, no. 1, pp. 1–21, 2002.
- [30] T. Hewett, "Fractal Distributions of Reservoir Heterogeneity and Their Influence on Fluid Transport," in *Proceedings of the SPE Annual Technical Conference and Exhibition*, New Orleans, LA, USA, 1986.
- [31] S. Painter and L. Paterson, "Fractional Lévy motion as a model for spatial variability in sedimentary rock," *Geophysical Research Letters*, vol. 21, no. 25, pp. 2857–2860, 1994.
- [32] A. G. Guzman and S. Neuman, "Field air injection experiments," in *Apache Leap Tuff INTRAVEL Experiments: Results and Lessons Learned*, T. Rasmussen, S. Rhodes, A. Guzman, and S. Neuman, Eds., Nuclear Regulatory Commission, 1996.
- [33] F. J. Molz, H. Rajaram, and S. Lu, "Stochastic fractal-based models of heterogeneity in subsurface hydrology: Origins, applications, limitations, and future research questions," *Reviews of Geophysics*, vol. 42, no. 1, 2004.
- [34] D. Veneziano and A. K. Essiam, "Nonlinear spectral analysis of flow through multifractal porous media," *Chaos, Solitons & Fractals*, vol. 19, no. 2, pp. 293–307, 2004.
- [35] V. Ganti, A. Singh, P. Passalacqua, and E. Foufoula-Georgiou, "Subordinated Brownian motion model for sediment transport," *Physical Review E: Statistical, Nonlinear, and Soft Matter Physics*, vol. 80, no. 1, 2009.
- [36] M. Siena, A. Guadagnini, M. Riva, and S. P. Neuman, "Extended power-law scaling of air permeabilities measured on a block of tuff," *Hydrology and Earth System Sciences*, vol. 16, no. 1, pp. 29–42, 2012.
- [37] A. Guadagnini, S. P. Neuman, M. G. Schaap, and M. Riva, "Anisotropic statistical scaling of soil and sediment texture in a stratified deep vadose zone near Maricopa, Arizona," *Geoderma*, vol. 214–215, pp. 217–227, 2014.
- [38] B. Jafarpour and M. Khodabakhshi, "A probability conditioning method (PCM) for nonlinear flow data integration into multipoint statistical facies simulation," *Mathematical Geosciences*, vol. 43, no. 2, pp. 133–164, 2011.

## Research Article

# Characterization of Origin and Evolution of Formation Water in Buried Hill of Jizhong Depression, China, Using Multivariate Statistical Analysis of Geochemical Data

Fei Li<sup>1,2</sup> and Jianhui Zeng<sup>1,2</sup>

<sup>1</sup>State Key Laboratory of Petroleum Resource and Prospecting, China University of Petroleum, Beijing, China

<sup>2</sup>College of Geosciences, China University of Petroleum, Beijing, China

Correspondence should be addressed to Jianhui Zeng; [zengjh@cup.edu.cn](mailto:zengjh@cup.edu.cn)

Received 30 June 2017; Accepted 7 November 2017; Published 19 December 2017

Academic Editor: Jet-Chau Wen

Copyright © 2017 Fei Li and Jianhui Zeng. This is an open access article distributed under the Creative Commons Attribution License, which permits unrestricted use, distribution, and reproduction in any medium, provided the original work is properly cited.

Groundwater samples from buried hill of Jizhong Depression were evaluated using two statistical analyses: hierarchical cluster analysis (HCA) and principal component analysis (PCA). The samples were classified into four clusters, C1–C4, in HCA and the hydrochemical types of C1–C4 are  $\text{HCO}_3\text{-Na}$ ,  $\text{Cl}\cdot\text{HCO}_3\text{-Na}$ ,  $\text{Cl-Na}$ , and  $\text{Cl-Na-Ca}$ . From C1 to C2, C3, and C4, the water-rock interaction becomes increasingly intensive, and  $r\text{Na}/r\text{Cl}$  gets lower while total dissolved solids and  $r(\text{Cl-Na})/r\text{Mg}$  get higher. Three components of PCA explain 86.87% of the variance. Component1 (PC1), characterized by highly positive loadings in  $\text{Na}^+$  and  $\text{Cl}^-$ , is related to evaporation concentration. Component2 (PC2) is defined by highly positive loading in  $\text{HCO}_3^-$  and is related to influence of atmospheric water. With high positive loadings in  $\text{Ca}^{2+}$  and high negative loadings in  $\text{Na}^+$  and  $\text{SO}_4^{2-}$ , component3 (PC3) suggests plagioclase albition. The combination of HCA and PCA within the hydrogeological contexts allowed the division of study area into five dynamic areas. From recharge area to discharge area, the influence of atmospheric water gets weaker and water-rock interactions such as evaporation concentration and plagioclase albition become intensive. Therefore groundwater in buried hill showed paths of hydrochemical evolution, from C1, to C2, C3, and C4. Buried hill reservoir in Jizhong Depression is mainly distributed in hydrodynamic blocking and discharge area; therefore the two regions can be the favorable areas for petroleum migration.

## 1. Introduction

In petroleum basins, hydrocarbon is always associated with formation water in porous stratigraphic units. Hydrocarbon generation, migration, accumulation, preservation, and loss all take place in the environment of formation water or are all accompanied by the participation of formation water (Davisson et al. 1991 [1–3]). Formation water in petroleum basins plays a vital role as media for the transport and redistribution of material and energy during the process of hydrocarbon generation, migration, and accumulation. The chemical composition, origin, and evolution can directly or indirectly reflect the closedness of sedimentary basin and hydrocarbon preservation conditions [4–6]. Therefore, understanding the origin, evolution, and controls on the composition of formation water is of considerable importance for successful

appraisal of hydrocarbon exploration targets in sedimentary basins [7]. The chemical and isotopic compositions of formation water are widely applied in sedimentary basins to study the origins, evolution, and hydrogeological conditions. However, the origin and evolution of formation water are still being debated [8, 9]. Generally speaking, origins of formation water have previously been attributed to meteoric water, evaporation concentrated seawater, or halite dissolution [10–12].

In recent decades, multivariate statistical techniques such as hierarchical cluster analysis (HCA) and principal components analysis (PCA) have been successfully used as an effective tool to analyze the origin and evolution of shallow groundwater which is less than 200 m deep. Farnham et al. [13] applied principal components and clusters analysis to

trace element chemistry of groundwater and identify rock-water interaction processes. In the study of Cloutier et al. [14], multivariate statistical methods were applied to classify the groundwater samples and to identify geochemical processes controlling groundwater geochemistry. Yidana et al. [15] applied cluster and factor analysis to assess the main controls on the chemistry of surface water resources. The above studies show that multivariate statistical techniques, such as HCA and PCA, significantly help to classify shallow groundwater and identify major mechanisms influencing groundwater chemistry.

As a second major tectonic unit of the Bohai Bay basin, the Jizhong Depression is a very typical area in China with enrichment of buried hill hydrocarbon reservoirs. The largest buried hill oilfield in China-Renqiu oilfield, covering an area of  $80 \text{ km}^2$ , was discovered in Jizhong Depression in 1975 [16]. In the next ten years following its discovery, more than 20 buried hill oilfields were successively discovered. The proven oil reserves in these buried hill oilfields amount to  $5.5 \times 10^8 \text{ t}$ , accounting for 60% of the total proven oil reserves in Jizhong Depression in that period [17, 18]. However, the exploration of buried hill oil reservoirs entered a quiet stage in Jizhong Depression and few buried hill oil reservoirs were discovered in the following 20 years. In recent years, much progress has been made in the exploration technology of buried hill oil reservoirs and some buried hill oil reservoirs have been discovered, including Wengu 3, Niudong 1, Chang 3, and Chang 6, demonstrating good exploration prospect of buried hill oil reservoirs in Jizhong Depression [19–21].

Several studies have been performed to study the origin of formation water in buried hill [22–24], most of which used conventional graphical interpretative tools, such as piper plots, scatter plots, box plots, and stiff pattern diagram, to classify and account for the geochemical data. The understanding of the hydrogeochemistry of buried hill represents a good chance to further use statistical analysis, a quantitative method allowing us to classify formation water samples, to investigate correlations between the chemical parameters, and to appraise the similarity between the formation water samples. Compared to conventional graphical interpretative tools, the use of statistical methods for better identifying the processes controlling the geochemical evolution of formation water has some advantages. First of all, the utilisation of conventional graphical approach alone is always limited due to lack of objective criteria to discriminate different types of formation waters and the division into different hydrochemical facies is always qualitative rather than quantitative [25]. Secondly, conventional graphical methods are always short of clarity where large datasets are displayed [26].

The migration, accumulation, and preservation of oil reservoirs are also closely related to the movement of formation water and there is a good corresponding between petroleum accumulation and chemical composition. Li et al. [27] studied the chemical composition of Yanchang formation water in the Ordos Basin and revealed that the formation water with major ions of  $\text{Cl}^-$  and  $\text{Na}^+$  is more favorable for oil reservoir preservation. Wang et al. [28] investigated the implications of formation water features for

hydrocarbon accumulation in Wenliu region in Dongpu sag, Bohai Bay Basin; the results showed that the areas with high concentration of  $\text{Cl}^-$ ,  $\text{Na}^+$ , and  $\text{Ca}^{2+}$  correlate well to hydrocarbon enrichment areas. Therefore, understanding the chemical composition, origin, evolution, and controls on the composition of formation water will provide theoretical and practical guidance for exploration of buried hill oil reservoirs in Jizhong Depression. The depth of buried hill in Jizhong Depression is more than 2000 m and the deepest up to 5000 m. In previous studies, multivariate statistical techniques such as HCA and PCA were mainly applied to analyze the origin and evolution of shallow groundwater. The shallow groundwater with lower temperature ( $<50^\circ\text{C}$ ) is less than 200 m deep and human activities impact and atmospheric water play important part roles during the formation of shallow groundwater. Compared with shallow groundwater, the formation water in buried hill with high temperature ( $>100^\circ\text{C}$ ) is more than 2000 m deep; the influences of human activities impact and atmospheric water get weak and water-rock interactions become intensive. Besides, some water-rock interactions can only occur in deep formation water with high temperature. Take plagioclase albition effect, for example, it can only occur at the temperature ranging from  $100^\circ\text{C}$  to  $150^\circ\text{C}$  [29]. In this study, two multivariate methods, HCA and PCA, were used to analyze the geochemical data, and geological and hydrogeological conditions were employed to better assess the origin and evolution of deep formation water in buried hill of Jizhong Depression. Based on the distribution features of proved oil reserves in buried hill, the implication between evolution of formation water and hydrocarbon distribution, which will provide theoretical and practical guidance for exploration of similar oil reservoirs, has been investigated.

## 2. Geology and Hydrogeology

Jizhong Depression, located in the west of Bohai Gulf Basin (BGB) (Figure 1), is a Cenozoic sedimentary depression which formed on the basement of Huabei Platform. It is an elongated half-graben, bordered by the Yanshan uplift to the north, Xingheng uplift to the south, Taihangshan uplift to the west, and Cangxian uplift to the east, which covers an area of  $32000 \text{ km}^2$  (Figure 1). It is divided into three areas by two EW and SWW transformation belts, which are the east, middle, and west district, respectively. The Southern district included Shijiazhuang Sag, Jinxiang Sag, Sulu Sag, and Jining uplift, the middle district consists of Raoyang Sag, Baoding Sag, Shenxian Sag, Gaoyang uplift, Shenze uplift, and Lixian Slope, and the north district can be divided into Beijing Sag, Daguang Sag, Langgu Sag, Xushui Sag, Wuqing Sag, Baxian Sag, Daxing uplift, Niutuozhen uplift, Rongcheng uplift, Niubei Slope, Yangcun Slope, and Wenan Slope.

In the extended geological period, Jizhong Depression experienced three developmental stages, namely, geosyncline, platform, and rifting stage. In the geosyncline developmental stage (3.5–1.8 billion years ago), the study area experienced the Fuping, Wutai, and Lvliang Orogenies, forming the ancient basement consisting of granite and hornblende schist. In the subsequent platform developmental stage (1.8–0.2

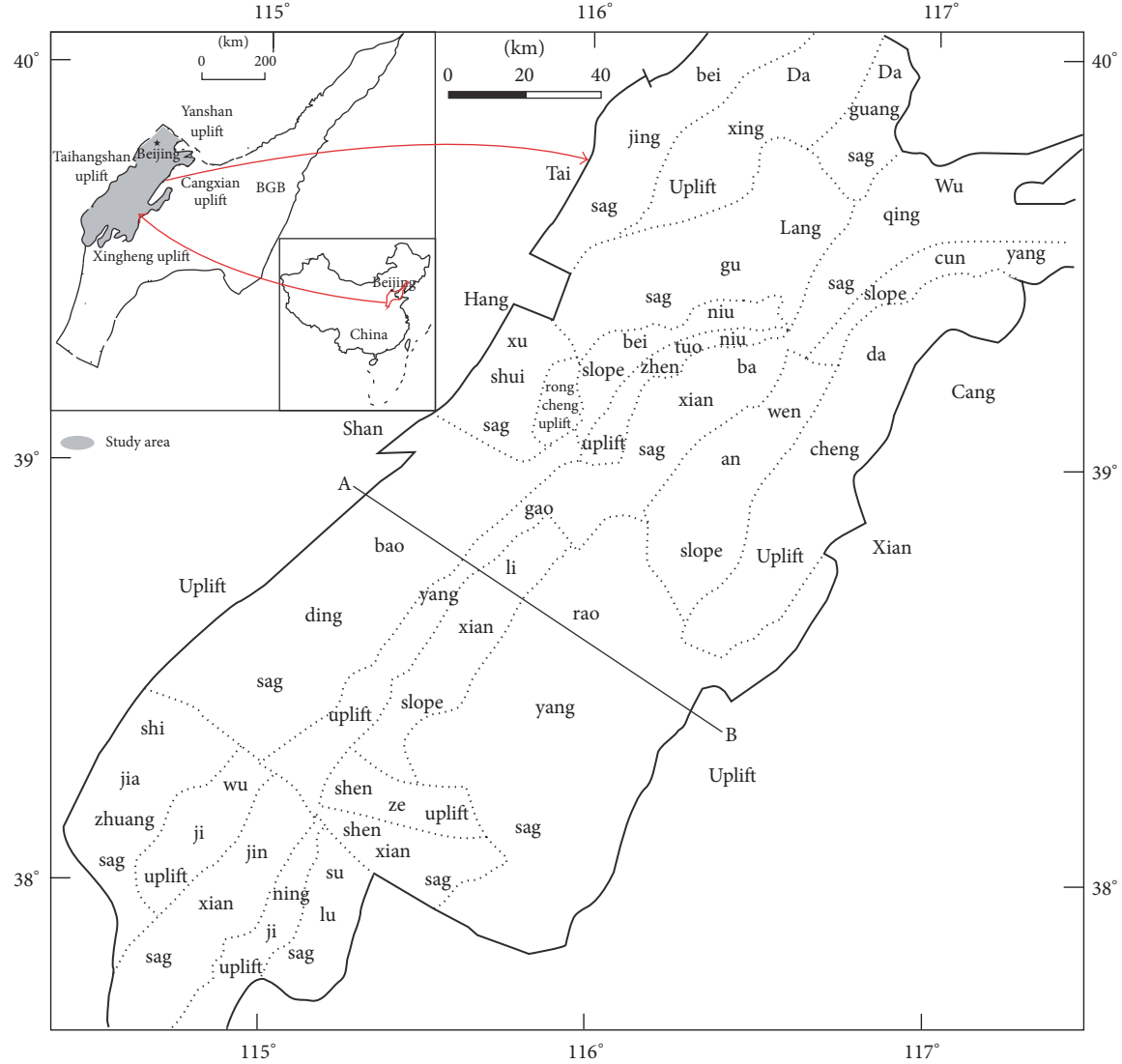


FIGURE 1: Sketch map showing location and structure of the Jizhong Depression.

billion years ago), the basin deposited a set of marine carbonate sediments with thicknesses of up to 6.8 km. Under the influence of the Hercynian and Indosinian Orogenies, the marine carbonates repeatedly suffered weathering and denudation and the buried hills were formed in this stage. After the Indosinian orogenies, the study area moved into the stage of rifting basin (0.2 billion years ago up to the present), sedimenting a set of terrestrial deposits of up to 8000 m [30, 31].

The basin fill of study area can be divided into two parts: the bottom part consists of Meso-Neoproterozoic through Paleozoic weathered marine carbonates, and the upper part is Cenozoic continental clastic sediment (Figures 2 and 3). From bottom to top, the upper part can be divided into six formations: the Kongdian (Ek), Shahejie (Es), Dongying (Ed), Guantao (Ng), Minghuazhen (Nm), and Pingyuan formations (Qp). The Pingyuan formations (Qp) includes yellow clay powder and fine sandstone. The Minghuazhen

formation (Nm) consists of light grey sandstone, conglomeratic sandstones, and palm red mudstone. The Guantao formation (Ng) consists of aubergine mudstone and light grey granular sandstone. The Dongying formation (Ed) is composed of three units: the lower part starts with amaranth mudstone and grey mudstone, the middle part is composed of grey mudstone interbedded with siltstone, and the upper part mainly consists of light grey sandstone and purple mudstone layer. The Shahejie formation (Es) can be further divided into four members based on lithology and electrical properties: Shahejie 1 ( $Es_1$ ), Shahejie 2 ( $Es_2$ ), Shahejie 3 ( $Es_3$ ), and Shahejie 4 ( $Es_4$ ). Shahejie 1 includes grey mudstone, calcareous shale, and calcareous sandstone, which gradually change upward into amaranth mudstone and grey sandstone. Shahejie 2 consists of red to purplish-red sandstone and mudstone. The Shahejie 3 is composed of dark grey mudstones interbedded with fine-grained sandstones, which is one of the most important source rocks. Shahejie 4 ( $Es_4$ ) consists

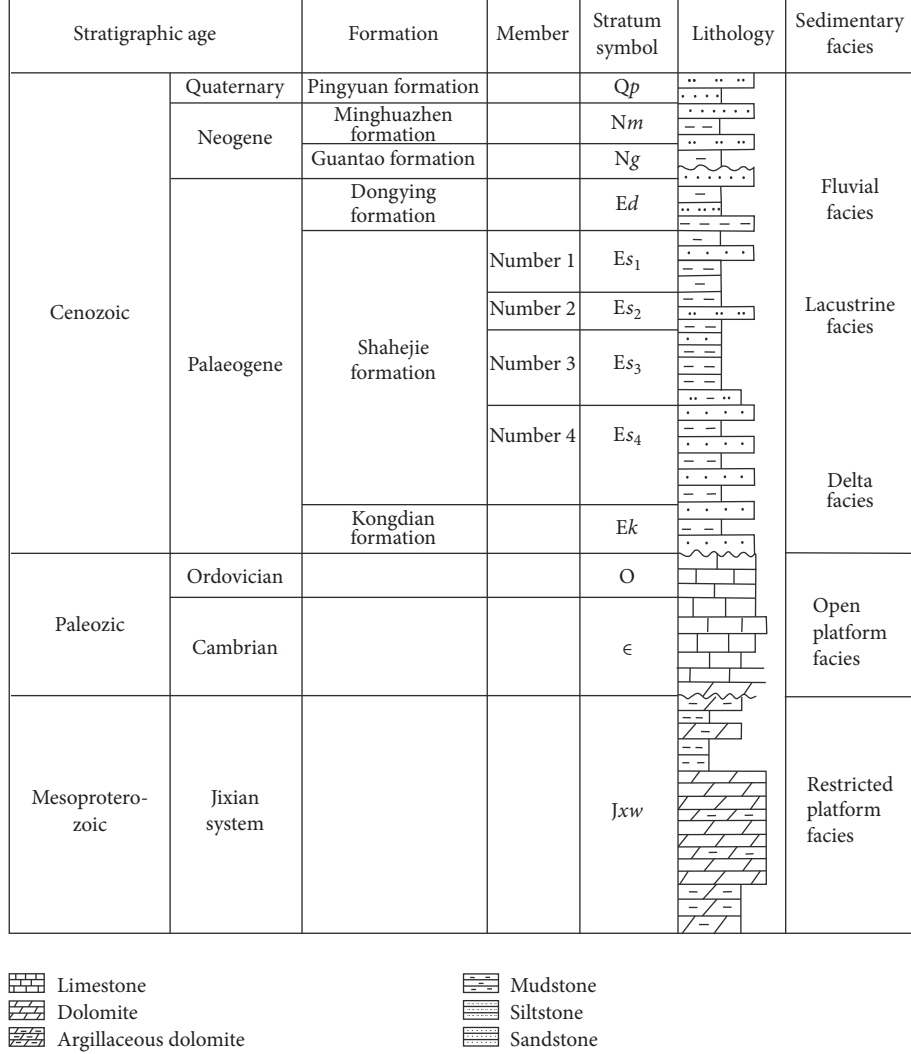


FIGURE 2: Stratigraphic histogram of the Jizhong Depression.

of grey mudstone and light grey sandstone interbedded with dolomite and gypsum, which is another important source rock. The Kongdian formation (Ek) includes variegated sandstone and red sandy mudstone, which gradually change upward into grey mudstone interbedded with gypsum mudstone [32].

The bottom part, weathered marine carbonate, consists of the Wumishan formation of the Jixian system (Jxw); Cambrian ( $\epsilon$ ) and Ordovician (O) are the focus of this study. The Wumishan formation of the Jixian system, mainly distributed in the west of study area, is composed of dolomite and argillaceous dolomite. Cambrian ( $\epsilon$ ) and Ordovician, mainly distributed in the east of study area, consist of limestone. The buried hills, consisting of weathered marine carbonates, are directly covered by Es<sub>4</sub>-Ek or Es<sub>3</sub> which are two primary hydrocarbon source rocks in study area. The hydrocarbon, generated from Es<sub>4</sub>-Ek or Es<sub>3</sub> source rocks, migrated directly or through the fault-unconformity to the buried hill trap.

In the study area, there are five aquifers (Ng, Ed, Es<sub>2</sub>, and Ek, and buried hill) and four aquitards (Nm, Es<sub>1</sub>, Es<sub>3</sub>,

and Es<sub>4</sub>). Formation water in the Ng formations consisting of fluvial facies is characterized by lower salinity (<5 g/l) and high rNa/rCl (>3.0) [33]. The stable isotope value of formation water in the Ng formation, which is similar to present rainwater, suggested that it is related to the influence of atmospheric water. The Ek, Es, and Ed formations, consisting of terrestrial facies lake basin depositions which are more than 2000 m deep, rarely outcrop. The formation water in Ek, Es, and Ed formations is characterized by higher salinity (10~100 g/l) and lower rNa/rCl (<3.0) [33]. In the study of Qu et al. [24], the application of isotopic composition is used to trace the origin of formation water in Ek, Es, and Ed, which is mainly from sedimentary water and small amount of atmospheric water. Evaporation concentration effect plays an important part role during the evolution of formation water in the Ek, Es, and Ed. Du et al. [33] studied the fluid potential of Ek, Es, and Ed and the migration direction of the formation water is from the depression center to the edge. The weathered marine carbonates widely outcrop in the west of Taihang Mountains; the main flow path of formation water in

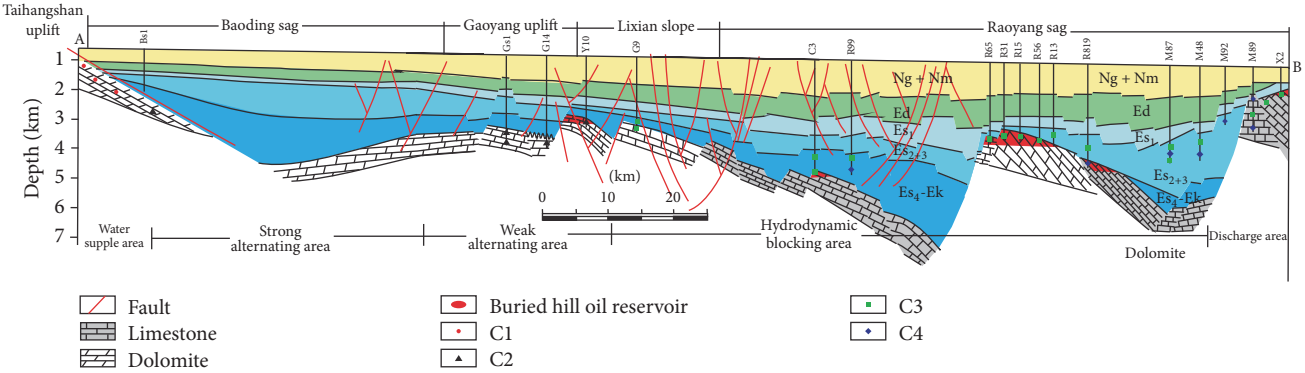


FIGURE 3: Schematic map of the cross-section A-B. See Figure 1.

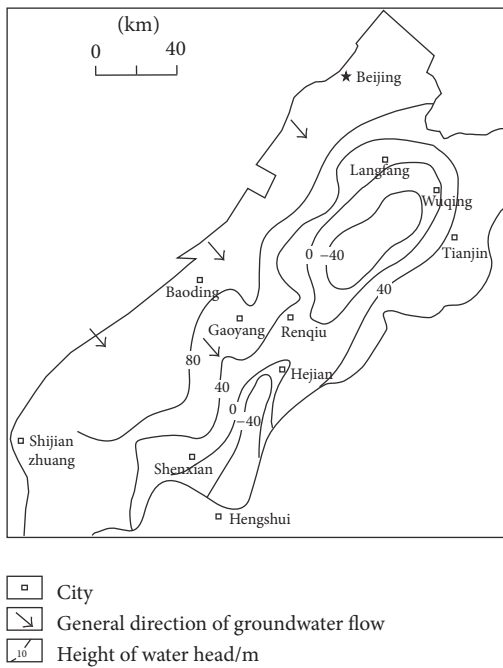


FIGURE 4: The water head of formation water in buried hill, Jizhong Depression.

buried hill is generally from west to east (Figure 4). Before the deposition of Ek formation, the formation water in buried hill is mainly from ancient meteoric water. During the deposition of Ek, Es, and Ed formations, the formation water from tertiary mudstone is expelled into the buried hill. Nowadays, the buried hill formation water at the edge of depression is mainly from meteoric water. Therefore, the formation water in buried hill is characterized of medium salinity (5~50 g/l) [33].

### 3. Methodology

As mentioned, each sampling site is characterized by a large number of chemical and physical variables, making the regional hydrogeochemical study a multivariate problem. In this study, 6 chemical variables ( $\text{Ca}^{2+}$ ,  $\text{Mg}^{2+}$ ,  $\text{Na}^+$ ,  $\text{HCO}_3^-$ ,  $\text{Cl}^-$ , and  $\text{SO}_4^{2-}$ ), in 459 samples were analyzed using hierarchical cluster analysis (HCA) and principal components analysis (PCA). The HCA and PCA were used as a quantitative and independent approach for groundwater classification allowing grouping of the groundwater samples and making of correlations between chemical parameters and groundwater samples, respectively.

**3.1. Hierarchical Cluster Analysis (HCA).** The hierarchical cluster analysis is a data classification method, which are widely applied in the classification of hydrogeochemical data [34, 35]. In this study, the square of the Euclidean distance (E) was used in HCA as the measure of similarity performed over all variables included in HCA ( $\text{Ca}^{2+}$ ,  $\text{Mg}^{2+}$ ,  $\text{Na}^+$ ,  $\text{HCO}_3^-$ ,  $\text{Cl}^-$ , and  $\text{SO}_4^{2-}$ ). HCA using Ward's algorithm was conducted on the remaining complete samples where all input variables were measured. Compared to other methods, Ward's method is much more effective in forming clusters because it uses an analysis of variance approach to evaluate the distances between clusters [35–37].

During the clustering procedure, HCA first considers each observation separately and then combines the two observations that are closest together to form a new group. After recomputing the distance between the groups, the two groups then closest together are combined, and this process is repeated until only one group remains. Resulting from this procedure is a dendrogram (e.g., [14]). To avoid misclassifications arising from the effect of parameters with the highest variances on the calculation of Euclidean distance [14], the variance for each variable is standardized to their corresponding Z scores, which are calculated by the following equation [38]:

$$Z_i = \frac{(X_i - \text{mean})}{s}, \quad (1)$$

where  $Z_i$  is the standardized Z scores,  $s$  is the standard deviation of the distribution, mean is the mean value of the normal distribution from each datum, and  $X_i$  is the value of each variable.

**3.2. Principal Component Analysis (PCA).** The PCA is a data transformation method that attempts to reduce the

TABLE 1: The geochemical characteristics of different types of formation water in buried hill, Jizhong Depression.

Type	Total dissolved solid (g/l)	Hydrochemical type		Main cation and anion (percentage of meq)	Ionic ratio (Min~Max average)		Occurrence location
		Surin classification	Shu kraft classification		rNa/rCl	r(Cl-Na)/rMg	
C1	<1	NaHCO <sub>3</sub>	HCO <sub>3</sub> -Na and HCO <sub>3</sub> -Na-Mg-Ca	HCO <sub>3</sub> <sup>-</sup> (64%) Na <sup>+</sup> (77%)	(3.0~5.0) 3.9	(-70~-50) -61	In west of Taihangshan uplift
C2	1~10	NaHCO <sub>3</sub>	Cl-HCO <sub>3</sub> -Na	Cl <sup>-</sup> (55%) HCO <sub>3</sub> <sup>-</sup> (39%) Na <sup>+</sup> (94%)	(1.1~2.8) 1.9	(-55~-10) -33	In high uplift of buried hill
C3	5~30	NaHCO <sub>3</sub> and CaCl <sub>2</sub>	Cl-Na	Cl <sup>-</sup> (95%) Na <sup>+</sup> (82%)	(0.85~1.4) 1.1	(-12~9) -3	The slope between the buried hill and sag
C4	8~50	CaCl <sub>2</sub>	Cl-Na-Ca	Cl <sup>-</sup> (93%) Na <sup>+</sup> (62%) Ca <sup>2+</sup> (33%)	(0.3~1.0) 0.7	(4~18) 8	In buried hill of sag

complexity of large multivariate datasets and reveal a simple underlying structure that is assumed to exist in the dataset [14, 39–41]. This technique, which is related to correlations between variables in the dataset, is referred to by Davis [38] as the R-mode. The number of components was based on the Kaiser criterion, for which only the components having eigenvalues greater than 1 are kept [42]. The principal component is expressed by the following linear equation:

$$z_{ij} = a_{i1} \cdot x_{1j} + a_{i2} \cdot x_{2j} + a_{i3} \cdot x_{3j} + \cdots + a_{im} \cdot x_{mj}, \quad (2)$$

where  $a$  is component loading,  $z$  the component score,  $x$  the measure value,  $i$  the component number,  $j$  the sample number, and  $m$  the total number of variables. The advantage of PCA is that it integrates message on all hydrogeochemical dates from the given sample into a single number allowing the simultaneous analysis of those parameters that control the variability of the data. Combined with spatial visualisation, PCA is a helpful method to identify the processes that control formation water evolution and the conceptual model of regional formation water flow.

## 4. Results

**4.1. Hierarchical Cluster Analysis (HCA).** The dendrogram shows the result of hierarchical cluster analysis of the 459 buried hill formation water samples (Figure 5). In the project, the Euclidean distance ( $E$ ) is used as the measure of similarity between different formation water samples. The samples with large similarity are first classified. Then, groups of samples are joined with a linkage rule, and the steps are repeated until all samples have been grouped [14, 25, 43]. In the study, the phenon line was drawn across the dendrogram at a linkage distance of about 30 (Figure 5). Therefore, formation water samples with a linkage distance less than 30 are classified into the same group. The location of the phenon line divided the dendrogram into four clusters of buried hill formation water samples which are C1, C2, C3, and C4 (Figure 5). Large

differences in geochemical characteristics among C1–C4 can be seen in Table 1 and Figures 6 and 7.

Samples from C1 with the lowest total dissolved solids (<1 g/l) primarily occur in the west of Taihangshan uplift, the main anion is HCO<sub>3</sub><sup>-</sup> and the main cation is Na<sup>+</sup>, hydrochemical type of Shu kraft classification is mainly HCO<sub>3</sub>-Na, and a small number is HCO<sub>3</sub>-Na-Mg-Ca. The type of Surin classification is NaHCO<sub>3</sub>. The ionic ratio ranges between 3.0 and 5.0 for rNa/rCl and between -70 and -50 for r(Cl-Na)/rMg. Based on the above dates, the C1 water is in open hydrogeochemical environment.

C2 with lower total dissolved solids (1–10 g/l) is mainly in high uplift of buried hill, the main anions are Cl<sup>-</sup> and HCO<sub>3</sub><sup>-</sup> and the main cation is Na<sup>+</sup>, and hydrochemical type of Shu kraft classification is Cl-HCO<sub>3</sub>-Na. The type of Surin classification is also NaHCO<sub>3</sub>. rNa/rCl values mainly vary between 1.1 and 2.8, and r(Cl-Na)/rMg values vary between -55 and -10. Based on the above dates, the C2 water is in semiopen hydrogeochemical environment.

C3 with higher total dissolved solids (5–30 g/l) is mainly in the slope between the buried hill and sag, the main anion is Cl<sup>-</sup> and the main cation is Na<sup>+</sup>, and hydrochemical type of Shu kraft classification is Cl-Na. The type of Surin classification is NaHCO<sub>3</sub> and CaCl<sub>2</sub>. rNa/rCl values mainly vary between 0.85 and 1.4, and r(Cl-Na)/rMg values vary between -12 and 9. Based on the above dates, the C3 water is in semiclosed hydrogeochemical environment.

C4 with the highest total dissolved solids (8–50 g/l) is mainly in buried hill of sag, the main anion is Cl<sup>-</sup> and the main cations are Na<sup>+</sup> and Ca<sup>2+</sup>, and hydrochemical type of Shu kraft classification is Cl-Na-Ca. The type of Surin classification is CaCl<sub>2</sub>. The rNa/rCl and r(Cl-Na)/rMg of C4 display relatively narrow range from 0.3 to 1.0 and from 4 to 18, respectively. Based on the above dates, the C4 water is in closed hydrogeochemical environment.

With the burial depth increment, the type of formation water changed from C1 to C2, C3, and then C4. The water-rock interaction becomes increasingly intensive and the total

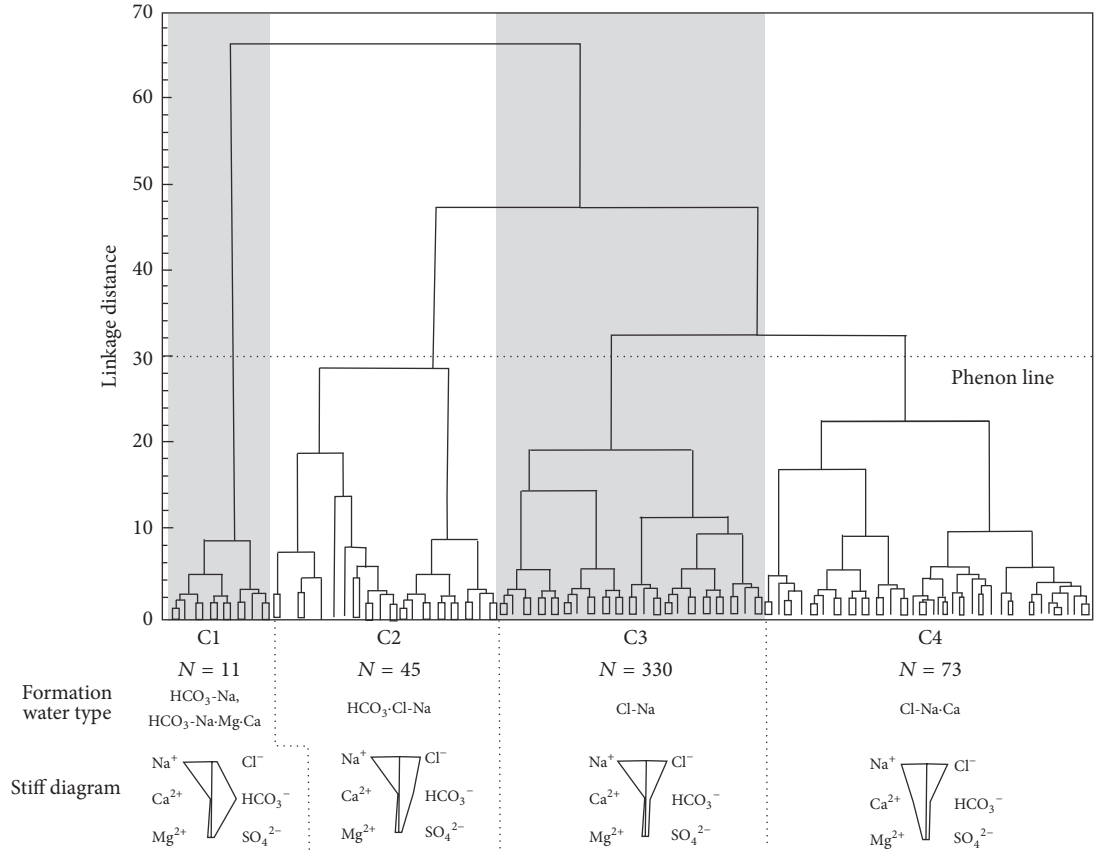


FIGURE 5: Dendrogram for the formation water samples in buried hill of Jizhong Depression, showing the division into four clusters and the median concentration Stiff diagram of each cluster.

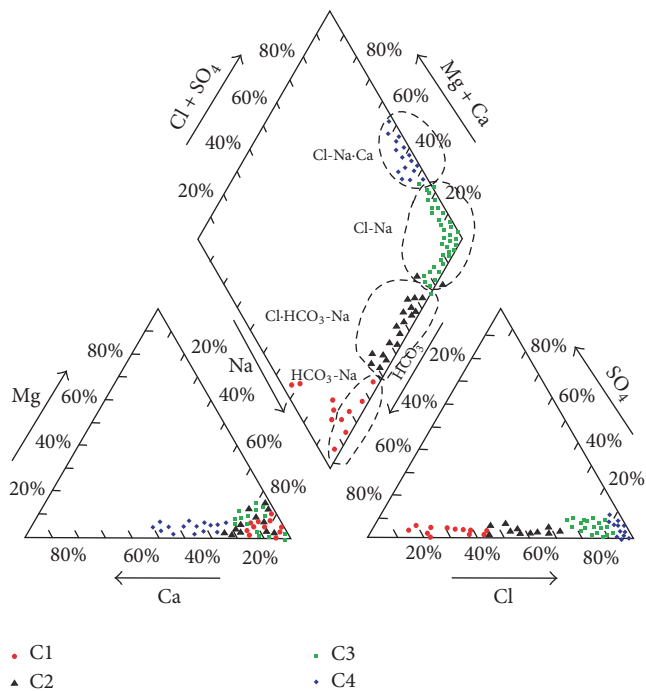


FIGURE 6: Piper diagram of formation water samples from buried hill of Jizhong Depression.

dissolved solid gets higher, resulting in a transition of the water chemical type; for example, rNa/rCl and the rSO<sub>4</sub> × 100/rCl get lower while r(Cl-Na)/rMg gets higher.

In this study, the types of formation water in Es<sub>3</sub> and Es<sub>4</sub> + Ek had also been studied (Figure 3). From Figure 3, samples from Es<sub>3</sub> and Es<sub>4</sub> + Ek have Cl-Na (C3) and Cl-Na-Ca (C4) formation water. Therefore, Es<sub>3</sub> and Es<sub>4</sub> + Ek, dominated by samples of C3 and C4, are in semiclosed-closed hydrogeochemical environment.

**4.2. Principal Components Analysis (PCA).** Three principal components were extracted from the standardized geochemical dataset of buried hill formation water, which suggests only the three principal components with eigenvalues greater than 1 (Table 2). The three components identified in this study cumulatively can account for 86.870% of the total variance in the original dataset. Table 2 presents the principal component loadings for the three components, as well as their respective explained variance. Component1 (PC1) accounts for the greatest amount of the variance (approximately 53.777%) and shows a strong positive loadings in Na<sup>+</sup> and Cl<sup>-</sup> which are 0.878 and 0.953, respectively (Figure 8 and Table 2). Component2 (PC2) explains 19.042% of the variance and is characterized by highly positive loadings in HCO<sub>3</sub><sup>-</sup> which is 0.799 (Figure 8 and Table 2). Component3 (PC3) explains

TABLE 2: Table of component weightings, principal component eigenvalues, and variance of principal components.

Parameters	PC1	PC2	PC3
$\text{Na}^+$	<b>0.878</b>	0.256	<b>-0.682</b>
$\text{Mg}^{2+}$	0.281	-0.137	0.280
$\text{Ca}^{2+}$	0.219	-0.219	<b>0.756</b>
$\text{HCO}_3^-$	0.288	<b>0.799</b>	0.324
$\text{Cl}^-$	<b>0.953</b>	0.093	0.249
$\text{SO}_4^{2-}$	0.571	0.021	<b>-0.570</b>
Eigenvalue variance	3.227	1.343	1.043
Explained variance (%)	53.777	19.042	14.051
Cumulative % of variance	53.777	72.820	86.870

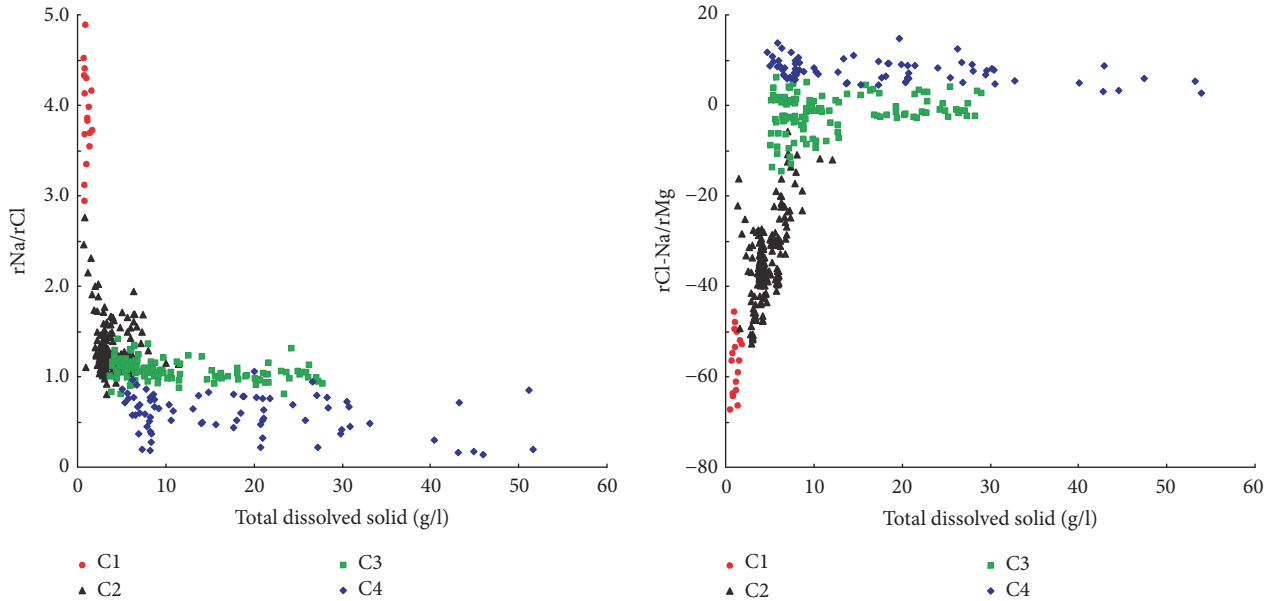


FIGURE 7: The relationship between salinity and sodium chloride coefficient and metamorphic coefficient from different types of formation water in buried hill of Jizhong Depression.

about 14.051% of the variance and shows a strong negative loading of  $\text{SO}_4^{2-}$  and  $\text{Na}^+$  and strong positive loadings of  $\text{Ca}^{2+}$  which are -0.570, -0.682, and 0.756, respectively (Figure 8 and Table 2). Figure 9 shows a scatter plot of the projected scores of PC1-PC2 and PC1-PC3 for the above four types of formation water. From Figure 9, C1 is mainly affected by PC2, C2 is mainly affected by PC1 and PC2, C3 is mainly affected by PC1, and C4 is mainly affected by PC1 and PC3.

## 5. Discussion

**5.1. Origin of Formation Water in Buried Hill.** Formation water in sedimentary basin is usually derived from leached water, sedimentation water, endogenous water, or the mixture of them [44, 45]. The leached water is mainly meteoric water enriched in  $\text{CO}_2$  and  $\text{O}_2$ , sedimentation water is the ancient groundwater which evolved from the ancient surface water, and endogenous water is the high heat fluid from deep earth [46]. The origin of formation water and a series of physical and chemical reaction, such as halite dissolution, evaporation

concentrated seawater, generation of organic matter, and biodegradation, will affect the hydrochemical characteristic of formation water. The multivariate statistical methods of HCA and PCA do not indicate cause-and-effect relationships; they can only provide information from which such relationships can be inferred. Therefore, in order to better identify the physical and chemical processes controlling the geochemical evolution of groundwater, the results of the multivariate statistical analysis have to be combined with the knowledge of the geological and hydrogeological setting [47, 48].

**5.1.1. C1 Type of Water.** Samples from C1 have  $\text{HCO}_3\text{-Na}$  and  $\text{HCO}_3\text{-Na}\text{-Mg}\text{-Ca}$  formation water type and are characterized by the lowest total dissolved solids and  $r(\text{Cl-Na})/\text{rMg}$ , highest  $r\text{Na}/r\text{Cl}$  of all clusters, suggesting that C1 is in open hydrogeochemical environment. According to the above study, C1 is mainly affected by PC2 which shows a strong positive loadings in  $\text{HCO}_3^-$ . Generally speaking, there are main three sources of  $\text{HCO}_3^-$  which are atmospheric water, dissolution of carbonate rocks, and weathering dissolution

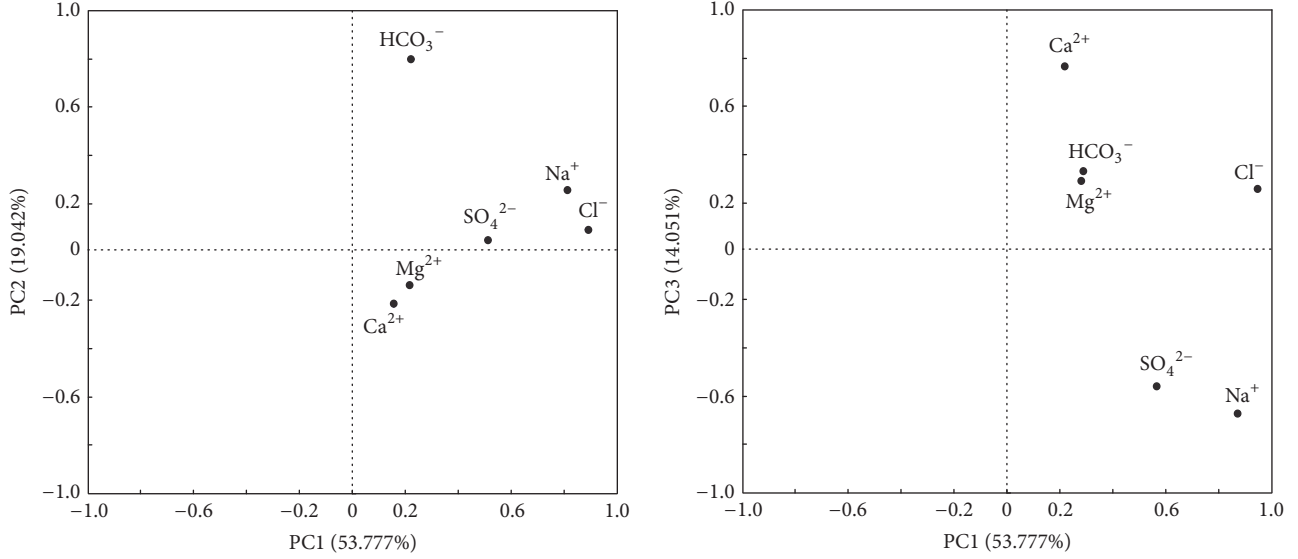


FIGURE 8: Plot of loadings for the three components with Varimax normalized rotation.

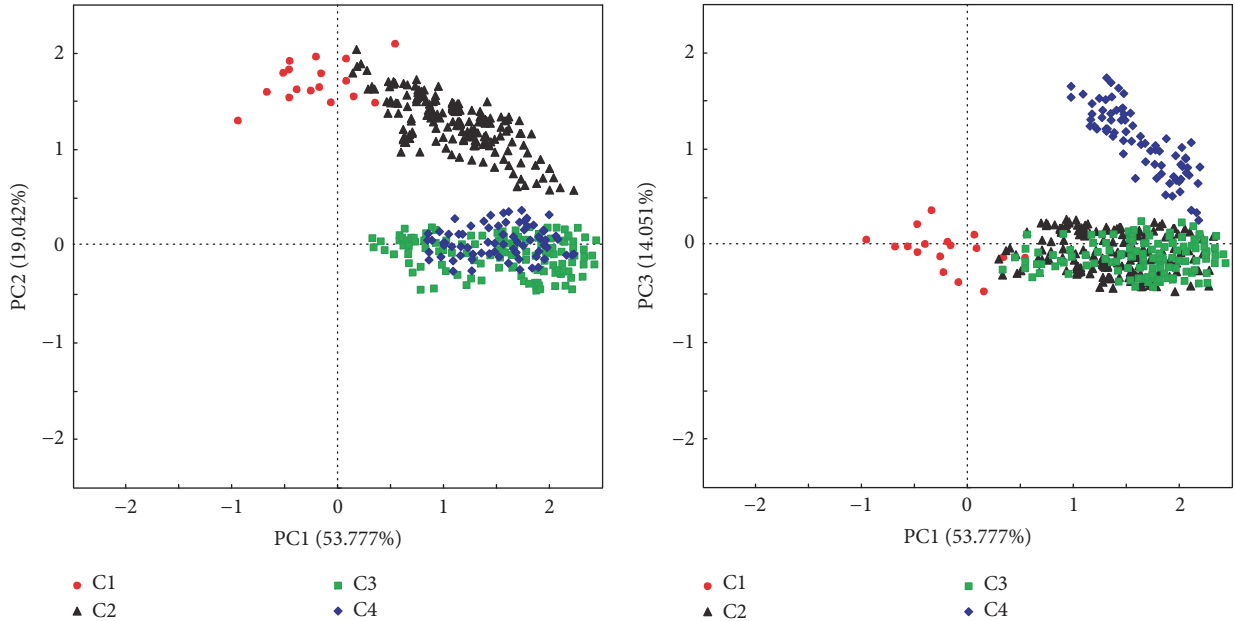


FIGURE 9: Plot of principal component scores for the first three components for the water samples labeled with the groundwater clusters.

of aluminosilicate minerals in magmatic and metamorphic rock areas. The lithology of the buried hill in the study area is mainly marine carbonates rocks, so the explanation that sources of  $\text{HCO}_3^-$  are from weathering dissolution of aluminosilicate minerals can also be eliminated. C1 with the lowest total dissolved solids ( $<1\text{ g/l}$ ) primarily occurs in the west of Taihangshan uplift where the weathered marine carbonates widely outcrop. So C1 may be from the dissolution of dolomite. The stable isotope values of C1 range between  $-80.49\text{\textperthousand}$  and  $-71.53\text{\textperthousand}$  for  $\delta D$  and between  $-11.37\text{\textperthousand}$  and  $-9.17\text{\textperthousand}$  for  $\delta^{18}\text{O}$ , respectively, which are similar to stable isotope values of the present rainwater ( $\delta D = -72.48\text{\textperthousand} \sim -80.22\text{\textperthousand}$ ,  $\delta^{18}\text{O} = -10.31\text{\textperthousand} \sim -11.28\text{\textperthousand}$ ) [33]. In a word,

PC2 is related to the influences of atmospheric water and C1 is mainly derived from atmospheric water, partly affected by the dissolution of dolomite.

**5.1.2. C2 Type of Water.** Samples from C2 have  $\text{Cl}-\text{HCO}_3-\text{Na}$  formation water and are characterized by the lower total dissolved solids and  $r(\text{Cl}-\text{Na})/r\text{Mg}$ , higher  $r\text{Na}/r\text{Cl}$  of all clusters, suggesting that C2 is in semiopen hydrogeochemical environment. The main differences between C1 and C2 are that C2 has higher  $\text{Na}^+$  and  $\text{Cl}^-$  concentration and lower  $\text{HCO}_3^-$  concentration than C1. C2 is mainly affected by PC1 and PC2. PC1 is defined by highly positive loading in  $\text{Na}^+$  and  $\text{Cl}^-$ , which are 0.878 and 0.953, respectively.

Geochemical processes of CP1 could be related to halite dissolution, evaporation concentrated seawater, or ground-water mixing with sea water. Davisson and Criss [49] used a mathematical transformation of Na, Ca, and Cl data an excess-deficit comparison of Na and Ca relative to seawater reference ratio, to explain the major ionic concentrations in numerous basinal fluids around the world. The mathematical transformations are

$$\text{Ca}_{\text{excess}} = \left[ \text{Ca}_{\text{meas}} - \left( \frac{\text{Ca}}{\text{Cl}} \right)_{\text{sw}} \times \text{Cl}_{\text{meas}} \right] \times \frac{2}{40.08} \quad (3)$$

$$\text{Na}_{\text{deficit}} = \frac{[(\text{Na}/\text{Cl})_{\text{sw}} \times \text{Cl}_{\text{meas}} - \text{Na}_{\text{meas}}]}{22.99},$$

where "sw" and "meas" refer to seawater concentrations and measured concentrations, respectively.

Figure 10 shows  $\text{Ca}_{\text{excess}}$ - $\text{Na}_{\text{deficit}}$  of formation water in buried hill. Samples from C2 show slight deficit in  $\text{Na}^+$  and no deficit and excess in  $\text{Ca}^{2+}$ , which are parallel to the sea evaporation line, suggesting that evaporation concentration effect plays an important role during the formation of C2. Therefore, PC1 is related to the evaporation concentration effect and C2 is mainly derived from atmospheric water and evaporation concentration effect.

**5.1.3. C3 Type of Water.** Samples from C3 have Cl-Na formation water and are characterized by the higher total dissolved solids and  $r(\text{Cl}-\text{Na})/r\text{Mg}$ , lower  $r\text{Na}/r\text{Cl}$  of all clusters, suggesting that C3 is in semiclosed-closed hydrogeochemical environment. C3 is mainly affected by PC1, suggesting that evaporation concentration effect plays an important part role during the formation of C3. This conclusion is also supported by Figure 10. Samples from C3 show much more deficit in  $\text{Na}^+$  and no deficit and excess in  $\text{Ca}^{2+}$ , which are also parallel to the sea evaporation line (Figure 10).

**5.1.4. C4 Type of Water.** Samples from C4 have Cl-Na-Ca groundwater and are characterized by the highest total dissolved solids and  $r(\text{Cl}-\text{Na})/r\text{Mg}$ , lowest  $r\text{Na}/r\text{Cl}$  of all clusters, suggesting that C4 is in closed hydrogeochemical environment. C4 is mainly affected by PC1 and PC3, and PC3 is defined by highly positive loading in  $\text{Ca}^{2+}$  and highly negative scores in  $\text{Na}^+$ , which are 0.878 and 0.953, respectively. This association of chemical parameters is related to  $\text{Ca}^{2+}$ - $\text{Na}^+$  ion exchange. Samples from C4 show deficit in  $\text{Na}^+$  and excess in  $\text{Ca}^{2+}$ , which are parallel to the Basinal Fluid Line (BFL), suggesting that plagioclase albitization effect plays an important part role during the formation of C4 (Figure 10). In a word, PC3 is related to the plagioclase albitization effect and C4 is mainly derived from evaporation concentration effect and plagioclase albitization effect.

**5.2. Evolution of Formation Water in Buried Hill.** According to the hydrodynamic conditions (relative hydraulic gradient) and hydrochemical parameters (TDS,  $r\text{Na}/r\text{Cl}$ , and  $r\text{Cl}-\text{Na}/r\text{Mg}$ ), the region can be divided into five main geochemical areas: (1) recharge area, (2) strong alternating area,

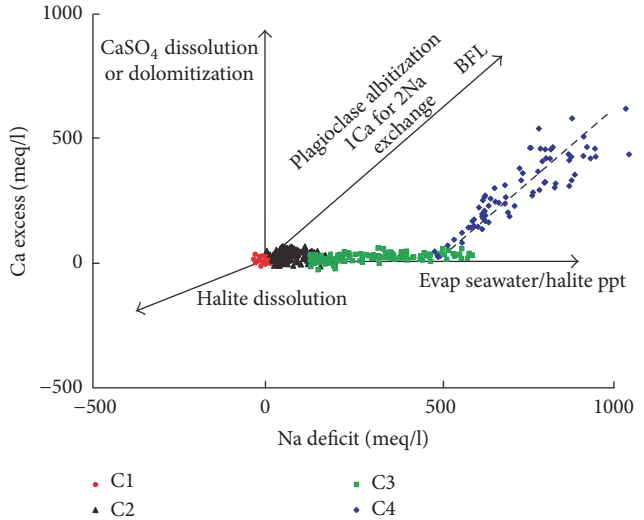


FIGURE 10: The diagram of Ca excess-Na deficit from different types of formation water in buried hill of Jizhong Depression.

(3) weak alternating area, (4) hydrodynamic blocking area, and (5) discharge area (Figure 11). More detailed description about the boundary of the five areas can be seen in Table 3. Table 3 also shows the main geochemical areas and geological and hydrogeological contexts with their respective groundwater clusters as well as the main geochemical processes inferred responsible for the hydrogeochemical evolution of groundwater.

**5.2.1. Recharge Area.** The recharge area, dominated by samples of C1, is in the west of Taihangshan uplift (Figure 11), with a high strong hydraulic gradient, and consists of dolostone. The main anion of C1 is  $\text{HCO}_3^-$  and the main cation is  $\text{Na}^+$ , hydrochemical type of Shu kraft classification is mainly  $\text{HCO}_3-\text{Na}$ , and a small number are  $\text{HCO}_3-\text{Na}\cdot\text{Mg}\cdot\text{Ca}$ . The type of Surin classification is  $\text{NaHCO}_3$ . The ionic ratio ranges between 3.0 and 5.0 for  $r\text{Na}/r\text{Cl}$  and between -70 and -50 for  $r(\text{Cl}-\text{Na})/r\text{Mg}$ . Because the rapid flow and strong influence of atmospheric water, the recharge area with the type of  $\text{HCO}_3-\text{Na}$  and  $\text{HCO}_3-\text{Na}\cdot\text{Mg}\cdot\text{Ca}$  formation water is characterized by the lowest total dissolved solids (<1 g/l) and  $r(\text{Cl}-\text{Na})/r\text{Mg}$  (<-40), highest  $r\text{Na}/r\text{Cl}$  (>3), suggesting that it is in open hydrogeochemical environment. With its high  $\text{HCO}_3^-$ ,  $\text{Na}^+$ ,  $\text{Mg}^{2+}$ , and  $\text{Ca}^{2+}$  concentrations, C1 is clearly recharge formation water. This formation water composition in recharge area results from atmospheric water and dissolution of dolomite.

**5.2.2. Strong Alternating Area.** The strong alternating area, characterized mainly by C2 and some C1, is next to the recharge area (Figure 11), with a relatively high hydraulic gradient, and consists of dolostone. The main anions of C2 are  $\text{Cl}^-$  and  $\text{HCO}_3^-$  and the main cation is  $\text{Na}^+$ , and hydrochemical type of Shu kraft classification is  $\text{Cl}\cdot\text{HCO}_3-\text{Na}$ . The type of Surin classification is also  $\text{NaHCO}_3$ .  $r\text{Na}/r\text{Cl}$  values mainly vary between 1.1 and 2.8, and  $r(\text{Cl}-\text{Na})/r\text{Mg}$  values vary between -55 and -10. The strong alternating area had  $\text{Cl}\cdot\text{HCO}_3-\text{Na}$  and  $\text{HCO}_3-\text{Na}$  formation water type,

TABLE 3: Main geochemical areas and geological and hydrogeological contexts related to groundwater clusters.

Properties of the geochemical areas	Water supply area	Strong alternating area	Weak alternating area	Hydrodynamic blocking area	Discharge area
TDS (g/l)	<1	0.5~4	4~15	5~40	5~40
rNa/rCl	>3	1.4~2.0	1.2~1.4	0.9~1.2	0.6~1.1
rCl-Na/rMg	<-40	-50~-20	-15~-5.0	-9~5	-5~15
Relative hydraulic gradient	Strong	Strong to moderate	Moderate	Moderate to small	Small
Hydrogeochemical environment	Open	Semiopen-open	Semiopen-semiclosed	Semiclosed-closed	Semiclosed-closed
Main groundwater clusters	C1	C1, C2	C2, C3	C3, C4	C3, C4
Main geochemical processes	(1) Atmospheric water (2) Dissolution of carbonates	(1) Atmospheric water (2) Evaporation concentration (3) Dissolution of carbonates	(1) Evaporation concentration (2) Atmospheric water	(1) Evaporation concentration (2) Plagioclase albition effect	(1) Evaporation concentration (2) Plagioclase albition effect
Proven oil reserves ( $\times 10^4$ t)	0	0	1696	42158	8038

which is characterized by the lower total dissolved solids (0.5~4 g/l) and r(Cl-Na)/rMg (-50~-20), higher rNa/rCl (1.4~2.0), suggesting that it is in open-semiopen hydrogeochemical environment. With its high  $\text{HCO}_3^-$ ,  $\text{Cl}^-$ , and  $\text{Na}^+$  concentrations, the formation water composition in strong alternating area mainly results from atmospheric water and partly from evaporation concentration.

**5.2.3. Weak Alternating Area.** The weak alternating area, characterized mainly by C2 and some C3, is in lower uplift (Figure 11), with a strong to moderate gradient, and consists of dolostone and limestone. Because the movement of formation water in weak alternating area is still relatively active, the weak alternating area had Cl-HCO<sub>3</sub>-Na and Cl-Na formation water type, which is characterized by the lower total dissolved solids (4~15 g/l) and r(Cl-Na)/rMg (-15~-5), higher rNa/rCl (1.2~1.4), suggesting that it is in semiopen-semiclosed hydrogeochemical environment. With its high  $\text{Cl}^-$ ,  $\text{Na}^+$ , and  $\text{HCO}_3^-$  concentrations, the formation water composition in weak alternating area mainly results from evaporation concentration and partly from atmospheric water.

**5.2.4. Hydrodynamic Blocking Area.** The hydrodynamic blocking area, dominated by samples of C3 and C4, is in the middle of Jizhong Depression (Figure 11), with a low hydraulic gradient, and consists of dolostone and limestone. The main anion of C4 is  $\text{Cl}^-$  and the main cations are  $\text{Na}^+$  and  $\text{Ca}^{2+}$ , and hydrochemical type of Shu kraft classification is Cl-Na-Ca. The type of Surin classification is CaCl<sub>2</sub>. The rNa/rCl and r(Cl-Na)/rMg of C4 display relatively narrow range from 0.3 to 1.0 and from 4 to 18, respectively. Based on the above dates, the C4 water is in closed hydrogeochemical environment. Due to being far away from recharge area, the flow of formation water in the hydrodynamic blocking area is slow. Hydrodynamic blocking area had Cl-Na and

Cl-Na-Ca formation water type, which is characterized by the higher total dissolved solids (5~40 g/l) and r(Cl-Na)/rMg (-8~5), lower rNa/rCl (0.9~1.2), suggesting that it is in semiclosed-closed hydrogeochemical environment. With its high  $\text{Cl}^-$ ,  $\text{Na}^+$ , and  $\text{Ca}^{2+}$  concentrations, the formation water composition in hydrodynamic blocking area mainly results from evaporation concentration and plagioclase albition effect.

**5.2.5. Discharge Area.** The discharge area, also dominated by samples of C3 and C4, is in the east of Jizhong Depression (Figure 11), with a low hydraulic gradient, and consists of limestone. The discharge area had Cl-Na and Cl-Na-Ca formation water type, which are characterized by the higher total dissolved solids (5~40 g/l) and r(Cl-Na)/rMg (-5~-15), lower rNa/rCl (0.6~1.1), suggesting that it is in semiclosed-closed hydrogeochemical environment. With its high  $\text{Cl}^-$ ,  $\text{Na}^+$ , and  $\text{Ca}^{2+}$  concentrations, the formation water composition in discharge area mainly results from evaporation concentration and plagioclase albition effect.

In conclusion, from the recharge area to the discharge area, the type of formation water in buried hill changed from C1 to C2, C3, and then C4 (Figure 11). The water-rock interaction becomes increasingly intensive and the total dissolved solid gets higher, resulting in a transition of the water chemical type; for example, rNa/rCl and  $r\text{SO}_4 \times 100/r\text{Cl}$  get lower while r(Cl-Na)/rMg gets higher. Due to the influence of atmospheric water and dissolution of dolomite, the recharge area is characterized by C1 formation water (HCO<sub>3</sub>-Na and HCO<sub>3</sub>-Na-Mg·Ca). From recharge area to strong alternating area, the influence of atmospheric water gets weak and evaporation concentration effect gets strong; formation water belonging to C1 (HCO<sub>3</sub>-Na and HCO<sub>3</sub>-Na-Mg·Ca) evolves along its flow path into formation water of C2 (Cl-HCO<sub>3</sub>-Na). From strong alternating area to weak

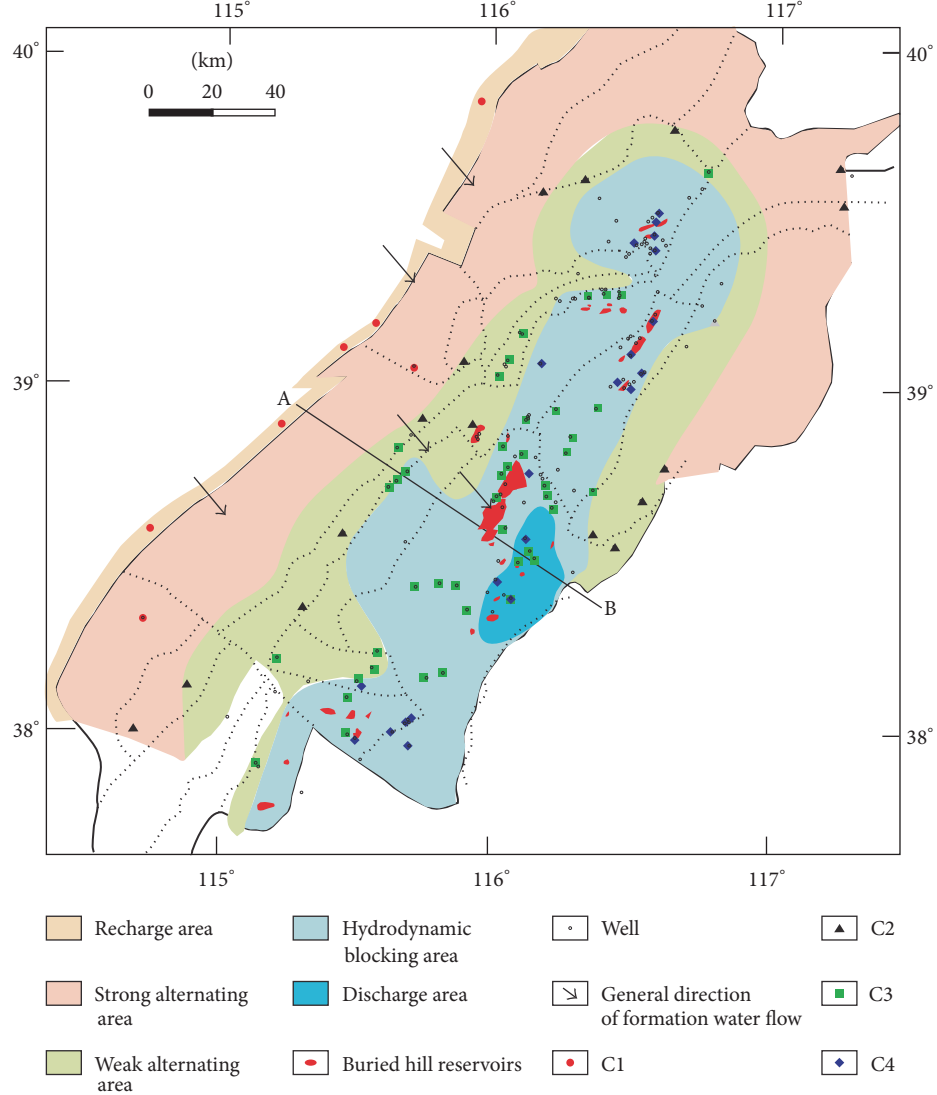


FIGURE 11: The analysis of hydrodynamic conditions in buried hill, Jizhong Depression.

alternating area, the influence of atmospheric water gets weaker and evaporation concentration effect gets stronger; formation water belonging to C2 ( $\text{Cl}-\text{HCO}_3-\text{Na}$ ) evolves along its flow path into formation water of C3 ( $\text{Cl}-\text{Na}$ ). From weak alternating area to hydrodynamic blocking area and discharge area, formation water belonging to C3 ( $\text{Cl}-\text{Na}$ ) evolves along its flow path by  $\text{Ca}^{2+}$ - $\text{Na}^+$  ion exchange (plagioclase albitization effect) into formation water of C4 ( $\text{Cl}-\text{Na}-\text{Ca}$ ) (Figure 11).

**5.3. The Implication of Origin and Evolution of Formation Water in Buried Hill for Hydrocarbon Distribution.** More than 23 buried hill oil fields and  $5.19 \times 10^8$  t proven oil in place in these fields have been discovered by the year 2015. Based on the analysis of the type of formation water and proven oil reserves in these 23 buried hill oil fields, the influence of the types of formation water in buried hill on the distribution of buried hill oil reserves was researched. The results showed that more than 87% ( $4.51 \times 10^8$  t) of proven oil reserves

are related to  $\text{Cl}-\text{Na}$  (C3) type water, 10% ( $0.51 \times 10^8$  t) of proven oil reserves are related to  $\text{Cl}-\text{Na}-\text{Ca}$  (C4) type water, 3% ( $0.17 \times 10^8$  t) of proven oil reserves are related to  $\text{Cl}-\text{HCO}_3-\text{Na}$  (C2) type water, and no oil is found in  $\text{HCO}_3-\text{Na}$  (C1) type water (Figure 12). Therefore, the buried hill reservoirs in Jizhong Depression are mainly related to the C3 ( $\text{Cl}-\text{Na}$ ) and C4 ( $\text{Cl}-\text{Na}-\text{Ca}$ ) types water which are in semiclosed-closed hydrogeochemical environment. No or less buried hill reservoir was found in  $\text{HCO}_3-\text{Na}$  (C1) and  $\text{Cl}-\text{HCO}_3-\text{Na}$  (C2) types water which are in semiopen-open hydrogeochemical environment.

The article also studied the influence of hydrodynamic environment on the distribution of buried hill oil reserves. The results showed that more than 81% ( $4.22 \times 10^8$  t) of proven oil reserves are distributed in hydrodynamic blocking area, 15% ( $0.81 \times 10^8$  t) of proven oil reserves are distributed in discharge area, 4% ( $0.17 \times 10^8$  t) of proven oil reserves are distributed in weak alternating area, and no oil was found in recharge area and strong alternating area (Figure 13). Because

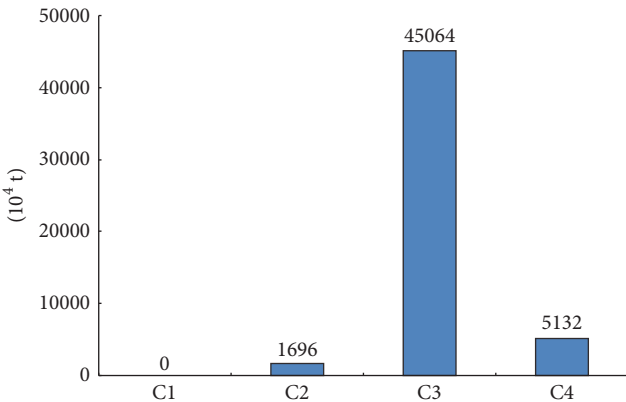


FIGURE 12: Proven oil reserves in different types of formation water in buried hill, Jizhong Depression.

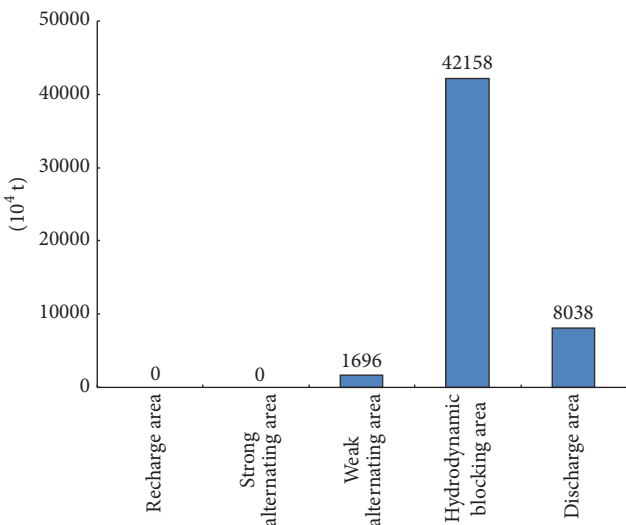


FIGURE 13: Proven oil reserves in different hydrodynamic systems of buried hill, Jizhong Depression.

the rapid flow and strong influence of atmospheric water, the preservation condition of oil and gas is poor and no oil and gas were found in recharge area and strong alternating area. The movement of formation water in weak alternating area is still relatively active and the oil and gas can only be preserved in relatively weak hydrodynamic areas. So less oil and gas were found in weak alternating area. Due to being far away from recharge area, the flow of formation water in the hydrodynamic blocking area and discharge area is slow and they are favorable regions to preserve oil and gas. Therefore, more than 95% of buried hill oil in Jizhong Depression is distributed in hydrodynamic blocking area and discharge area.

The above study shows that the buried hill reserves of Jizhong Depression are mainly distributed in hydrodynamic blocking area and discharge area whose formation water types are Cl-Na and Cl-Na-Ca, so the two regions can be the favorable areas for petroleum migration.

## 6. Conclusion

- (1) The hierarchical cluster analysis (HCA) classified 459 formation water samples in buried hill of Jizhong Depression into four geochemically distinct clusters (C1-C4). C1 is mostly located in recharge area of west Taihangshan uplift, the main anion is  $\text{HCO}_3^-$  and the main cation is  $\text{Na}^+$ , and hydrochemical type is  $\text{HCO}_3^-$ -Na, which is in open hydrogeochemical environment. C2 is mainly in high uplift of buried hill, the main anions are  $\text{Cl}^-$  and  $\text{HCO}_3^-$  and the main cation is  $\text{Na}^+$ , and hydrochemical type is  $\text{Cl}-\text{HCO}_3^-$ -Na, which is in semiopen hydrogeochemical environment. C3 is mainly in the slope between the buried hill and sag, the main anion is  $\text{Cl}^-$  and the main cation is  $\text{Na}^+$ , and hydrochemical type is Cl-Na, which is in semiclosed hydrogeochemical environment. C4 is mainly in the buried hill of sag, the main anion is  $\text{Cl}^-$  and the main cations are  $\text{Na}^+$  and  $\text{Ca}^{2+}$ , and hydrochemical type is  $\text{Cl}-\text{Na}\cdot\text{Ca}$ , which is in closed hydrogeochemical environment.
- (2) With the burial depth increment, the type of formation water in buried hill changed from C1 to C2, C3, and then C4; the water-rock interactions become increasingly intensive and the mineralization degree gets higher, resulting in a transition of the water chemical type, for example,  $r\text{Na}/r\text{Cl}$  gets lower while total dissolved solids and  $r(\text{Cl}-\text{Na})/r\text{Mg}$  get higher.
- (3) Three components of the principal components analysis (PCA) explain 86.87% of the variance in the dataset. PC1, characterized by highly positive loadings in  $\text{Na}^+$  and  $\text{Cl}^-$ , is related to evaporation concentration. PC2 is defined by highly positive loadings in  $\text{HCO}_3^-$  and is related to influence of atmospheric water. With high positive loadings in  $\text{Ca}^{2+}$  and high negative loadings in  $\text{Na}^+$  and  $\text{SO}_4^{2-}$ , PC3 suggests the influences of plagioclase albitionization.
- (4) C1 with  $\text{HCO}_3^-$ -Na formation water, mainly affected by PC2, is mainly from atmospheric infiltration water. C2 with  $\text{Cl}-\text{HCO}_3^-$ -Na formation water is affected by PC1 and PC2, suggesting that it is derived from atmospheric water and evaporation concentration effect. C3 with Cl-Na formation water is affected by PC1, suggesting that evaporation concentration effect plays an important part role during the formation of the C3. C4 with  $\text{Cl}-\text{Na}\cdot\text{Ca}$  formation water, mainly affected by PC2 and PC3, is mainly from the deposition water and evaporation concentration and plagioclase albitionization effect play important roles during the formation of C4.
- (5) The combination of HCA and PCA within the geological and hydrogeological contexts allowed the division of the study area into five dynamic areas (recharge area, strong alternating area, weak alternating area, hydrodynamic blocking area, and discharge area). From the recharge area to discharge area, the influence of atmospheric water gets weak and the water-rock interactions such as evaporation

- concentration and plagioclase albitization become increasingly intensive; therefore the recharge area is dominated by samples of C1, strong alternating area is dominated by samples of C1 and C2, weak alternating area is dominated by samples of C2 and C3, and hydrodynamic blocking area and discharge area are dominated by samples of C3 and C4.
- (6) Buried hill reservoir in Jizhong Depression is mainly distributed in hydrodynamic blocking area and discharge area; therefore the two regions can be the favorable areas for petroleum migration and the above statistical analyses' methodology can be used in the other study areas which have similar geological and hydrogeological background to the study area.
- ## Conflicts of Interest
- The authors declare that they have no conflicts of interest.
- ## Acknowledgments
- This study was financially supported by the National Science and Technology Special Grant (no. 2016ZX05006-001). Thanks are also given to Huabei Oilfield Company of Sinopec, which provided all the related data of Jizhong Depression.
- ## References
- [1] H. G. Machel, "Bacterial and thermochemical sulfate reduction in diagenetic settings - old and new insights," *Sedimentary Geology*, vol. 140, no. 1-2, pp. 143–175, 2001.
  - [2] K. Michael and S. Bachu, "Origin, chemistry and flow of formation waters in the Mississippian-Jurassic sedimentary succession in the west-central part of the Alberta Basin, Canada," *Marine and Petroleum Geology*, vol. 19, no. 3, pp. 289–306, 2002.
  - [3] X. Xie, Z. Fan, X. Liu, and Y. Lu, "Geochemistry of formation water and its implication on overpressured fluid flow in the Dongying Depression of the Bohaiwan Basin, China," *Journal of Geochemical Exploration*, vol. 89, no. 1-3, pp. 432–435, 2006.
  - [4] Y. Fu and H. Zhan, "On the origin of oil-field water in the Biyang Depression of China," *Environmental Geology*, vol. 58, no. 6, pp. 1191–1196, 2009.
  - [5] Y. Wang, H. Xu, C. Wang, and B. Jia, "Characteristics of the salinity and distribution of the Neopaleozoic formation water in Ordos Basin," *Shiyou Xuebao/Acta Petrolei Sinica*, vol. 31, no. 5, pp. 748–761, 2010.
  - [6] R. Bagheri, A. Nadri, E. Raeisi, H. G. M. Eggenkamp, G. A. Kazemi, and A. Montaseri, "Hydrochemical and isotopic ( $\delta^{18}\text{O}$ ,  $\delta^2\text{H}$ ,  $87\text{Sr}/86\text{Sr}$ ,  $\delta^{37}\text{Cl}$  and  $\delta^{81}\text{Br}$ ) evidence for the origin of saline formation water in a gas reservoir," *Chemical Geology*, vol. 384, pp. 62–75, 2014.
  - [7] J. S. Hanor and J. C. McIntosh, "Diverse origins and timing of formation of basinal brines in the Gulf of Mexico sedimentary basin," *Geofluids*, vol. 7, no. 2, pp. 227–237, 2007.
  - [8] Y. K. Kharaka and J. S. Hanor, "Deep Fluids in the Continents: I. Sedimentary Basins," *Treatise on Geochemistry*, vol. 5-9, pp. 1–48, 2003.
  - [9] M. Tesmer, P. Möller, S. Wieland, C. Jahnke, H. Voigt, and A. Pekdeger, "Deep reaching fluid flow in the North East German Basin: Origin and processes of groundwater salinisation," *Hydrogeology Journal*, vol. 15, no. 7, pp. 1291–1306, 2007.
  - [10] P. Birkle and R. A. Maruri, "Isotopic indications for the origin of formation water at the Activo Samaria-Sitio Grande oil field, Mexico," *Journal of Geochemical Exploration*, vol. 78–79, pp. 453–458, 2003.
  - [11] T. K. Lowenstein, L. A. Hardie, M. N. Timofeeff, and R. V. Demicco, "Secular variation in seawater chemistry and the origin of calcium chloride basinal brines," *Geology*, vol. 31, no. 10, pp. 857–860, 2003.
  - [12] S. V. Panno, K. C. Hackley, R. A. Locke et al., "Formation waters from Cambrian-age strata, Illinois Basin, USA: constraints on their origin and evolution," *Geochimica et Cosmochimica Acta*, vol. 122, pp. 184–187, 2013.
  - [13] I. M. Farnham, K. H. Johannesson, A. K. Singh, V. F. Hodge, and K. J. Stetzenbach, "Factor analytical approaches for evaluating groundwater trace element chemistry data," *Analytica Chimica Acta*, vol. 490, no. 1-2, pp. 123–138, 2003.
  - [14] V. Cloutier, R. Lefebvre, R. Therrien, and M. M. Savard, "Multivariate statistical analysis of geochemical data as indicative of the hydrogeochemical evolution of groundwater in a sedimentary rock aquifer system," *Journal of Hydrology*, vol. 353, no. 3-4, pp. 294–313, 2008.
  - [15] S. M. Yidana, D. Ophori, and B. Banoeng-Yakubo, "A multivariate statistical analysis of surface water chemistry data-The Ankobra Basin, Ghana," *Journal of Environmental Management*, vol. 86, no. 1, pp. 80–87, 2008.
  - [16] P. S. Yang and G. Z. Li, "Development of carbonate reservoirs in the Renqiu Oil Field," *Acta Petrolei Sinica*, vol. 1, pp. 57–64, 1980.
  - [17] X. Zhao, Q. Wang, F. Jin et al., "Main controlling factors and exploration practice of subtle buried-hill hydrocarbon reservoir in Jizhong depression," *Shiyou Xuebao/Acta Petrolei Sinica*, vol. 33, no. 1, pp. 71–79, 2012.
  - [18] C. H. Gao, M. Zha, X. Z. Zhao, and F. Peng, "Migration systems and hydrocarbon accumulation models of buried hill reservoirs in Jizhong Depression," *Lithologic Reservoirs*, vol. 2, pp. 26–30, 2015.
  - [19] X. Zhao, F. Jin, Y. Wang, Y. Guo, J. Liu, and R. Zheng, "Buried-hill reservoir-forming mode of 'old reservoir-old sealing formation' in Changyangdian area of Jizhong Depression," *Shiyou Xuebao/Acta Petrolei Sinica*, vol. 29, no. 4, pp. 489–493, 2008.
  - [20] X. Zhao, F. Jin, Q. Wang et al., "Niudong 1 ultra-deep and ultra-high temperature subtle buried hill field in Bohai Bay Basin: discovery and significance," *Shiyou Xuebao/Acta Petrolei Sinica*, vol. 32, no. 6, pp. 915–927, 2011.
  - [21] Q. H. Chen, H. G. Lao, K. Y. Wu, Z. H. Wu, and Y. Q. Cui, "Favorable hydrocarbon accumulation conditions for carbonate reservoirs in deepburied hills in the Jizhong Deprrssion," *Natural Gas Industry*, vol. 27, pp. 32–39, 2013.
  - [22] S. Sun, J. S. Xie, G. R. Li, and C. Y. Qiu, "Hydrogen and oxygen isotopic composition and genesis of the ground water in Jizhong Depression," *Oil Gas Geology*, vol. 3, pp. 240–250, 1982.
  - [23] B. P. Han, "Study on chemistry of oilfield water in buried block hill in Jizhong Depression," *Scientia Geologica Sinica*, vol. 3, pp. 263–273, 1989.
  - [24] Y. H. Qu, Z. C. Sun, X. J. Feng, and Z. M. Chen, "Middle-upper proterozoic buried hill groundwater geohydrologic character and significance for exploration in northern Jizhong depression

- basin," *Journal of Daqing Petroleum Institute*, vol. 23, pp. 8–11, 1999.
- [25] C. J. Daughney and R. R. Reeves, "Definition of hydrochemical facies in the New Zealand National Groundwater Monitoring Programme," *Journal of Hydrology (New Zealand)*, vol. 44, no. 2, pp. 105–130, 2005.
- [26] B. O'Shea and J. Jankowski, "Detecting subtle hydrochemical anomalies with multivariate statistics: An example from 'homogeneous' groundwaters in the Great Artesian Basin, Australia," *Hydrological Processes*, vol. 20, no. 20, pp. 4317–4333, 2006.
- [27] S. X. Li, M. J. Chu, T. F. Wang, and W. X. Zhang, "Features of formation water and implications for hydrocarbon accumulation in Chang 6 pay zone, Jiyuan area, Ordos Basin," *China Petroleum Exploration*, vol. 22, pp. 43–52, 2017.
- [28] J. Wang, Z. Lou, R. Zhu et al., "Hydrochemistry of Paleogene formation water and its relationship with hydrocarbon migration and accumulation in Wenliu region in Dongpu sag, Bohai Bay Basin," *Oil and Gas Geology*, vol. 35, no. 4, pp. 449–455, 2014.
- [29] M. L. Davisson, T. S. Presser, and R. E. Criss, "Geochemistry of tectonically expelled fluids from the northern Coast ranges, Rumsey Hills, California, USA," *Geochimica et Cosmochimica Acta*, vol. 58, no. 7, pp. 1687–1699, 1994.
- [30] K. S. Lu, Y. J. Li, and Y. K. Wu, "Tectonic evolution of buried hill in JiZhong Depression and petroleum geological significance," *Journal of oil and gas technology*, vol. 33, pp. 35–42, 2011.
- [31] D. Dong, L. Li, J. Liu, and J. Li, "Cenozoic tectonic evolution in the north-central Jizhong Depression," *Oil and Gas Geology*, vol. 34, no. 6, pp. 771–780, 2013.
- [32] H. G. Lao, K. Y. Wu, and Q. H. Chen, "Geology character and evolution of the accommodation zone in the JiZhong Depression," *Journal of geomechanics*, vol. 16, pp. 294–309, 2010.
- [33] J. H. Du, H. W. Zou, B. S. Fei, H. Y. Lei, F. Z. Zhang, and Y. M. Zhang, *Buried Hill Composite Hydrocarbon Accumulation Zone of Jizhong Depression*, Science Press, 2002.
- [34] R. K. Steinhorst and R. E. Williams, "Discrimination of groundwater sources using cluster analysis, MANOVA, Canonical Analysis and Discriminant Analysis," *Water Resources Research*, vol. 21, no. 8, pp. 1149–1156, 1985.
- [35] C. Güler, G. D. Thyne, J. E. McCray, and A. K. Turner, "Evaluation of graphical and multivariate statistical methods for classification of water chemistry data," *Hydrogeology Journal*, vol. 10, no. 4, pp. 455–474, 2002.
- [36] E. M. Adar, E. Rosenthal, A. S. Issar, and O. Batelaan, "Quantitative assessment of the flow pattern in the southern Arava Valley (Israel) by environmental tracers and a mixing cell model," *Journal of Hydrology*, vol. 136, no. 1-4, pp. 333–352, 1992.
- [37] P. P. Schot and J. van der Wal, "Human impact on regional groundwater composition through intervention in natural flow patterns and changes in land use," *Journal of Hydrology*, vol. 134, no. 1-4, pp. 297–313, 1992.
- [38] J. C. Davis, *Statistics and Data Analysis in Geology*, John Wiley & Sons Inc, New York, NY, USA, 1986.
- [39] A. Melloul and M. Collin, "The 'principal components' statistical method as a complementary approach to geochemical methods in water quality factor identification; application to the Coastal Plain aquifer of Israel," *Journal of Hydrology*, vol. 140, no. 1-4, pp. 49–73, 1992.
- [40] T. C. Winter, S. E. Mallory, T. R. Allen, and D. O. Rosenberry, "The use of principal component analysis for interpreting ground water hydrographs," *Groundwater*, vol. 38, no. 2, pp. 234–246, 2000.
- [41] G. Thyne, C. Güler, and E. Poeter, "Sequential analysis of hydrochemical data for watershed characterization," *Groundwater*, vol. 42, no. 5, pp. 711–723, 2004.
- [42] StatSoft Inc *STATISTICA (Data Analysis Software System, Version 6)*, 2004.
- [43] C. J. Daughney, M. Raiber, M. Moreau-Fournier, U. Morgenstern, and R. van der Raaij, "Use of hierarchical cluster analysis to assess the representativeness of a baseline groundwater quality monitoring network: comparison of New Zealand's national and regional groundwater monitoring programs," *Hydrogeology Journal*, vol. 20, no. 1, pp. 185–200, 2012.
- [44] W. J. Xiao, J. R. Lu, Q. X. Liu et al., "Analysis of geochemical characteristics and formation age of geyser fluid deposited in Beiyuan Jiayuan to Beijing Olympic Park Area," *Earth Science Frontiers*, vol. 16, pp. 384–395, 2009.
- [45] L. Luo, Z. Pang, and F. Yang, "Genesis analysis of sulfate thermal mineral water in carbonate aquifers at Jianhu Uplift, Subei Basin," *Earth Science Frontiers*, vol. 22, no. 2, pp. 263–270, 2015.
- [46] G. Lin, J. A. Nunn, and D. Deming, "Thermal buffering of sedimentary basins by basement rocks: Implications arising from numerical simulations," *Petroleum Geoscience*, vol. 6, no. 4, pp. 299–307, 2000.
- [47] I. M. Farnham, K. J. Stetzenbach, A. K. Singh, and K. H. Johannesson, "Deciphering groundwater flow systems in Oasis Valley, Nevada, using trace element chemistry, multivariate statistics, and geographical information system," *Mathematical Geology*, vol. 32, no. 8, pp. 943–968, 2000.
- [48] K. J. Stetzenbach, V. F. Hodge, C. Guo, I. M. Farnham, and K. H. Johannesson, "Geochemical and statistical evidence of deep carbonate groundwater within overlying volcanic rock aquifers/aquitards of southern Nevada, USA," *Journal of Hydrology*, vol. 243, no. 3-4, pp. 254–271, 2001.
- [49] M. L. Davisson and R. E. Criss, "Na-Ca-Cl relations in basinal fluids," *Geochimica et Cosmochimica Acta*, vol. 60, no. 15, pp. 2743–2752, 1996.

## Research Article

# Three-Dimensional Hydromechanical Modeling during Shearing by Nonuniform Crust Movement

Yuqing Zhao,<sup>1,2</sup> You-Kuan Zhang,<sup>1,3</sup> and Xiuyu Liang<sup>1,2</sup>

<sup>1</sup>Center for Hydrosciences Research, Nanjing University, Nanjing, Jiangsu 210093, China

<sup>2</sup>School of Earth Sciences and Engineering, Nanjing University, Nanjing, Jiangsu 210093, China

<sup>3</sup>School of Environment Sciences and Engineering, Southern University of Science and Technology, Shenzhen, Guangdong 518055, China

Correspondence should be addressed to You-Kuan Zhang; zhangyk@sustc.edu.cn and Xiuyu Liang; xyliang@nju.edu.cn

Received 29 June 2017; Accepted 8 November 2017; Published 17 December 2017

Academic Editor: Jet-Chau Wen

Copyright © 2017 Yuqing Zhao et al. This is an open access article distributed under the Creative Commons Attribution License, which permits unrestricted use, distribution, and reproduction in any medium, provided the original work is properly cited.

Hydromechanical modeling of a geological formation under shearing by the nonuniform crust movement during 10000 years was carried out to investigate the solid stress and pore pressure coupling processes of the formation from the intact to the fractured or faulted. Two three-dimensional numerical models were built and velocities in opposite directions were applied on the boundaries to produce the shearing due to the nonuniform crust movement. The results show that the stress and pore pressure became more and more concentrated in and around the middle of the formation as time progresses. In Model I with no fault, stress and pore pressure are concentrated in the middle of the model during shearing; however, in Model II with a fault zone of weakened mechanical properties, they are more complex and concentrated along the sides of the fault zone and the magnitudes decreased. The distribution of stress determines pore pressure which in turn controls fluid flow. Fluid flow occurs in the middle in Model I but along the sides of the fault zone in Model II. The results of this study improve our understanding of the rock-fluid interaction processes affected by crustal movement and may guide practical investigations in geological formations.

## 1. Introduction

It is commonly recognized that fluid flow in bedrock regions is mainly controlled by faults and fractures [1–4] and that faults and fractures were usually generated by crust movements resulting from the mantle convection based on the theory of plate tectonics [5, 6]. Existence of faults or fractures significantly affects the flow and transport in geological formation [5, 7]. It is critically important to understand how the solid stress and fluid pressure evolved in a formation due to crust movement and what is the effect of an existing fault on the evolution and distribution of the stress and pressure in various research areas and engineering applications, such as earthquake prediction and construction of repositories for radioactive waste, dam foundations, underground tunnels, and oil and gas facilities.

The speed of the earth crust movement in a formation is generally nonuniform. Based on the GPS data, for example, Niu et al. [6] pointed out that “the South China block and

North China block in eastern China move EES-ward relative to the stable Eurasia. The velocities increase toward the south . . . .” The average velocity of the crustal movement to the SEE direction from 1999 to 2011 is about 2.50 mm/year in the Northeast China and about 2.90 mm/year in the same direction in South China [8]. The speed difference of 0.40 mm/year seems small but the difference in the accumulative moving distances of the North and South China is huge in geological time. Such a difference in the crustal movement may generate shear stress which in turn creates the strike of faults and fractures along the NWW-SEE direction in eastern China. In fact, Xiao devoted his whole life from 1950s to 2000s to identify the new and active faults and fractures in eastern China for the purpose of locating water-supply wells which commonly have the large capacity of water-supply located in the active faults and fractures [5]. He found that most active faults and fractures in eastern China are oriented in the SEE-NWW direction. The objective of this study is to improve our understanding of the coupled processes of the solid

stress and fluid pressure in the formations by carrying out a hydromechanical modeling of shallow geological formations under shearing induced by the nonuniform crust movement.

The coupling processes of bedrock deformations and pore pressure changes can be described by the theory of poroelasticity [9–13]. Garven investigated the mechanics of flow near a fault on the fold and thrust margin of a basin, especially during active faulting [14]. Forster and Evans conducted the experiments and numerical simulations to characterize the permeability structure of thrust zones and found that the regional groundwater flow patterns were controlled by thrust faults and topographies [15]. Bredehoeft et al. found that the fluid flow plays an important role in geologic processes and the overpressure affects the development of geological structures [16]. Ge and Garven built a two-dimensional numerical model to investigate the effects of the instantaneous compressional tectonics on the regional groundwater flow [17]. Saffer [18], Ge and Screamton [19], and Zhou and Hou [20] considered the impacts of the effective stress on fault deformations or other structural developments in the subsurface geological evolution. All above studies considered the case of instantaneous loading rather than continuous loading. On the other hand, most of previous studies on the impacts of faults or fractures on groundwater were either based on the faults or fractures that already exist [21–25] or based on the condition that rock containing microcracking and microvoiding which are the main reasons for deformation and failure of brittle materials like rocks, concrete, and ceramics [26, 27].

In this study, we carried out hydromechanical simulations to investigate the coupling processes of solid stress and fluid pressure in a shallow geological formation under a continuous loading caused by the nonuniform crustal movement during 10000 years. Two three-dimensional solid-fluid coupling models were built: Model I without a fault zone and Model II with a fault zone. Based on the simulation results, we analyzed the evolution of the solid stress and fluid pressure in the formation during this time period. The results of this study help to improve our understanding of these complex processes. In the following, we will first describe the methodology, then present the results and discussion, and finally draw some conclusions.

## 2. Methodology

As mentioned before, the speed of the earth crust movement is uneven and this nonuniform movement may create fractures and/or faults. Groundwater flow in bedrocks is usually controlled by faults and fractures. The coupling processes of the solid stress and pore pressure of bedrocks from the intact to the fractured or faulted under the nonuniform crust movement are very important in controlling the groundwater flow pattern. Therefore, two solid-fluid coupling numerical models were built. One model is for a homogenous formation without a fault zone (Model I, Figure 1(a)) and the other is for a formation with a fault zone (Model II, Figure 1(b)). The dimensions of two models are the same and the lengths along  $x$ -,  $y$ -, and  $z$ -axis are  $L_x = 1000$  m,  $L_y = 500$  m, and  $L_z = 300$  m, respectively. The fault zone is located in the middle

of the formation and parallel to  $y$ -axis with the size of 80 m  $\times$  500 m  $\times$  300 m (Figure 1(b)). The medium is isotropic and elastoplastic. Two velocity fields normal to the  $XZ$ -plane in opposite direction were imposed at the boundaries,  $0 \leq x \leq L_x/2$  and  $y = L_y$ , and  $L_x/2 \leq x \leq L_x$  and  $y = 0$  (the shaded areas in Figure 1), to simulate the shearing process generated by the nonuniform crust movement [28].

**2.1. Mathematical Model.** The solid phase is governed by the elasticity equations including the kinetic equation, the geometric equation, and the constitutive equation. The liquid phase is governed by a constitutive equation based on Darcy's law. The coupled behavior of solid and fluid is governed by the equilibrium equation between the volumetric strains, pore pressure, and saturation.

**2.1.1. Solid Phase.** Based on the elastic theory and movement equation, the solid stress is governed by the kinetic equation:

$$\frac{\partial \sigma_{ij}}{\partial x_j} + \rho g_i = \rho \frac{\partial \dot{u}_i}{\partial t}, \quad (1)$$

where  $\sigma_{ij}$  is stress tensor [ $N/L^2$ ],  $x_i$  is coordinate vector [ $L$ ],  $\rho = (1 - n)\rho_s + n\rho_w$  is the bulk density [ $M/L^3$ ],  $\rho_s$  and  $\rho_w$  are densities of the solid and fluid phase, respectively [ $M/L^3$ ],  $n$  is porosity [-],  $s$  is saturation [-],  $g_i$  is gravitational acceleration [ $L/T^2$ ],  $\dot{u}_i$  is velocity vector [ $L/T$ ],  $u_i$  is displacement vector [ $L$ ], and  $i = x, y$ , and  $z$  present three coordinate orientations.

Velocities cause changes in strains, and thus the relationship between the velocity and strain can be described with the geometric (compatibility) equation:

$$\dot{\varepsilon}_{ij} = \frac{1}{2} \left[ \frac{\partial \dot{u}_i}{\partial x_j} + \frac{\partial \dot{u}_j}{\partial x_i} \right], \quad (2)$$

where  $\dot{\varepsilon}_{ij}$  is strain rate tensor [ $1/T$ ] and  $\varepsilon_{ij}$  is strain tensor [-].

Based on the linear poroelasticity theory, the strain-stress relation for small deformation of the porous geological media is commonly described by the following constitutive equation:

$$\varepsilon_{ij} = \frac{1}{E} \left[ (1 + \nu) \sigma_{ij} - \nu \sigma_{kk} \delta_{ij} \right], \quad (3)$$

where  $E$  is elasticity modulus [ $N/L^2$ ],  $\nu$  is Poisson's ratio [-],  $\sigma_{kk} = \sigma_x + \sigma_y + \sigma_z$ ,  $\delta_{ij}$  is Kronecker delta.

**2.1.2. Liquid Phase.** The fluid flow in the bedrock is described by Darcy's law:

$$q_i = -\frac{k_{ij}}{\mu} \hat{k}(s) \frac{\partial}{\partial x_j} (P - \rho_w x_j g_j), \quad (4)$$

where  $q_i$  is the specific discharge vector [ $L/T$ ];  $k_{ij}$  is permeability tensor of medium [ $L^2$ ];  $\hat{k}(s)$  is the relative permeability which is a function of saturation  $s$  [-];  $P$  is pore pressure [ $N/L^2$ ];  $\mu$  is fluid viscosity [ $M/(L \times T)$ ].

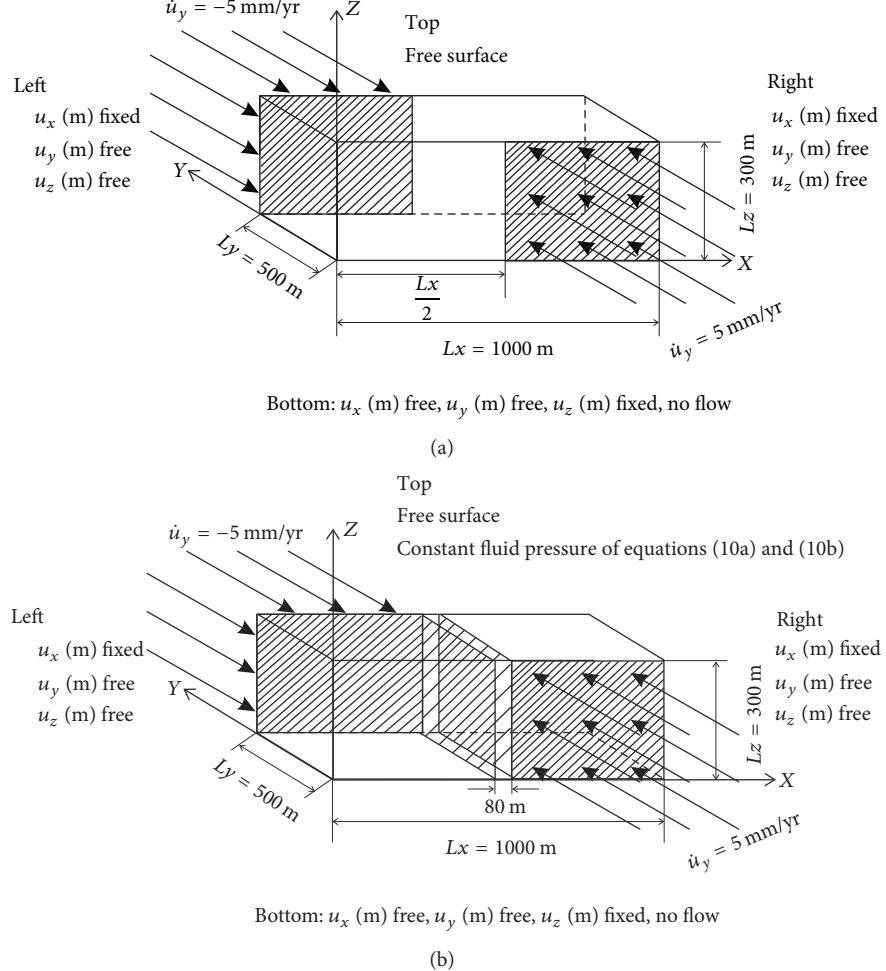


FIGURE 1: The two conceptual models: (a) is Model I and (b) is Model II. Two opposite velocity fields were applied to the two boundary faces (the shaded areas) to simulate the shear stress generated from nonuniform crust movement. The unit of the displacement,  $u_x$ ,  $u_y$ , and  $u_z$ , is meter and that of the velocity  $\dot{u}_y$  is mm per year.

Fluid mass can be expressed with continuity equation as follows:

$$-\frac{\partial q_i}{\partial x_i} + q_v = \frac{\partial \theta}{\partial t}, \quad (5)$$

where  $q_v$  is the volumetric fluid source intensity [1/T] and  $\theta$  is the fluid content (fluid volume per unit volume of porous material) as introduced by Biot [9] [-].

**2.1.3. Coupled Equation.** The change in the fluid content is related to the change in pore pressure ( $P$ ), saturation ( $s$ ), and mechanical volumetric strains ( $\varepsilon$ ); the response equation for the pore fluid is formulated as

$$\frac{1}{M} \frac{\partial P}{\partial t} + \frac{n}{s} \frac{\partial s}{\partial t} = \frac{1}{s} \frac{\partial \theta}{\partial t} - \alpha \frac{\partial \varepsilon}{\partial t}, \quad (6)$$

where  $M$  is Biot modulus [ $N/L^2$ ],  $\alpha$  is Biot coefficient [-], and  $\varepsilon$  is volumetric strain [-]. In the saturated case ( $s = 1$ ), if the

compressibility of the medium's particles is negligible ( $\alpha = 1$ ), (6) can be reduced to

$$\frac{\partial P}{\partial t} = M \left( \frac{\partial \theta}{\partial t} - \frac{\partial \varepsilon}{\partial t} \right). \quad (7)$$

**2.1.4. Initial Conditions and Boundary Conditions.** The initial and mechanical boundary conditions for deformation of the two model are the same and are set as follows:

$$u_z = 0 \quad \text{at } z = 0 \text{ m} \quad (8a)$$

$$u_x = 0 \quad \text{at } x = 0 \text{ m, } x = L_x \quad (8b)$$

$$\dot{u}_y = 5 \text{ mm/year} \quad \text{at } y = 0, \quad \frac{L_x}{2} \leq x \leq L_x \quad (8c)$$

$$\dot{u}_y = -5 \text{ mm/year} \quad \text{at } y = L_y, \quad 0 \leq x \leq \frac{L_x}{2} \quad (8d)$$

$$\sigma_{ij} = \sigma_o \quad \text{when } t = 0. \quad (8e)$$

TABLE 1: Parameters for Models I and II.

	Bulk modulus (Pa)	Cohesion (Pa)	Shear modulus (Pa)	Tension (Pa)	Friction (°)	Dilation (°)	Hydraulic conductivity (m/yr)	Porosity
Bedrock	$7.0E + 9$	$1.0E + 7$	$1.0E + 9$	$1.0E + 7$	30	0	$1.0E - 5$	0.5
Fault	$7.0E + 8$	$1.0E + 7$	$1.0E + 8$	$1.0E + 7$	15	0	1	0.6

The boundary condition (8a) means that the bottom of the model was constrained to have no vertical movements ( $z$ -direction) as generally adopted by previous researches [17] but it can move in the  $y$ -direction, that is,  $\dot{u}_y \neq 0$ . There is no displacement in  $x$ -direction (see (8b)) at the boundaries of  $x = 0$  and  $x = L_x$ . The top boundary ( $z = L_z$ ) is the ground surface and is free. In order to study the changes of the stress and pore pressure of the bedrock or the formation of a fault zone under continuous tectonic geostress, the velocity of  $\dot{u}_y = -5.0$  mm/year is loaded on the  $XZ$ -plane at  $y = L_y$  and  $0 \leq x \leq L_x/2$  (the shaded area on the left of Figure 1) and the velocity of  $\dot{u}_y = 5.0$  mm/year at the  $XZ$ -plane at  $y = 0$  and  $L_x/2 \leq x \leq L_x$  (see (8c) and (8d)) (the shaded area on the right in Figure 1). The magnitude of the velocity refers to the GPS observed velocities of the crustal movement in the southwest of China [29–31].  $\sigma_o$  is initial stress filed that is obtained using the solutions of steady-state kinetic equation (1) with the boundary conditions (8a) and (8b).

The initial and boundary conditions for fluid flow of two models are different. For Model I,

$$h(x, y, z, t) = h_0 \quad \text{when } t = 0 \quad (9a)$$

$$\frac{\partial h(x, y, z, t)}{\partial n} = 0 \quad \text{at all boundaries} \quad (9b)$$

$$h(x, y, z) = z \quad \text{at } z = L_z \quad (9c)$$

and for Model II

$$h(x, y, z, t) = h_0 \quad \text{when } t = 0 \quad (10a)$$

$$h(x, y, z) = L_z \quad \text{at } y = 0, 460 \text{ m} \leq x \leq 540 \text{ m} \quad (10b)$$

$$h(x, y, z) = L_z \quad \text{at } y = L_y, 460 \text{ m} \leq x \leq 540 \text{ m} \quad (10c)$$

$$\frac{\partial h(x, y, z)}{\partial n} = 0 \quad \text{at the other boundaries.} \quad (10d)$$

For Model I, the initial hydraulic head is equal to the static pressure (see (9a)). All boundaries are set as impermeable boundaries in Model I (see (9b)). The solid medium is considered as saturated and unconfined. The pore pressure at the top boundary is equal to the atmospheric condition. For Model II, the boundaries of the fault zone ( $y = 0$  and  $y = L_y$  when  $460 \text{ m} \leq x \leq 540 \text{ m}$ ) are set as constant heads in order to investigate the effect of the boundary condition on the groundwater flow. The rest boundaries are all impermeable.

The densities of the formation and groundwater are taken to be  $2500 \text{ kg/m}^3$  and  $1000 \text{ kg/m}^3$ , respectively. Relative large porosity values of the bedrock are adopted in order to generate optimistic scenarios for the pore pressure redistribution induced by the continuous plate movement. The

other material mechanical and physical parameters used in the computation of Models I and II are listed in Table 1 which are based on the previous literatures [32–35].

**2.2. Numerical Models.** The two numerical models were constructed with FLAC3D which is a three-dimensional finite difference numerical software for solving problems in engineering mechanics, that is, static and dynamic mechanics and hydraulic effects, including their coupling process [20]. According to the previous literatures, such as Papanastasiou and Thiercelin [36], Papanastasiou [37], and Zhou and Hou [20], the material deformation can be simulated using the Mohr-Coulomb constitutive model which was commonly used for simulating crack propagation when the material reached the yield limits. In this study, we coupled the static and dynamic mechanics and hydraulics with the Mohr-Coulomb constitutive model in FLAC3D.

As mentioned above, two models were built with dimension of  $1000 \text{ m} \times 500 \text{ m} \times 300 \text{ m}$ , and we generated a three-dimensional mesh of  $50 \times 10 \times 10$  with a total of 6171 nodes for Model I and a mesh of  $50 \times 10 \times 10$  ( $40 \times 10 \times 10$  in the bedrock and  $10 \times 10 \times 10$  in the fault zone) with a total of 6171 nodes for Model II. The dynamic damping type is Rayleigh with two relevant parameters  $\xi_{\min}$  and  $\omega_{\min}$  where  $\xi_{\min}$  is set to be 0.05 which is a normal value of the minimum critical damping ratio in geomaterial according to the FLAC3D manual, and  $\omega_{\min}$  is 0.122 which was generated by the natural frequency of vibration of two models under the gravity. We used a desktop computer with Intel(R) Core(TM) i7-6700 CPU @ 2.60 GHz 2.60 GHz, 64 GB ram, and 1 TB external storage to run the simulation. It took about 81 hours to run the simulation of Model I and about 45 hours of Model II. The computing efficiency was mainly controlled by the convergence criterion and the size of the time step. The optimal convergence criterion of the maximum unbalanced force and time step we chose is  $1E - 20$  and 0.001 yr, respectively.

### 3. Results and Discussion

The coupled equation (7) for the solid and liquid phases with the initial and boundary conditions (see (8a)–(10d)) for the two models was solved with FLAC3D and the simulation results for the stress and pore pressure are presented and explained as follows.

**3.1. Change of the Maximum Principal Stress.** The changes of the maximum principal stress ( $S_{\max}$ ) with time in three  $X$ - $Z$  cross sections at  $Y = 0 \text{ m}$ ,  $125 \text{ m}$ , and  $250 \text{ m}$  for Model I were presented in Figure 2(a). The initial ( $t = 0$ ) stress field is mainly controlled by gravity and thus  $S_{\max}$  is constant along the horizontal  $X$ -direction but varies in the vertical

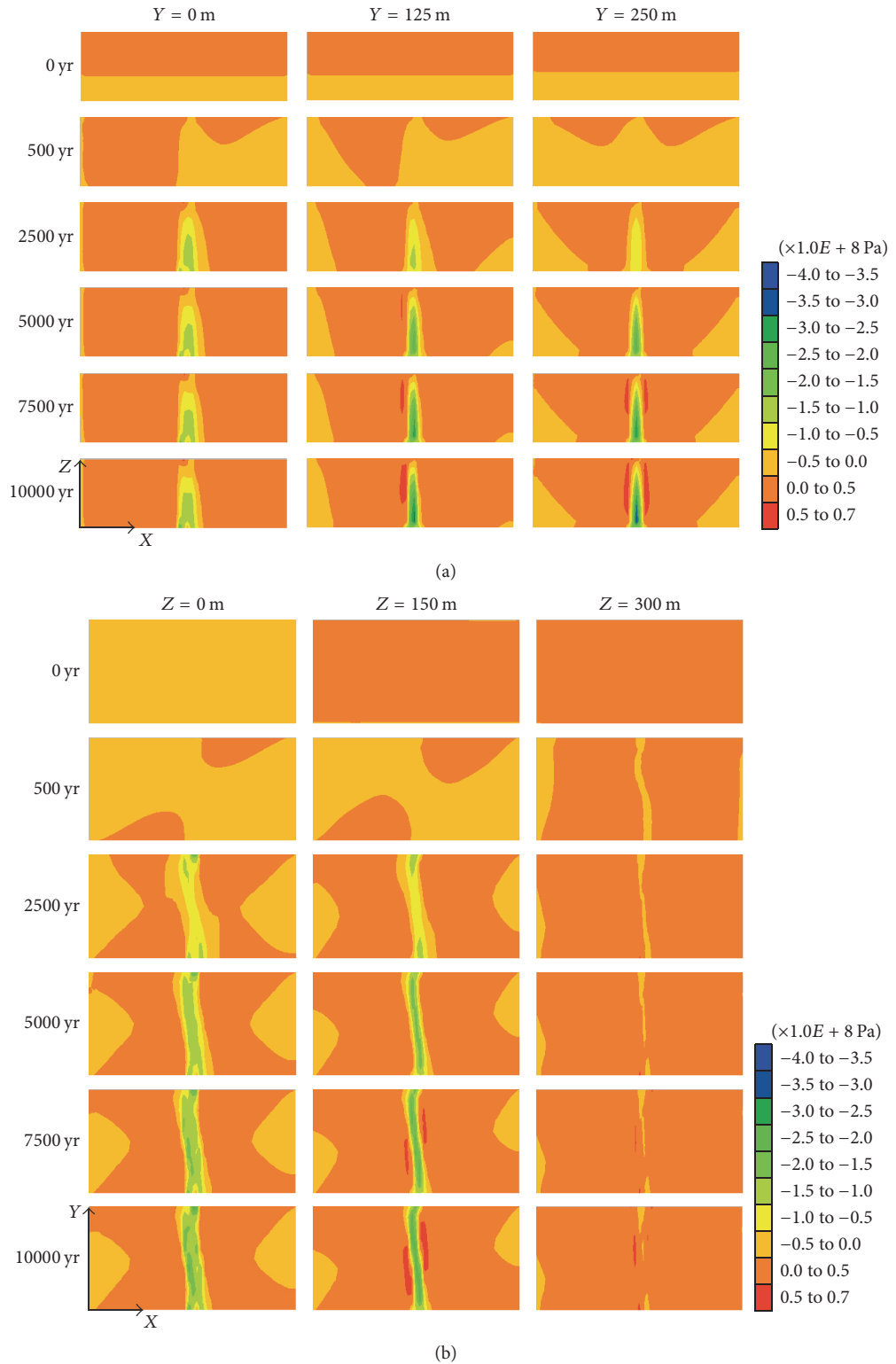


FIGURE 2: Contour map of the maximum principle stress ( $S_{\max}$ ) for Model I at different times. (a) is three vertical cross sections of  $Y = 0$ , 125 m, and 250 m; (b) is three horizontal cross sections of  $Z = 0$ , 150 m, and 300 m.

$Z$ -direction (the first row). It is positive (tensile) at the top and changed to negative (compressive) at the bottom due to the fixed horizontal displacement in  $X$ -direction and the fixed vertical displacement at the bottom and free in  $Y$ -direction. As time progresses,  $S_{\max}$  became more and more concentrated in the middle of the cross sections due to the shear stress generated by the opposite velocities applied at the two boundary faces.

At  $t = 2500$ th year,  $S_{\max}$  around the middle of the  $X$ - $Z$  cross sections decreases as  $Y$  increases because the stress at the boundary ( $Y = 0$ ) is most affected by the velocity applied and this effect is weakened away from the boundary. At  $t = 10000$ th year,  $S_{\max}$  in the middle of the sections increases as  $Y$  increases and became the largest in the cross section of  $Y = 250$  m (the bottom-right graph) at which a plastic failure zone may appear. At this time a strong tensile stress is formed around the middle of the section (the red area in the bottom-right graph). It is noticed that the distributions of  $S_{\max}$  at  $Y = 0$  and 125 m (the graphs in the left and middle columns) are asymmetric, being mostly compressive on the right half and tensile on the left half (the first graph on second row) while  $S_{\max}$  at  $Y = 250$  m (the graphs in the right column) is symmetric since it is located in the middle in  $X$ - $Z$  section.

The changes of the horizontal distribution of  $S_{\max}$  with time in three cross sections of  $Z = 0$ , 150 m, and 300 m are provided in Figure 2(b). The initial  $S_{\max}$  (the top row) is constant and positive on the top ( $Z = 300$  m) and negative at the bottom ( $Z = 0$ ). As time goes,  $S_{\max}$  becomes concentrated in the middle due to the shear stress produced by the boundary conditions. The value of  $S_{\max}$  at  $Z = 0$  (the bottom-left graph) is largest because the bottom boundary is fixed in the vertical direction and decreases upwards. It is noticed that two small red areas of tensile stress (positive  $S_{\max}$ ) are formed around the middle green zone of high compressive stress (the two bottom graphs in the middle column). The distribution of  $S_{\max}$  is antisymmetric against the line of  $Y = 250$  m in the horizontal cross sections.

Similar to Figure 2 for Model I, Figure 3 presents the changes of  $S_{\max}$  with time for Model II in the same cross sections. As mentioned previously, the only difference between these two models is that a fault zone ( $80$  m  $\times$   $500$  m  $\times$   $300$  m) with weaker mechanical properties and different hydraulic parameters is contained in Model II in order to investigate the effect of an existing fault on the distribution of the stress and pore pressure under the continuous tectonic movement. The other boundary conditions and parameters are the same with Model I. Overall, the changes of  $S_{\max}$  in Model II is similar with those in Model I except around the fault zone that has weaker mechanical properties. The effect of the fault zone is to reduce the range of the values of  $S_{\max}$ : the maximum value of  $S_{\max}$  is reduced from  $0.7 \times 10^8$  in Model I to  $0.25 \times 10^8$  in Model II and the minimum is increased from  $-4.0 \times 10^8$  to  $-2.0 \times 10^8$  and to make the stress field more complex around and inside the fault zone.

**3.2. Change of the Pore Pressure.** Corresponding to  $S_{\max}$  in Figure 2(a), the changes of the pore pressure ( $P$ ) with time for Model I in three  $X$ - $Z$  vertical cross sections at  $Y = 0$  m, 125 m, and 250 m are shown in Figure 4(a). As expected, the

distribution of  $P$  is mainly controlled by that of  $S_{\max}$ . Initially,  $P$  is hydrostatic which varies vertically. In earlier times, for example, at  $t = 500$ th year, an abnormal positive pressure zone is formed in the middle of the cross sections due to the concentrated compressive stress generated by the boundary conditions.  $P$  at  $Y = 0$  (the first graphs in the second row) is positive and largest around the middle and decreases as  $Y$  increases. For  $t = 2500$ th year,  $P$  at  $Y = 0$  becomes strongly positive on the right side of the middle line (the yellow-red areas in the first graph on the second row in the left column) and negative on the left side (the blue region) due to the strong compressive stress on the right and tensile stress on the left. As time goes, the positive pressure at  $Y = 0$  decreases while the negative pressure becomes more negative. As  $Y$  increases, the positive pressure decreases while the negative pressure becomes more negative. The distribution of  $P$  in these cross sections is asymmetric at  $Y = 0$  and 125 m but is symmetric at  $Y = 250$  m just like that of  $S_{\max}$  in Figure 2.

Corresponding to  $S_{\max}$  in Figure 2(b), the horizontal distribution of  $P$  in three  $X$ - $Y$  cross sections of  $Z = 0$ , 150 m, and 300 m at different times is provided in Figure 4(b). The initial  $P$  (the top row) is constant horizontally. As time goes,  $P$  around the middle either increases to be more positive or decreases to be negative depending on the relative location to the boundary faces. At  $t = 2500$ th year, a zone of large positive pressure appears around the middle (yellow-red region) with two small areas of negative pressure (blue region). As time goes, the positive  $P$  decreases but the negative  $P$  becomes stronger and stronger due to the concentrated characteristics of  $S_{\max}$  in this area. The positive pressure is the largest at the bottom ( $Z = 0$ ) and decreases upwards at  $Z = 150$  m and 300 m while the negative pressure becomes stronger and stronger upwards. Similar to that of  $S_{\max}$ , the distribution of  $P$  on the  $X$ - $Y$  planes is antisymmetric against the middle line of  $Y = 250$  m in the three horizontal cross sections.

Two typical cross sections of  $Y = 0$  and  $Z = 0$  (Figure 5) were selected to display the flow direction at  $t = 500$  yr and 5000 yr in order to observe the fluid flow clearly in Model I. Based on the spatial-temporal variations of  $P$  in Model I, it is inferred that, initially, the fluid is static since there is no pressure gradient. In early time, for example, at  $t = 500$ th year (Figure 5(a)), fluid flows from higher  $P$  to lower  $P$  in the same height. In later time, fluid flows from positive  $P$  (the yellow-red area in Figure 5(b) at  $t = 5000$  yr) to negative  $P$  (the blue area) as positive pressure is strongly concentrated on the right side of the middle line and negative pressure on the left side.

Corresponding to  $S_{\max}$  in Figure 3(a), the changes of  $P$  for Model II in three  $X$ - $Z$  cross sections at  $Y = 0$  m, 125 m, and 250 m are shown in Figure 6(a). The boundary conditions for the liquid phase of Model II are the same as those for Model I except for the fact that two constant head boundaries are set for the fault zone between 460 m and 540 m in  $x$ -axis at  $Y = 0$  m and  $Y = 500$  m to allow fluid flow to cross the boundaries under the uneven crust movement as the fault zone is an aquifer. It is clearly seen that the initial  $P$  at  $t = 0$  (the first row) is constant horizontally and varies vertically. As time progresses, the effect of the fault zone becomes more evident: the positive pressure is concentrated around the fault zone in early times, for example,  $t = 500$  yr (the second row),

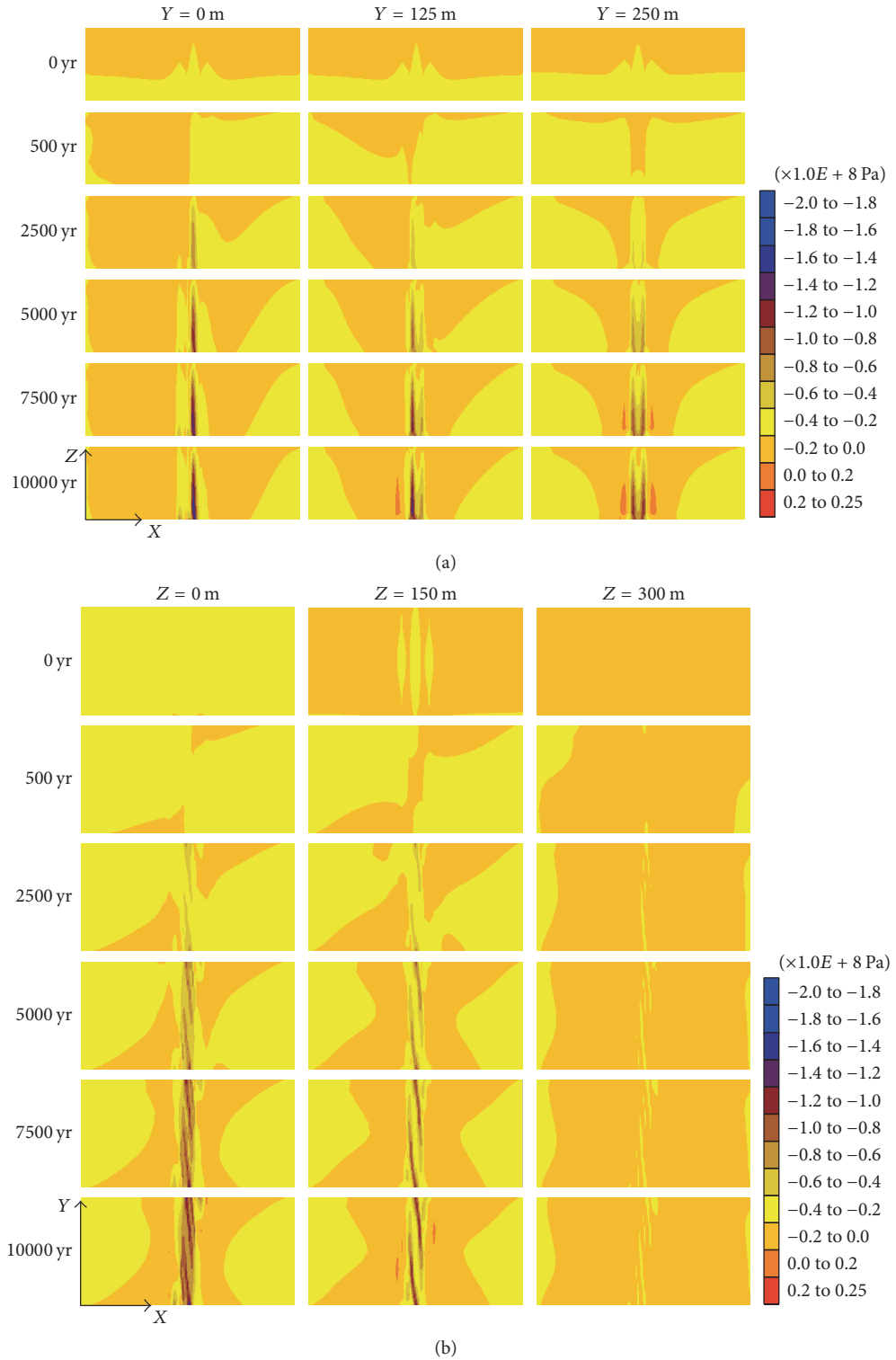


FIGURE 3: Contour map of the maximum principle stress ( $S_{\max}$ ) for Model II at different times. (a) is three vertical cross sections of  $Y = 0$ ,  $125 \text{ m}$ , and  $250 \text{ m}$ ; (b) is three horizontal cross sections of  $Z = 0$ ,  $150 \text{ m}$ , and  $300 \text{ m}$ .

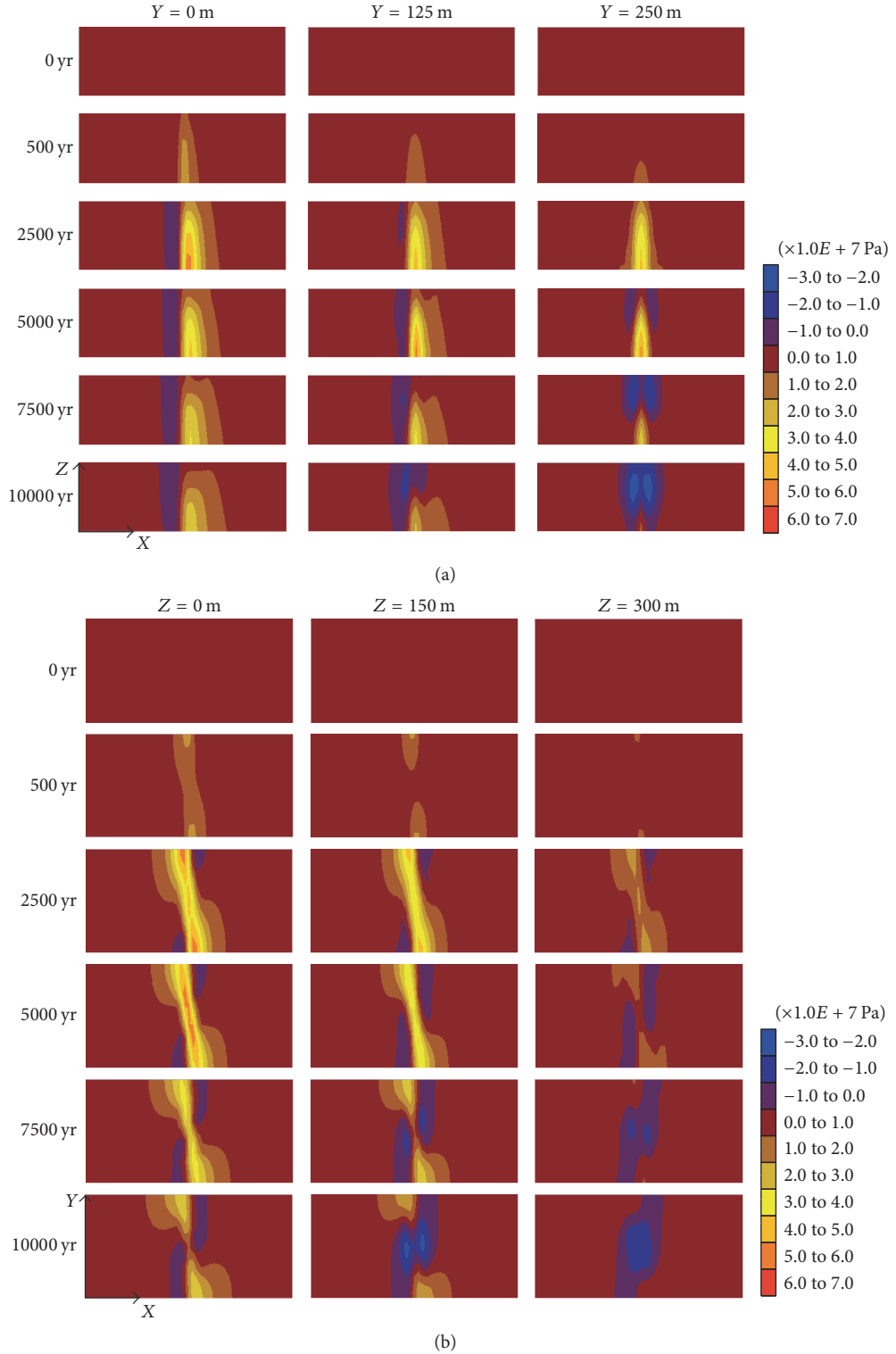


FIGURE 4: Contour map of the pore pressure ( $P$ ) for Model I at different times. (a) is three vertical cross sections of  $Y = 0, 125 \text{ m}$ , and  $250 \text{ m}$ ; (b) is three horizontal cross sections of  $Z = 0, 150 \text{ m}$ , and  $300 \text{ m}$ .

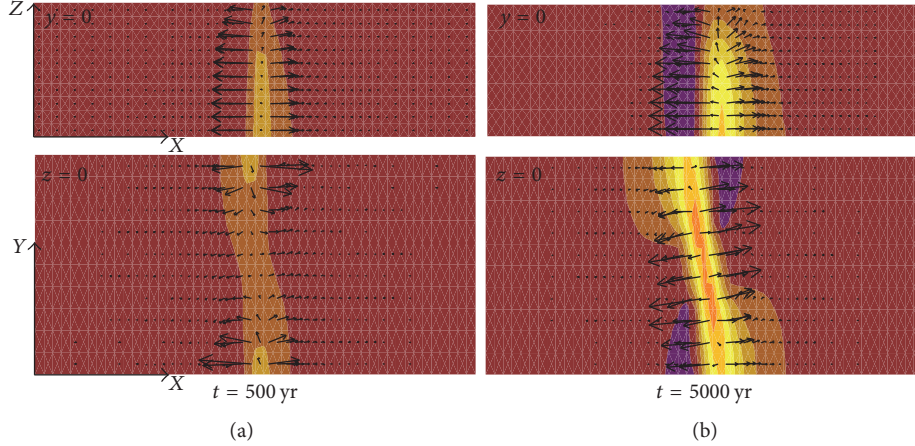


FIGURE 5: The flow direction in two cross sections ( $Y = 0$  and  $Z = 0$ ) of Model I at  $t = 500$  yr and 5000 yr.

and, in later times, the higher positive pressure (red region) due to compressive stress is formed on the right side of the fault zone and that of negative pressure (purple region) on the left. As  $Y$  increases to 125 m, the positive pressure decreases while the negative pressure becomes more negative. At  $Y = 250$  m, the  $P$  around the fault zone is symmetric and negative (the bottom-right graph in (a)).

Corresponding to  $S_{\max}$  in Figure 3(b), the effect of the fault zone on the horizontal cross sections of  $Z = 0$ , 150 m, and 300 m is shown in Figure 6(b). The initial  $P$  is constant horizontally. As time progresses,  $P$  is antisymmetric against the middle line ( $Y = 250$  m) of these cross sections. In earlier times, for example, at  $t = 500$ th year, a positive pressure zone is formed in the middle of the cross sections like Model I due to the compressive stress concentrated in this area. In later times, the distribution of  $P$  was affected by the fault zone greatly, it is seen that  $P$  is mainly concentrated around the sides of the fault zone and is in opposite directions on the two sides of the fault zone: the negative pressure becomes stronger and stronger due to the positive  $S_{\max}$  concentrated in this area; the positive pressure is stronger concentrated as the negative  $S_{\max}$  is concentrated here. The  $P$  is the largest at the bottom ( $Z = 0$ ) and decreases upwards at  $Z = 150$  m and 300 m.

The same cross sections were selected to display the flow direction in Model II (Figure 7). Similar to Model I, the initial fluid is static. As time progresses, the fluid flows from higher to lower pressure at the same height in early time, for example,  $t = 500$  yr. The fluid flows out of the model through the two constant head boundaries (the arrows (a) at  $t = 500$  yr) due to the higher  $P$  concentrated in the middle of the model. In later time, for example,  $t = 5000$  yr, fluid flow occurs mainly along the sides of the fault zone and is in opposite directions along the two sides of the fault zone (the arrows (b) at  $t = 5000$  yr): from positive  $P$  (the yellow-red area) at  $Y = 0$  m to negative  $P$  (the blue area) at  $Y = 0$  m and from positive  $P$  at  $Y = 500$  m to negative  $P$  at  $Y = 500$  m; that is, fluid flows from both the matrices and the fault zone to their interfaces. The fluid flows

into the fault zone through the constant head boundaries (the arrows at  $t = 5000$  yr of Figure 7(b)).

It is worth noting that the distribution of  $S_{\max}$ ,  $P$  in two models varies significantly under the nonuniform movement of the formation due to the fault zone, and the groundwater flow pattern also varies temporally and spatially. A region with enhanced stress and pore pressure usually occurs around a fault zone, consistent with the theory of mechanics of materials [38]. The stress field determines the distribution of the pore pressure which in turn controls the direction of fluid flow. A fault zone may act as a conduit, a barrier, or a combined conduit/barrier system which is essential to the study of faulted flow systems [16, 39]. Our simulation results show that even with the relatively simple models built in this study a complex stress, pore pressure, and flow fields can be formed in a geological formation under uneven movement of the earth crust. In a formation with no fault, the pore pressure and fluid flow are concentrated in the middle of the formation under different or opposite horizontal velocities. In a formation with a fault zone, however, they are concentrated along the interfaces between the fault zone and the surrounding rock matrices. Geological formations are usually more complicated than the ones simulated and so do the stress, pore pressure, and flow fields.

The distribution of  $S_{\max}$  in two models varies significantly at different times under the opposite velocity fields due to the fault zone, which results in large changes in  $P$ . For example, in Model I the initial  $S_{\max}$  (i.e.,  $t = 0$ ) is constant horizontally and varies vertically, and thus the initial  $P$  has similar changes. As time goes,  $S_{\max}$  became more and more concentrated in the middle of the cross sections (Figure 2), and  $P$  is also concentrated in this area; especially the positive  $P$  is concentrated on the right side of the middle line (the yellow-red areas in Figure 4) and the negative  $P$  on the left side (the blue areas) due to the strong compressive stress on the right and tensile stress on the left. The changes of  $S_{\max}$  in Model II (Figure 3) are similar to those in Model I except around the fault zone. The initial  $P$  is also constant

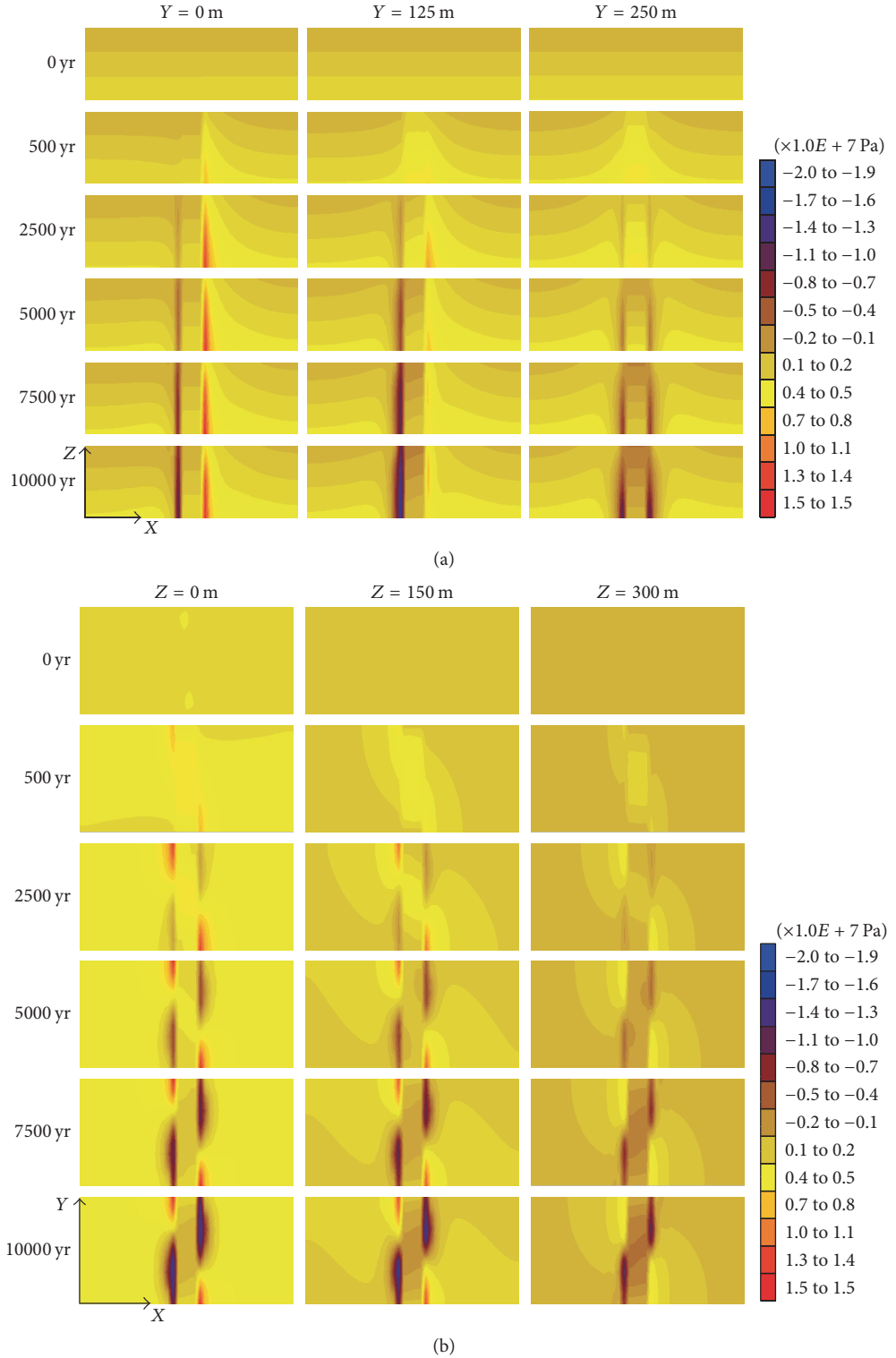


FIGURE 6: Contour map of the pore pressure ( $P$ ) for Model II at different times. (a) is three vertical cross sections of  $Y = 0, 125 \text{ m}$ , and  $250 \text{ m}$ ; (b) is three horizontal cross sections of  $Z = 0, 150 \text{ m}$ , and  $300 \text{ m}$ .

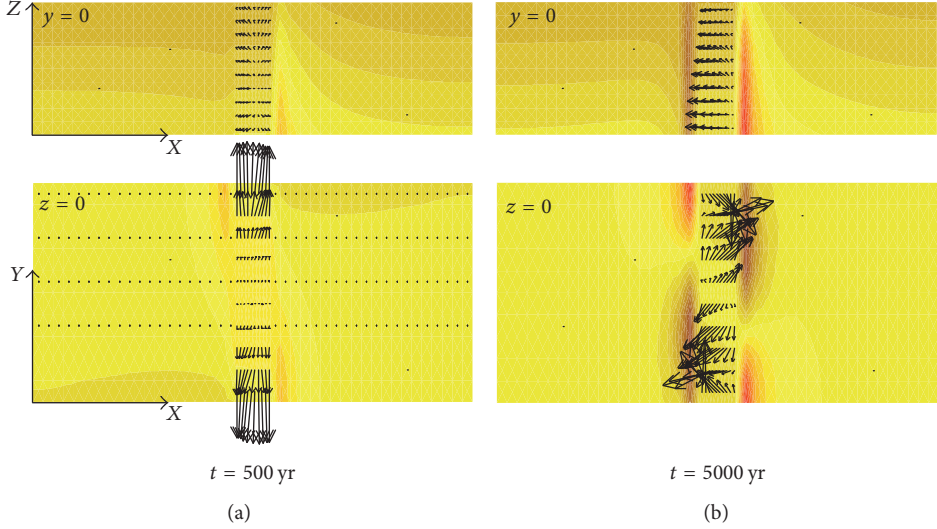


FIGURE 7: The flow direction in two cross sections ( $Y = 0$  and  $Z = 0$ ) of Model II at  $t = 500$  yr and 5000 yr.

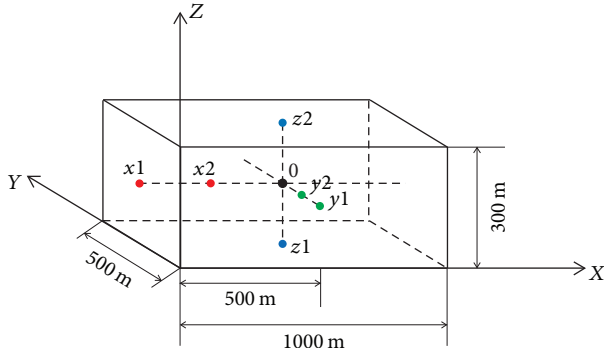


FIGURE 8: Locations of the seven observation points.

horizontally and varies vertically. As time progresses,  $P$  is more and more concentrated around the sides of the fault zone and the positive  $P$  (the yellow-red areas in Figure 6) and the negative  $P$  (the blue areas) are in opposite directions on the two sides of the fault zone due to the concentrated  $S_{\max}$ .

**3.3. Changes of Pore Pressure at Selected Points.** The changes of the pore pressure with time at seven observation points in the models are depicted in order to better understand the coupling process of rock deformation and fluid flow. Figure 8 shows the locations of the seven observation points (see Table 2 for their coordinates): two along each of the three axes plus the point at the center of the models. It is pointed out that all points except  $x_1$  and  $x_2$  are located along the plane of  $X = 500$  m, where the largest shear stress is generated by the boundary conditions.

Figure 9(a) displays the changes of the pore pressure with time at the seven points for Model I. In general, the pore pressure at all points except  $x_1$  and  $x_2$  increases with time to reach their respective peak values and then decreases at late time. The pore pressure at  $y_1$  (the short-dashed green curve)

TABLE 2: Locations of the seven observation points.

Observation points	0	$x_1$	$x_2$	$y_1$	$y_2$	$z_1$	$z_2$
$x$	500	0	250	500	500	500	500
$y$	250	250	250	0	250	250	250
$z$	150	150	150	150	150	0	300

increases earlier and faster than that at other points because  $y_1$  is located on the boundary of  $Y = 0$  where the velocity field is applied, and, definitely, the pore pressure at  $y_1$  is larger than that at  $y_2$  and 0. The  $P$  at  $z_1$  (the short-dashed blue curve) has the largest peak value because  $z_1$  is located at the fixed bottom while  $z_2$  is at the free top face of the formation. At  $t = 10000$  years, the pore pressure at  $y_1$ ,  $y_2$ , and  $z_1$  (the two green and the short-dashed blue curves) stays positive while  $P$  at 0 and  $z_2$  (the black and the long-dashed blue curves) falls below 0, that is, becomes negative, which are due to the tensile stress concentrated area appearing in the middle of the model and becoming larger and larger when time is big enough. The pore pressure at  $x_1$  and  $x_2$  (the two red lines) which are away from the concentrated shear stress stays almost the same during 10,000 years, indicating that the changes of  $S_{\max}$  and  $P$  mainly occur in the middle of the model. Figure 9(b) shows changes of the pore pressures with time at the same points for Model II. It is seen that the effect of the existing fault zone on the pressure is obvious. First, the magnitudes of the pore pressure at all points are significantly reduced because of the weaker mechanical properties of the fault zone. Secondly, the pore pressure at  $y_2$ ,  $z_1$ ,  $z_2$ , and 0 reaches their respective peak values earlier and decreases to negative earlier than that at Model I. Little change is observed in the pore pressure at  $x_1$  and  $x_2$  that are located away from the fault zone. No pressure change at  $y_1$  which is located at the boundary where the head is set to be constant.

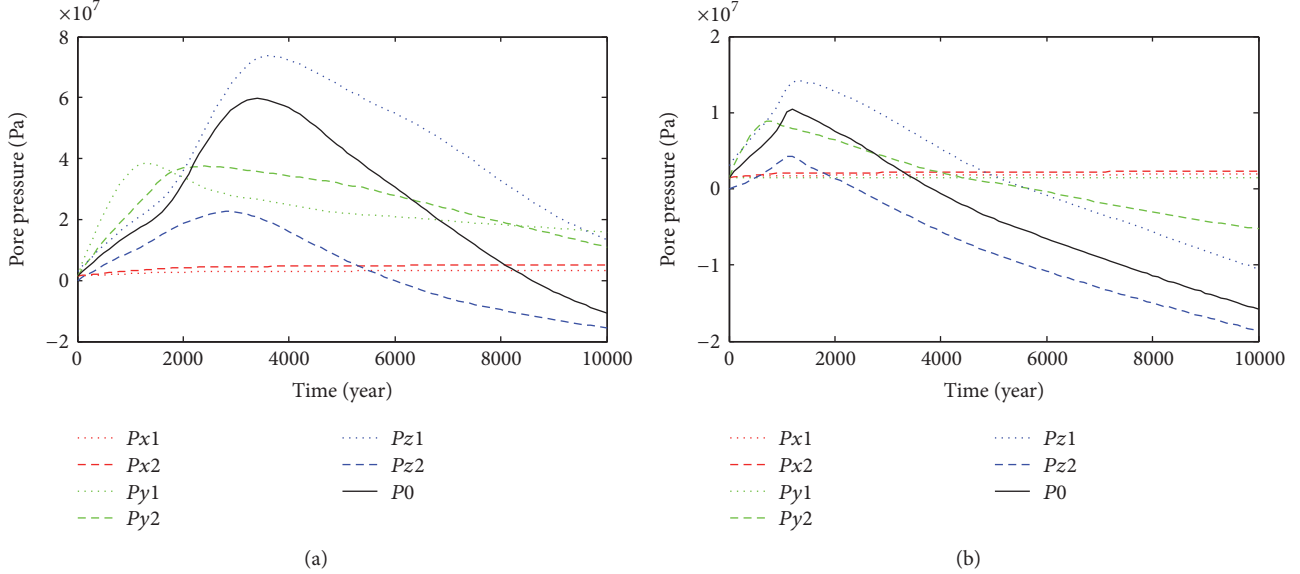


FIGURE 9: Changes of the pore pressure ( $P$ ) with time at the seven observation points for (a) Model I and (b) Model II.

#### 4. Summary and Conclusions

In this study we carried out hydromechanical modeling of a geological formation: Model I without a fault zone and Model II with a fault zone, to investigate the coupling processes of the solid strain and pore pressure of the formation under shearing by the nonuniform crust movement during 10000 years. The changes of the maximum principal stress ( $S_{\max}$ ) and pore pressure ( $P$ ) in two three-dimensional models were simulated with FLAC3D and the results show that distributions of  $S_{\max}$  and  $P$  are significantly affected by the existence of a fault zone. Our simulation results show that, even with the relatively simple models built in this study, complex stress, pore pressure, and flow fields can be formed in a geological formation under uneven movement of the earth crust. Specific conclusions drawn in this study are as follows:

- (1) The initial stress field controlled by gravity is positive (tensile) at the top of the formation and changes to negative (compressive) at the bottom. As time progresses,  $S_{\max}$  became more and more concentrated in the middle of the formation during shearing generated by continuous loadings on two boundary faces. For Model I, a belt of higher compressive stress (the green areas in Figure 2) along the direction of shearing ( $X = 500$  m) appears in the middle of the formation which is surrounded by a zone of high tensile stress, especially on the plane of  $Y = 250$  m (the red areas in the bottom-right graph in Figure 2(a)).
- (2) The distribution of  $P$  is mainly controlled by that of  $S_{\max}$ . Initially,  $P$  is hydrostatic and constant horizontally but varies vertically. As time goes, a zone with abnormal  $P$  appears in the middle of the formation due to the elevated stress in this zone. For Model

I,  $P$  is strongly positive at the bottom-left corner of the loading face (the red-yellow areas in Figure 4) and strongly negative on the other side and near the surface of the formation.

- (3) The changes of  $S_{\max}$  in Model II is similar to those in Model I except around the fault zone that has weaker mechanical properties. The effect of the fault zone is to reduce the magnitudes of  $S_{\max}$  and to make the stress field more complex around and inside the fault zone. And, fluid flow in Model II occurs mainly along the sides of the fault zone and is in opposite directions on the two sides of the fault zone.
- (4) The distribution of  $P$  is significant affected by the fault zone: the abnormal positive and negative pressures (the red area) are mainly distributed along the two interfaces between the fault zone and the surrounding matrices, instead of the middle of the formation in the case of no fault zone. Based on the spatial-temporal variations of  $P$ , it is inferred that the fluid is initially static. As time goes, fluid starts to move from higher to lower pressure.
- (5) The pore pressure in the middle of the formation increases with time to reach their respective peak values and then decreases at late time during shearing. At the rest of the formation, the pore pressure stays relatively constant. The effect of the existing fault zone on the pressure is to reduce the magnitude (including the peak) of  $P$  and to move the peak time earlier.

#### Conflicts of Interest

The authors declare that they have no conflicts of interest.

## Acknowledgments

This study was partially supported by the research grants from the National Nature Science Foundation of China (NSFC-41272260; NSFC-41330314; NSFC-41302180), the Department of Science and Technology of Jiangsu Province (BE2015708), and the research fund provided by the Southern University of Science and Technology, China.

## References

- [1] M. Babiker and A. Gudmundsson, "The effects of dykes and faults on groundwater flow in an arid land: the Red Sea Hills, Sudan," *Journal of Hydrology*, vol. 297, no. 1-4, pp. 256–273, 2004.
- [2] D. Krásný and D. Sharp, *Groundwater in Fractured Rocks: IAH Selected Paper Series*, CRC Press, Boca Raton, Fla, USA, 2007.
- [3] M.-A. Brideau, M. Yan, and D. Stead, "The role of tectonic damage and brittle rock fracture in the development of large rock slope failures," *Geomorphology*, vol. 103, no. 1, pp. 30–49, 2009.
- [4] G. Karay and G. Hajnal, "Modelling of groundwater flow in fractured rocks," *Procedia Environmental Sciences*, vol. 25, pp. 142–149, 2015.
- [5] N. Xiao, *Analysis of Neotectonics and its Application in Groundwater Exploration*, China Geology Press, Beijing, China, 1986.
- [6] Z. Niu, M. Wang, H. Sun et al., "Contemporary velocity field of crustal movement of Chinese mainland from Global Positioning System measurements," *Chinese Science Bulletin*, vol. 50, no. 9, pp. 939–941, 2005.
- [7] National Research Council, *Rock Fracture and Fluid Flow: Contemporary Understanding and Applications*, The National Academies Press, Washington, DC, USA, 1996.
- [8] G. Zhao, H. Sun, L. Ren et al., "Analysis and research of time series for GPS fiducial stations from the crustal movement observation network of China," *Recent Developments in World Seismology*, vol. 412, pp. 19–29, 2013 (Chinese).
- [9] M. A. Biot, "General solutions of the equations of elasticity and consolidation for a porous material," *Journal of Applied Mechanics*, vol. 23, pp. 91–96, 1956.
- [10] M. A. Biot, "Theory of deformation of a porous viscoelastic anisotropic solid," *Journal of Applied Physics*, vol. 27, no. 5, pp. 459–467, 1956.
- [11] J. R. Rice and M. P. Cleary, "Some basic stress diffusion solutions for fluid saturated elastic porous media with compressible constituents," *Reviews of Geophysics*, vol. 14, no. 2, pp. 227–241, 1976.
- [12] H. F. Wang, *Theory of Linear Poroelasticity with Applications to Geomechanics and Hydrogeology*, Princeton University Press, Princeton, NJ, USA, 2001.
- [13] R. Olsson and N. Barton, "An improved model for hydromechanical coupling during shearing of rock joints," *International Journal of Rock Mechanics and Mining Sciences*, vol. 38, no. 3, pp. 317–329, 2001.
- [14] G. Garven, "A hydrogeologic model for the formation of the giant oil sands deposits of the Western Canada sedimentary basin," *American Journal of Science*, vol. 289, no. 2, pp. 105–166, 1989.
- [15] C. B. Forster and J. P. Evans, "Hydrogeology of thrust faults and crystalline thrust sheets: results of combined field and modeling studies," *Geophysical Research Letters*, vol. 18, no. 5, pp. 979–982, 1991.
- [16] J. D. Bredehoeft, K. Belitz, and S. Sharp-Hansen, "The hydrodynamics of the Big Horn Basin: a study of the role of faults," *AAPG Bulletin*, vol. 76, no. 4, pp. 530–546, 1992.
- [17] S. Ge and G. Garven, "Hydromechanical modeling of tectonically driven groundwater flow with application to the Arkoma foreland basin," *Journal of Geophysical Research: Solid Earth*, vol. 97, no. 6, pp. 9119–9144, 1992.
- [18] D. M. Saffer, "Pore pressure development and progressive dewatering in underthrust sediments at the Costa Rican subduction margin: comparison with northern Barbados and Nankai," *Journal of Geophysical Research: Solid Earth*, vol. 108, no. 5, 2003.
- [19] S. Ge and E. Screaseon, "Modeling seismically induced deformation and fluid flow in the Nankai subduction zone," *Geophysical Research Letters*, vol. 32, no. 17, pp. 1–4, 2005.
- [20] L. Zhou and M. Z. Hou, "A new numerical 3D-model for simulation of hydraulic fracturing in consideration of hydro-mechanical coupling effects," *International Journal of Rock Mechanics and Mining Sciences*, vol. 60, pp. 370–380, 2013.
- [21] J. S. Caine, J. P. Evans, and C. B. Forster, "Fault zone architecture and permeability structure," *Geology*, vol. 24, no. 11, pp. 1025–1028, 1996.
- [22] E. Radi, D. Bigoni, and B. Loret, "Steady crack growth in elastic-plastic fluid-saturated porous media," *International Journal of Plasticity*, vol. 18, no. 3, pp. 345–358, 2002.
- [23] Y. L. Lu, D. Elsworth, and L. G. Wang, "Microcrack-based coupled damage and flow modeling of fracturing evolution in permeable brittle rocks," *Computers & Geosciences*, vol. 49, pp. 226–244, 2013.
- [24] J. F. Bauer, S. Meier, and S. L. Philipp, "Architecture, fracture system, mechanical properties and permeability structure of a fault zone in Lower Triassic sandstone, Upper Rhine Graben," *Tectonophysics*, vol. 647, pp. 132–145, 2015.
- [25] C. Yan and H. Zheng, "Three-dimensional hydromechanical model of hydraulic fracturing with arbitrarily discrete fracture networks using finite-discrete element method," *International Journal of Geomechanics*, vol. 17, no. 6, 2017.
- [26] Z. P. Bazant and J. Planas, *Fracture and Size Effect in Concrete and Other Quasibrittle Materials*, CRC Press, Boca Raton, Fla, USA, 1998.
- [27] G. Z. Voyatzis, M. I. Alsah, and K. A. Alshibli, "Evolving internal length scales in plastic strain localization for granular materials," *International Journal of Plasticity*, vol. 21, no. 10, pp. 2000–2024, 2005.
- [28] J. He, W. Xia, S. Lu, and H. Qian, "Three-dimensional finite element modeling of stress evolution around the Xiaojiang fault system in the southeastern Tibetan plateau during the past ~500 years," *Tectonophysics*, vol. 507, no. 1-4, pp. 70–85, 2011.
- [29] Q. Deng, P. Zhang, Y. Ran, X. Yang, W. Min, and Q. Chu, "Basic characteristics of active tectonics of China," *Science China Earth Sciences*, vol. 46, no. 4, pp. 356–372, 2003.
- [30] X. Xu, X. Wen, R. Zheng et al., "Pattern of latest tectonic motion and its dynamics for active blocks in Sichuan-Yunnan region, China," *Science in China Series D: Earth Sciences*, vol. 46, supplement 2, pp. 210–226, 2003.
- [31] Z.-K. Shen, J. Lü, M. Wang, and R. Bürgmann, "Contemporary crustal deformation around the southeast borderland of the Tibetan Plateau," *Journal of Geophysical Research: Solid Earth*, vol. 110, no. 11, Article ID B11409, 2005.
- [32] H. Zhou and D. Nie, "The getting evaluating indicators of rock-mass structure in river-bed dam foundation of hydropower station," *Journal of Hunan University of Science & Technology*, vol. 25, no. 4, pp. 54–58, 2010 (Polish).

- [33] H. Jia, P. Cao, C. Pu, and R. Chen, "Study on the change of rock shear strength parameters in saturation state," *Minernal Engineering Research*, vol. 25, no. 3, pp. 29–32, 2010.
- [34] K. Li, K. Hou, and C. Zhang, "Experiment study on shear characteristics of saturated rock mass," *Journal of Central South University*, vol. 40, no. 2, pp. 538–542, 2009.
- [35] W. Xiao, R. Deng, X. Fu, and C. Wang, "Experimental study of deformation and strength properties of simulated columnar jointed rock masses under conventional triaxial compression," *Chinese Journal of Rock Mechanics and Engineering*, vol. 34, pp. 2817–2826, 2015.
- [36] P. Papanastasiou and M. Thiercelin, "Influence of inelastic rock behaviour in hydraulic fracturing," *International Journal of Rock Mechanics and Mining Sciences*, vol. 30, no. 7, pp. 1241–1247, 1993.
- [37] P. Papanastasiou, "The influence of plasticity in hydraulic fracturing," *International Journal of Fracture*, vol. 84, no. 1, pp. 61–79, 1997.
- [38] F. P. Beer, *Mechanics of Materials*, McGraw-Hill, New York, NY, USA, 2011.
- [39] J. Marler and S. Ge, "The permeability of the Elkhorn Fault Zone, South Park, Colorado," *Groundwater*, vol. 41, no. 3, pp. 321–332, 2003.